FIBER-OPTIC BUNDLED ARRAY CABLE REACTORS FOR HETEROGENEOUS PHOTOCATALYSIS AND WASTE STREAM REMEDIATION

Thesis by

Nicola J. Peill

In Partial Fulfillment of the Requirements

for the Degree of

Doctor of Philosophy

California Institute of Technology

Pasadena, California

1997

(Submitted September 4, 1996)

boundaries of potential exist only in the mind

i imagine and i will achieve

to my family for their gifts of life and love

Acknowledgments

I am truly indebted to the Caltech community for the experiences of last five years. These years have been a period of tremendous opportunity and spiritual and mental growth for which I am forever thankful. The spirit and the quality of the people and of the research conducted here is unequivocal. I can only hope that I have taken full advantage and, in some small way, contributed to Caltech's legacy.

Were it not for the generosity of my advisor and mentor, Michael Hoffmann, I would not have been able to indulge in the exploration of this great community. Michael has shown great patience and perseverance in developing me as a scientist and an author, thank you.

Continual support from and brain picking of Peter Green, Won Yong Choi, Patrick Lang, Ron Siefert, Ralph Hoechemer, Inez Hua, Andreas Termin, and Simo Pehkonen helped me to develop sound scientific techniques and to avoid tedious searches through manuals and text books. I reserve special thanks to Janet Kesselman, Scot Martin and Tom Lloyd for their stimulating discussions and debates (not always scientific) that have honed my critical thinking over the years and for their friendships that I hope will endure beyond these years.

And without the people who are the nuts and bolts of Caltech, nothing would be accomplished. For this I thank my secretary Linda Scott for her daily smiles and warming family stories; the EES secretary, Carmen Lopez, who has the patience of a saint and the organizational and diplomatic skills of a campaign manager; the EES librarians Susan Leising and Rayma Harrison for their tireless (and successful) searches for cryptic references; Rick Gerhart at the glass shop who made all of my OFR experimental vessels; and Mike Gerfen of Central Engineering who never gave up on the solar OFR no matter how many times he burned his fingers!

During my time at Caltech I have had the good fortune to nurture lasting friendships. The trying times would have been much less bearable and the good times much less fun without them: Kim Mislick, Jen Sun (my roommate of five years), Eric Bax, Raff D'Andrea, Brian Sullivan, Selena Forman, Kelly Johnson and Laura Lee Chin.

Finally, without my family, with whom I've had weekly conversations over the past five years, none of this would be meaningful. Their unwavering support throughout my life has made me who I am today; they never said "No." Thank you for everything, Maggie, Jerry and Ivan, Hugh and Eileen, Jackie and Walter, and Margot and Dieter.

Abstract

Application of semiconductor photocatalysis in a fixed-bed fiber-optic bundled array cable reactor (OFR) for the purification of contaminated water is investigated in this thesis. An optical fiber cable is employed as a means of light transmission and distribution to solid-supported TiO_2. The system is designed for remote delivery of light to the photocatalyst, to allow for measurement of light fluxes for direct determination of quantum yields and for reuse of the reactor to test various coatings and light input angles, and to minimize possible heat build-up and delamination problems.

Experiments are carried out to determine the operational factors affecting the chemical efficiency of the OFR system. The uniformity and extent of light propagation down the fiber, the degree of light absorption by the TiO_2 coating, the fiber diameter, the input light intensity, and the ability of the chemical substrates to diffuse into the TiO_2 coating are determined to be important parameters. In addition, a TiO_2 coating that minimizes the interfacial surface area of the quartz core and TiO_2 particles and operation with incident irradiation angles near 90° enhance light propagation down the fibers. Relative quantum efficiencies in the OFR are found to be comparable to slurry-phase photochemical reaction systems.

The OFR is shown to effectively degrade several model chemical contaminants such as pentachlorophenol (PCP), 4-chlorophenol (4CP), dichloroacetate (DCA), and oxalate (OX) under varying reaction conditions. Relatively high quantum efficiencies of ϕ = 0.010, 0.015, 0.08, and 0.17, respectively, and complete mineralization to CO_2, H_2O and HCl are observed.

When iron(III)-doped quantum-sized (Q) TiO_2 (Fe/Q-TiO_2) is used as a photocatalytic coating, the extent of linear light transmission in a single fiber is doubled relative to Degussa P25. However, the Fe/Q-TiO_2 coating is found to have inferior light

absorption properties and chemical reactivity leading to lower relative quantum efficiencies.

A concentrating, solar powered prototype OFR is designed and tested. Photoefficiencies with sunlight were comparable to that achieved with a Xe-arc source. Lower light intensity-to-photocatalytic surface area ratios result in increased relative quantum efficiencies.

A mathematical model of a fiber-optic bundled array reactor system is developed using Langmuir-Hinshelwood kinetics and compared to experimental data. A global quantum efficiency, ϕ_{global}, is defined and used as a model fitting parameter. It incorporates reaction parameters such as the absorbed light intensity, the intrinsic rate constant, and the effects of other adsorbed reactants and reaction intermediates. An empirical term to describe the radiation field within the coated fiber is derived and normalized by the coating photocatalyst particle concentration to account for the inverse relationship between the absorbed light intensity and the reaction quantum efficiency. The ϕ_{global} is determined to be independent of the absorbed light intensity and calculated values are in excellent agreement with experimental values.

An analysis of conventional and advanced remediation technologies is performed (Appendix). The chemistry and engineering behind advanced oxidation systems is reviewed, and a means of technical evaluation and comparison is presented. The "electrical energy per order," or EEO is defined as the electrical energy required to reduce the concentration of a given pollutant by one order of magnitude in 1000 gal of water. The EEO can be used to compare the efficacy of remediation technologies with other AOT's and conventional systems for a particular cleanup application.

Table of Contents

List of Figures

Chapter I

Chapter II

Chapter III

Chapter IV

Chapter V

Chapter VI

Chapter VII

Appendix

List of Tables

Chapter I

Chapter III

Chapter IV

Chapter V

Chapter VI

Appendix

Chapter I

Introduction and Overview

Introduction

General Background. Over the last half of the twentieth century, there has been a growing need for innovative and economically viable technologies to address environmental problems and challenges such as site remediation, end-of-pipe cleanup, and pollution prevention. Due to rapid industrialization and expansion in the 1940's and 50's and defense activities at military facilities that ignored long-term environmental impacts, the nation is now faced with a plethora of environmental problems relating to hazardous waste disposal, surface and groundwater contamination, and the control of toxic air emissions. The projected costs of remediation of contaminated sites alone is staggering. Cleanup of more than 1800 U.S. military installations has been estimated to be $30 billion over the next 10 years. The U.S. produces annually more than 540 million metric tons of hazardous waste (1). The elimination of hazardous substances from waste effluents and contaminated sites has become a national priority. Current production of waste emissions from power utilities, petrochemical facilities, and small, privately-owned operations, etc., is becoming highly regulated and increasingly more costly.

In order to address these cleanup and pollution control challenges, the EPA has regulated the use of Best Available Technology (BAT). BAT technologies have been found by the EPA to meet the standards and specifications that provide safe and sufficient pollution control of industrial processes and remediation of contaminated sites. The accepted treatment technologies are air stripping, carbon absorption, high-temperature incineration, biological remediation, and catalytic oxidation. Only air stripping, carbon adsorption and biological remediation are typically applied to aqueous-phase waste streams, which represent the bulk of remediation and pollution control problems. Except for bioremediation, these technologies are nondestructive; that is, the contaminants are not destroyed but transferred from one phase to another which may require further processing and/or disposal.

More recently, the EPA has approved the inclusion of advanced oxidation technologies (AOT's) in the BAT category which may prove to be more economically efficient for certain remediation and pollution control applications. These AOT systems have the advantages of on-site destruction of contaminants with little to no air emissions and no generation of residuals such as ash or spent carbon that require further handling. These benefits alleviate the liability associated with off-site destruction and media transfer that is characteristic of the conventional pollution control technologies. AOT's include UV/oxidation, ultraviolet radiation in conjunction with oxidants and photocatalysts, chemical oxidation employing ozone, hydrogen peroxide, etc., super critical water oxidation (SCWO), and wet air oxidation.

These technologies have been the focus of intensive research over the past two decades. Benchscale research provides crucial insight into chemical process optimization, while field and pilot testing demonstrate the use of these processes on a practical level and reveal the advantages and drawbacks relative to conventional approaches.

As early as 1978, in a detailed study on the cleanup of PCB's at manufacturing sites comparing carbon adsorption with an UV/oxidation(ozone) process, it was concluded that the AOT process was thought to be highly promising as an economical destructive method (2). BTEX pollutants were successfully destroyed during field testing of solar photocatalytic detoxification of jet-fuel-contaminated groundwater at Tyndall Air Force Base (3). Over the last five years, the number of full scale UV/oxidation facilities has grown enormously. At present the city of South Gate in California is operating a UV/O_3 system at a 950 gpm wastewater treatment plant to remove trichloroethylene (TCE) and perchloroethylene (PCE) from ground water (4). Trade names such as Rayox^R, Ultrox^R, and Purox-pure^R are becoming industry standards. However, at present, no single technology offers the most efficient solution, both technically and

economically, for every pollution treatment problem. Nonetheless, AOT's show great promise either as stand alone or as complementary remediation methods.

Advanced Oxidation Processes. Advanced oxidation processes have been defined broadly as those aqueous-phase chemical processes whose mechanism involves primarily active radical species, typically the hydroxyl radical (•OH), leading to the complete destruction of the target pollutant. Some advanced oxidation processes can also be applied to gas-phase waste streams such as UV photolysis, UV/ozone, and UV/photocatalysis. Unlike some conventional treatment technologies, oxidation of a pollutant, generally an organic molecule, such as acetone, or a halogenated hydrocarbon, such as PCB (polychlorinated biphenyl), will lead to the complete mineralization of that compound eliminating the need for further treatment or disposal. Mineralization refers to the conversion of a compound to CO_2, H_2O, and residual inorganic salt or acid, such as HCl. The following equation represents a generalized oxidation process:

$$\underset{\text{chlorinated organic molecule}}{} \xrightarrow{O_2/\bullet OH} \underset{\text{oxygenated intermediates}}{} \xrightarrow{O_2/\bullet OH} CO_2 + H_2O + Cl^- \qquad (1)$$

The hydroxyl radical is one of the most powerful oxidizing agents after molecular fluorine. Table 1 lists common oxidants and their oxidation potentials (5). Hydroxyl radical reacts with substrates either via H-atom abstraction or direct electron transfer as follows:

$$\bullet OH + RH \rightarrow R\bullet + H_2O \qquad (2)$$

$$\bullet OH + RX \rightarrow RX^{\bullet +} + OH^- \qquad (3)$$

where RH is a generic hydrocarbon compound and X is a halogen substituent such as Cl. In the presence of oxygen, these reactions (Eqs. 2 and 3) will initiate a squence of thermal reactions involving R• and peroxyl radicals, $RO_2^{\bullet}$, that eventually lead to complete mineralization of the organic species as follows:

$$C_xH_yCl_x + (x + \frac{y-z}{4})O_2 \rightarrow xCO_2 + zH^+ + zCl^- + \frac{(y-z)}{2}H_2O \quad (4)$$

In advanced oxidation processes, hydroxyl radicals are produced by the photolysis of hydrogen peroxide, H_2O_2 (Eq. 5), by conversion of ozone (O_3) to hydrogen peroxide and finally to •OH (Eq. 6), and by the oxidation of an adsorbed OH^- species (or H_2O) on a solid photocatalytic surface, such as titanium dioxide (TiO_2) ($>Ti^{IV}OH$)

$$H_2O_2 \xrightarrow{hv\ (\lambda<300nm)} \bullet OH + OH^- \quad (5)$$

$$O_3 \xrightarrow{hv\ (\lambda<310nm)} O_2 + O(^1D) \quad (6a)$$

$$O(^1D) + H_2O \rightarrow H_2O_2 \quad (6b)$$

$$H_2O_2 + H_2O \rightarrow HO_2^- + H_3O^+ \quad (6c)$$

$$HO_2^- + O_3 \rightarrow O_3^- + HO_2^\bullet \quad (6d)$$

$$O_3^- + \rightarrow H_3O^\bullet + OH^- \quad (6e)$$

$$H_3O^\bullet \rightarrow \bullet OH + O_2 \quad (6f)$$

$$>TiO_2 \xrightarrow{hv\ (\lambda<375nm)} h_{vb}^+ + e_{cb}^- \quad (7a)$$

$$>Ti^{IV}OH \rightarrow \{>Ti^{IV}OH\bullet\}^+ \quad (7b)$$

The above reactions represent the basis for UV/H_2O_2 (Eq. 5), UV/O_3 (Eq. 6), and UV/TiO_2 (Eq. 7) advanced oxidation processes, respectively. In addition, any combination of H_2O_2, O_3, and TiO_2 may also be used.

Semiconductor Photocatalysis and Photochemical Reactors. Heterogeneous photocatalysis on metal oxide semiconductor particles has been shown to be an effective means of removing organic and inorganic pollutants from water and air streams (1, 6-8). It has been applied to a wide range of problems of environmental interest including the destruction of microorganisms (9, 10), odor control and ambient air purification (11), and the clean-up of oil spills (12-14).

Absorption of light energy equal to or greater than the semiconductor band gap energy by the photocatalyst generates active charge pair species which include conduction band electrons, e^-, and valence band holes, h^+, as illustrated in Fig. 1. These charge pairs can act as reductants (+0.5 to -1.5 V vs NHE) and oxidants (+1.0 to +3.5 V vs. NHE depending on the semiconductor and pH), respectively. Subsequent reactions with surface-sorbed electron donors (e.g., organic contaminants) and acceptors (e.g., O_2) form highly reactive species such as hydroxyl and superoxide radicals. Most hydrocarbon pollutants have been shown to be oxidized by the photogenerated holes or trapped holes (i.e., surface-bound OH•) while some hydrocarbon contaminants and metals can be degraded or removed via a reductive pathway (15). The effects of photocatalyst composition, structure, crystal size, band gap energy, incident light intensity, and the nature of the electron donors and acceptors on photocatalytic reactivity have been investigated (16-30).

The UV photocatalytic process has several unique characteristics compared to other advanced oxidation processes. Photocatalysts such as TiO_2 can absorb photons at wavelengths into the near UV (e.g., $\lambda < 385$ nm). This means that the TiO_2 system can utilize a greater portion of the lamp output than the UV/H_2O_2 and UV/O_3 processes. Furthermore, it can utilize 4% of the solar spectrum allowing for application in areas where sunlight is an efficient UV radiation source and/or where electrical power is not readily available or economically feasible. In addition, metals such as chromium (19, 20, 31), copper (32, 33), and mercury (19, 34, 35) can be removed via a reduction and plating process from aqueous-phase waste streams which is unique among the UV/oxidation processes (36). UV photocatalysis can also be used for treatment of gas-phase waste streams for which UV/O_3, carbon absorption, incineration, and catalytic oxidation are also competing technologies. Unlike these other processes, though, the activated photocatalyst can effect both oxidation and reduction reactions. Thus, contaminants that

are not amenable to oxidation by O_3 and H_2O_2 can be reduced by the photocatalyst. Finally, unlike O_3 and H_2O_2, TiO_2, which is highly photocatalytically active, is inexpensive, easy to handle, robust, and environmentally benign.

The main disadvantage of the UV/photocatalyst process is that it is generally less efficient than other advanced oxidation processes at converting electrical power into hydroxyl radicals despite enhanced light absorption at the higher wavelengths compared to O_3 ($\lambda < 300$ nm) and H_2O_2 ($\lambda < 254$ nm). Photochemical quantum efficiencies, ϕ, (i.e., the moles of pollutant converted per moles of photons absorbed) are also correspondingly low, ~1-10% for semiconductor photocatalysts compared to 50-100% for H_2O_2 and O_3 (37). Furthermore, ϕ is inversely dependent on the absorbed light intensity (i.e., as the light intensity increases ϕ decreases). On the other hand, the rate of radical production and, hence, degradation rate, is proportional to the light intensity. Thus, in order to effect timely degradation, based on current reactor designs, the system needs to be operated at high light intensities in a regime where the photocatalyst is less efficient. Nonetheless, ongoing work to enhance photocatalyst quantum efficiencies by metal ion doping (38, 39), metal loading (40-42), improved electron acceptors (15, 43), periodic illumination (44), the use of additional oxidants (24, 45-49), and reducing charge carrier recombination and interfacial transfer times (50-52) continues to improve the competitiveness of this process.

Practical application of photocatalytic oxidation often requires the immobilization of the photocatalyst in the reactor that allows continuous use of the photocatalyst by eliminating the need for post-process filtration and resuspension. Legrini et al. (5) have argued that the chemical viability of TiO_2 photocatalysis has been established and that the next stage of development of the process will depend on new ideas for fixation of TiO_2 and on new designs for photochemical reactors. Immobilization of the photocatalyst can lead to a mass transfer limited reaction, although mass transfer

limitations can be mitigated by efficient reactor design. A variety of heterogeneous supports have been explored including glass beads (53, 54), lamp casings (20, 55), glass plates (56), reactor walls (54, 57), fiberglass mesh (58), and porous films on glass substrates (59, 60). Some of these configurations are shown in Fig. 2.

Thesis Work

In order to meet this reactor design challenge, a fixed-bed system that employs a bundled optical fiber cable array as a means of light transmission to solid-supported TiO_2 is developed. The viability of such a design and the basic parameters governing the chemical efficiency of the reactor system are investigated in this thesis. The basic premise of the configuration is that light traveling down an optical fiber can be refracted out of the fiber and into a photocatalytic coating thus activating it as shown in the photograph in Fig. 3. This novel approach was first proposed by Ollis and Marinangeli in 1977 (61, 62). However, they predicted that photocatalytic-optical fiber reactor systems would not be practical due to catalyst deactivation caused by heat buildup in a bundled array. Hofstadler et al. (63) have shown recently that TiO_2-coated quartz fiber rods fixed in a tubular reactor configuration can be used to carry out oxidation of 4-chlorophenol. They reported effective quantum yields of 0.0002. Gapen and Anderson (64) investigated the use of an optical-fiber cable reactor for photocatalytic oxidation. Problems with delamination of the TiO_2 coating resulted in partial degradation of 3-chlorosalicylic acid. However, a maximum quantum efficiency of 0.069 for the partial photolytic and photocatalytic oxidation of 3-chlorosalicylic acid was estimated. They concluded that a method for obtaining a stable photocatalytic coating needed to be developed before an optical fiber system would be practical.

With these hurdles in mind, the system is designed for remote delivery of light to the photocatalyst, to allow for measurement of light fluxes for direct determination of

quantum yields and for reuse of the reactor to test various coatings and light input angles, and to minimize possible heat build-up and delamination problems (Fig. 4). This reactor configuration enhances the uniformity and distribution, and, potentially, the illuminated surface-area of the light-activated catalyst within a given reaction volume relative to conventional fixed-bed reactor designs. This should result in reduced mass transport limitations to photochemical conversion and allow for higher processing capacities. The system can be operated in both gas- and aqueous-phase modes.

The work described in Chapter II establishes the feasibility of an OFR system for the effective destruction of hydrocarbon contaminants and determines the parameters that govern the chemical efficiency of the OFR. These operational factors are: the uniformity and extent of light propagation down the fiber, the degree of light absorption by the TiO_2 coating of the refracted light, and the ability of the chemical substrates to diffuse into the TiO_2 coating. A TiO_2 coating layer that minimizes the interfacial surface area of the quartz core and TiO_2 particles and operation with incident irradiation angles near 90°, enhance light propagation down the fibers. Relative quantum efficiencies of up to ϕ = 0.011 for the photooxidation of 4-chlorophenol are observed. These values are comparable to a slurry-phase reaction system operated under similar conditions.

In Chapter III further efficiency studies are detailed and the effective degradation of several model hydrocarbon contaminants such as pentachlorophenol (PCP), 4-chlorophenol (4CP), dichloroacetate (DCA), and oxalate (OX) under varying reaction conditions is demonstrated. The distribution of light as a function of fiber diameter and the effect of incident light intensity on the relative photochemical quantum efficiency is explored. Light propagation down individual fibers is found to increase with increasing fiber diameter. An increased linear transmission of light results in increased quantum efficiencies, while a two-order of magnitude reduction in incident light intensity results in a four-fold increase (ϕ = 0.010 to 0.042) in quantum efficiency for the degradation of 4-

chlorophenol. The rates of degradation of dichloroacetate and oxalate have strong pH-dependencies. Relatively high apparent quantum efficiencies of ϕ = 0.010, 0.015, 0.08, and 0.17 for PCP, 4-CP, DCA, and OX, respectively, and complete mineralization to CO_2, H_2O and HCl are observed.

In Chapter IV, the important aspects of an OFR photocatalytic coating are investigated. In the previous studies, Degussa P25 TiO_2 had been used exclusively and is, here, used as a baseline for comparison with a coating consisting of quantum-sized, iron(III)-doped TiO_2 (Fe/Q-TiO_2). Previous work in our lab found Fe/Q-TiO_2 to have photoefficiencies comparable to P25 for the photooxidation of chloroform (15). In addition, scanning electron microscope (SEM) analysis of Fe/Q-TiO_2-coated optical fibers reveal unique characteristics which indicate that a Q-TiO_2 coating might increase the linear light transmission down the fiber relative to a P25 coating. Extension of the linear light transmission has been found to enhance the system's photochemical quantum efficiency. (65). In this chapter, we compare the linear light transmission characteristics in single fibers and the relative quantum efficiencies for the photodegradation of 4-chlorophenol with three different TiO_2 coatings: Fe/Q-TiO_2 coatings made from hydrosols of varying Fe/Q-TiO_2 content (5 to 23 wt%), a 13 wt% P25 coating, and a layered hybrid Fe/Q-TiO_2/P25 (5/13 wt%) coating. The light absorption efficiencies of the Fe/Q-TiO_2 coatings are inferior to the P25 coating, absorbing a maximum of only 80% of the input light compared to greater than 95% for P25 and 90% for the hybrid coating. The Fe/Q-TiO_2 coatings are found to increase the linear light transmission in a single optical fiber relative to P25 coated fibers by a factor of two due to a reduced interfacial surface coverage of the photocatalyst particles on the quartz fiber. The hybrid coating does not significantly enhance linear light transmission.

Slurry-phase photoefficiencies for the photooxidation of 4-chlorophenol for the Fe/Q-TiO_2 photocatalyst are found to be significantly lower than those measured for P25,

$\phi_{Fe/Q\text{-}TiO2}$ = 0.002 vs. ϕ_{P25} = 0.012. In addition, the length of the coated fiber-bundle used in the OFR is insufficient to capitalize on the increased light transmission for the Fe/Q-TiO_2 coating. Thus, it is not possible to determine the effect of increased light transmission on the photoefficiency of the system. Initial reaction rates for the photooxidation of 4-chlorophenol range from 2.0 to 4.5 $\mu M\text{-}hr^{-1}$ generally increasing with increasing hydrosol Fe/Q-TiO_2 content and an average relative quantum efficiency of $\phi_{Fe/Q\text{-}TiO2} = 0.004 \pm 0.001$ is observed. These values are significantly low compared to initial rates and relative quantum efficiencies of 18.0 $\mu M\text{-}hr^{-1}$ and $\phi_{Fe/Q\text{-}TiO2/P25}$ = 0.011 and 20.4 $\mu M\text{-}hr^{-1}$ and ϕ_{P25} = 0.012 for the hybrid and P25 coatings, respectively.

The feasibility of using solar radiation to power an OFR is explored in Chapter V. The photocatalytic process has been criticized as being uneconomical compared to other oxidative treatment systems due to its low photochemical conversion efficiencies resulting in higher energy costs (66, 67). There is, however, a growing body of laboratory and field studies which suggest that the use of solar radiation to power photocatalytic reactor systems may lead to more economical treatment alternatives for certain applications (68-81). Chapter V presents the design and testing of a second-generation solar-powered fiber-optic cable reactor (OFR2) for the photocatalytic destruction of organic pollutants. The performance of the OFR2 using solar and artificial UV radiation are compared. The system is also compared to the first-generation fiber-optic cable reactor (OFR1) having a 50% higher photocatalytic surface area-to-reactor volume ratio to investigate mass transport limitations. Reaction rates for the oxidation of 4-chlorophenol of 25 and 12 $\mu M\text{-}min^{-1}$ were measured for solar and artificial UV sources, respectively. The faster reaction rate using solar radiation is due to a higher UV light flux compared to the artificial source. The reaction rates in both fiber optic reactor systems were not limited by mass transport to the reactive surfaces. Relative quantum efficiencies of ϕ = 0.014 and ϕ = 0.020 were determined for the solar and artificial

irradiations, respectively. In agreement with the findings in Chapter III, enhanced quantum efficiencies are attributed to a lower absorbed light intensity-to-photocatalytic surface area ratio.

In order to better understand the OFR system, a basic mathematical model to describe the degradation of a single compound in a fiber-optic bundled array photocatalytic batch reactor (OFR) using a Langmuir-Hinshelwood kinetic expression is developed and presented in Chapter VI. An empirical global quantum efficiency, ϕ_{global}, which incorporates reaction parameters such as the absorbed light intensity, intrinsic rate constants, concentration of adsorbed reactants, and reaction intermediates, is used as a fitting parameter. An empirical term to describe the radiation field within the coated fiber is derived experimentally and normalized by the photocatalyst particle concentration within the fiber optic coating to account for the inverse relationship observed between absorbed light intensity and reaction quantum efficiency. Results of the mathematical model are compared to experimental data generated in an OFR for the photocatalytic oxidation of 4-chlorophenol (4CP), pentachlorophenol (PCP), and dichloroacetate (DCA). The global quantum efficiency, ϕ_{global}, was found to be independent of absorbed light intensity. Calculated kinetic profiles are in excellent agreement with experimental observation.

A final chapter, which is presented in the appendix, reviews the science and engineering behind AOT's in relationship to factors affecting energy efficiencies that have a direct impact on both the capital and operating costs of a practical system. An economic comparison among the various AOT's and conventional technologies is prepared.

Literature

(1) Hoffmann, M. R.; Martin, S. T.; Choi, W.; Bahnemann, D. W. *Chem. Rev.* **1995**, *95*, 69-96.

(2) Hackman III, E. E. In *Toxic Organic Chemicals: Destruction and Waste Treatment*; E. E. Hackman III, Eds.; Noyes Data Coporation: Park Ridge, NJ, 1978; p 285-317.

(3) Turchi, C. S.; Klausner, J. F.; Marchani, E.; Goswami, D. Y. In *Chemical Oxidation: Technology for the Nineties*, Nashville, TN, 1993; pp 1-10.

(4) Glaze, W. H. In *Chemical Oxidation: Technology for the Nineties*, Nashville, TN, 1993; pp 1-10.

(5) Legrini, E.; Oliveros, E.; Braun, A. M. *Chem. Rev.* **1993**, *93*, 671.

(6) Fox, M. A.; Dulay, M. T. *Chem. Rev.* **1993**, *93*, 341-357.

(7) Ollis, D. F.; Al-Ekabi, H. *Photocatalytic Purification and Treatment of Water and Air*; Elsevier: Amsterdam, 1993.

(8) Kamat, P. V. *Chem. Rev.* **1993**, *93*, 267-300.

(9) Ireland, J. C.; Klostermann, P.; Rice, E. W.; Clark, R. M. *Appl. Environ. Microbiol.* **1993**, *59*, 1668-1670.

(10) Sjogren, J. C.; Sierka, R. A. *Appl. Environ. Microbiol.* **1994**, *60*, 344-347.

(11) Suzuki, K. In *Photocatalytic Purification and Treatment of Water and Air*; D. F. Ollis and H. Al-Ekabi, Eds.; Elsevier Science Publishers, B. V.: Amsterdam 1993; p 421-434.

(12) Gerischer, H.; Heller, A. *J. Electrochem. Soc.* **1992**, *139*, 113-118.

(13) Nair, M.; Luo, Z. H.; Heller, A. *Ind. Eng. Chem. Res.* **1993**, *32*, 2318-2323.

(14) Jackson, N. B.; Wang, C. M.; Luo, A.; Schwitzgebel, J.; Ekerdt, J. G.; Brock, J. R.; Heller, A. J. *J. Electrochem. Soc.* **1991**, *138*, 3660-3664.

(15) Choi, W.; Hoffmann, M. R. *Environ. Sci. Technol.* **1995**, *29*, 1646-1654.

(16) Abdullah, M.; Low, G. K. C.; Matthews, R. W. *J. Phys. Chem.* **1990**, *94*, 6820.

(17) Kormann, C.; Bahnemann, D. W.; Hoffmann, M. R. *J.Phys.Chem.* **1988**, *92*, 5196.

(18) Kormann, C.; Bahnemann, D. W.; Hoffmann, M. R. *Environ. Sci. Technol.* **1991**, *25*, 494-500.

(19) Prairie, M. R.; Evans, L. R.; Stange, B. M.; Martinez, S. L. *Environ. Sci. Technol.* **1993**, *27*, 1776-1782.

(20) Sabate, J.; Anderson, M. A.; Aguado, M. A.; Gimenez, J.; Cerveramarch, S.; Hill, C. G. *J. Mol. Catal.* **1992**, *71*, 57-68.

(21) Herrmann, J. M.; Disdier, J.; Pichat, P. *J. Phys. Chem.* **1986**, *90*, 6028-6034.

(22) Erbs, W.; Desilvestro, J.; Borgarello, E.; Gratzel, M. *J. Phys. Chem.* **1984**, *88*, 4001-4006.

(23) Matthews, R. W. *Water Res.* **1986**, *20*, 569.

(24) Pelizzetti, E.; Carlin, V.; Minero, C.; Grätzel, M. *New J. Chem.* **1991**, *15*, 351.

(25) Hoffmann, A. J.; Yee, H.; Mills, G.; Hoffmann, M. R. *J. Phys. Chem.* **1992**, *96*, 5540.

(26) Choi, W.; Termin, A.; Hoffmann, M. R. *Angew. Chem.* **1994**, *106*, 1148-1149.

(27) Grätzel, M. *Heterogeneous Photochemical Electron Transfer*; CRC Press: Boca Raton, FL, 1989.

(28) Fox, M. A. *Photochem. Photobiol.* **1990**, *52*, 617.

(29) Matthews, R. W. *J. Catal.* **1988**, *111*, 264-272.

(30) Turchi, C. S.; Ollis, D. F. *J. Catalysis* **1990**, *122*, 178.

(31) Aguado, M. A.; Gimenez, J.; Cervera-March, S. *Chem. Eng. Commun.* **1991**, *104*, 71-85.

(32) Peral, J.; Domenech, X. *J. Chem. Technol. and Biotechnol.* **1992**, *53*, 93-96.

(33) Foster, N. S.; Noble, R. D.; Koval, C. A. *Environ. Sci. Technol.* **1993**, *27*, 350-356.

(34) Tennakone, K.; Thaminimulle, C. T. K.; Senadeera, S.; Kumarasinghe, A. R. *Photochem. Photobiol. A: Chem.* **1993**, *70*, 193-195.

(35) Serpone, N.; Ah-You, Y. K.; Tran, T. P.; Harris, R.; Pelizzetti, E.; Hidaka, H. *Solar Energy* **1987**, *39*, 491-498.

(36) Miller, R.; Fox, R. In *Photocatalytic Purification and Treatment of Water and Air: Trace Metals in the Environment*; D. F. O. a. H. Al-Ekabi, Eds.; Elsevier Science Publishers B.V.: Amsterdam, N.V. 1993; p 573-578.

(37) Venkatadri, R.; Peters, R. W. *Hazardous Waste & Hazardous Materials* **1993**, *10*, 107-149.

(38) Martin, S. T.; Morrison, C. L.; Hoffmann, M. R. *J. Phys. Chem.* **1994**, *98*, 13695.

(39) Choi, W.; Termin, A.; Hoffmann, M. R. *J. Phys. Chem.* **1994**, *98*, 13669-13679.

(40) Harada, K.; Hisanaga, T.; Tanaka, K. *Water Res.* **1990**, *24*, 1415.

(41) Rose, T. L.; Nanjundiah, C. *J. Phys. Chem.* **1985**, *89*, 3766.

(42) Hisanaga, T.; Harada, K.; Tanaka, K. *J. Photochem. Photobiol. A: Chem.* **1990**, *54*, 113.

(43) Martin, S. T.; Lee, A. T.; Hoffmann, M. R. *Environ. Sci. Technol.* **1995**, *29*,

(44) Sczechowski, J. G.; Koval, C. A.; Noble, R. D. *J. Photochem. Photobiol. A: Chem.* **1993**, *74*, 273-278.

(45) Tanaka, K.; Hisanaga, T.; Harada, K. *Nouv. J. Chim.* **1989**, *13*, 5.

(46) Al-Ekabi, H.; Edwards, G.; Holden, W.; Safaazadeh-Amiri, A.; Story, J. In *Chemical Oxidation*; W. W. Eckenfelder, A. R. Bowers and J. A. Roth, Eds.; Technomic Publishing Company: Lancaster, PA, 1992; p 254-261.

(47) Ollis, D. F.; Pelizzetti, E.; Serpone, N. *Environ. Sci. Technol.* **1991**, *25*, 1522-1529.

(48) Hackley, V. A.; Anderson, M. A.; Spooner, S. *J. Matls. Res.* **1992**, *7*, 2555-2571.

(49) Halmann, M. *J. Photochem. Photobiol. A: Chem.* **1992**, *66*, 215.

(50)Martin, S. T.; Herrmann, H.; Choi, W.; Hoffmann, M. R. *J. Chem. Soc. Faraday Trans.* **1994**, *90*, 3315.

(51) Martin, S. T.; Herrmann, H.; Hoffmann, M. R. *J. Chem. Soc. Faraday Trans.* **1994**, *90*, 3323.

(52) Herrmann, H.; Martin, S.; Hoffmann, M. R. *J. Phys. Chem.* **1995**, *99*, 16641-16645.

(53) Serpone, N. *Sol. Energy* **1986**, *14*, 121-126.

(54) Al-Ekabi, H.; Serpone, N. *J. Phys. Chem.* **1988**, *92*, 5726-5731.

(55) Sabate, J.; Anderson, M. A.; Kikkawa, H.; Edwards, M.; Hill, C. G. *J. Catal.* **1991**, *127*, 167-177.

(56) Anderson, M. A.; Gieselmann, M. J.; Xu, Q. Y. *J. Membr. Sci.* **1988**, *39*, 243-258.

(57) Matthews, R. W.; Abdullah, M.; Low, G. K. C. *Anal. Chim. Acta* **1990**, *233*, 171-179.

(58) Al-Ekabi, H.; Safarzadey-Amiri, A.; Sifton, W.; Story, J. *Intl. J. Environ. Pollut.* **1991**, *1*, 125-136.

(59) Sabate, J.; Anderson, M. A.; Kikkawa, H.; Xu, Q.; Cerveramarch, S.; Hill, C. G. *J. Catal.* **1992**, *134*, 36-46.

(60) Aguado, M. A.; Anderson, M. A.; Hill, C. G. *J. Mol. Catal.* **1994**, *89*, 165-178.

(61) Ollis, D. F.; Marinangeli, R. E. *AIChE J.* **1977**, *23*, 415-425.

(62) Ollis, D. F.; Marinangeli, R. E. *AIChE J.* **1980**, *26*, 1000-1007.

(63) Hofstadler, K.; Bauer, R.; Novalic, S.; Heisler, G. *Environ. Sci. Technol.* **1994**, *28*, 670-674.

(64) Gapen, D. C., Photocatalytic Degradation of Chlorinated Hydrocarbons, M. S., Institution, 1991.

(65) Peill, N. J.; Hoffmann, M. R. *Environ. Sci. Technol.* **1995**, *29*, 2974.

(66) Wilson, E. *Chem. Engrng. News* **1996**, 29.

(67) Renner, R. *Environ. Sci. Technol.* **1996**, *30*, 284.

(68) Bockelman, D.; Goslich, R.; Weichgrebe, D.; Bahnemann, D. In *Photocatalytic Purification and Treatment of Water and Air*; D. F. Ollis and H. Al-Ekabi, Eds.; Elsevier Science Publishers B. V.: Amsterdam 1993; p 771-776.

(69) Mehos, M. S.; Turchi, C. S. *Environ. Prog.* **1993**, *12*, 194-199.

(70) Matthews, R. W. *Solar Energy* **1987**, *38*, 405-413.

(71) *Chem. Eng. News* **1985**, *41*.

(72) Pacheco, J. E.; Prairie, M. R.; Yellowhorse, L. *J. Solar Energy Eng.* **1993**, *115*, 123-129.

(73) Crittenden, J. C.; Zhang, Y.; Hand, D. W.; Perram, D. L.; Marchand, E. G. *Wat. Environ. Res.* **1996**, *68*, 270-278.

(74) Zhang, Y.; Crittenden, J. C.; Hand, D. W.; Perram, D. L. *J. Solar Energy Engnrg.* **1996**, *118*, 123-129.

(75) Pugh, K. C.; Kiserow, D. J.; Sullivan, J. M.; Grinstead, J. H. In *ACS Industrial and Engineering Chemistry Special Symposium*, Atlanta, GA, 1995; pp 174-194.

(76) Minero, C.; Pelizzetti, E.; Malato, S.; Blanco, J. *Chemosphere* **1993**, *26*, 2103-2119.

(77) Muradov, N. Z. *Solar Energy* **1994**, *52*, 283-288.

(78) Wyness, P.; Klausner, J. F.; Goswami, D. Y.; Schanze, K. S. *J. Solar Energy Eng. Trans. ASME* **1994**, *116*, 2-7.

(79) Wyness, P.; Klausner, J. F.; Goswami, D. Y.; Schanze, K. S. *J. Solar Energy Eng. Trans. ASME* **1994**, *116*, 8-13.

(80) Zhang, Y.; Crittenden, J. C.; Hand, D. W.; Perram, D. L. In *American Water Works Association Annual Conference*, San Antonio, TX, 1993.

(81) Zhang, Y.; Crittenden, J. C.; Hand, D. W.; Perram, D. L. *Environ. Sci. Technol.* **1994**, *28*, 435-442.

SPECIES	OXIDATION POTENTIAL (V)
Fluorine (F_2)	-3.03
Hydroxyl radical (•OH)	-2.80
Atomic oxygen (O)	-2.42
Ozone (O_3)	-2.07
Hydrogen peroxide (H_2O_2)	-1.78
Perhydroxyl radical ($HO_2^•$)	-1.70
Permanganate (MnO_4^-)	-1.68
Hypobromous acid (HOBr)	-1.59
Chlorine dioxide (ClO_2)	-1.57
Hypochlorous acid (HOCl)	-1.49
Hypoiodous acid (HOI)	-1.45
Chlorine (Cl_2)	-1.36
Bromine (Br_2)	-1.09
Iodine (I_2)	-0.54

Table 1. Oxidation Potentials of various chemical species.

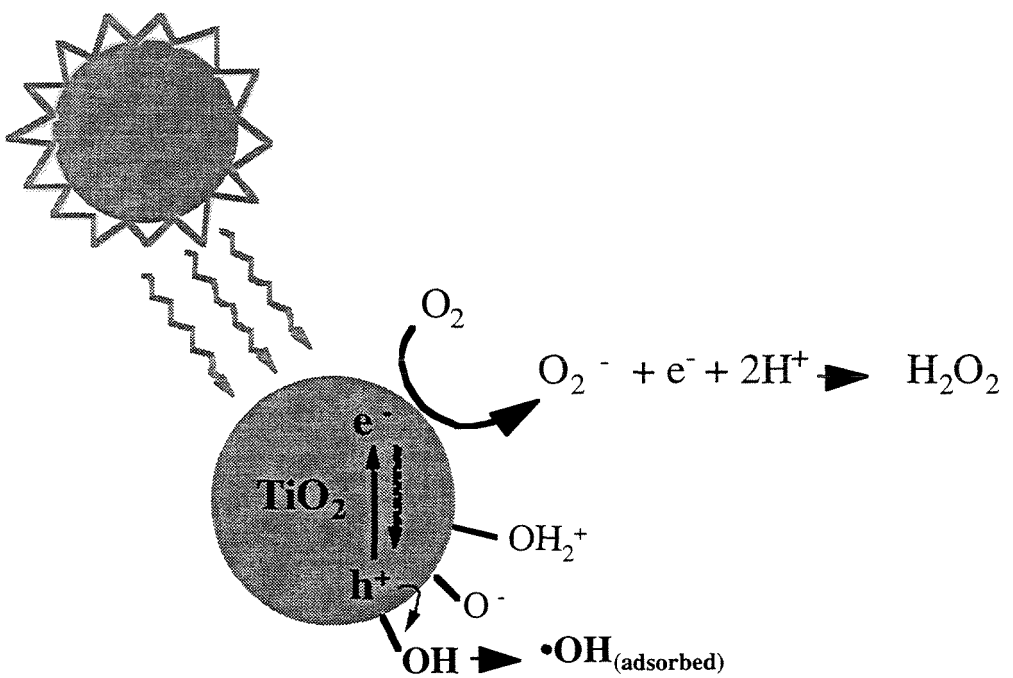

Figure 1. Photocatalysis at activated TiO_2 particle surface.

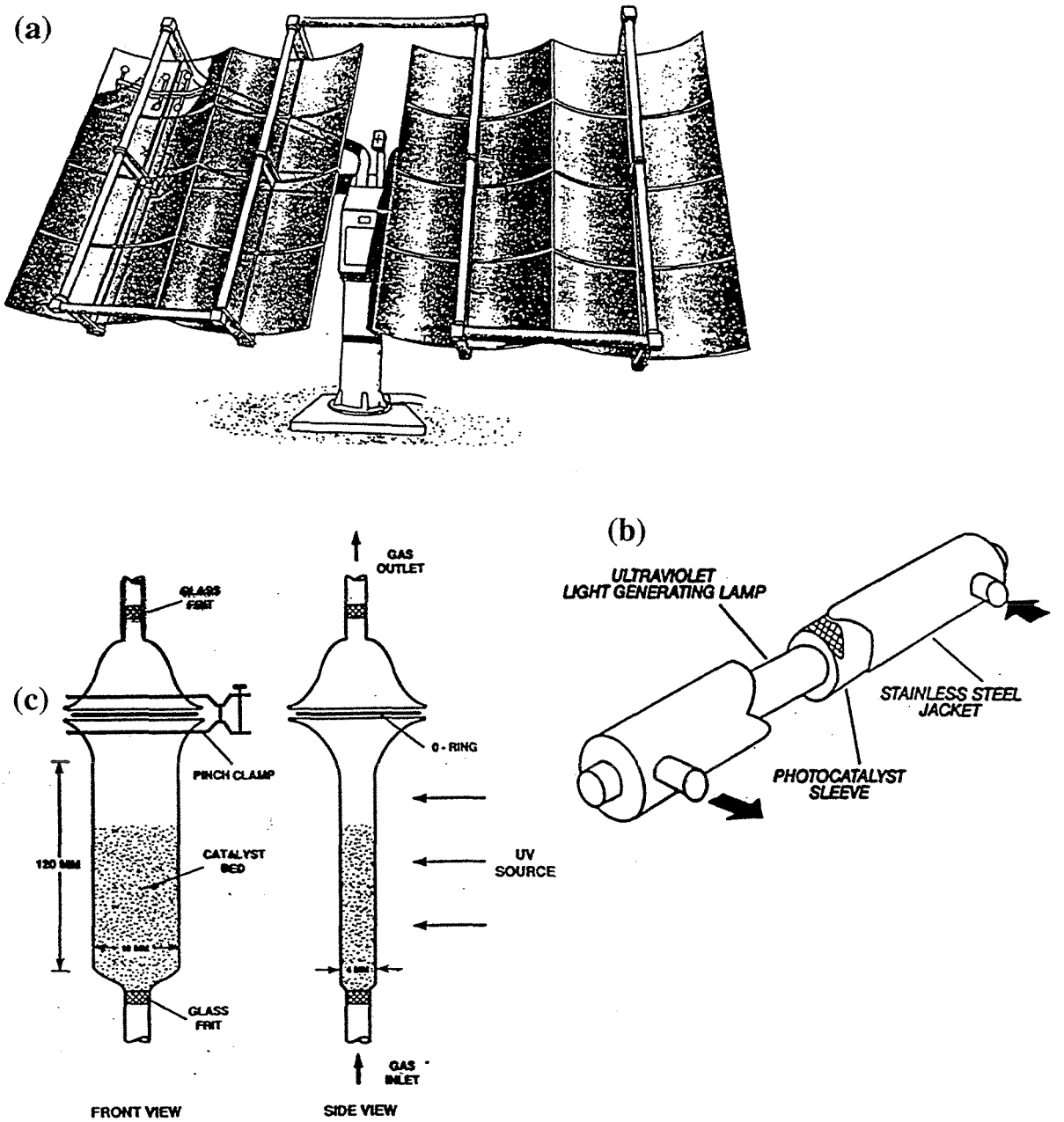

Figure 2. Continuous flow photochemcial reactor configurations: (a) Helioman-type solar-powered slurry-phase reactor (reprinted from Minero, C.; Pelizzetti, E.; Malato, S.; Blanco, J. *Chemosphere* **1993** *25*, 2103); (b) fluidized-bed gas reactor (reprinted from Dibble, L. A.; Raupp, G. B. *Environ. Sci. Technol.* ***1992, 26***, 492-495); (c) aqueous- and gas-phase fixed-bed reactor (reprinted from Al-Ekabi, H.; Serpone, N. *J. Phys. Chem.* **1988**, *92*, 5726-5731).

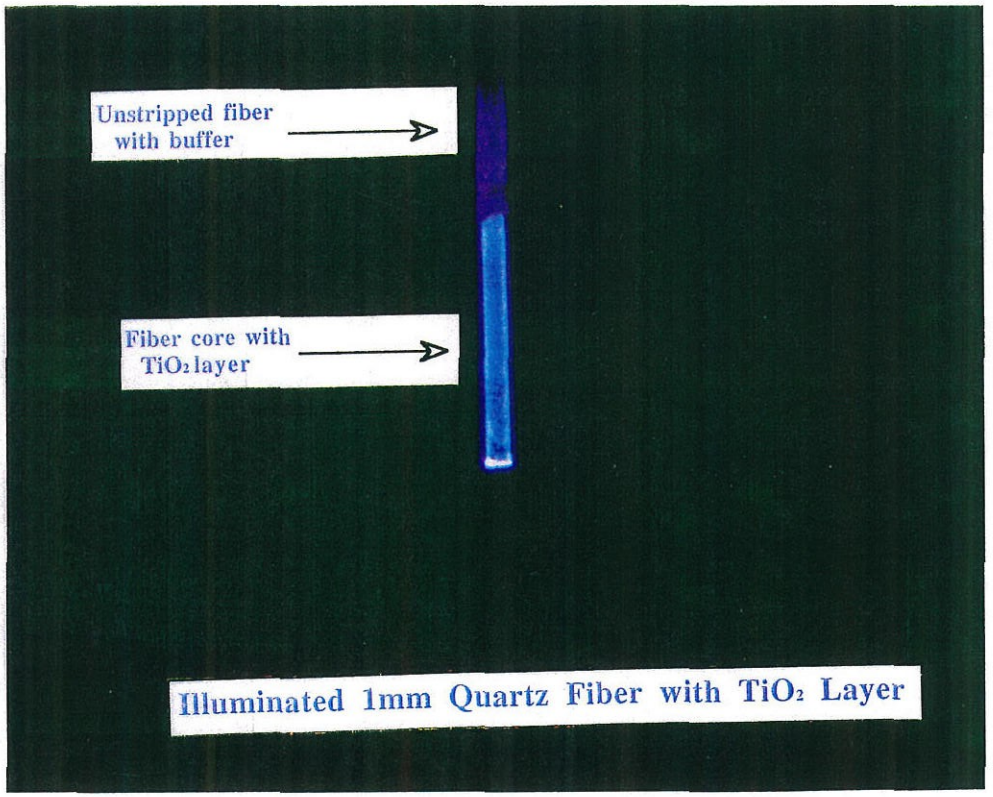

Figure 3. Light traveling down a 1 mm-diameter quartz optical fiber coated with TiO_2.

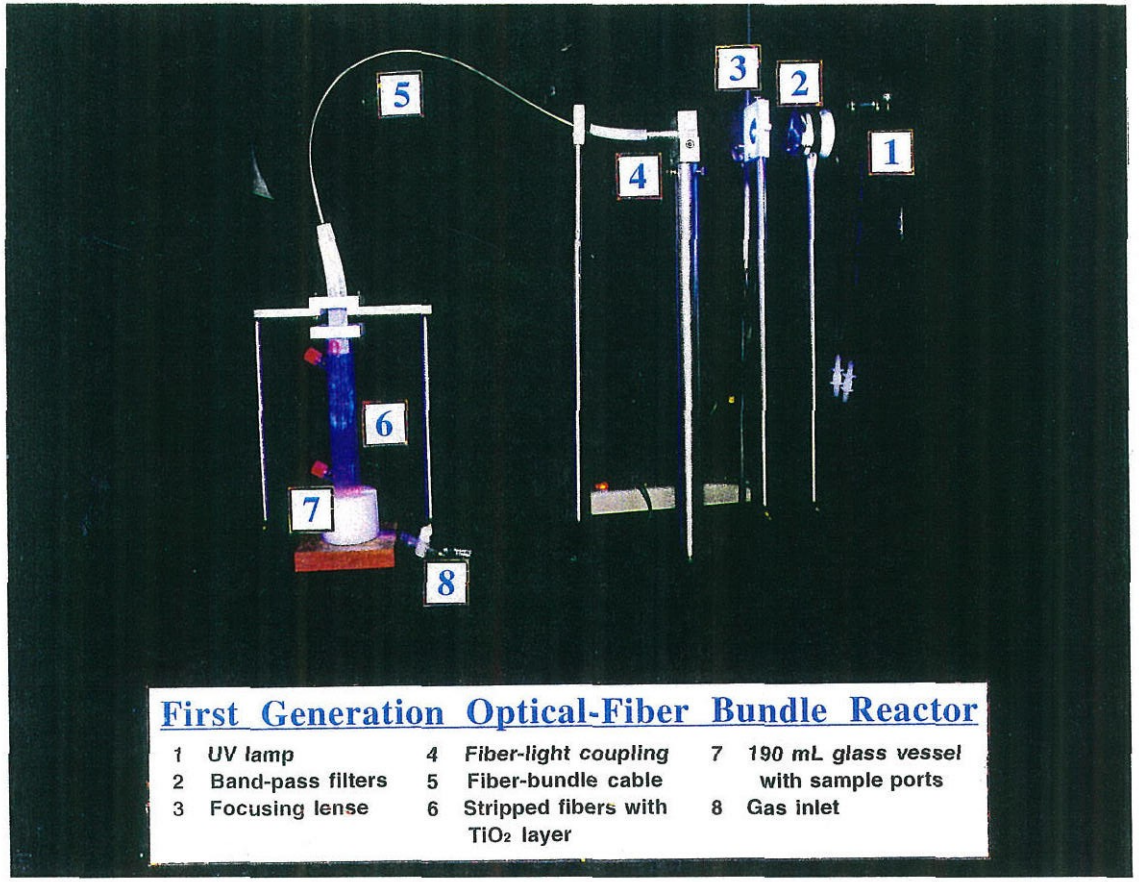

Figure 4. Photograph of first-generation optical fiber reactor system.

Chapter II

Development and Optimization of a TiO_2-Coated Fiber Optic Cable Reactor: Photocatalytic Degradation of 4-Chlorophenol

Appears in *Environmental Science and Technology*, Vol. 29, 1995

Nicola Peill and Michael Hoffmann

Abstract

We have developed, characterized and utilized a photochemical reactor system that employs an optical fiber cable as a means of light transmission to solid-supported TiO_2. Light energy is transmitted to TiO_2 particles, which are chemically anchored onto quartz fiber cores, via radial refraction of light out of the fiber. Operational factors that influence the efficiency of the bundled-array optical fiber reactor are: the uniformity and extent of light propagation down the fiber, the degree of light absorption by the TiO_2 coating of the refracted light, and the ability of the chemical substrates to diffuse into the TiO_2 coating. A TiO_2 coating layer that minimizes the interfacial surface area of the quartz core and TiO_2 particles, and operation with incident irradiation angles near 90° enhance light propagation down the fibers. A maximum quantum efficiency of $\phi = 0.011$ for the oxidation of 4-chlorophenol was achieved. This can be compared to a maximum quantum efficiency of $\phi = 0.0065$ for 4-chlorophenol oxidation in a TiO_2-slurry reactor operated under similar conditions.

Introduction

Heterogeneous photocatalysis on metal oxide semiconductor particles has been shown to be an effective means of removing organic and inorganic pollutants from water and air streams (1-4). The effects of photocatalyst composition, structure, crystal size, band-gap energy, incident light intensity, and the nature of the electron donors and acceptors on photocatalytic reactivity have been investigated (5-19).

Practical application of metal oxide semiconductors as photocatalysts often requires immobilization of the photocatalyst in a fixed-bed reactor configuration that allows the continuous use of the photocatalyst for treating aqueous- or gaseous effluent streams by eliminating the need for post-process filtration. In conventional fixed-bed reactors, the photocatalyst is coated on the walls of the reactor, on a support matrix, or around a casing containing the light source (18, 20-25). However, these configurations present several drawbacks such as low light-utilization efficiencies due to absorption and scattering of the light by the reaction medium and restricted processing capacities due to mass transport limitations.

A novel approach to solving these problems employing optical fibers as a means of light transmission and distribution to solid-supported photocatalysts was first proposed by Ollis and Marinangeli (26, 27). However, they predicted that photocatalytic-optical fiber reactor systems would not be practical due to catalyst deactivation caused by heat buildup in a bundled array. Hofstadler et al. (28) have shown recently that TiO_2-coated quartz fiber rods fixed in a tubular reactor configuration can be used to carry out oxidation of 4-chlorophenol. They reported effective quantum yields of 0.0002. Gapen and Anderson (29) investigated the use of an optical-fiber cable reactor for photocatalytic oxidation. Problems with delamination of the TiO_2 coating resulted in partial degradation of 3-chlorosalicylic acid. However, a maximum quantum efficiency of 0.069 for the partial photolytic and photocatalytic oxidation of 3-chlorosalicylic acid was estimated. They

concluded that a method for obtaining a stable photocatalytic coating needed to be developed before an optical fiber system would be practical. In this regard, we have constructed and characterized a fixed-bed photocatalytic reactor system that employs a fiber-optic cable. The system was designed for remote delivery of light to the photocatalyst, to allow for measurement of light fluxes for direct determination of quantum yields and for reuse of the reactor to test various coatings and light input angles, and to minimize possible heat build-up and delamination problems.

Experimental Section

TiO_2 Coating Characterization. A three-step process of dipping, drying, and heat treatment was used to coat the quartz optical fiber and rod substrates. Initial bonding of a mono-layer of TiO_2 particles to the quartz substrate is primarily due to electrostatic interactions (30, 31). Hydrated quartz and TiO_2 (Degussa P25) are amphoteric with pH_{zpc}'s of 2 and 6.6, respectively (32, 33).

Quartz rods (GM Associates, Inc.) with a diameter of 3 mm and quartz optical fibers (3M Power-Core FT-1.0-UMT) with a diameter of 1 mm were used as coating substrates. Concentrated suspensions of TiO_2 (Degussa P25) in purified water (Milli-Q, 18 MΩ) were prepared and dispersed by sonication (Branson 5200) and stirring. TiO_2 suspensions of 0.05, 0.1, 1, 5, 9, and 17 wt% were used. The pH of the coating hydrosol was 5.5. A length of optical fiber was completely stripped of its protective buffer and cladding using a wire stripper and acetone to expose the quartz core. Of the quartz rods or fibers 10 cm sections were dipped into the stirred TiO_2 hydrosol suspension and then air dried for 24 hrs. Selected TiO_2-coated rods and fibers were fired in a high-temperature furnace (Lindberg Model 55322 Moldatherm) at 200 or 500°C for 1 hr. Second and third coatings were achieved by air-drying between dippings followed by a final firing.

The heat treated samples were cut into 3-5 mm lengths for analysis by SEM (Camscan Series 2) using secondary electrons and back-scattered electron images. These samples were gold-coated using a standard vacuum evaporation procedure. Maximum, minimum, and an average thickness were recorded for each sample.

Input and Absorbed Intensity Measurements. Input and absorbed light intensities for the single fiber and fiber bundle experiments were measured by chemical actinometry using α-(2,5-dimethyl-3-furylethylidene) (isopropylidene) succinic anhydride (Aberchrome 540) according to the method of Heller and Langan (34). In general, the treated portion of the fiber/fiber bundle was immersed concentrically in a quartz vessel containing distilled water. The water and quartz vessel were transparent to the UV light. The quartz vessel was then suspended in a jacketing glass vessel containing the actinometry solution. In order to prevent photocatalytic oxidation of the Aberchrome, it was necessary to separate the TiO_2-coated fibers from the actinometry solution. Nitrogen was bubbled from the bottom through a glass frit to enhance mixing. The difference between the uncoated and coated flux measurements was taken to be the flux absorbed by the TiO_2 layer. The input light intensities were a function of the focusing lens used and the corresponding coupling efficiency of the light beam to the fiber/fiber-bundle face.

Single-Fiber Light Distribution Experiments. A 1000 W Xe arc lamp (Oriel Model 6269) was used as a UV radiation source. Light was filtered through a 10-cm IR water filter and a UV band pass filter (310-370 nm, Corning). The filtered light was focused into the optical fiber using one of three plano-convex quartz lenses, having varying focal lengths, (Newport-Klinger Rolyn Optics) to achieve minimum incident angles of 71°, 76°, and 84°. As the focal length increases, the minimum incident angle, measured from the normal to the fiber wall, increases. A section of the optical fiber was stripped and coated, as described above, at increasing lengths. At each length and for each coating

suspension concentration, total and tip flux measurements were made of the uncoated and coated fibers. The tip flux was determined by masking the coated fiber with Teflon tape. The difference between the coated total and tip flux measurements was taken to be the radial light not absorbed by the TiO_2 coating. The coatings were completely removed by wiping the fiber with a damp cloth. Because it was necessary to measure the light fluxes without decoupling the fiber from the light source, the fiber coating was not fired. However, a heat gun was used to dry the coated fibers at 100°C. Stripped lengths of 1, 2, 5, 10, and 15 cm, sol TiO_2 content of 1, 5, 7, 9, and 17 wt%, and minimum incident angles of 71°, 76°, and 84° were studied.

Optical-fiber Reactor (OFR). An optical-fiber bundled array reactor was developed. A schematic diagram of the optical-fiber photocatalytic reactor system is shown in Fig. 1. The reactor system consists of a light source, a coated fiber-optic bundle, and a reaction vessel. Light is focused into the bundle and transmitted through the fibers, as described above. The fiber bundle consists of 72 1-mm quartz optical fibers (3M Power-Core FT-1.0-UMT). A 20-cm length of the fibers was stripped down to the quartz core, as described above. The prepared fibers were bundled and polished by Fiberoptic Systems Inc., Simi Valley, CA. The 227 mL (25 x 3.4-diam. cm) cylindrical reactor vessel was constructed from Pyrex with a glass frit (fine), and bottom gas inlet for the introduction of air or oxygen. Sample ports are located at the top, middle, and bottom of the vessel and are fitted with Teflon-coated septum screw caps. The dual lid and fiber spacer is constructed from Teflon with a 2 mm-deep groove to fit over the reactor vessel. The hole spacings are concentrically arranged at a spacing of 2.5 mm center-to-center. The fiber bundled array fits coaxially into the reactor vessel.

The fibers in the OFR were coated with Degussa P25 TiO_2 by inverting the bundle and pipetting the coating solution down the tips of the fibers. After air drying, the stripped portion of the fiber bundle was inserted vertically into an open-ended tube furnace and fired

at 300°C for one hour. The bundle was differentially fired over the stripped length from a peak temperature of 300°C at the end, to about 110° at the unstripped portion. In order to test various coating suspension concentrations, coatings were removed by immersing the coated fibers in an ultrasonic bath overnight.

Photoxidation of 4-chlorophenol. A 190 mL, 0.1 mM solution of 4-chlorophenol (4-CP) was prepared from a 1.0 mM stock solution (Aldrich, 99+%). Chloride-ion production during the course of oxidation was followed with a chloride ion-selective electrode (Orion 9617BN, 1.0 M $NaNO_3$ matrix) and by ion chromatography (Dionex BIOLC 4500*i* Series). The pH was determined with a Radiometer PHM85 pH meter. Disappearance of 4-CP was followed spectrophotometrically at λ = 224, 280 nm (Shimadzu UV-2101PC and HP8451A Diode Array) and by HPLC (HP SeriesII 1090). Oxygen (Liquid Air) was used to saturate the reaction solution and to ensure proper mixing. An in-line gas purifier (Alltech 8132) was used to remove particulates and hydrocarbons.

Results

TiO_2 Coating Characterization. A hydrosol-dip coating method was employed because of the geometry of the optical-fiber substrate. From the SEM analyses, it appears that the sintering temperature had no discernible effect on the resulting coating thickness. SEM micrographs of a 1 mm quartz-fiber sample with three coats of a 5 wt% suspension are shown in Figs. 2a and b. A coating depth of 2.1 to 4.3 nm was measured. No multiple-coating layering effects are evident. Distinct agglomerated particles and some clumping can be seen. In Fig. 3, coating thickness is plotted as a function of the hydrosol TiO_2 content and the number of successive coatings. Final mean single-coating thicknesses for the 0.05, 0.1, 1, 2.5, and 5 wt% samples are 0.75, 0.5, 1.6, 1.5, and 2.0 μm, respectively. For the 1, 5, 9, and 17 wt% multiple coating samples, very little increase in

thickness is apparent for a second and third coating within the resolution of the analysis. The large ranges found for the multi-coating samples may be attributable to excessive clumping and fragmentation of the coating during sample preparation.

Single Fiber Tests. The light distribution in a single fiber was determined as a function of the minimum incident angle and the hydrosol TiO_2 content, which was used as an indirect indication of thickness. Input light fluxes varied with the minimum incident angle configured. A plot of the absorption efficiency, the ratio of light absorbed by the TiO_2 layer to the input light, as a function of the sol TiO_2 content, for 10 and 15 cm stripped lengths, is shown in Fig. 4. At these lengths, less than 5% of the input light propagates through the fiber tip. The fraction of input light absorbed by the TiO_2 increases with increasing sol TiO_2 content. The absorbed fraction is greater than 60% for all but the 1 wt% sol coating, absorbing about 30%, and approaches 100% for the 17 wt% sol coatings.

The light distribution as a function of TiO_2 coating length for three coating sols of 1, 7, and 17 wt%, at a fixed minimum incident angle of 76°, is shown in Fig. 5a. Measurements taken at incremental stripped lengths simulate the light distribution as it travels down the fiber. Before the fiber is stripped, all the light emanates from the tip. No radial fluxes were detected for all uncoated stripped lengths. As the fiber is stripped and coated at greater lengths, more light is refracted. This is expected since there is more opportunity for the light to be refracted as the quartz-TiO_2 interfacial area increases for greater stripped and coated lengths. At a 2 cm stripped length, radial fluxes are at least 40% for each coating sol. And at a stripped length of 10 cm, greater than 95% of the light has been refracted for the 7 and 17 wt% sol coatings. At each stripped length, the portion of refracted light absorbed by the TiO_2 layer increases with increasing sol TiO_2 content. This result is consistent with the absorption efficiency findings. A single coat of the 17 wt% coating sol provided a sufficient thickness to absorb > 95% of the refracted light. For

a given stripped length, refraction also increases with increasing sol TiO_2 content. Percent increases from 10 to 90% are observed and are higher for shorter stripped lengths.

The corresponding light distribution as a function of stripped length for three minimum incident angles, 71°, 76°, and 84° using a 5 wt% sol, is shown in Fig. 5b. As the minimum incident angle approaches 90°, parallel to the TiO_2 layer-quartz core interface, the degree of refraction, absorbed and penetrated, decreases for each stripped length.

Oxidation of 4-chlorophenol in the Optical Fiber Reactor. The effect of critical reactor parameters (i.e., coating thickness, degree of interfacial coverage and incident angles) on the rate of 4-CP degradation was explored (35):

$$HOC_6H_4Cl + 6.5\ O_2 \rightarrow H^+ + Cl^- + 6\ CO_2 + 2\ H_2O \qquad (1)$$

Control measurements of 4-CP were taken immediately after and one hour after bundle immersion without illumination; no change in the 4-CP concentration was observed. A two-orders of magnitude reduction of 4-CP ($[4\text{-CP}]_{final} \approx 0.01[4\text{-CP}]_o$) took 5 to 13 hours depending on the specific reactor parameters. The input light fluxes were 10.8 ± 0.8, 13.4 ± 0.8, and 7.6 ± 0.2 $\mu E\ min^{-1}$ for incident angle geometries of 71°, 76°, and 84°, respectively. 4-chlorophenol oxidation and chloride ion production as a function of time are shown in Fig. 6.

The result of increasing the minimum incident angle on the quantum efficiency of the fiber-bundle reactor system is shown in Fig. 7. The change in the quantum efficiency as the incident angle is increased from 71° to 84° is plotted versus the coating sol concentration. Quantum efficiency was calculated as the ratio of the initial rate of oxidation of 4-CP to the flux of absorbed photons; it is defined as $\phi' \equiv \left| \left(\frac{-d[4-CP]}{dt} \right)_o \Big/ I_{absorbed} \right|$. In each case, increasing the minimum incident angle resulted in an increase in the measured quantum efficiency. For a 5 wt% sol coating, the quantum efficiency rose from 0.006 to 0.011 as the minimum incident angle was increased from 71° to 84°, an 83% increase. No apparent trend is seen with respect to the measured quantum efficiency and the input flux;

thus, it is unlikely that the enhanced efficiency observed might be due to a reduction in the absorbed flux. As the coating sol concentration is increased, the relative efficiency enhancement, $\Delta\phi$, is reduced significantly, from 0.005 to 0.0004.

The observed increase in absorption efficiency with increasing TiO_2 content is also seen for the coated fiber bundle. The absorption efficiencies for the coated single-fiber and the coated fiber bundle as a function of the TiO_2 content in the hydrosol are compared in Fig. 4. With a sol coating concentration of 17 wt%, absorption of the input light approaches 95%. The bundle absorption efficiency is consistently higher than the single-fiber absorption efficiency for each coating sol. This may be due in part to a secondary effect of "leaking" refracted light being absorbed by a neighboring coated fiber. With this in mind, it appears that the overall light absorption efficiency of the bundled array is a function of both the fiber coating characteristics and the density of fibers in the array. Minor delamination of the 17 wt% coating was observed during the oxidation experiments. However, the delamination did not significantly affect the measured light absorption or the ability of the OFR to degrade the 4-chlorophenol. TiO_2 from a 13 wt% coating that had been removed by sonication was filtered from the sonicated solution and weighed. The equivalent slurry-phase concentration was approximately 0.03 wt%.

The quantum efficiency for 4-CP degradation versus sol TiO_2 content at a fixed minimum incident angle of 71° is shown in Fig. 8a. Mean quantum efficiencies range from 0.005 to 0.0085. From this data no correlation is seen. However, when the effective quantum efficiency, defined as $\phi'' \equiv \left|\left(\frac{-d[4-CP]}{dt}\right)_o \Big/ I_{input}\right|$, is plotted versus sol TiO_2 content (Fig. 8b), a linear correlation is apparent. The mean effective quantum efficiency increases as the sol TiO_2 content increases from about 0.0025 for the 1 wt% sol coatings to about 0.0075 for the 17 wt% coatings.

Comparison of Efficiencies of the OFR to a Conventional Slurry Reactor. The relative quantum efficiency of a slurry-phase reactor setup consisting of a 200 mL

well-mixed solution of 0.1 mM 4-CP and 0.1 wt% Degussa P25 TiO_2, irradiated with 7.6 $\mu E\ min^{-1}$ ($310 \leq \lambda \leq 375$ nm) in a 250 mL uncovered beaker for 2 hours, was determined. An average relative quantum efficiency of 0.0065 ± 0.0002 was measured. This value can be compared to an average value of 0.006 and a maximum value of 0.011 for the OFR operating under comparable conditions.

Discussion

Light Propagation in a Waveguide. The optical fibers in the OFR can be treated as elementary waveguides. In this case, light in the form of a plane wave which propagates in the core medium (1) having a refractive index n_1, and which is incident on an interface with an outer medium (2) having a refractive index n_2, can be reflected and/or refracted. Snell's Law states that the ratio of the sine of the wave's incident angle, θ_i, and the sine of the wave's refracted angle, θ_{refr}, is constant. This ratio is equal to the ratio of the wave's velocities in the respective mediums and the inverse ratio of the refractive indices,

$$\frac{\sin\theta_i}{\sin\theta_{refr}} = \frac{v_1}{v_2} = \frac{n_2}{n_1} \tag{2}$$

In a system in which the core refractive index is higher than the refractive index of the nonabsorbing interfacing medium, the propagating wave will be internally reflected with 100% efficiency when the angle of incidence exceeds the critical angle. This critical angle, θ_c, is defined as the arcsine of the ratio of the refractive indices of the core to outer mediums. Some degree of refraction will occur if the angle of incidence is less than the critical angle. However, if the refractive index of the core medium is less than the outer medium, then refraction will occur for all incident angles.

If the interfacing medium absorbs the incident light with an absorption coefficient α, in units of inverse length, n_2 is replaced with a complex refractive index, $\hat{n}_2$:

$$\hat{n}_2 = n_2(1 - i\kappa_2) \tag{3}$$

The attenuation index, κ, is related to α by

$$n\kappa = \alpha c / 4\pi v \tag{4}$$

where c and v are the velocities of the light wave in a vacuum and in the medium, respectively.

For all wavelengths the index of refraction of a single TiO_2 rutile crystal is greater than quartz, which is constant at about 1.4 (36). Values for n in the nonabsorbing region (> 375 nm) are constant at about 2.8. As the wavelength approaches the absorption onset of the photocatalyst, the index of refraction of the TiO_2 crystal increases reaching 5.5 at about 300 nm. Values for κ similarly increase from 0 to about 1.5. As a consequence, incident light will be refracted to some degree for all incident angles. The ratio of the energy transmission to the TiO_2 coating to the incident radiation at each reflection depends on the incident angle, the wavelength, and the refractive indices according to the Fresnel equations:

$$\left(\frac{E_r}{E_i}\right)_{\perp} = 1 - \left|\frac{n_1\cos\theta_i - [(n_2 - i\kappa_2)^2 - n_1^2\sin^2\theta_i]^{1/2}}{n_1\cos\theta_i + [(n_2 - i\kappa_2)^2 - n_1^2\sin^2\theta_i]^{1/2}}\right|^2 \tag{5}$$

$$\left(\frac{E_r}{E_i}\right)_{//} = 1 - \left|\frac{(n_2 - i\kappa_2)^2\cos\theta_i - n_1[(n_2 - i\kappa_2)^2 - n_1^2\sin^2\theta_i]^{1/2}}{(n_2 - i\kappa_2)^2\cos\theta_i + n_1[(n_2 - i\kappa_2)^2 - n_1^2\sin^2\theta_i]^{1/2}}\right|^2 \tag{6}$$

where E_r and E_i are the energies of the refracted and incident radiation, respectively, and the subscripts $\perp$ and // refer to the transverse electric and magnetic (TE and TM, respectively) polarizations of the incident light (37). The refraction for perpendicular polarizations monotonically decreases from a given value at normal incidence (0°) to zero at the grazing angle, parallel to the quartz-coating interface. The refraction for parallel polarizations increases as the incident angle increases, reaching a maximum of 100% at

Brewster's angle, $\left(\theta_B = \tan^{-1} n_1/\hat{n}_2\right)$, and then falls sharply to zero as the incident angle approaches the grazing angle. The shapes of these curves are a function of the indices of refraction for quartz and the TiO_2 particles (complex) and the extinction coefficient of the photocatalyst. Light incident upon a quartz-water or quartz-air interface, representative of a coating pore interface, will be totally internally reflected for incident angles greater than the corresponding critical angle with no refracted transmission of energy because the refractive index of the quartz core is greater than that of air and water. This assumption is an oversimplification of the system since the wavelength is probably at least an order of magnitude greater than the interfacial pore surface area. In this case, the interaction between the pore interface and the photon is a function of the "effective" refractive index of the pore interface. It has been postulated that for a powder material composed of particles, which are small compared to the incident wavelength, the refractive index of the material will be a statistical composite of the refractive indices of the particles and the void material (e.g., H_2O) (38). In addition, the absorption of the material increases significantly as the packing fraction of the powder increases.

Semiconductor Fiber Coating. Knowledge of the thickness, porosity, and pore size of the TiO_2 coatings are important for interpreting the results of the single-fiber light distribution and 4-CP oxidation efficiency experiments. Degussa P25 TiO_2, which was used in this study, is synthesized by a gas-phase, high temperature process. It is composed of an 80/20 mixture of anatase and rutile phases, respectively, with crystal sizes averaging 20 nm and a specific surface area of 50 m^2/g (33, 39). The general crystal structure is believed to have a plate-like morphology. These crystals, which are in an agglomerated state having characteristic lengths averaging 1 μm, form the resulting coating matrix. It may be for this reason that minimum thicknesses of only 0.5 μm were observed for even very dilute sols, assuming the 1 μm dimension of the agglomerated particle is the larger one. Determination of the effect of sol TiO_2 content on the interfacial coverage was

not possible using SEM analysis (Figs. 2a/b). Many coating studies have been done to determine the effect of firing temperature, sol TiO_2 content and pH, and number of coatings on the resulting coating properties such as specific surface area, porosity and pore size, thickness, light absorption, and reactivity (30, 31, 40, 41). These characterization studies provide insight into assumptions made about the coating used in our system. In general, TiO_2 coating porosities range from about 30 to 75% for firing temperatures less than 500°C; pore radii of about 10-20 Å are relatively constant for heat treatment below 350°C; and the single-coat thickness is controlled primarily by the pH, viscosity, and surface tension of the sols.

The fraction of refracted light absorbed by the photocatalyst coating should increase as the thickness of the coating increases, following from Beer's Law:

$$I_{absorbed}/I_{interface} = 1 - e^{-\varepsilon\delta} \qquad (7)$$

where ε and δ are the extinction coefficient and thickness of the coating, respectively. The extinction coefficient for solid-state TiO_2 is 0.006 nm^{-1} (33). Since the TiO_2 coatings on the quartz fibers is porous, we assume that the effective extinction coefficient is $\leq$ 0.006 nm^{-1}. The 5 and 17 wt% coatings are approximately 2 and 5 μm thick with absorption efficiencies of 45 and 95%, respectively. Based on Eq. 14 we calculate corresponding extinction coefficients of 0.0006 and 0.0003 nm^{-1}. Aguado et al. (40) estimated average coefficients ranging from 0.0006 to 0.001 nm^{-1} for coatings comprised of nano-sized crystallites derived from various TiO_2 sols. Since we are unable to quantitatively correlate the suspension sol concentration with the resulting coating thickness, quantitative estimations of coating porosity and extinction coefficients are not possible. Therefore, in our analyses we use the sol TiO_2 concentration as an indirect measure of thickness (30, 31).

Fiber Core Light Distribution. In order to optimize the OFR system of Fig. 1, the dependence of the radial light transmission on the angle of incidence and the thickness and interfacial coverage of the TiO_2 coating was determined. Our objective was to provide sufficient illumination of the TiO_2 coating to achieve photo-activation while maximizing the axial extent of light propagation, which in turn maximizes the activated surface area.

Light distribution within a coated optical fiber was seen to be a function of the thickness and interfacial coverage of the photocatalytic coating and the incident angle of the input light (Figs. 3-5). Absorption of the refracted light is enhanced by thicker coatings derived from higher coating sol TiO_2 content (Fig. 4). However, an optimal thickness, with respect to photo-activation of the coating, is determined by the extinction coefficient of the coating. The detection of light penetrating through the TiO_2 layer demonstrates that sufficient light is being refracted out of the fiber to penetrate thoroughly and to activate the TiO_2 layer. The coating thickness of the 17 wt% sol appears to be approaching the penetration limit of the refracted light. Results from the single-fiber light distribution experiments (Figs. 5a and b) confirmed that the effective refractive index of the TiO_2 coating is greater than that of the quartz fiber core. Light energy appears to be transmitted to the TiO_2 coating primarily via radial refraction of the light. Increases in refraction with increases in the sol TiO_2 content suggest that the composite refractive index of the TiO_2-matrix at the quartz-core interface increases with the coating sol TiO_2 concentration. We postulate that as the TiO_2 content of the coating sol increases, so does the degree of coverage of TiO_2 particles at the interface which would result in enhanced refraction. With increasing interfacial coverage, the probability of an incident photon being refracted out of the quartz fiber increases. Increasing the minimum incident angle from 71° to 84° resulted in 10 to 60% reductions in refraction. This trend is theoretically predicted by the Fresnel equations for incident angles greater than the Brewster angle. Also, geometrically, a light wave will undergo fewer reflections for a given length at larger incident angles. As a

consequence, the light is distributed more uniformly over and propagated further down the length of the fiber increasing the activated surface area (Fig. 5b).

It has been demonstrated that energy transmission to the TiO_2 coating via refraction in a single coated fiber can be controlled by adjusting the thickness and interfacial coverage of the coating and the angle of incidence of the input light. Minimal interfacial photocatalyst coverage and a large incident angle, approaching 90°, serve to minimize the refraction per reflection and the number of reflections for a given length of fiber thereby increasing the activated photocatalytic surface area. Coating thicknesses approaching four or five times ε^{-1} maximize the absorption efficiency of the refracted light and the activated surface area. With our coating technique, an increase in the coating thickness also increases the TiO_2 interfacial coverage. It may be possible to start with a suspension solution pH that is greater than the pH_{zpc}'s of both the quartz and the TiO_2 (e.g., pH 8 or 9) to minimize the interfacial coverage. This may, however, affect the stability of the coating.

OFR Optimization. The light distribution within the single-fiber photocatalyst system has been shown to have a measurable effect on the efficiency of the OFR system (Figs. 6-8). The overall activated surface area of the coating was found to be the most important factor affecting efficiency. The coating thickness and the uniformity and the extent of light propagation down the fiber determined the activated surface area. The effect of coating thickness on the oxidation rate of 4-chlorophenol can be seen in Fig. 6. Increasing the coating sol TiO_2 content from 1 to 17 wt% reduced the degradation time by approximately 35%. The input light flux was 10.8 $\mu E\ min^{-1}$. However, the total absorbed light flux of the 17 wt% coating was 96% greater than the 1 wt%. In a fiber optic reactor system, the reactive surface area can be increased readily by adding more coated fibers to the bundle without increasing light scattering which limits reaction rates (42, 43).

Results from the single-fiber experiments suggest that increasing the incident angle increases the photo-activated surface area. The effect of this increase on the quantum efficiency can be seen in Fig. 7. The observed efficiency enhancements, however, diminish as the sol TiO_2 content is increased. This result may be explained by the increase in refraction per reflection with increasing interfacial coverage as observed in the single-fiber experiments. The reduced reflections per unit length of fiber and refraction per reflection with an increase in the incident angle is offset by enhanced refraction as a result of increased interfacial coverage. Increases in the quantum efficiency at lower input and absorbed light intensities due to a reduction in charge-carrier recombination seen in other studies was not observed (44, 45). The highest intensities occurred at a minimum incident angle of 76°. If this type of intensity effect were significant, then we would expect the lowest efficiencies at this incident angle. However, this predicted trend is not observed and thus we conclude that the "lower-intensity effect" is not important.

By controlling the incident angle and the thickness and interfacial coverage of the coating, the activated surface area can be optimized. A coating with minimal interfacial surface area of the quartz core and the TiO_2 particles and an incident angle approaching 90° will extend the light propagation down the fiber concomitantly increasing the illuminated surface area. An optimal coating having a thickness equal to four or five times the inverse of its extinction coefficient should achieve 100% absorption of incident refracted photons. This optimal coating thickness has a much greater impact on the activated surface area, and hence the efficiency, than the extent of the photocatalyst activated (i.e., the extent of light propagation down the fiber as shown in Figure 8b).

The oxidation efficiency of the system is also dependent on the ability of the chemical species of interest to diffuse into the illuminated photocatalyst matrix and/or the charge carriers to migrate to the photocatalyst-reaction solution interface. In order for the charge carriers generated in the inner layers to be effectively utilized, 4-CP must diffuse

into the activated inner layers of the TiO_2 on the fibers and/or the charge carriers must migrate outward toward the solid-liquid interface. The characteristic time for pore diffusion of 4-CP can be estimated as follows:

$$t_{diffusion} = \frac{L^2}{D} \tag{8}$$

where L and D are the characteristic length of the TiO_2-matrix and the molecular diffusivity of 4-CP, respectively. The mean pore radii for TiO_2 sol gel membranes are approximately five times greater than the size of a chlorophenol molecule (ca. 4 Å) (30, 31, 40). For a pore radius of 20 Å and $D_{4\text{-}CP} = 10^{-9}$ m^2s^{-1}, the characteristic time for diffusion is 3 ns. The characteristic time for the oxidation of 4-CP by •OH is much longer than 3 ns. Therefore, it is more appropriate to use the characteristic length for diffusion through a porous medium, generally taken to be three times the coating layer thickness due to pore tortuosity. In this case, with a pathlength of 15 μm, the characteristic time for pore diffusion is 0.2 s. Although the local [•OH] and [4-CP] cannot be determined from our data, an estimate of the reaction rate based on literature values of $k \approx 1$ $\mu Mmin^{-1}$ (1), for TiO_2 films and slurries, indicates that we are operating in a reaction-limited regime, in which the availability of 4-CP at the photocatalytic interface is not limiting.

The weak positive correlation between the quantum efficiency and the sol TiO_2 content shown in Figure 8a suggests that the light absorbed by the coatings of varying thickness is being used equally well. The effective quantum efficiency, however, is strongly correlated with the sol TiO_2 content (Fig. 8b). This suggests that the oxidation of 4-CP is not mass transport limited. A thicker coating with a higher active surface area appears to be effective in utilizing absorbed photons to effect degradation. Thus, the charge carriers generated in the inner layers of the photocatalyst appear to be as efficient at inducing redox chemistry as those generated in the outer layers. In a diffusion-limited system, productive use of the e^-/h^+ pairs generated in the inner photocatalyst layers would require their migration to the redox substrates in the outer layers (46-50).

Slurry System Comparison Study. In an attempt to establish a benchmark for the effectiveness of the immobilized photocatalyst in our system, we compared the characteristic quantum efficiency of a slurry-phase system to our OFR system. Unlike most fixed-bed reactor configurations, a slurry-phase configuration has the inherent advantage of a uniformly-distributed photocatalyst and a high photocatalytic surface-area-to-reactor-volume ratio. Quantum efficiencies of 0.0065 were measured. Thus, the OFR system has the advantages of a fixed-bed system described earlier while also achieving similar reaction efficiencies of a slurry-phase system.

Many of the problems encountered in previous studies (26-29), associated with the use of optical-fibers for light transmission and for solid supports for heterogeneous photocatalysis, were overcome in our system. No deactivation of the photocatalyst due to heat buildup as predicted by Ollis and Marinangeli (26, 27) was observed. We believe that separation of the coated fibers and heat removal by the reaction solution served to control the temperature of the photocatalyst coating. Quantum efficiencies, that were two orders of magnitude greater than those reported for the tubular reactor of the Hofstadler et al. (28) for the oxidation of 4-chlorophenol, were achieved. The use of a fiber separator and stiffer fibers eliminated the delamination problem observed by others except for the thickest coatings. Moreover, the delamination observed in the latter case did not significantly affect the efficiency of the OFR for 4-chlorophenol degradation.

The OFR system has the inherent advantages of a fixed-bed design coupled with the reaction efficiencies of a slurry-phase reactor. The OFR configuration enhances the uniformity and distribution of activated photocatalyst throughout a given reaction volume relative to conventional fixed-bed reactor designs. These characteristics reduce the mass transport limitations to photochemical conversion efficiency and allows for higher processing capacities. In addition, the possibility of light loss via absorption or scattering

by the reaction medium is minimized. The OFR system can be used in either batch- or continuous-flow operation for both liquid- and/or gas-phase reactions. The transmission cable allows for remote delivery of light to the photocatalyst which is not possible with any other photocatalytic reactor configuration. As a result, catalyst-coated quartz-fiber optical cables could be utilized for *in situ* remediation of contaminated subsurface environments; and treatment of either aqueous- and/or vapor-phase contaminants such as chlorinated hydrocarbons.

Acknowledgments

We are grateful to ARPA and ONR {NAV 5 HFMN N000149J1901} for financial support and to Janet Kesselman, Scot T. Martin, Dr. Andreas Termin, and Wonyong Choi for scientific support. We would also like to thank 3M and Degussa for their donations of the optical fiber samples and the P25 photocatalyst, respectively.

Literature Cited

(1) Hoffmann, M. R.; Martin, S. T.; Choi, W.; Bahnemann, D. W. *Chem. Rev.* **1995**, *95*, 69.

(2) Ollis, D. F.; Al-Ekabi, H. *Photocatalytic Purification and Treatment of Water and Air*; Elsevier: Amsterdam, 1993.

(3) Blake, D. M., Bibliography of Work on the Photocatalytic Removal of Hazardous Compounds from Water and Air. National Renewal Energy Laboratory, 1994.

(4) *Homogeneous and Heterogeneous Photocatalysis*; Pellizzetti, E., Serpone, N., Ed.; NATO ASI Series 174, 1986.

(5) Abdullah, M.; Low, G. K. C.; Matthews, R. W. *J. Phys. Chem.* **1990**, *94*, 6820.

(6) Kormann, C.; Bahnemann, D. W.; Hoffmann, M. R. *J.Phys.Chem.* **1988**, *92*, 5196.

(7) Kormann, C.; Bahnemann, D. W.; Hoffmann, M. R. *Environ. Sci. Tech.* **1991**, *25*, 494.

(8) Prairie, M. R.; Evans, L. R.; Stange, B. M.; Martinez, S. L. *Environ. Sci. Tech.* **1993**, *27*, 1776.

(9) Sabate, J.; Anderson, M. A.; Aguado, M. A.; Gimenez, J.; Cerveramarch, S.; Hill, C. G. *J. Mol. Catal.* **1992**, *71*, 57.

(10) Herrmann, J. M.; Disdier, J.; Pichat, P. *J. Phys. Chem.* **1986**, *90*, 6028.

(11) Erbs, W.; Desilvestro, J.; Borgarello, E.; Gratzel, M. *J. Phys. Chem.* **1984**, *88*, 4001.

(12) Matthews, R. W. *Wat. Res.* **1986**, *20*, 569.

(13) Pelizzetti, E.; Carlin, V.; Minero, C.; Grätzel, M. *New J. Chem.* **1991**, *15*, 351.

(14) Hoffman, A. J.; Yee, H.; Mills, G.; Hoffmann, M. R. *J. Phys. Chem.* **1992**, *96*, 5540.

(15) Choi, W.; Termin, A.; Hoffmann, M. R. *Angew. Chem.* **1994**, *106*, 1148.

(16) Grätzel, M. *Heterogeneous Photochemical Electron Transfer*; CRC Press: Boca Raton, FL, 1989.

(17) Fox, M. A. *Photochem. Photobiol.* **1990**, *52*, 617.

(18) Matthews, R. W. *J. Catal.* **1988**, *111*, 264.

(19) Turchi, C. S.; Ollis, D. F. *J. Catal.* **1990**, *122*, 178.

(20) Yamazaki-Nishida, S.; Nagano, K. J.; Phillips, L. A.; Cerveramarch, S.; Anderson, M. A. *J. Photochem. Photobiol. A: Chem.* **1993**, *70*, 95.

(21) Xu, Y. M.; Menassa, P. E.; Langford, C. H. *Chemosphere* **1988**, *17*, 1971.

(22) Wyness, P.; Klausner, J. F.; Goswami, D. Y.; Schanze, K. S. *J. Solar Engy. Eng. Trans. Asme* **1994**, *116*, 2.

(23) Dibble, L. A.; Raupp, G. B. *Environ. Sci. Tech.* **1992**, *26*, 492.

(24) Peral, J.; Ollis, D. F. *J. Catal.* **1992**, *136*, 554.

(25) Yue, P. L.; Khan, F.; Rizzuti, L. *Chemi. Eng. Sci.* **1983**, *38*, 1893.

(26) Ollis, D. F.; Marinangeli, R. E. *AIChE J.* **1977**, *23*, 415.

(27) Ollis, D. F.; Marinangeli, R. E. *AIChE J.* **1980**, *26*, 1000.

(28) Hofstadler, K.; Bauer, R.; Novalic, S.; Heisler, G. *Environ. Sci. Tech.* **1994**, *28*, 670.

(29) Gapen, D. C., "Photocatalytic Degradation of Chorinated Hydrocarbons," M. S., University of Wisconsin, 1991.

(30) Xu, Q. Y.; Anderson, M. A. *J. Mat. Res.* **1991**, *6*, 1073.

(31) Hu, L. L.; Yoko, T.; Kozuka, H.; Sakka, S. *Thin Solid Films* **1992**, *219*, 18.

(32) Stumm, W.; Morgan, J. J. In *Aquatic Chemistry*; Ed.; Wiley:New York, 1981; pp 637.

(33) *Degussa Technical Bulletin* **1990**, *No. 56*,

(34) Heller, H. G.; Langan, J. R. *J. Chem. Soc. Perkin Trans.* **1981**, *2*, 341.

(35) Mills, A.; Morris, S. *J. Photochem. Photobiol. A: Chem.* **1993**, *71* , 75.

(36) Personal communication with R. H. French, DuPont, 1994.

(37) Harrick, N. J. In *Internal Reflection Spectroscopy*; Ed.; Interscience Publishers:Briarcliff Manor, NY, 1967; pp 13.

(38) Bruno, W. M., "Powder Core Dielectric Waveguides," California Institute of Technology, 1986.

(39) Bickley, R. I.; Gonzalez-Carreno, T.; Lees, J. S.; Palmisano, L.; Tilley, R. J. D. *J. Solid State Chem.* **1991**, *92*, 178.

(40) Aguado, M. A.; Anderson, M. A.; Hill, C. G. *J. Mol. Catal.* **1994**, *89*, 165.

(41) Orgaz, F.; Capel, F. *J. Mat. Sci.* **1987**, *22*, 1291.

(42) Tseng, J. M.; Huang, C. P. *Wat.Sci. Tech.* **1991**, *23*, 377.

(43) Al-Sayyed, G.; D'Oliveira, J. C.; Pichat, P. *J. Photochem. Photobiol. A: Chem.* **1991**, *58*, 99.

(44) Albery, W. J.; Brown, G. T.; Darwent, J. R.; Saievariranizad, E. *J. Chemi. Soci. Farad.Trans.I* **1985**, *81*, 1999.

(45) Mills, G.; Hoffmann, M. R. *Environ. Sci. Tech.* **1993**, *27*, 1681.

(46) Martin, S. T.; Morrison, C. L.; Hoffmann, M. R. *J. Phys. Chem.* **1994**, *98*, 13695.

(47) Konenkamp, R.; Henninger, R.; Hoyer, P. *J. Phys. Chem.* **1993**, *97*, 7328.

(48) Liu, D.; Kamat, P. V. *J. Phys. Chem.* **1993**, *97*, 10769.

(49) Sodergren, S.; Hagfeldt, A.; Olsson, J.; Lindquist, S. E. *J. Phys. Chem.* **1994**, *98*, 5552.

(50) Vogel, R.; Hoyer, P.; Weller, H. *J. Phys. Chem.* **1994**, *98*, 3183.

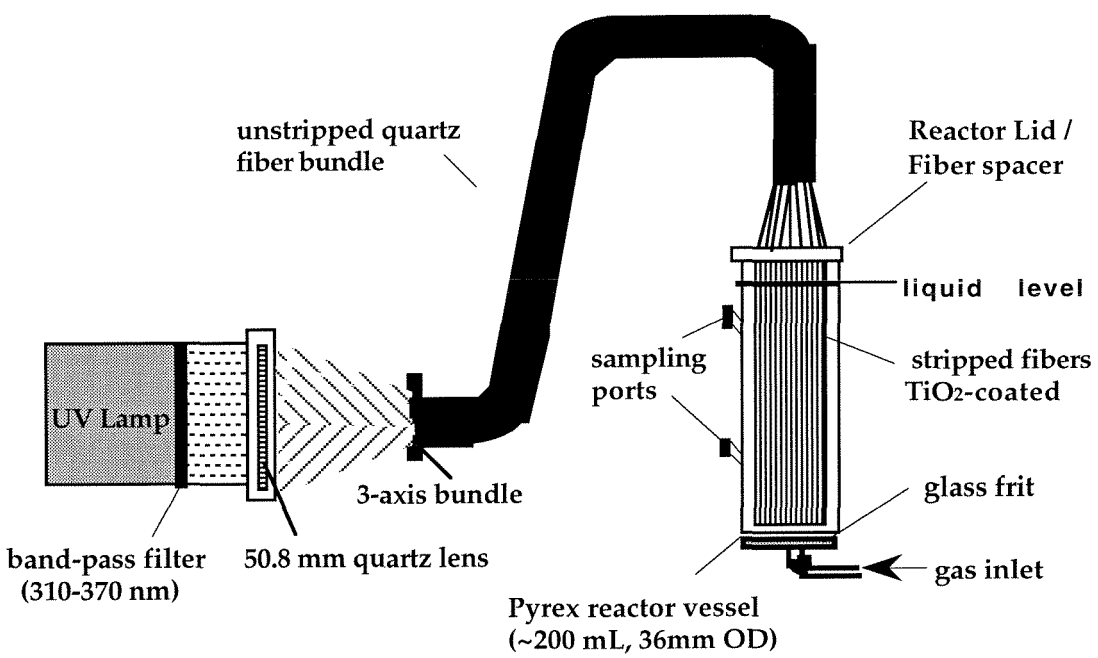

Figure 1. Schematic of optical-fiber bundled array photocatalytic reactor system.

(a)

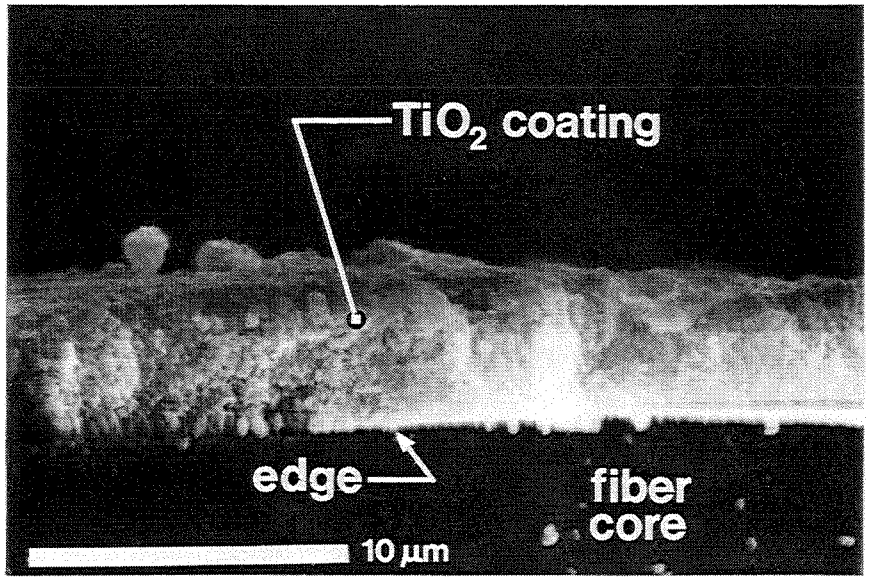

(b)

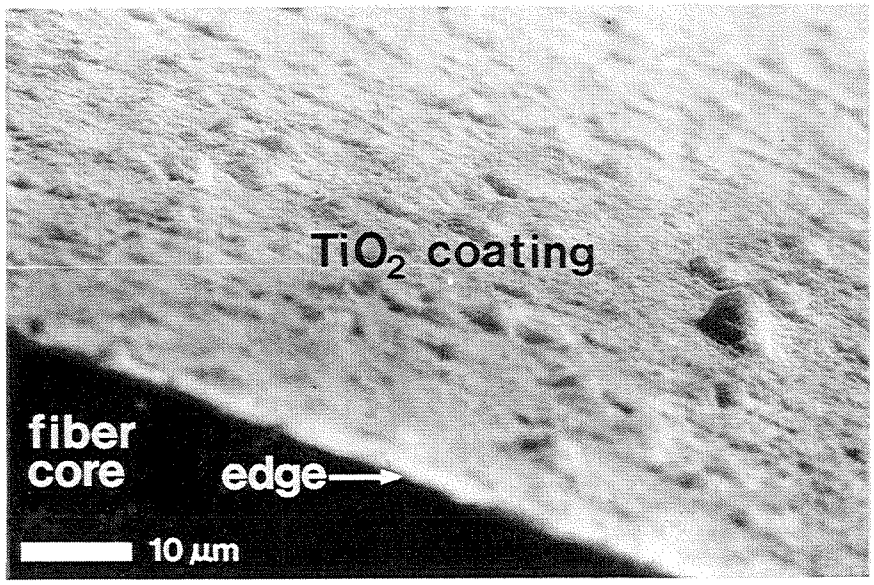

Figure 2. SEM micrographs of TiO_2 on 1-mm diameter quartz optical fiber substrate: (a) 9 wt% coating, (b) oblique view of 5 wt% coating.

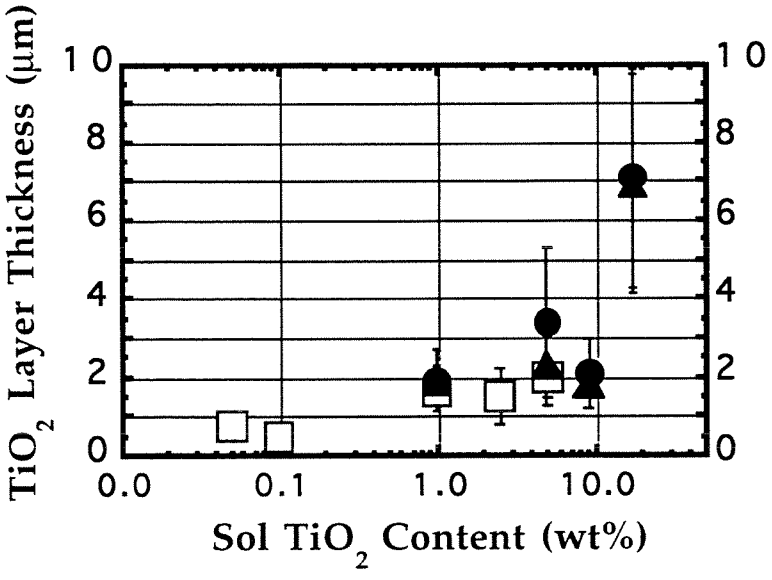

Figure 3. Average coating thickness on quartz substrates as a function of sol TiO_2 content for (□) 1 coat, (▲) 2 coats, and (●) 3 coats. Samples were fired at 200°C.

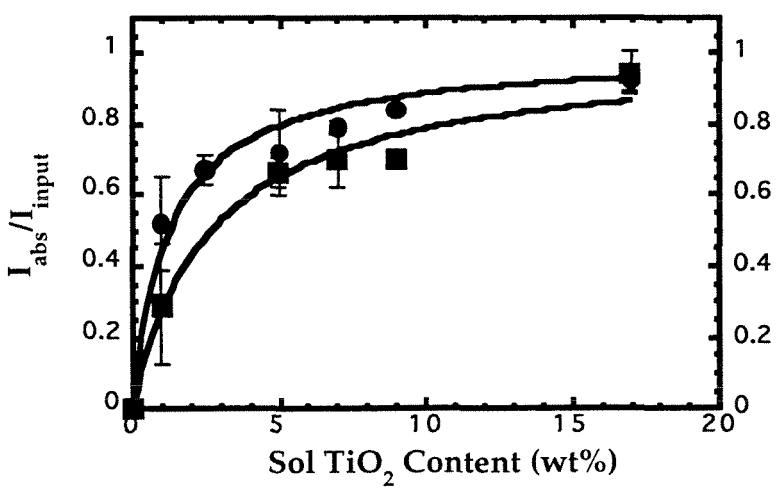

Figure 4. Absorption efficiency of input light as a function of sol TiO_2 content for all minimum incident angles for (■) single fiber and (●) fiber bundle. Single fiber data were for stripped and coated lengths of 10 and 15 cm.

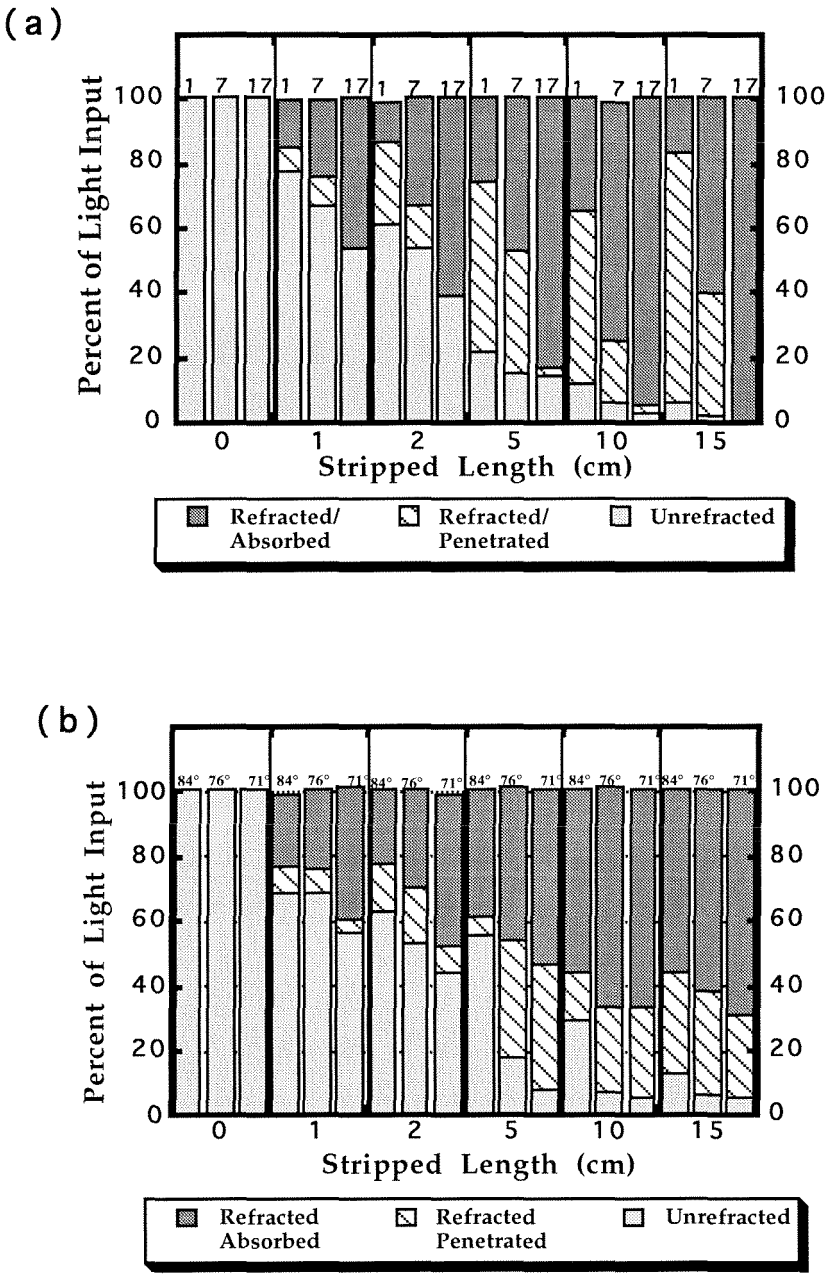

Figure 5. Light distribution within a single fiber as a function of (a) coating sol TiO_2 concentration for 1, 7, and 17 wt%, $\theta_i = 76°$; and (b) minimum incident angle of input light for $\theta_i = 71°$, 76°, and 84° and 5 wt% TiO_2 coating sol. $\lambda = 310\text{-}370$ nm.

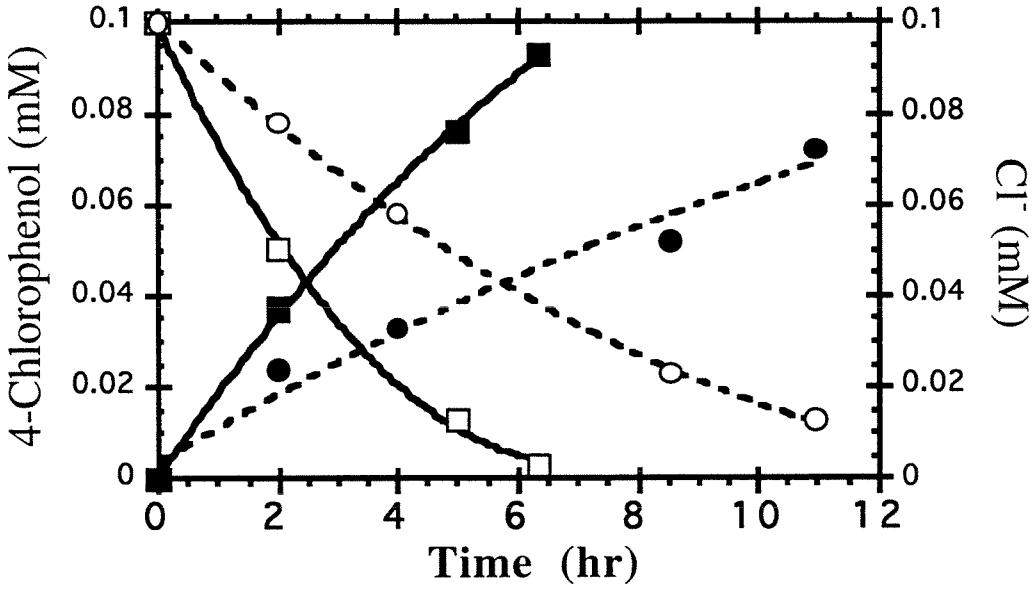

Figure 6. 4-chlorophenol and Cl^- concentrations as a function time for two TiO_2 coating contents, 1 wt%: (O) 4-CP, (●) Cl^-, I_{abs} = 5.0 μE min^{-1} and 17 wt%: (□) 4-CP, (■) Cl^-, I_{abs} = 9.8 μE min^{-1}; I_{input} = 10.8±0.8 μE min^{-1} for θ_i = 71°, $[4\text{-CP}]_o$ = 0.10 mM, pH_o = 5.5, λ = 310-370 nm.

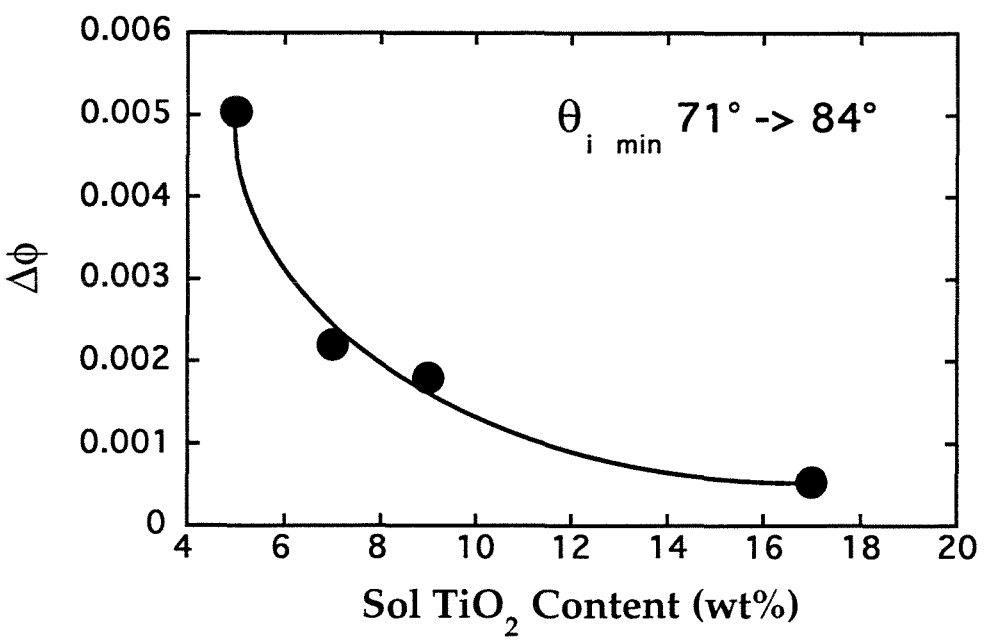

Figure 7. Quantum efficiency enhancement, $\Delta\phi$, as a function of increasing sol TiO_2 content, for a change in incident angle from 71° to 84°. I_{input} = 10.8±0.8, 13.4±0.8 and 7.6±0.2 μE min^{-1} for θ_i = 71°, 76°, and 84°, respectively. $[4\text{-CP}]_o$ = 0.10 mM, pH_o = 5.5, λ = 310-370 nm.

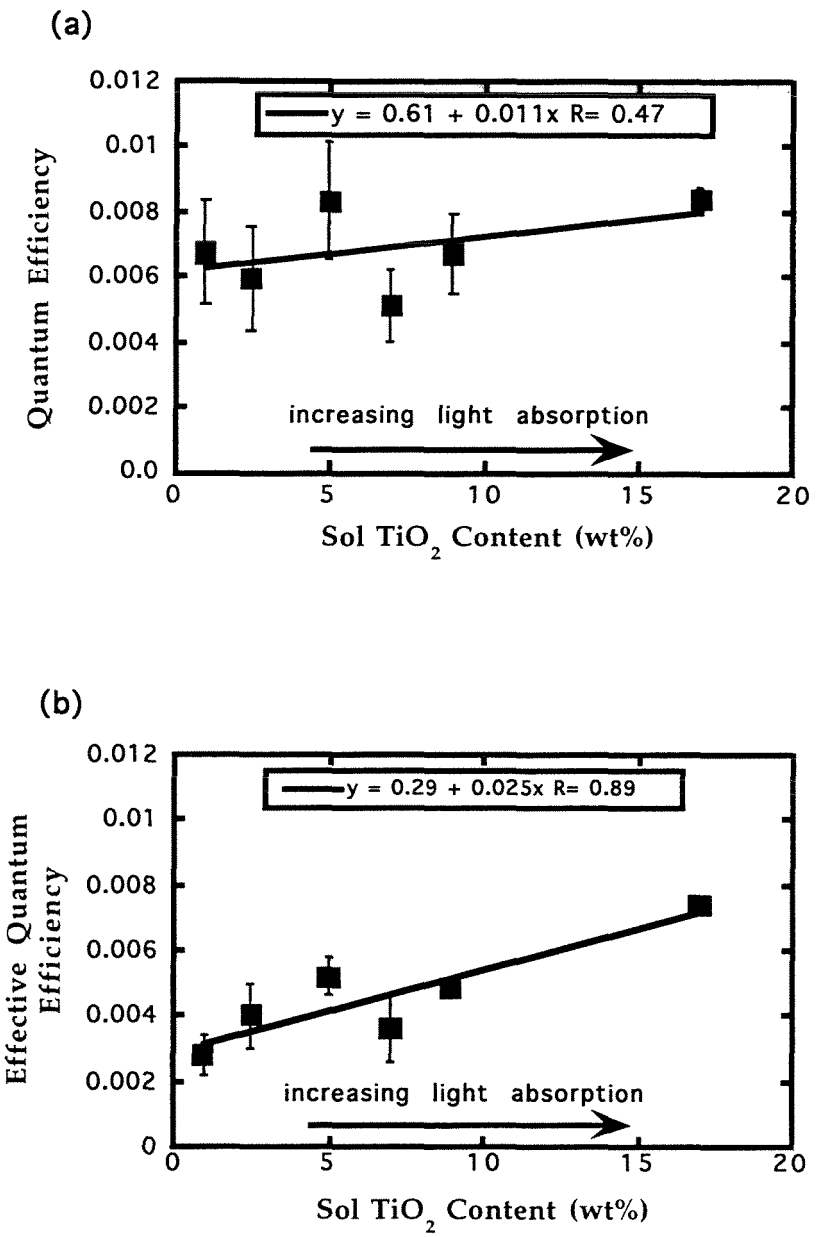

Figure 8. (a) Mean quantum efficiency and (b) mean effective quantum efficiency versus sol TiO_2 content for $\theta_i = 71°$, $I_{input} = 10.8 \pm 0.8$ μE min^{-1}, $[4\text{-CP}]_o = 0.10$ mM, $pH_o = 5.5$, $\lambda = 310\text{-}370$ nm.

Chapter III

Chemical and Physical Characterization of a TiO_2-Coated Fiber Optic Cable Reactor

Appears in *Environmental Science & Technology* , Vol 30, 1996

Nicola Peill and Michael Hoffmann

Abstract

Practical application of metal oxide photocatalysts for the remediation of contaminated wastestreams often requires immobilization of the photocatalyst in a fixed-bed reactor configuration that allows the continuous use of the photocatalyst by eliminating the need for post-process filtration. A novel optical fiber cable reactor (OFR) is used to transmit UV light to solid-supported TiO_2 in order to investigate the photocatalytic degradation of pentachlorophenol (PCP), 4-chlorophenol (4-CP), dichloroacetate (DCA), and oxalate (OX). The distribution of light in a single fiber as a function of fiber diameter and the relative quantum efficiencies for the OFR as a function of incident light intensity are investigated. Light propagation down individual fibers is found to increase with increasing fiber diameter. An increased linear transmission of light results in increased quantum efficiencies, while a two-order of magnitude reduction in incident light intensity results in a four-fold increase (ϕ = 0.010 to 0.042) in quantum efficiency for the degradation of 4-chlorophenol. The rates of degradation of dichloroacetate and oxalate have strong pH-dependencies. Relatively high apparent quantum efficiencies of ϕ = 0.010, 0.015, 0.08, and 0.17 for PCP, 4-CP, DCA, and OX, respectively, and complete mineralization to CO_2, H_2O and HCl are observed in the OFR system.

Introduction

Photocatalysis employing wide band-gap metal oxide semiconductors has been shown to be an effective method for the remediation of chemical waste streams (1-4). In the laboratory, photocatalysis with TiO_2/UV has been studied extensively (5-19). Legrini et al. (20) have argued that the chemical viability of TiO_2 photocatalysis has been established, and that the next stage of development of the process will depend on new ideas for fixation of TiO_2 and on new designs for photochemical reactors. Fixation of a photocatalyst in a reactor system is necessary for the continuous use of the catalyst by eliminating the need for filtration. A variety of heterogeneous supports have been explored including glass beads (21, 22), lamp casings (9, 23), glass plates (24), reactor walls (22, 25), fiberglass mesh (26), and porous films on glass substrates (27, 28).

In order to meet this reactor design challenge, we have developed a fixed-bed system that employs a bundled optical fiber cable array as a means of light transmission to solid-supported TiO_2 (29). Ollis and Marinangeli (30-32) and Gapen (33) conducted preliminary investigations of this type of system. This reactor configuration enhances the spacial uniformity and distribution, and, potentially, the illuminated surface-area, of the light-activated catalyst within a given reaction volume relative to conventional fixed-bed reactor designs. This should result in reduced mass transport limitations to photochemical conversion and allow for higher processing capacities. The system can be operated in both gas- and aqueous-phase modes (29). In addition, the optical fiber reactor system (OFR) allows for remote delivery of light over a distance of up to several kilometers. An OFR system could be used for the *in situ* treatment of contaminated sites in the subsurface environment.

In our previous study (29) we found apparent quantum efficiencies of the optical fiber reactor comparable to those reported for slurry-phase reactors for the oxidation of 4-chlorophenol. The OFR was optimized by using a coating thickness of 7 μm that results in

100% absorption of radially-refracted light out of the fibers and into the photocatalyst layer, and by maximizing the propagation of light down the optical fibers. Optimization of the OFR resulted in an increase in the activated photocatalytic surface area and in a corresponding increase in the apparent quantum efficiency. Enhancement of linear light transmission was achieved by maximizing the incident angle of light introduction into the fibers, θ_i, and by minimizing interfacial contact area of TiO_2 coating particles on the quartz fiber.

In this paper, we explore the effects of fiber diameter on linear light propagation and absorbed light intensity on the photochemical quantum efficiency. In addition to a physical characterization of the OFR, the reactor was used to investigate the photodegradation of pentachlorophenol, 4-chlorophenol, dichloroacetic acid and oxalic acid as a function of pH and ionic strength.

Experimental Section

The optical-fiber bundled array reactor employed for all photooxidation experiments has been described in detail (29). The basic components are a xenon-arc UV-radiation source, a 310 - 375 nm band pass filter, a focusing lens, a light transmitting TiO_2-coated fiber-optic bundle consisting of 72 1-mm diameter, 1.2 m long fibers (3M Power-Core FT-1.0-UMT), and a 227 mL cylindrical Pyrex reaction vessel with a bottom-fritted gas inlet. The TiO_2-laden fibers were prepared by stripping the terminal 20 cm of the fibers to expose the quartz core, coating with a 13 wt% aqueous slurry of TiO_2 (Degussa P25), and firing at 300°C maximum. The coated fibers are spaced at a distance of 2.5 mm center-to-center.

Input and absorbed light intensities for the single-fiber light distribution and fiber-bundle photooxidation experiments were measured by chemical actinometry using α-(2,5-dimethyl-3-furylethylidene) (isopropylidene) succinic anhydride (Aberchrome 540). The experimental methods have been previously described (29).

Light flux measurements were made for uncoated and coated fibers. The difference between the two was taken to be the photon flux absorbed by the TiO_2 layer, I_{abs}. The input light intensities, I_{input}, were found to be a function of the focusing lens used and the corresponding coupling efficiency of the light beam to the fiber/fiber-bundle face.

Fiber-Diameter Optimization. Light from the UV source was focused into a single, 1 mm diameter quartz optical fiber (3M) at a minimum incident angle of θ_i=76° using a plano-convex quartz lens (Newport-Klinger Rolyn Optics). The fiber was stripped and coated at *increasing lengths. At each length, uncoated total, coated total, and coated tip light flux* measurements were made. The difference between uncoated total and coated tip flux measurements was taken to be the portion of the input flux that was refracted out of the fiber. Fiber diameters of 400, 600, and 1000 μm and stripped lengths of 5, 10, and 15 cm were studied.

Light Intensity Dependence. Photooxidation of 4-chlorophenol (4-CP) was carried out to test the relationship between the incident light intensity in the OFR and the resulting quantum efficiency. The input light intensity was reduced to 37%, 10%, and 1% of the maximum using neutral density filters (Oriel Corp.) with $[4\text{-CP}]_o$ = 100 μM. In order to factor out concentration effects, photooxidation was allowed to take place until $[4\text{-CP}]_t$ = 86 μM. This concentration level was obtained after 1 hour of irradiation for the highest-intensity case. The 4-CP concentration was followed spectrophotometrically (Shimadzu UV-2101PC) and by HPLC (HP SeriesII 1090) at λ = 224 and 280 nm. No changes in 4-CP concentration due to the volatilization of 4-CP or water evaporation were observed for a 100 μM solution that was sparged with O_2 for 30 h in the dark.

Ionic Strength, pH, and Stoichiometry. Sample solutions (190 mL) of 4-chlorophenol (Aldrich), pentachlorophenol (PCP) (Aldrich), dichloroacetate (DCA) (Spectrum), and oxalate (Sigma) of varying initial concentrations, pH, and ionic strength (Table 1) were prepared from stock solutions. Before irradiation, the coated-fiber bundle was immersed in the reaction solution and allowed to equilibrate for 30 min. Nylon (Nalgene 0.45 μm) or Teflon (Acrodisc 4CRPTFE 0.45 μm) syringe filters were used to filter all samples.

Chloride production was followed by chemical potentiometry using a Cl^- specific electrode (Orion 9617BN, 1.0 M $NaNO_3$ matrix) and by ion chromatography (Dionex BIOLC 4500i Series). The pH was determined with a Radiometer PHM85 pH meter while constant pH was maintained with a pH-stat (Radiometer PHM85 pH meter, a Radiometer TTT80 Titrator, and a Radiometer ABU80 autoburet). 4-CP and PCP and associated intermediates were analyzed spectrophotometrically and by HPLC (λ = 224/280 and 224/250 nm, respectively). TOC was determined with a TOC analyzer (Shimadzu TOC-5000). Oxalate and DCA were quantified by ion chromatography (Dionex BIOLC 4500i series). Pure (Liquid Air) oxygen was used at saturation as the primary electron acceptor and to mix the reactor via continuous sparging, which was passed through an in-line gas purifier (Alltech 8132).

The photooxidation rates for 0.5 mM solutions of DCA and OX at pH 3, 5, 8, and 11 and at pH 4.25, 5.25, 6.6, and 8, respectively, were determined. pH adjustments were made by the addition of HNO_3 or KOH using the pH stat system described above. In a separate set of experiments, the oxidation of a 100 μM 4-CP solution was carried out at ionic strengths of μ = 0.005, 0.05, and 0.5 M (KNO_3) at an initial pH of 5.5. Reaction rates were determined over 2 h.

Results

Fiber Diameter Optimization. The UV-light distribution down a single quartz fiber as a function of length for fiber diameters of 400, 600, and 1000 μm was determined. The percentage of light remaining in the fiber as a function of the TiO_2-coating lengths are shown in Fig. 1. For a given fiber diameter, the amount of light remaining in the fiber decreases for each coating length. For a given coated fiber length, less light is transmitted down the fiber as the fiber diameter is decreased. For example, all of the light has been refracted out of the 400 μm fiber within the first 5 cm of coated fiber, while 11% and 14% of the initial light flux is transmitted further down the 600 and 1000 μm fibers, respectively. A small fraction of light is transmitted through the entire 15 cm coated sections for the 600 and 1000 μm diameter fibers.

Light Intensity Variation. The apparent quantum efficiency for the photooxidation of 4-CP was determined as a function of absorbed light intensity. The quantum efficiency, ϕ, is defined as the ratio of the initial degradation rate to the absorbed light flux. Experimentally, it was calculated as the ratio of the change in 4-CP concentration, in this case 14 μM, divided by the time to achieve this predetermined level of degradation, t, divided by the absorbed light flux, I_{abs},

$$\phi \equiv \frac{\frac{d[4CP]}{dt}}{\frac{d[h\nu]_{abs}}{dt}} \cong \frac{([4CP]_o - [4CP]_t)/t}{I_{abs}} \qquad (1)$$

Absorbed light intensities of 23.1 ± 4.8, 9.0 ± 2.1, 2.4 ± 0.5, and 0.2 ± 0.1 μE L^{-1} min^{-1} were measured. Irradiation times, t, of 1, 2, 6, and 30 h were required to achieve 14% degradation of 4-CP for the respective absorbed light intensities. These experiments yield quantum efficiencies of ϕ = 0.010 ± 0.002, ϕ = 0.013 ± 0.002, ϕ = 0.019 ± 0.005, and ϕ = 0.042 ± 0.006 for the decreasing absorbed light fluxes. A four-fold increase in the

quantum efficiency was achieved for a two-order of magnitude reduction in the absorbed light intensity (Fig. 2).

Ionic Strength and pH Dependencies. The reaction conditions and results for variations of ionic strength and pH are summarized in Table 1. No reduction in the reaction rate for the photooxidation of 4-CP was observed over the ionic strength range of 0.005 to 0.5 M. The reaction rate was found to be constant (7.6 ± 0.5 μM h^{-1}) over the wide range of ionic strength.

The pH dependence of the photochemical oxidation of DCA is shown in Fig. 3a. The observed photooxidation rate is the highest at pH 3 and decreases progressively to zero at pH >8.

A strong, discrete pH dependence for the photooxidation of $C_2O_4^{2-}$ is shown in Fig. 3b. Over the pH range of 4.0-4.5, photooxidation of $C_2O_4^{2-}$ (0.5 mM) was complete within 2.5 h with $-d[OX]_i/dt \approx 0.2$ mM h^{-1}. However, when the pH range was increased slightly to 5.0-5.5, the initial rate of photodegradation of a 0.5 mM solution was reduced to 0.16 mM h^{-1}.

The pH and ionic strength conditions also had an affect on the stability of the TiO_2 coating. During irradiation of reaction solutions of 0.5 M ionic strength, pH 3 and pH 11, the reaction solution became slightly cloudy. This indicates that a delamination of the coating had occurred. At pH < 3 and at pH > 11, the attachment of the TiO_2 coating to the α-SiO_2 fibers was altered.

Kinetics and Stoichiometry. In order to determine the ability of a bundled-array OFR system to degrade effectively various hydrocarbon species of interest, a two-orders of magnitude reduction ($[organic]_{final} \approx 0.01[organic]_o$) of 4-CP, PCP, DCA, and oxalate were investigated. The reaction conditions and results of these experiments are listed in

Table 1. The time-dependent chemical concentration profiles for the oxidation of 4-CP and for the production of intermediates and products are shown in Fig. 4. Complete degradation of 4-CP was achieved after 10 h of irradiation at I_{ads} = 5.3 μE min^{-1} and pH 5.5 with a stoichiometric production of Cl^-. No intermediates were detected, although both benzoquinone and hydroquinone were detected in other photooxidation experiments at concentrations less than 10 μM. However, they were subsequently photooxidized. Complete disappearance of total organic carbon (TOC) was observed within 12 h with a net quantum efficiency of $\phi = 0.010$ for 4-CP degradation.

PCP was totally degraded after 6 h with mineralization achieved after 13 h of irradiation with a stoichiometric production of Cl^- (Fig. 5). Tetrachlorohydroquinone was detected as an intermediate at a maximum concentration of 30 μM. A photochemical reaction half-life of 3.0 h and a quantum efficiency of $\phi = 0.015$ were determined.

The photooxidation of DCA (Fig. 6) was examined at two different absorbed light intensities (i.e., 7.0 and 4.2 μE min^{-1}) that correspond to the minimum incident angles of light introduction into the fibers of θ_i=76° and θ_i=84°, respectively. In general, larger incident angles were shown to result in higher quantum efficiencies (29). Complete degradation of DCA was achieved after 10 h of irradiation at the higher intensity while 96% degradation was achieved after 14 h at the lower intensity. Chloride production was 100% and 88% of the stoichiometric values for the higher and lower intensity irradiations, respectively. In addition, 98% and 91% of the TOC levels were eliminated after 13.5 and 14 h, respectively. However, the quantum efficiency for the lower intensity (i.e., 4.2 μE min^{-1}), higher incident angle irradiation was higher ($\phi = 0.095$) than the higher intensity irradiation ($\phi = 0.07$).

Complete mineralization of $C_2O_4^{2-}$ (1.0 mM) over the pH range of 4.5-5.0 was observed after five h of irradiation. TOC reduction was only slightly out of phase compared to $-d[C_2O_4^{2-}]/dt$. In the case of $C_2O_4^{2-}$, $\phi_{C_2O_4^{2-}} = 0.18$.

Discussion

Enhancing the activated photocatalytic surface area of the coated fibers by maximizing light propagation down each fiber appears to result in an increased quantum efficiency for an OFR (29). Light propagation down a single fiber was found to be extended by increasing the incident angle of light introduced into the fiber (i.e., to 90° relative to the normal to the fiber wall, Fig. 7) and minimizing the interfacial SiO_2 - TiO_2 contact surface area.

As the fiber thickness is increased, photons undergo fewer reflections at the quartz-TiO_2 interface for a fixed incident angle and a given length. With a larger diameter fiber, the probability that a photon will be refracted through the quartz-TiO_2 interface is reduced, and, thus, the light propagation down the fiber is extended. The results shown in Fig. 1 are consistent with this interpretation which is illustrated schematically in Fig. 7.

If findings from our previous study (29) are applied to an optimal fiber diameter, then the chemical efficiency will be enhanced in an OFR employing larger diameter fibers in the fiber bundle.

Previous studies have shown an inverse relationship between the absorbed light flux and the quantum efficiency (6, 29, 34-38). In illuminated semiconductor photocatalysts, the charge-carrier recombination and interfacial charge transfer are second and first order processes, respectively. The charge-carrier density increases with an increase in the absorbed light intensity. As a result, at a high absorbed light intensity, the rate of charge-carrier recombination is increased relative to interfacial charge transfer and this leads to a lower relative quantum efficiency. However, a lower absorbed light flux yields slower overall reaction rates as the rate of charge pair generation becomes rate-determining. A unique feature of the OFR system is its ability to minimize the negative light intensity effects on ϕ, while maintaining a high input light intensity necessary for rapid overall degradation. This optimization can be achieved readily by increasing the fiber

number density in the fiber bundle as illustrated in Fig. 8. In this case, the same input photon flux can be divided among a larger number of fibers, and distributed over a greater photocatalytic surface area. For a given fiber bundle cross-sectional area, smaller fibers support a higher photocatalytic surface area. For a given reaction system, an upper limit to the fiber number density will be dictated by the onset of restricted flow through the fiber bundle which will result in poorer degradation performance.

In order to test this hypothesis, in part, the input light intensity was successively reduced to 37%, 10%, and 1% of the maximum input value and the corresponding quantum efficiencies were determined (Fig. 2). The measured relative quantum efficiencies were compared at an equivalent level of degradation (14%) rather than for a given reaction time in order to factor out concentration effects. A four-fold increase in the quantum efficiency is achieved for a two-order of magnitude reduction in light intensity. The apparent quantum efficiency of $\phi = 0.042$ (4.2%) for the aqueous-phase, photocatalytic oxidation of 4-chlorophenol on TiO_2 is high relative to previously reported values for slurry suspension reactors. In our previous study (29), we measured an average apparent quantum efficiency of $\phi = 0.065$ for slurry-phase photooxidation of 4-CP at low light intensity (e.g., 7.6 $\mu E\text{-}min^{-1}$) and a TiO_2 loading (Degussa P25) of 1 $g\text{-}L^{-1}$. Al-Sayyed et al. (36) reported quantum efficiencies of $\phi = 0.009$ and $\phi = 0.013$ for light intensities of 1,000-10,000 $\mu E\text{-}min^{-1}$, respectively, and a TiO_2 loading (Degussa P25) of 2 $g\text{-}L^{-1}$. Thus, the relative quantum efficiency may be significantly enhanced in OFR systems without a net reduction in overall reaction rates. Reaction rates in a given photocatalytic system are a function of the total absorbed light intensity and the relative quantum efficiencies. Although these two factors are inversely related, in general, reaction rates increase with an increase in the total absorbed power. For example, an order of magnitude increase in the light intensity resulted in a 25-fold increase in the reaction rate, r, where $r = \phi * I_{abs}$ (Fig. 2). These results suggest that a large total light flux into an OFR system,

similar to those used in slurry reactor studies, will result in rapid reaction rates since a high fiber number density will minimize the light intensity per individual fiber and thus allow the OFR to operate in the high ϕ domain.

In the OFR system for a given reaction system, the relative quantum efficiencies and reaction rates are a function of the absorbed light intensity-to-photocatalytic surface area ratio and the activated photocatalytic surface area-to-reaction volume (APSARV) ratio. Three key considerations in designing the OFR to maximize the relative quantum efficiency are the minimization of mass transport limitations and the ratio of absorbed light intensity-to-photocatalytic surface area, and activation of the entire photocatalytic coating. Mass transport limitations can be mitigated by optimally distributing the activated photocatalyst uniformly throughout a given reaction solution volume. Fiber bundle parameters such as fiber number, spacing, length, and diameter will affect this distribution. Together these bundle parameters will directly influence the intensity and extent of coating activation and, thus, the APSARV. In order to avoid reactor dead space, illumination of the entire extent of coated fibers should be achieved. In addition, complete absorption of the input light is desirable. Assuming no mass transport limitations, both the illumination intensity and the APSARV ratio will affect the reaction rate. The higher the illumination intensity and APSARV ratio, the higher the rate of reaction. Increasing the illumination intensity relative to the photocatalytic surface area will also result in faster degradation rates but at the expense of lower quantum efficiencies (vide supra).

The pH and ionic strength of contaminated waste streams are highly variable. These solution characteristics can influence the speciation of compounds, the nature and magnitude of electrostatic interactions at the semiconductor photocatalyst (metal oxide) surface, and the competition for reactive surface sites. Variations in pH, μ, and T have demonstrable effects on the oxidation rates measured in TiO_2/UV systems (6, 7, 39). In the OFR, the oxidation rates of both DCA and oxalate were investigated and found to be

highly pH dependent (Fig. 3). Oxalate (pK_{a1} = 1.2; pK_{a2} = 4.0) and DCA (pK_a = 1.5) have been found to form inner sphere surface complexes with TiO_2 at low pH values (40, 41). The reaction rates are highest in the pH region where the adsorbate and TiO_2 surface are oppositely charged. As the pH approaches the pH_{zpc} of TiO_2, 6.8 (6), the repulsive forces between the negatively charged TiO_2 surface and adsorbate (e.g., $Cl_2CHCO_2^-$) overcome the tendency toward inner-sphere complexation with a resulting loss of photoreactivity. While the reaction rates for DCA appear to be highly correlated with the surface charge density of the TiO_2 surface as given in Table 2, the oxalate oxidation rates are nonzero at and above the pH_{zpc} of TiO_2. This suggests that inner-sphere complexation of oxalate with the TiO_2 surface is significant. In the case of 4-CP, however, ionic strength did not influence the observed oxidation rate since 4-CP has weak inner-sphere and electrostatic interactions at low pH with the TiO_2 surface (36). Therefore, the influence of increasing ionic strength on the spatial extent of the electrical double-layer does not affect the oxidation rates of 4-CP at low pH.

The observed partial delamination of the coating at the highest ionic strength, 0.5 M, and at pH values below pH 3 and above pH 11, suggests that repulsive electrostatic forces cause destablization of the coating. At these pH values and ionic strength, the net charge on the TiO_2 particles is either quite positive or negative relative to the mid-pH range as shown in Table 2 (42). At high ionic strengths the electrical double-layer would be compressed supporting a higher surface charge density at the same pH allowing the coating to destabilize. These conditions may produce a repulsive force sufficient to cleave TiO_2 particles from each other and from the α-SiO_2 surface. Destablization of the interfacial layer may also be due to acid- (H^+) and base- (OH^-) catalyzed hydrolysis of the >Si-O-Ti< bonds.

4-CP, PCP, DCA, and OX undergo photocatalytic oxidation via several mechanistic pathways including direct and indirect hole transfer and inner- and outer-sphere

electron transfer (Eqs. 2 - 5). These compounds have moderate to high water solubilities and low volatilities. 4-CP and PCP have been reported to undergo hydroxyl radical insertion as an initial step in the overall oxidation (35, 36, 39). DCA and oxalate are believed to undergo hydrogen abstraction and direct hole transfer, respectively, according to the following generally accepted mechanisms (1, 43):

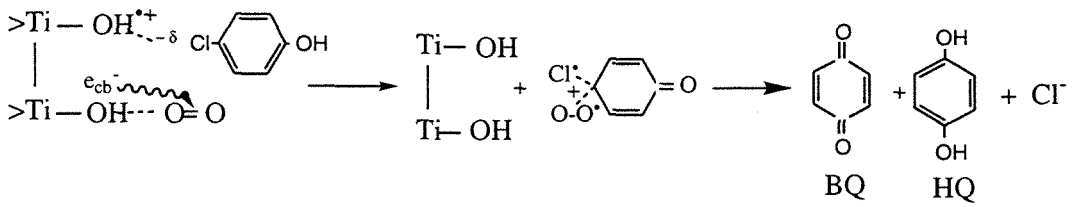

(2)

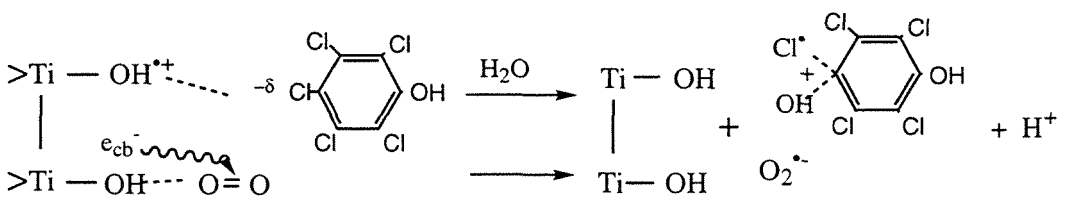

(3)

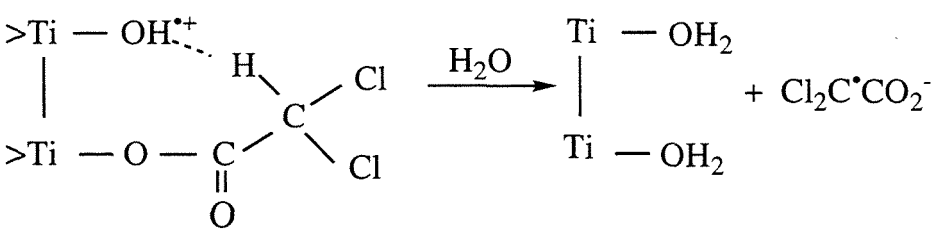

(4)

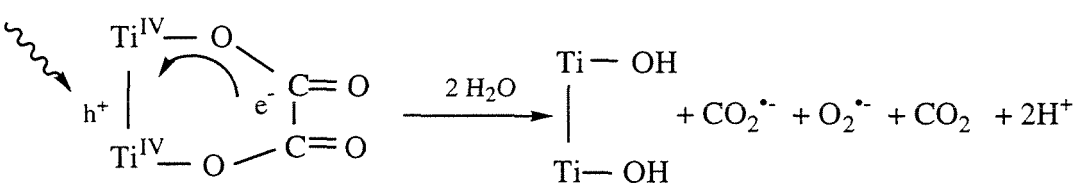

(5)

Apparent quantum efficiencies are comparable to those reported for slurry-phase oxidations. For example, the apparent quantum efficiencies of 0.065 (29) and 0.013 (36)

for slurry-phase oxidation of 4-CP have been reported. Hofstadler et al. (44) achieved apparent quantum efficiencies of only 0.0002 in a fixed-bed reactor employing TiO_2-coated quartz fiber rods. An apparent quantum efficiency of $\phi \approx 0.013$ was reported by Mills and Hoffmann (35) for slurry-phase oxidation of PCP for I = 9.1 $\mu E\ min^{-1}$ and a TiO_2 loading of 0.2 $g\text{-}L^{-1}$ at pH 5. Based on data presented by Barbeni et al. (45) for the photocatalytic degradation of PCP, apparent quantum efficiencies ranging from $\phi = 0.022 - 0.037$ for pH values of 3.0 and 10.5, respectively, and for I = 33 $\mu E\ min^{-1}$ and a 2 $g\text{-}L^{-1}$ TiO_2 loading were determined. It should be noted that, in general, relative quantum efficiencies determined for slurry-phase systems represent lower limits due to scattering of some fraction of the input light by the photocatalyst (46-48). Total mineralization (i.e., conversion to CO_2, H^+, Cl^-) was observed. The relatively long irradiation times, up to 14 h, were due to the low light intensities employed (e.g., 6 compared to 500 $\mu E\ L^{-1}\ min^{-1}$). Higher light intensities can be achieved by employing a larger fiber cable collector with a greater number of fibers and with more efficient light coupling interfaces.

We have demonstrated that an OFR is a promising configuration for the practical application of TiO_2 photocatalysis for the remediation of contaminated wastestreams. The OFR system has the inherent advantages of a fixed-bed reactor, coupled with the photochemical quantum efficiencies of a slurry-phase reactor. The OFR is operable over a broad range of pH and ionic strength, and it can catalyze the degradation of a broad range of chemical compounds. In conclusion, the OFR system has the potential to substantially enhance photocatalytic efficiencies and to be applied in remote locations such as in groundwater wells or underground storage tanks.

Acknowledgments

We are grateful to ARPA and ONR (NAV 5 HFMN N000149J1901) for financial support and to Tim Wu, Janet Kesselman, Scot T. Martin, and Wonyong Choi for scientific support. We would also like to thank 3M and Degussa for their donations of the optical fiber samples and the P25 photocatalyst, respectively.

Literature Cited

(1) Hoffmann, M. R.; Martin, S. T.; Choi, W.; Bahnemann, D. W. *Chem. Rev.* **1995**, 95, 69-96.

(2) Ollis, D. F.; Al-Ekabi, H. *Photocatalytic Purification and Treatment of Water and Air*; Elsevier: Amsterdam, 1993.

(3) NATO. In NATO *Advanced Research Workshop on Homogeneous and Heterogeneous Photocatalysis*, Maratea, Italy, 1985; NATO: 1985, p 721.

(4) Fox, M. A.; Dulay, M. T. *Chem. Rev.* **1993**, 93, 341.

(5) Kormann, C.; Bahnemann, D. W.; Hoffmann, M. R. *J. Phys. Chem.* **1988**, 92, 5196-5201.

(6) Kormann, C.; Bahnemann, D. W.; Hoffmann, M. R. *Environ. Sci. Technol.* **1991**, 25, 494-500.

(7) Abdullah, M.; Low, G. K. C.; Matthews, R. W. *J. Phys. Chem.* **1990**, 94, 6820-6825.

(8) Prairie, M. R.; Evans, L. R.; Stange, B. M.; Martinez, S. L. *Environ. Sci. Technol.* **1993**, 27, 1776-1782.

(9) Sabate, J.; Anderson, M. A.; Aguado, M. A.; Gimenez, J.; Cerveramarch, S.; Hill, C. G. *J. Mol. Catal.* **1992**, 71, 57-68.

(10) Herrmann, J. M.; Disdier, J.; Pichat, P. *J. Phys. Chem.* **1986**, 90, 6028-6034.

(11) Matthews, R. W. *Water Res.* **1986**, 20, 569-578.

(12) Pelizzetti, E.; Carlin, V.; Minero, C.; Grätzel, M. *New J. Chem.* **1991**, 15, 351.

(13) Hoffmann, A. J.; Yee, H.; Mills, G.; Hoffmann, M. R. *J. Phys. Chem.* **1992**, 96, 5540.

(14) Choi, W.; Termin, A.; Hoffmann, M. R. *J. Phys. Chem.* **1994**, 98, 13669-13679.

(15) Grätzel, M. *Heterogeneous Photochemical Electron Transfer*; CRC Press: Boca Raton, FL, 1989.

(16) Fox, M. A. *Photochem. Photobiol.* **1990**, 52, 617.

(17) Matthews, R. W. *J. Catal.* **1988**, 111, 264.

(18) Bahnemann, D. W. *Isr. J. Chem.* **1993**, 33, 115.

(19) Matthews, R. W. *J. Cataly.* **1988**, 111, 264-272.

(20) Legrini, E.; Oliveros, E.; Braun, A. M. *Chem. Rev.* **1993**, 93, 671.

(21) Serpone, N. *Sol. Energy* **1986**, 14, 121-126.

(22) Al-Ekabi, H.; Serpone, N. *J. Phys. Chem.* **1988**, 92, 5726-5731.

(23) Sabate, J.; Anderson, M. A.; Kikkawa, H.; Edwards, M.; Hill, C. G. *J. Catal.* **1991**, 127, 167-177.

(24) Anderson, M. A.; Gieselmann, M. J.; Xu, Q. Y. *J. Membr. Sci.* **1988**, 39, 243-258.

(25) Matthews, R. W.; Abdullah, M.; Low, G. K. C. *Anal. Chim. Acta* **1990**, 233, 171-179.

(26) Al-Ekabi, H.; Safarzadey-Amiri, A.; Sifton, W.; Story, J. *Intl. J. Environ. Pollut.* **1991**, 1, 125-136.

(27) Sabate, J.; Anderson, M. A.; Kikkawa, H.; Xu, Q.; Cerveramarch, S.; Hill, C. G. *J. Catal.* **1992**, 134, 36-46.

(28) Aguado, M. A.; Anderson, M. A; Hill, C. G. *J. Mol. Catal.* **1994**, 89, 165-178.

(29) Peill, N. J.; Hoffmann, M. R. *Environ. Sci. Technol.* **1995**, 29, 2974.

(30) Ollis, D. F.; Marinangeli, R. E. *AIChE J.* **1977**, 23, 415-425.

(31) Ollis, D. F.; Marinangeli, R. E. *AIChE J.* **1980**, 26, 1000-1007.

(32) Marinangeli, R. E.; Ollis, D. F.; Alfano, O. M.; Negro, A. C. *J. AIChE J.* **1982**, 28, 945-955.

(33) Gapen, D. C. Photocatalytic Degradation of Chlorinated Hydrocarbons. M.S. Thesis, University of Wisconsin, 1991.

(34) D'Oliveira, J. C.; Al-Sayyed, G.; Pichat, P. *Environ. Sci. Technol.* **1990**, 24, 990.

(35) Mills, G.; Hoffmann, M. R. *Environ. Sci. Tech.* **1993**, 27, 1681-1689.

(36) Al-Sayyed, G.; D'Oliveira, J. C.; Pichat, P. *J. Photochem. Photobiol. A: Chem.* **1991**, 58, 99-114.

(37) Albery, W. J.; Brown, G. T.; Darwent, J. R.; Saievariranizad, E. *J. Chem. Soc. Farad. Trans. 1* **1985**, 81, 1999-2007.

(38) Ollis, D. F. In *Photochemical Conversion and Storage of Solar Energy*; Pellizzetti, E., and Schiavello, M., Eds.; Kluwer Academic Publishers: Dordrecht, Netherlands 1991; pp 593-622.

(39) Tseng, J. M.; Huang, C. P. *Wat. Sci. Technol.* **1991**, 23, 377-387.

(40) CRC *Handbook of Chemistry and Physics*; CRC Press: Boca Raton, 1990-91.

(41) Hug, S. J.; Sulzberger, B. *Langmuir* **1994**, 10, 3587-3597.

(42) Martin, S. T.; Kesselman, J. M.; Park, D. S.; Lewis, N. S.; Hoffmann, M. R. *Environ. Sci. Technol.* **1996**, 30, 0000-0000.

(43) Choi, W.; Hoffmann, M. R. *Environ. Sci. Technol.* **1995**, 29, 1646-1654.

(44) Hofstadler, K.; Bauer, R.; Novalic, S.; Heisler, G. *Environ. Sci. Technol.* **1994**, 28, 670-674.

(45) Barbeni, M.; Pramauro, E.; Pelizzetti, E. *Chemosphere* **1985**, 14, 195.

(46) Cabrera, M. I.; Alfano, O. M.; Cassano, A. E. *Ind. Eng. Chem. Res.* **1994**, 33, 3031-3042.

(47) Cabrera, M. I.; Alfano, O. M.; Cassano, A. E. *Ind. Eng. Chem. Res.* **1995**, 34, 500-509.

(48) Cabrera, M. I.; Cassano, A. E. *Ind. Eng. Chem. Res.* **1995**, 34, 488-499.

Substrate	μ (M)	pH_o	$[C]_i$ (mM)	I_{abs} (μE min^{-1})	Initial Rate (mM h^{-1})	ϕ
Ionic Strength						
4-CP	0.005	5.5	0.100	6.1	18.0×10^{-3}	0.009
4-CP	0.05	5.5	0.100	6.1	17.0×10^{-3}	0.009
4-CP	0.5	5.5	0.100	6.1	17.8×10^{-3}	0.009
pH						
DCA	0.001	3.0 pH_{stat}	0.5	5.7	0.11	0.061
DCA	0.001	5.0 pH_{stat}	0.5	5.8	0.08	0.044
DCA	0.001	8.0 pH_{stat}	0.5	6.0	0.0	0.0
DCA	0.003	11.0 pH_{stat}	0.5	5.8	0.0	0.0
OX	0.0005	4.25	0.5	9.3	0.20	0.034
OX	0.0005	5.25	0.5	9.3	0.16	0.028
OX	0.0005	6.6 pH_{stat}	0.5	9.3	0.04	0.007
OX	0.0005	8 pH_{stat}	0.5	9.3	0.01	0.001
Kinetics & Stoichiometry						
4-CP	-	5.5	0.100	5.3 (θ_i=84°)	17.5×10^{-3}	0.010
PCP	-	5.5-6.0 pH_{stat}	0.062	3.9 (θ_i=84°)	18.5 x 10-3	0.015
DCA	0.001	3.0	1.0	4.2 (θ_i=84°)	0.125	0.095
OX	0.0005	4.5-5.0 pH_{stat}	0.5	6.6	0.35	0.017
Incident Angle (θ_i)						
DCA	0.001	3.0	1.0	7.0	0.15	0.070
DCA	0.001	3.0	1.0	4.2 (θ_i=84°)	0.125	0.095

Table 1. Reaction conditions, initial rates and relative quantum efficiencies, ϕ, for photooxidations of 4-CP, PCP, DCA, and OX. The solution pH was unadjusted and an incident angle of light into the fiber bundle of $\theta_i = 76°$ was used unless otherwise noted.

pH	μ (M)	Charge Density (C/m^2)
4.3	10^{-3}	+0.026
5.5	10^{-3}	+0.009
6.3	10^{-3}	-0.004
6.9	10^{-3}	-0.005
7.9	10^{-3}	-0.017
8.7	10^{-3}	-0.028
9.7	10^{-3}	-0.047
5.5	10^{-2}	+0.015
5.5	10^{-1}	+0.025
5.5	10^{0}	+0.030

Table 2. TiO_2 (Degussa P25) surface charge density as a function of pH and ionic strength.

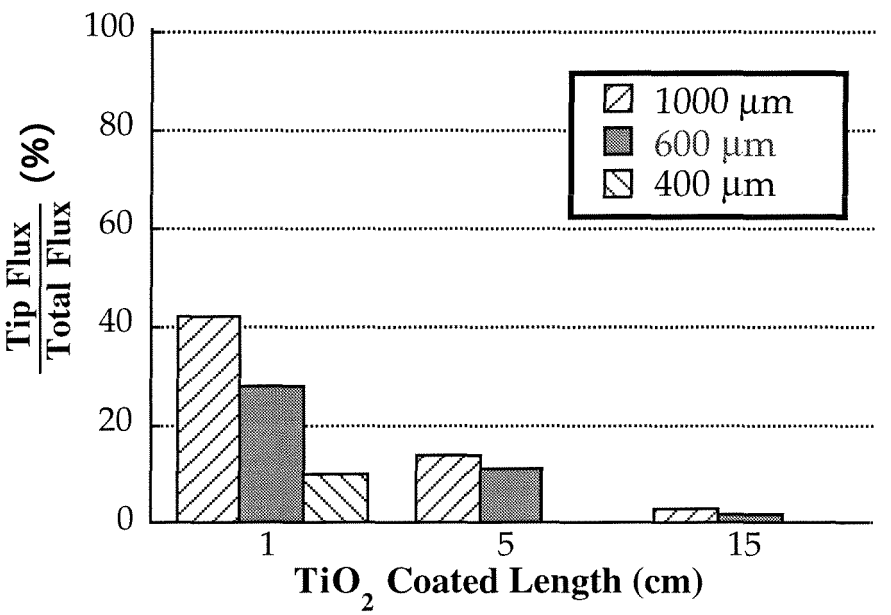

Figure 1. Percent of light flux leaving fiber tip as a function of coated length for quartz optical fibers with diameters of 400, 600, and 1000 µm. 13 wt% Degussa P25 coating, $\theta_i = 76°$.

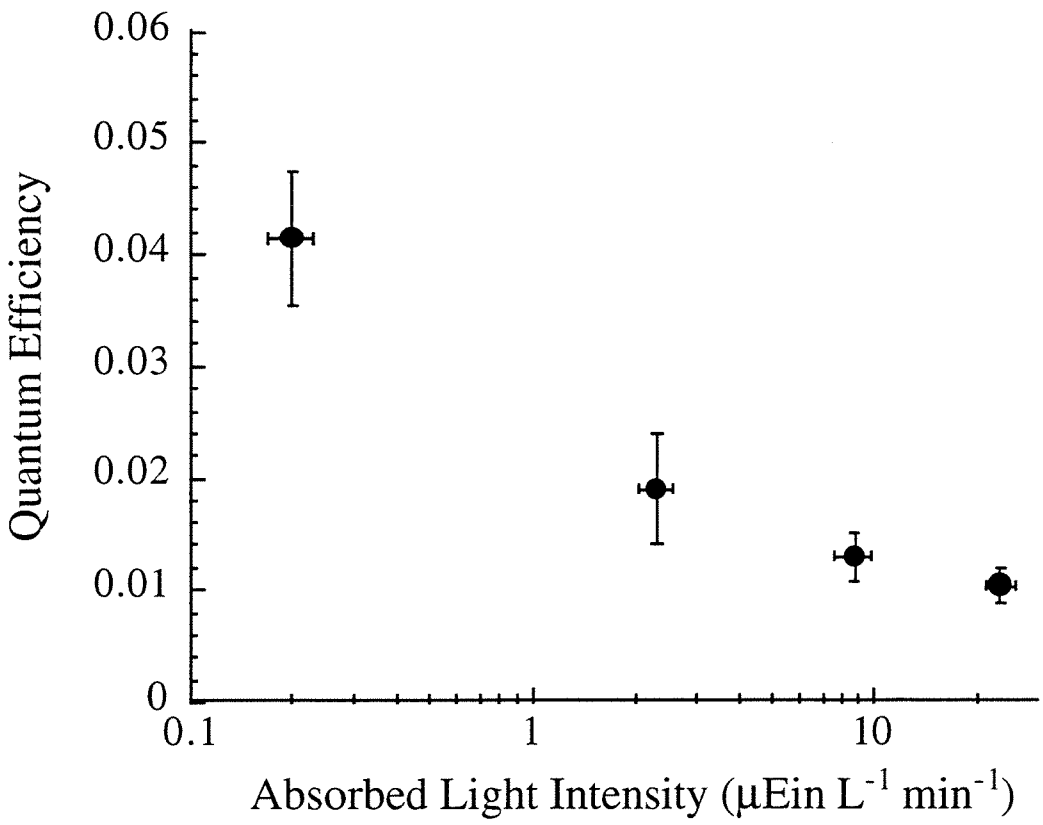

Figure 2. Quantum efficiency for the oxidation of 4-chlorophenol as a function of absorbed light intensity. For each oxidation, the 4-chlorophenol concentration was reduced from 100 to 86 μM. $pH_i \approx 5.5$, 13-wt% coating.

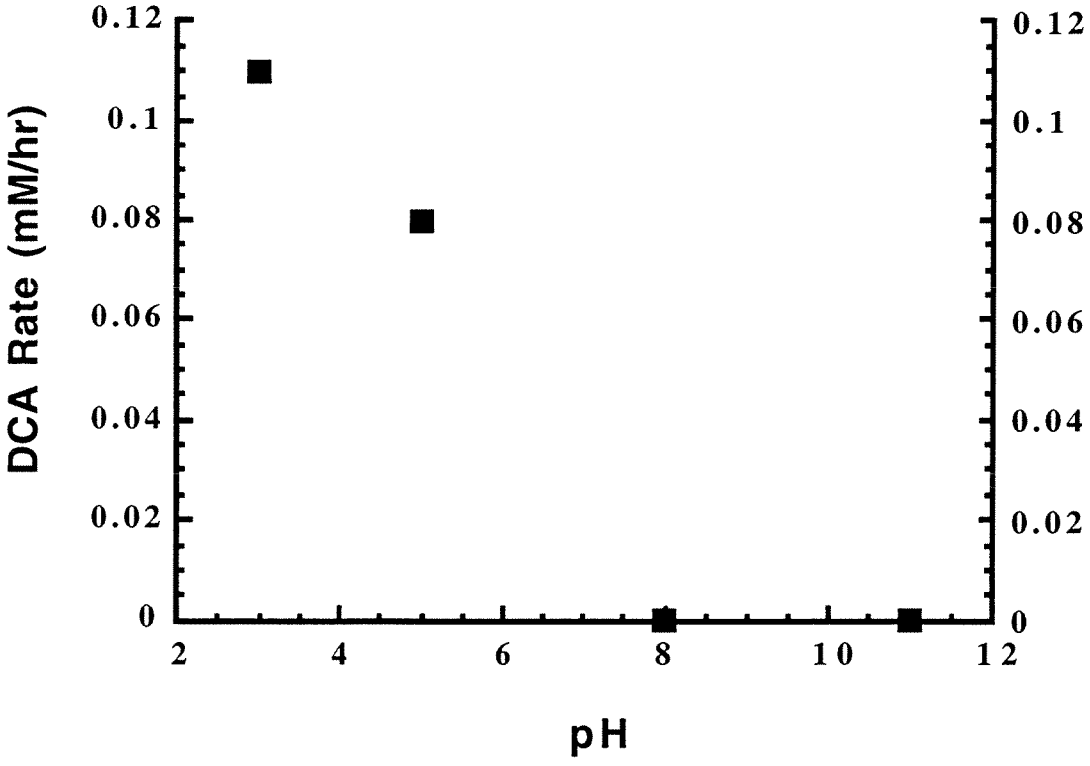

Figure 3a. Oxidation rate of DCA as a function of pH. Reaction conditions are given in the text and in Table 1.

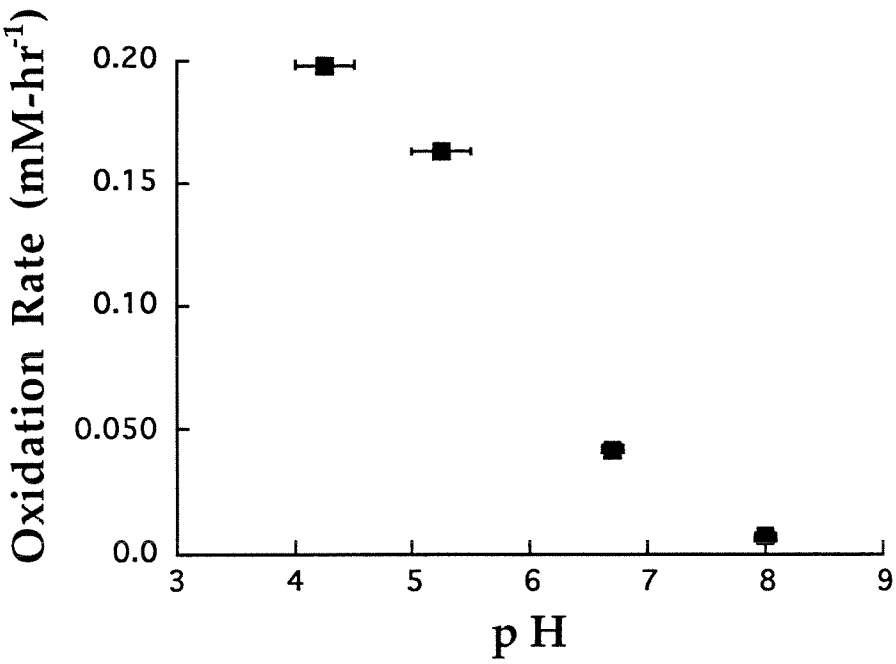

Figure 3b. Photooxidation rate of oxalate as a function of pH. Error bars indicate range of pH during experiment. Reaction conditions are given in the text and in Table 1.

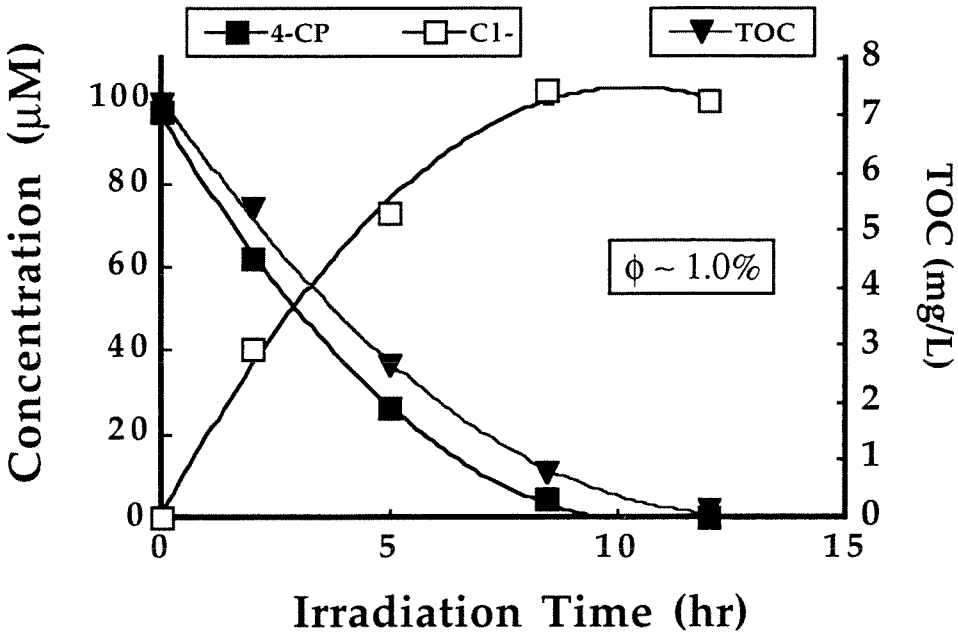

Figure 4. Concentration vs. time plots for 4-chlorophenol degradation at pH_i = 5.5, I_{abs} = 5.3 μE min^{-1} at a 13 wt% TiO_2 coating. The final pH was 4.4.

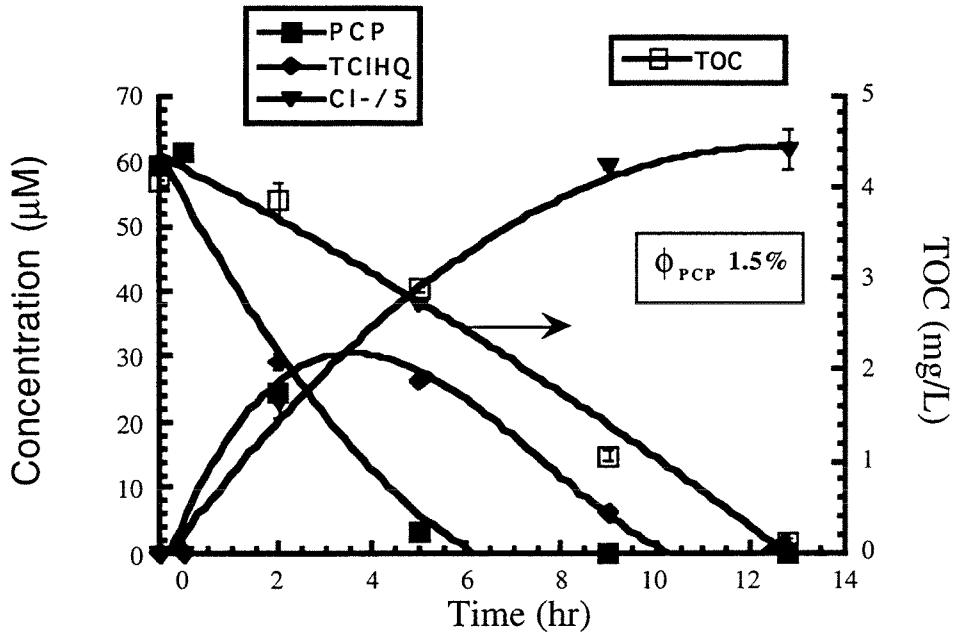

Figure 5. Concentration vs. time plots for pentachlorophenol degradation in pH range pH_i 5.5 - 6.0, I_{abs} = 3.9 μE min^{-1} at a 13 wt% TiO_2 coating.

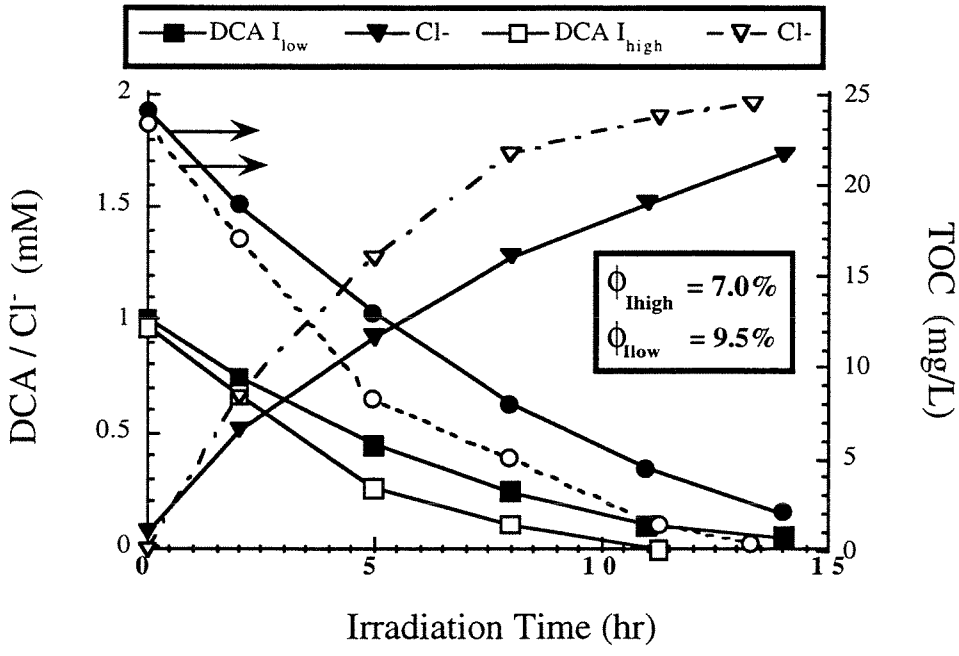

Figure 6. Concentration vs. time plots for DCA degradation at $pH_i = 3.0$ for I_{low} (θ_i = 84°) = 4.2 and I_{high} ($\theta_i = 76°$) = 7.0 μE min^{-1} at a 13 wt% TiO_2 coating. The final pH values were 2.7 and 2.4, respectively.

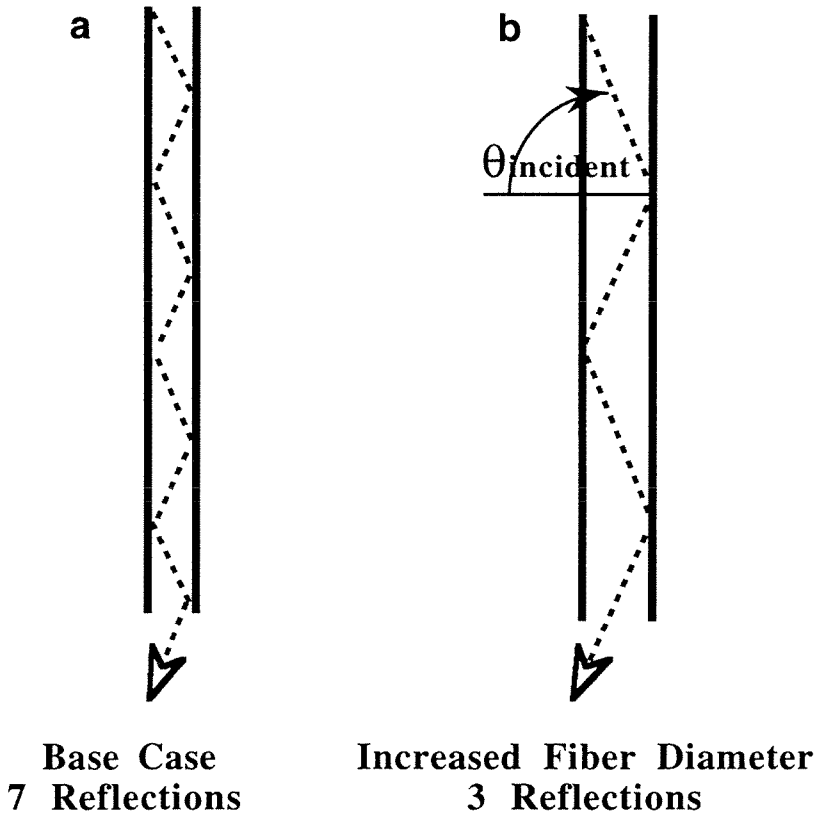

Figure 7. Decrease in reflections per unit length with an increase in fiber diameter: a) Base case 7 reflections; b) Increased fiber diameter with 3 reflections.

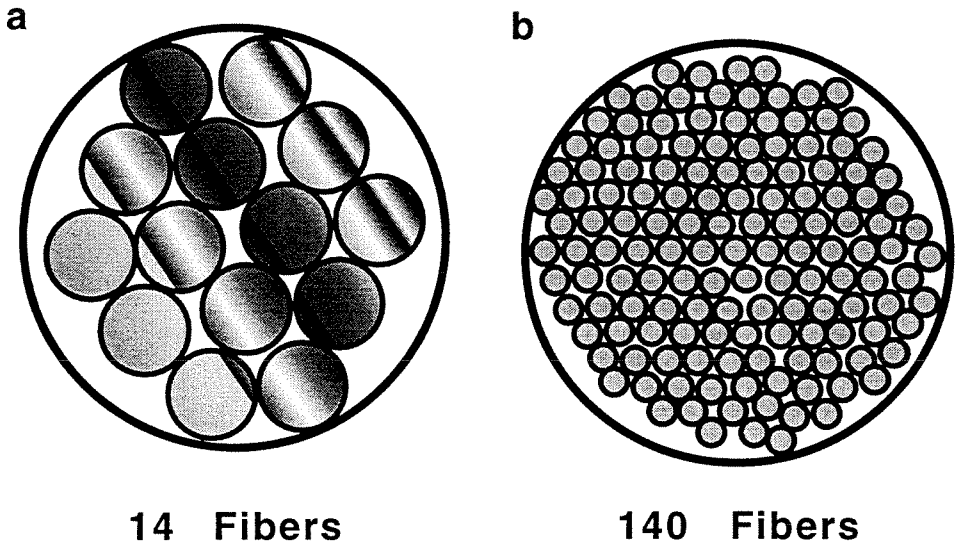

Figure 8. Fiber-bundle head: increase in fiber number density decreases the number of photons to which a fiber's photocatalytic coating is exposed: a) $I_{fiber} = I_{input}/14$; b) $I_{fiber} = I_{input}/140$.

Chapter IV

Iron(III)-doped Q-sized TiO_2 Coatings in a Fiber-Optic Cable Photochemical Reactor

Submitted to *Photochemistry and Photobiology*
October 1996

Abstract

The photochemical quantum efficiencies and oxidation performance of iron(III)-doped quantum-sized TiO_2 (Fe/Q-TiO_2), Degussa P25 (P25), and hybrid Fe/Q-TiO_2/P25 photocatalytic coatings are investigated using an optical fiber bundled array reactor (OFR). Fe/Q-TiO_2 coatings made from hydrosols of varying Fe/Q-TiO_2 content, 5 to 20 wt%, a 13 wt% P25 coating, and a hybrid, layered Fe/Q-TiO_2/P25 (5/13 wt%) coating are tested. The light absorption efficiencies of the Fe/Q-TiO_2 coatings are inferior to the P25 coating, absorbing a maximum of only 80% of the input light compared to greater than 95% for P25 and 90% for the hybrid coating. The Fe/Q-TiO_2 coatings are found to increase the linear light transmission in a single optical fiber relative to P25 coated fibers by a factor of two due to a reduced interfacial surface coverage of the photocatalyst particles on the quartz fiber. The hybrid coating does not significantly enhance linear light transmission.

Slurry-phase photoefficiencies for the photooxidation of 4-chlorophenol for the Fe/Q-TiO_2 photocatalyst are found to be significantly lower than those measured for P25, $\phi_{Fe/Q\text{-}TiO2} = 0.002$ vs. $\phi_{P25} = 0.012$. In addition, the length of the coated fiber-bundle used in our reactor is insufficient to capitalize on the increased light transmission for the Fe/Q-TiO_2 coating. Thus, we are unable to investigate the effect of increased light transmission on the photoefficiency of the system. Initial reaction rates for the photooxidation of 4-chlorophenol range from 2.0 to 4.5 $\mu M\text{-}hr^{-1}$ generally increasing with increasing hydrosol Fe/Q-TiO_2 content and an average relative quantum efficiency of $\phi_{Fe/Q\text{-}TiO2} = 0.004 \pm 0.001$ is observed. These values are significantly low compared to initial rates and relative quantum efficiencies of 18.0 $\mu M\text{-}hr^{-1}$, and $\phi_{Fe/Q\text{-}TiO2/P25} = 0.011$ and 20.4 $\mu M\text{-}hr^{-1}$ and $\phi_{P25} = 0.012$ for the hybrid and P25 coatings, respectively.

Introduction

Semiconductor photocatalysis appears to be an effective means of mineralizing organic pollutants in both aqueous and gaseous waste streams (1-5). Absorption of light energy by the photocatalyst generates active charge pair species, conduction band electrons and valence band holes. These charge pairs can act as powerful oxidants (+1.0 to +3.5 V vs. NHE depending on the semiconductor and pH) and reductants (+0.5 to -1.5 V vs. NHE). Reaction with surface-sorbed electron donors and acceptors form reactive species such as hydroxyl and superoxide radicals. Most hydrocarbon pollutants have been shown to be oxidized by the photogenerated holes or trapped holes (i.e., surface-bound OH•) while some hydrocarbon contaminants and metals can be degraded or removed via a reductive pathway.

In a practical reactor system, immobilization of the photocatalyst is required to allow for the continuous use of the photocatalyst and to eliminate the need for post process filtration. Previous methods of fixation have included glass beads (6, 7), lamp casings (8, 9), glass plates (10), reactor walls (7, 11), fiberglass mesh (12), and ceramic membranes (13, 14). These configurations, however, have several inherent drawbacks such as low light-utilization due to the scattering and absorption of light by the reaction medium. In addition, mass transport limitations induced by low activated surface-area-to-reaction-volume ratios restrict processing capacities.

We have previously investigated a fiber-optic bundled array reactor as a means of light transmission to a solid supported TiO_2 semiconductor (Degussa P25) (15, 16). This reactor configuration enhances the uniformity and distribution of the light-activated catalyst within a given reaction volume relative to conventional fixed-bed reactor designs. This results in reduced mass transport limitations to photochemical conversion and allows for higher processing capacities. The system can be operated in both gas- and aqueous-phase modes (15). In addition, the optical fiber reactor system (OFR) allows for remote delivery

of light over a distance of up to several kilometers. An OFR system could be used for the *in situ* treatment of contaminated sites in the subsurface environment. Apparent quantum efficiencies of the OFR were found to be comparable to slurry-phase reactors for the oxidation of 4-chlorophenol using Degussa P25 TiO_2 (P25) as the photocatalyst (16). A maximum yield of 0.042 was observed for the OFR system. The photochemical quantum efficiency of the OFR system was optimized by varying system parameters, such as the incident angle of light into the reactor, input light intensities, and the coating thickness (15).

In this work, we investigate the use of iron(III)-doped quantum-sized TiO_2 (Fe/Q-TiO_2) as the photocatalytic coating in the OFR. Previous work in our lab found Fe/Q-TiO_2 to have photoefficiencies comparable to P25 for the photooxidation of chloroform (17). In addition, scanning electron microscope (SEM) analysis of Fe/Q-TiO_2-coated optical fibers reveal unique characteristics which indicate that a Q-TiO_2 coating might increase the linear light transmission down the fiber relative to a P25 coating. Extension of the linear light transmission has been found to enhance the system's photochemical quantum efficiency (16). In this paper, we compare the linear light transmission characteristics in single fibers and the relative quantum efficiencies for the photodegradation of 4-chlorophenol with three different TiO_2 coatings: Fe/Q-TiO_2 coatings made from hydrosols of varying Fe/Q-TiO_2 content (5 to 23 wt%), a 13 wt% P25 coating, and a layered hybrid Fe/Q-TiO_2/P25 (5/13 wt%) coating.

Experimental

The optical-fiber bundled array reactor employed for all photooxidation experiments, shown in Fig. 1, has been described in detail elsewhere (15). The basic components are a xenon-arc UV-radiation source, a 310 - 375 nm band pass filter, a focusing lens, a 227 mL cylindrical Pyrex reaction vessel with a bottom-fritted gas inlet, and a TiO_2-coated fiber-optic bundle. The 1.2 m length bundle consists of 72, 1 mm-

diameter quartz optical fibers (3M FT-1.0UMT). The TiO_2-laden fibers were prepared by stripping the terminal 20 cm of the fibers to expose the quartz core, coating with an aqueous slurry of Fe/Q-TiO_2 and/or Degussa P25 TiO_2, and air-dried overnight; thermal treatment has been found to reduce the photoreactivity of Q-sized photocatalysts (18, 19). Plano-convex quartz lenses (Newport-Klinger Rolyn Optics) were used to focus the light into the fiber-optic bundle at a minimum incident angle of 76° for the single-fiber light distribution experiments, and 84° for the 4-CP oxidation experiments.

Fe/Q-TiO_2 Synthesis and Characterization. Iron-doped Q-TiO_2 powders used for the coatings were prepared using the method employed by Choi et al. (20) to achieve an iron dopant level of 0.5 atom%. A 4.2 mL aliquot of a 50 mL aqueous solution containing 0.202 g of $Fe(NO_3)_3$ was added to 500 mL of purified water (Milli-Q, 18MΩ) (4°C) adjusted to pH 1.5 with nitric acid. A 2.5 mL sample of titanium tetraisopropoxide (Aldrich, 97%) dissolved in 50 mL of absolute ethanol (200 proof) was then added dropwise under vigorous stirring. The resulting clear suspension was left to stir for an additional 2 hours and then placed in cold storage (4°C). The final suspension concentration was 1.34 g Fe/Q-TiO_2L^{-1}.

The colloidal suspensions were dialyzed to between pH 4 and pH 5 using Spectraphor dialysis membranes in batch volumes of approximately 100 mL. The dialyzed solutions were then rotovapped (Brinkman) to obtain a Q-sized powder. The average particle size of the Fe/Q-TiO_2 powders were determined by X-ray Diffraction (XRD) (Scintag).

TiO_2 Coating Studies. A three-step process of coating, drying, and heat treatment was used to coat the quartz optical fibers. Initial bonding of a monolayer of TiO_2 particles to the quartz substrate is primarily due to electrostatic interactions (21, 22). Hydrated quartz and TiO_2 (Degussa P25) are amphoteric with pH_{zpc}'s of 2 and 6.6, respectively (23, 24).

Quartz optical fibers (3M Power-Core FT-1.0-UMT) with a diameter of 1 mm were used as a coating substrate. Concentrated hydrosols of TiO_2 (Fe/Q-TiO_2 and Degussa P25) in purified water (Milli-Q, 18 MΩ) were prepared and dispersed by sonication (Branson 5200) and stirring. Hydrosols of 5, 9, 13, 17, 20, and 23 wt% were prepared. The pH of the coating hydrosol ranged between 3 and 4. A length of optical fiber was completely stripped of its protective buffer and cladding using a wire stripper and acetone to expose the quartz core. An aliquot of the hydrosol was pipetted over a 10 cm long section of exposed fiber. The sections were then air dried for 24 hr. The TiO_2-coated fibers were fired in a high-temperature furnace (Lindberg Model 55322 Moldatherm) at 300°C for 1 hr. For the single-fiber light distribution experiments, a heat gun was used to dry the coated fibers at 100°C.

The heat treated samples were cut into 3-5 mm lengths for analysis by SEM (Camscan Series 2) using secondary electrons and back-scattered electron imaging. These samples were gold-coated using a standard vacuum evaporation procedure. Maximum, minimum, and an average thickness were recorded for each sample.

Input and Absorbed Intensity Measurements. Input and absorbed light intensities for the single-fiber light distribution and fiber-bundle photooxidation experiments were measured by chemical actinometry using α-(2,5-dimethyl-3-furyethylidene) (isopropylidene) succinic anhydride (Aberchrome 540). The experimental methods have been previously described (15) . In general, the treated portion of the fiber/fiber bundle was immersed in a 1 cm-diameter quartz tube containing distilled water. The water and quartz tube were transparent to the UV light. The quartz vessel was then suspended in a jacketing glass vessel containing the actinometry solution. In order to prevent photocatalytic oxidation of the Aberchrome, it was necessary to separate the TiO_2-coated fibers from the actinometry solution. Nitrogen was bubbled from the bottom through a glass frit to enhance mixing.

Light flux measurements were made for uncoated and coated fibers. The difference between the two was taken to be the photon flux absorbed by the TiO_2 layer, I_{abs}. The input light intensities, I_{input}, were found to be a function of the focusing lens used and the corresponding coupling efficiency of the light beam to the fiber/fiber-bundle face.

Light Distribution in Single Fiber. Light flux measurements were made at increasing coated lengths to determine the distribution of light in a single coated fiber. The coatings employed were 5, 13, and 20 wt% Fe/Q-TiO_2, a 13 wt% P25, and a hybrid 5/13 wt% Fe/Q-TiO_2/P25 coatings. The fiber coating method used for the light distribution experiments is as described above. To prepare the layered, hybrid coating, a fiber was first coated with a 5 wt% Fe/Q-TiO_2 hydrosol. After drying with a heat gun for several minutes, the fiber was then coated with a 13 wt% P25 hydrosol. Fe/Q-TiO_2 hydrosol concentrations greater than 5 wt% resulted in the partial delamination of the coating upon application of the P25 coating and drying. Therefore, only a 5/13 wt% Fe/Q-TiO_2/P25 hybrid coating was tested.

In general, a section of optical fiber was stripped and coated at increasing lengths of 5, 10, 15, 20, 25, 30, and 35 cm. For coating absorption determination, uncoated total and coated total measurements were made at each length and for each coating. The difference between the uncoated and coated total fluxes was taken to be the light flux absorbed by the coating. To determine the amount of light refracted out of the fiber, the tip of the fiber was submerged in the actinometry solution and an uncoated and coated tip flux measurements were taken. The difference between these two measurements was taken to be the light flux refracted out of the fiber. The coatings were removed by wiping the fiber with a damp cloth.

4-Chlorophenol Oxidation. To compare the oxidation and quantum efficiency performance of the various photocatalytic coatings, photooxidation of 4-chlorophenol was

carried out in the OFR. Fibers were coated with the method described above but were air-dried overnight rather than oven-fired. A 190 mL, 0.1 mM solution of 4-chlorophenol (4-CP) was prepared from a 1.0 mM stock solution (Aldrich, 99+%) with an initial pH of 5.5. Chloride ion production during the course of oxidation was followed by ion chromatography (Dionex BIOLC 4500i Series). pH was determined with a Radiometer PHM85 pH meter. Disappearance of 4-CP was followed spectrophotometrically at λ = 224 and 280 nm (Shimadzu UV-2101PC and HP8451A Diode Array) and by HPLC (HP SeriesII 1090). Oxygen (Liquid Air) was used to saturate the reaction solution and to ensure proper mixing. An in-line gas purifier (Alltech 8132) was used to remove particulates and hydrocarbons. The coated fibers were immersed in the reaction solution and allowed to equilibrate for 30 minutes. Quantum efficiencies were determined after 2 hours of irradiation and overall oxidation performance compared after 14 hours of irradiation.

Results

Fe/Q-TiO_2 Powder and Coating Characterization. The average particle size of the Fe/Q-TiO_2 powder was found to be 4 nm, and anatase was determined to be the predominant phase with some rutile present.

SEM micrographs showing a cross-sectional (a) and an angled side view (b) for 5 and 17 wt% Fe/Q-TiO_2 coatings are presented in Figs. 2ab and 3ab, respectively. The micrographs reveal Fe/Q-TiO_2 coatings that are non uniform in coverage and thickness, and made up of very coarse, irregular particles. Exposed areas of quartz fiber are visible. The average thickness and maximum particle size do not appear to vary significantly with an increase in the hydrosol coating concentration. Average thicknesses of 5-7, 3-5, 4-9, 2-4, and 4-12 μm are measured for the 5, 9, 17, 20, and 23 wt% coatings, respectively. Maximum sizes of 14, 16, 20, 15, and 20 are observed for concentrations of 5, 9, 13, 20,

and 23 wt%. Although the maximum particle size does not appear to be correlated with the hydrosol coating concentration, the number of maximum-sized particles does. Qualitatively, the interfacial coverage of the particles on the quartz surface appears to increase as the hydrosol coating concentration is increased.

Single-fiber Light Distribution. The percentage of input light refracted out of a single fiber as a function of coated length for 5, 13, and 20 wt% Fe/Q-TiO_2, 13 and 17 wt% P25, and 5/13 wt% Fe/Q-TiO_2/P25 hybrid coatings is shown in Fig. 4. In each case, the amount of light refracted increases as the coated length increases. The 13 and 17 wt% P25 coatings refract the highest percentage of light at each length refracting 80 and 87% within 5 cm and 100% by 30 cm. Whereas the Fe/Q-TiO_2 coatings consistently retain more light in the fiber at each length, from 60 to 80% at 5 cm and 12 to 22% at 35 cm, with the degree of refraction increasing as the coating hydrosol concentration increases from 5 to 20 wt%.

Figure 5 is a plot of the percentage of input light absorbed by the Fe/Q-TiO_2 coating as a function of the hydrosol Fe/Q-TiO_2 concentration. Data for the P25 and hybrid Fe/Q-TiO_2/P25 coatings are shown for comparison. As the hydrosol Fe/Q_2-TiO concentration is increased from 5 to 20 wt% the percentage of light absorbed increases from 28 to 70% for a single coated fiber. Absorption efficiencies for the coated fiber bundle are consistently higher increasing from 53 to 83% over the same concentration range. The P25 coatings for both the single-fiber and fiber bundle absorb significantly more of the input light than the Fe/Q_2-TiO_2 coatings ranging from 65 and 73%, respectively, to greater than 90% as the coating concentration is increased from 5 to 17 wt%.

Photooxidation and Photochemical Efficiency. The initial reaction rates and apparent quantum efficiencies for all coatings investigated are given in Table 1. The apparent quantum efficiency is calculated as the ratio of the initial rate of oxidation of 4-CP

to the flux of absorbed photons. The relative quantum efficiencies for the Fe/Q-TiO_2 coatings are 25 to 45% lower than for the P25 coatings ($\phi_{Fe/Q\text{-}TiO2}$ = 0.003-0.005 vs. ϕ_{P25} = 0.012). No correlation with respect to the hydrosol Fe/Q-TiO_2 content is observed.

Oxidation profiles for 4-CP for 5, 13, and 20 wt% Fe/Q-TiO_2 coatings and a 13 wt% P25 coating are shown in Fig. 6. The corresponding input and absorbed light intensities are 2.3/4.0, 2.7/4.0, 5.5/6.7, and 5.3/5.9 $\mu E\text{-}min^{-1}$, respectively. With the P25 coating, complete oxidation of the 4-CP after 8 hours of irradiation is achieved with an initial rate of 20.4 μMhr^{-1}. Sixty-five percent of the 4-CP is degraded after 12 hours for the 20 wt% Fe/Q-TiO_2 coating; whereas the 5 and 13 wt% Fe/Q-TiO_2 coatings achieve only a 20% level of degradation after 14 hours, with corresponding initial rates of 7.0, 4.5, and 2.2 μMhr^{-1}, respectively.

Comparison of Efficiencies of Fe/Q-TiO_2 in the OFR to a Conventional Slurry Reactor. The relative quantum efficiency of a slurry-phase reactor setup consisting of a well-mixed solution of 0.1 mM 4-CP and 0.5 wt% Fe/Q-TiO_2, irradiated with 1.8 $\mu E\text{-}min^{-1}$ ($310 \leq \lambda \leq 375$ nm) in a 50 mL quartz cell for 2 h, was determined. A relative quantum efficiency of 0.002 ± 0.000 was measured (Table 1).

Layered, Hybrid Fe/Q-TiO_2/P25 Coating. The degree of refraction and absorption efficiency data for a 5/13 wt% Fe/Q-TiO_2/P25 coating are shown in Figures 4 and 5. The light distribution for the hybrid coating is similar to the P25 coating refracting 68% of the input light within 5 cm and a maximum of 90% by 30 cm, and absorbing 90% of the refracted light. The measured relative quantum efficiency, listed in Table 1, is slightly lower than the P25 coating ($\phi_{Fe/Q\text{-}TiO2/P25}$ = 0.011) with an initial rate of 18.0 μMhr^{-1}.

Discussion

In our previous studies (15, 16) bulk-sized Degussa P25 TiO_2 is used as the photocatalytic coating. The photochemical efficiency of the OFR is optimized by minimizing the incident light intensity; employing a coating thickness of 7 μm that results in 100% absorption of radially-refracted light; and maximizing the linear transmission of light down the optical fibers. The two latter optimizations result in an increase in the activated photocatalytic surface area and a corresponding increase in the apparent quantum efficiency. Relative increases in linear light transmission are achieved by maximizing the incident angle, θ_i, of light introduced into the fibers, e.g., 90°, and minimizing interfacial contact area of the photocatalyst particles on the quartz fibers.

Our interest in investigating the use of Fe/Q-TiO_2 as the photocatalyst coating in the OFR is two-fold. Previous studies in our lab show the photoreactivity of Fe/Q-TiO_2 to be comparable to P25 for the photooxidation of chloroform (18, 19). In addition, preliminary SEM coating analysis (vide infra) suggests that the interfacial contact area of Fe/Q-TiO_2 particles on the quartz fibers may be lower than for P25 coatings leading to enhanced linear light transmission and higher photoefficiencies.

In a semiconductor system where the charge transfer to a sorbed substrate is rate-limiting, an increase in the band gap energy, is thought to lead to enhanced photoefficiencies (25). It has been shown that the band gap of a semiconductor can be increased in part by reducing the size of the crystals comprising the photocatalyst particles (26, 27). When the crystallite dimensions become "quantized", smaller than approximately 10 nm, an increase in the band gap and a shift in the band edges occurs leading to larger driving forces for both oxidation and reduction reactions. Since the solvent reorganization free energy for charge transfer to a substrate remains unchanged, this increase is expected to result in a higher rate constant for interfacial charge transfer. Thus, quantum-sized

semiconductor colloids may provide a means of enhancing photoefficiencies in chemical systems where charge transfer is rate-limiting.

Furthermore, it has been shown that metal-ion dopants can improve semiconductor photoefficiencies (28-32). In studies involving Fe(III) doping of TiO_2 (Fe/Q-TiO_2), the quantum efficiencies for the photoreduction of N_2 and methyl viologen have been shown to increase (29-31). In a study conducted by Bockelman et al., the degradation of dichloroacetic acid was found to be almost four times as efficient using TiO_2 particles with an iron content of 2.5 atom% at pH 2.6 compared to undoped TiO_2 colloids (32). This improved efficiency has been attributed, in part, to the action of the ferric ions within the TiO_2 matrix inhibiting photogenerated charge pair recombination. In some systems, however, Fe(III) doping has had little or even a negative effect, such as in the case of phenol degradation (30, 31).

Choi et al. selectively doped Fe/Q-TiO_2 particles to study the photocatalytic effects of various metal-ion dopants in Fe/Q-TiO_2 (18, 19). A systematic study was conducted using 21 metal ion dopants at a dopant level of 0.1-0.5 atom%. Maximum enhancements were seen using Fe(III) at a dopant level of 0.5 atom% relative to the undoped Fe/Q-TiO_2 counterpart. Specifically, 18-fold and 15-fold increases in quantum efficiency were seen for Fe(III)-doped TiO_2 in CCl_4 reduction and $CHCl_3$ oxidation, respectively. Overall, it was determined that the photoreactivity of Q-size, doped TiO_2 is a complex function of dopant concentration, the energy levels and the distribution of dopants within the TiO_2 lattice, and the incident light intensity. The authors concluded that enhanced interfacial charge transfer in the presence of effective dopants appears to be the most important factor in increased photoreactivity of doped TiO_2.

Fe/Q-TiO_2 Coating Characterization. SEM analysis reveals nonuniform coating thicknesses that do not appear to be correlated with the hydrosol coating concentration (Figs. **2** and **3**). This result may be explained by the observation that the size ranges of the

particles made up of agglomerated Fe/Q-TiO_2 crystals also appear not to be correlated with the hydrosol coating concentration. The largest particles observed are two to four times greater than the average coating thickness (15 μm vs. 2-4 μm). Qualitatively, the interfacial contact area of the particles appears to be greatly reduced compared to the P25 coatings shown in Fig. 7. This relative reduction may be a result of larger agglomerated Fe/Q-TiO_2 particles that don't adhere consistently to the quartz surface leaving behind open patches of exposed quartz.

The nonuniformity and large variability in the particle sizes of the Fe/Q-TiO_2 coatings are in stark contrast to the P25 coatings (Fig. 7). P25 is comprised of bulk-sized crystals of 20-50 nm which are agglomerated to sizes up to 1 μm. The resulting coating is uniformly thick and opaque with a high interfacial contact area. The coating thickness is found to be positively correlated with the hydrosol coating concentration. Based on the findings from the previous efficiency enhancement study (vide supra), the reduced interfacial contact coverage of Fe/Q-TiO_2 coatings indicates that an Fe/Q-TiO_2 coating might be effective in increasing the linear light transmission in the coated fibers which, in turn, may enhance the photochemical quantum efficiencies.

Single-fiber Light Distribution. The reduced refraction of input light for the Fe/Q-TiO_2 coatings compared to P25 support the hypothesis of reduced interfacial contact area (Fig. 4) assuming similar refractive indices for the Fe/Q-TiO_2 and P25 crystals. Fe/Q-TiO_2 coatings double the linear light transmission relative to P25 coatings, > 35 cm (with 12 to 22% of the light still remaining in the fiber) and 20 cm , respectively. A decrease in the interfacial particle coverage decreases the probability that a photon will be incident at a quartz-TiO_2 interface and refracted out of the fiber as illustrated in Fig. 8. Thus, the linear light transmission down the fiber is extended resulting in the activation of a greater length of coating and increased activated surface area. Consistent increases in the degree of refraction with increasing Fe/Q-TiO_2 hydrosol coating concentration may indicate that the

interfacial contact area increases correspondingly, although this trend was not evident from the SEM micrographs.

Although the Fe/Q-TiO_2 coating thickness does not appear to be correlated with the hydrosol concentration, the percentage of input light absorbed for a 35 cm coated length of fiber doubles from 25% to about 70% for hydrosol contents from 5 to 20 wt% (Fig. 5). The increase in the absorption efficiency may be due to an increase in the interfacial coverage of particles and in the number of larger particles as the hydrosol concentration is increased. While the larger particles do not appear to significantly alter the average coating thickness, they absorb more light.

The Fe/Q-TiO_2 coating absorption efficiencies are higher for the coated bundle (20 cm length), increasing from about 53 to 82%. Fibers in the bundle can absorb light penetrating through the coating of neighboring fibers. Even for the highest hydrosol concentration, 23 wt%, the Fe/Q-TiO_2 coatings achieved an absorption efficiency of only 82% compared to > 95% for the P25 coatings (15). An absorption efficiency of 100% is desired since refracted light not absorbed by the coating is unproductive and may be achieved using higher hydrosol concentration coatings.

Oxidation and Quantum Efficiency Performance Comparison. The expected higher photoefficiencies at lower hydrosol coating concentration as a result of increased linear light transmission are not observed (Table 1, Fig. 6). That is, there is no trend in the photoefficiencies with respect to the Fe/Q-TiO_2 hydrosol coating concentration. However, we believe that the 20 cm coated length of fibers in the OFR bundle is insufficient to capitalize on the increased linear light transmission of the Fe/Q-TiO_2 coatings which exceed 20 cm for all the Fe/Q-TiO_2 coatings investigated. In order to see an increasing photoefficiency trend as the hydrosol coating concentration is decreased due to enhanced activated photocatalytic surface area, a coated bundle length of 50 cm would be needed. Further investigation would require the construction of a new reactor system. Due to the

inferior photoefficiencies of the Fe/Q-TiO_2 coatings compared to the P25 coatings, we did not pursue this avenue of investigation.

The measured apparent quantum efficiencies for the Fe/Q-TiO_2 coatings ($\phi = 0.004 \pm 0.001$) are slightly higher than those measured for a slurry-phase reactor using Fe/Q-TiO_2 ($\phi = 0.002$). However, these values are about 30% lower than photoefficiencies measured for the P25 coatings in this and previous studies (15, 16). The 20 wt% Fe/Q-TiO_2 coating shows the best performance with an initial rate of 7.0 μMhr^{-1}; but the apparent quantum efficiency remains low at $\phi = 0.004$. Accelerated oxidation of the 4-chlorophenol with an increase in the hydrosol concentration (Table 1, Fig. 6) is probably due to correspondingly higher absorbed light intensities. The poorer performance of the Fe/Q-TiO_2 coatings for the oxidation of 4-CP is attributed to the inherently lower photoreactivity of the Fe/Q-TiO_2 photocatalyst as measured in a slurry-phase reactor.

Fe/Q-TiO_2/P25 Layered, Hybrid Coating. As a result of the lower photoreactivities of the Fe/Q-TiO_2 coatings, a layered, hybrid Fe/Q-TiO_2/P25 coating is investigated. The objective is determine whether the linear light transmission enhancement effect of an inner Fe/Q-TiO_2 coating and the superior photoreactivities of a P25 coating could be combined to maximize the photochemical quantum efficiency.

The degree of refraction of the layered, hybrid coating approaches that for the P25 coating suggesting that the interfacial contact coverage is also relatively high, greatly mitigating any linear light transmission enhancement effect by the inner 5 wt% Fe/Q-TiO_2 coating. Destablization of hybrid coatings with higher Fe/Q-TiO_2 hyrosol concentrations (> 5 wt%) may indicate that the P25 particles bind to and are stabilized by the quartz surface, effectively filling in the patches of the Fe/Q-TiO_2 coating. Consequently, at higher Fe/Q-TiO_2 hydrosol concentrations, there is not sufficient contact between the P25 particles and the quartz surface. This observation also supports the hypothesis that the interfacial contact coverage increases as the Fe/Q-TiO_2 hydrosol coating concentration is increased.

The oxidation performance of the hybrid, layered coating approaches that of the P25 coating (R = 18.0 $\mu M\text{-}hr^{-1}$ and ϕ = 0.011) (Table 1). The slightly lower quantum efficiency reflects the contribution of the lower photoreactivity of the Fe/Q-TiO_2 portion of the coating and the absence of any linear light transmission enhancement effect by the inner 5 wt% Fe/Q-TiO_2 coating.

Conclusions

Iron-doped Q-sized coatings are found to enhance the linear light transmission in a single, optical fiber relative to bulk-sized Degussa P25 TiO_2, due to a reduced interfacial contact area of the photocatalyst particles on the quartz surface. This enhancement is not observed to increase the photoefficiencies for the oxidation of 4-chlorophenol in the OFR system possibly due to insufficient coated fiber length. Measured relative quantum efficiencies for the Fe/Q-TiO_2 coatings are 30% lower compared to P25 coatings due in part to the lower inherent photoreactivity of the Fe/Q-TiO_2 photocatalyst compared to P25 for the photooxidation of 4-chlorophenol. The light absorption efficiencies of the Fe/Q-TiO_2 coatings are also inferior to the P25 coatings.

In general, extension of the linear light transmission will increase the length of coated fiber that is illuminated, thus increasing the overall activated photocatalytic surface area. Higher activated surface area is important for reducing mass transport limitations and maximizing efficiencies and processing capacities. Due to the poor photoreactivity of the Fe/Q-TiO_2 coating, other means of achieving increased linear light transmission should be investigated. These methods may include selective stripping and/or coating of the optical fiber, or mixing the photocatalyst with a photonically-inert filler such as granulated activated carbon or silica.

Acknowledgments

We are grateful to ARPA and ONR (NAV 5 HFMN N000149J1901) for financial support and to Lisa Bourne and Tim Wu for their help in the lab, and Janet Kesselman, Scot T. Martin, and Wonyong Choi for scientific support. We would also like to thank 3M and Degussa for their donations of the optical fiber samples and the P25 photocatalyst, respectively.

Literature Cited

(1) Hoffmann, M. R.; Martin, S. T.; Choi, W.; Bahnemann, D. W. *Chem. Rev.* **1995**, *95*, 69-96.

(2) Legrini, E.; Oliveros, E.; Braun, A. M. *Chem. Rev.* **1993**, *93*, 671.

(3) Fox, M. A.; Dulay, M. T. *Chem. Rev.* **1993**, *93*, 341.

(4) Matthews, R. W. *Wat. Res.* **1990**, *24*, 653-660.

(5) Ollis, D. F.; Al-Ekabi, H. *Photocatalytic Purification and Treatment of Water and Air*; Elsevier: Amsterdam, 1993.

(6) Serpone, N. *Sol. Energy* **1986**, *14*, 121-126.

(7) Al-Ekabi, H.; Serpone, N. *J. Phys. Chem.* **1988**, *92*, 5726-5731.

(8) Sabate, J.; Anderson, M. A.; Kikkawa, H.; Edwards, M.; Hill, C. G. *J. Catal.* **1991**, *127*, 167-177.

(9) Sabate, J.; Anderson, M. A.; Aguado, M. A.; Gimenez, J.; Cerveramarch, S.; Hill, C. G. *J. Mol. Catal.* **1992**, *71*, 57-68.

(10) Anderson, M. A.; Gieselmann, M. J.; Xu, Q. Y. *J. Membr. Sci.* **1988**, *39*, 243-258.

(11) Matthews, R. W.; Abdullah, M.; Low, G. K. C. *Anal. Chim. Acta* **1990**, *233*, 171-179.

(12) Al-Ekabi, H.; Safarzadey-Amiri, A.; Sifton, W.; Story, J. *Intl. J. Environ. Pollut.* **1991**, *1*, 125-136.

(13) Sabate, J.; Anderson, M. A.; Kikkawa, H.; Xu, Q.; Cerveramarch, S.; Hill, C. G. *J. Catal.* **1992**, *134*, 36-46.

(14) Aguado, M. A.; Anderson, M. A.; Hill, C. G. *J. Mol. Catal.* **1994**, *89*, 165-178.

(15) Peill, N. J.; Hoffmann, M. R. *Environ. Sci. Technol.* **1995**, *29*, 2974.

(16) Peill, N. J.; Hoffmann, M. R. *Environ. Sci. Technol.* **1996**, *30*, 2806-2812.

(17) Choi, W.; Hoffmann, M. R. *Environ. Sci. Technol.* **1995**, *29*, 1646-1654.

(18) Choi, W.; Termin, A.; Hoffmann, M. R. *Angew. Chem.* **1994**, *106*, 1148.

(19) Choi, W.; Termin, A.; Hoffmann, M. R. *J. Phys. Chem.* **1994**, *98*, 13669-13679.

(20) Choi, W. Y.; Termin, A.; Hoffmann, M. R. *Angew. Chem.-Intl Edition In English* **1994**, *33*, 1091-1092.

(21) Xu, Q. Y.; Anderson, M. A. *J. Matls. Res.* **1991**, *6*, 1073-1081.

(22) Hu, L. L.; Yoko, T.; Kozuka, H.; Sakka, S. *Thin Solid Films* **1992**, *219*, 18-23.

(23) Stumm, W.; Morgan, J. J. In *Aquatic Chemistry*; Eds.; Wiley: New York 1981; p 637.

(24) *Degussa Technical Bulletin* **1990**, *No. 56*,

(25) Marcus, R. A. *J. Phys. Chem.* **1990**, *94*, 1050.

(26) Hoffmann, A. J.; Yee, H.; Mills, G.; Hoffmann, M. R. *J. Phys. Chem.* **1992**, *96*, 5540.

(27) Hoffmann, A. J.; Mills, G.; Yee, H.; Hoffmann, M. R. *J. Phys. Chem.* **1992**, *96*, 5546.

(28) Gratzel, M.; Howe, R. F. *J. Phys. Chem.* **1990**, *94*, 2566.

(29) Soria, J.; Conesa, J. C.; Augugliaro, V.; Palmisano, L.; Schiavello, M.; Sclafani, A. *J. Phys. Chem.* **1991**, *95*, 274-282.

(30) Palmisano, L.; Augugliaro, V.; Sclafani, A.; Schiavello, M. J. *J. Phys. Chem.* **1988**, *92*, 6710-6713.

(31) Sclafani, A.; Palmisano, L.; Schiavello, M. *Chem. Intermed.* **1992**, *18*, 211.

(32) Bockelman, D.; Goslich, R.; Bahnemann, D. In *Solar Thermal Energy Utilization*; M. Becker, K. H. Funken and G. Schneider, Eds.; Springer Verlag GmbH: Heidelberg 1992.

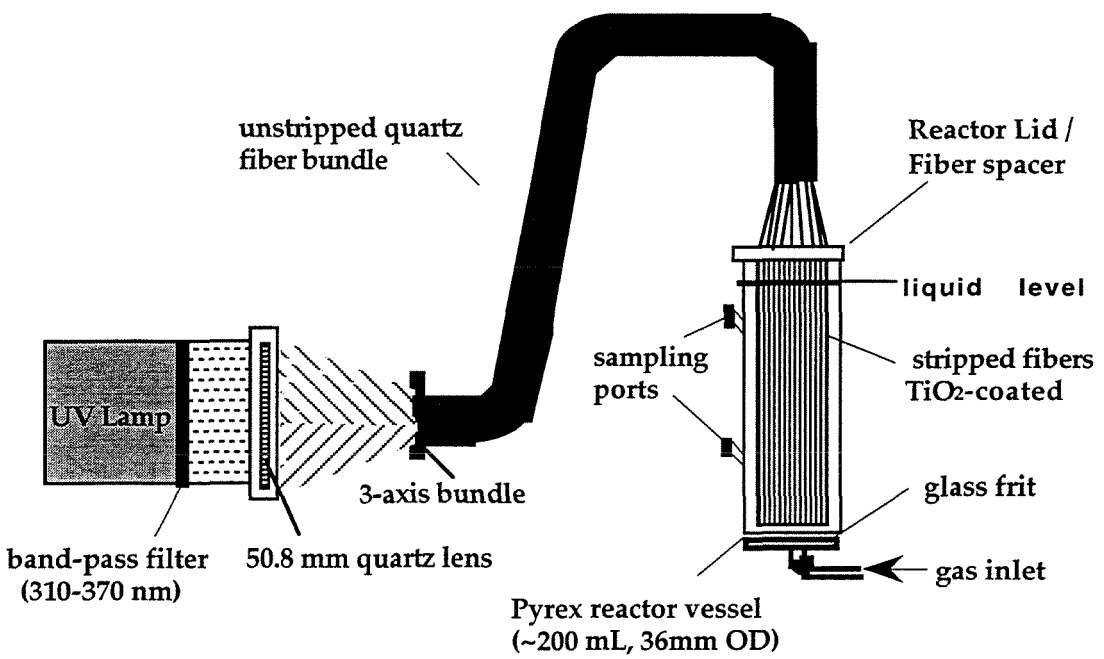

Figure 1. Schematic of optical fiber bundled array photocatalytic reactor system.

(a)

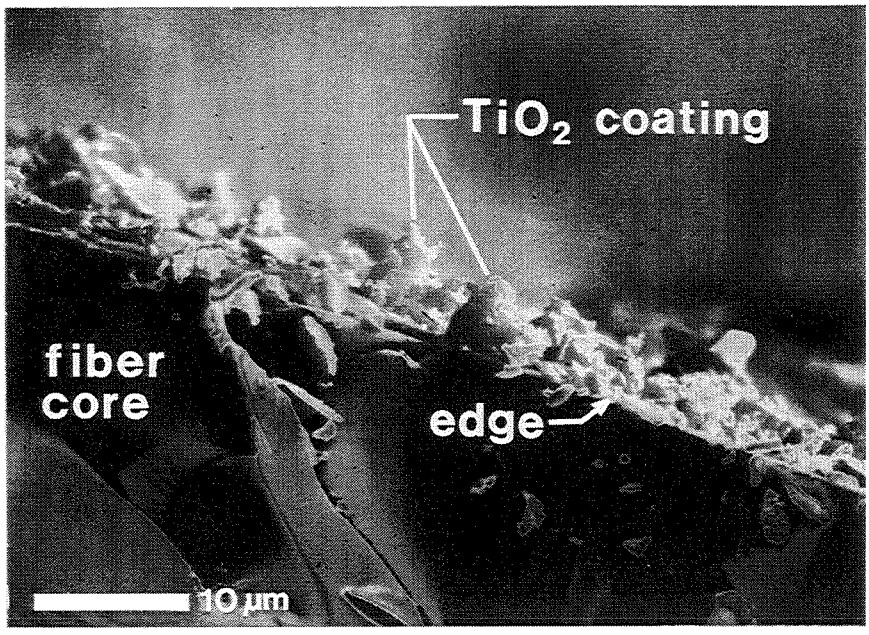

(b)

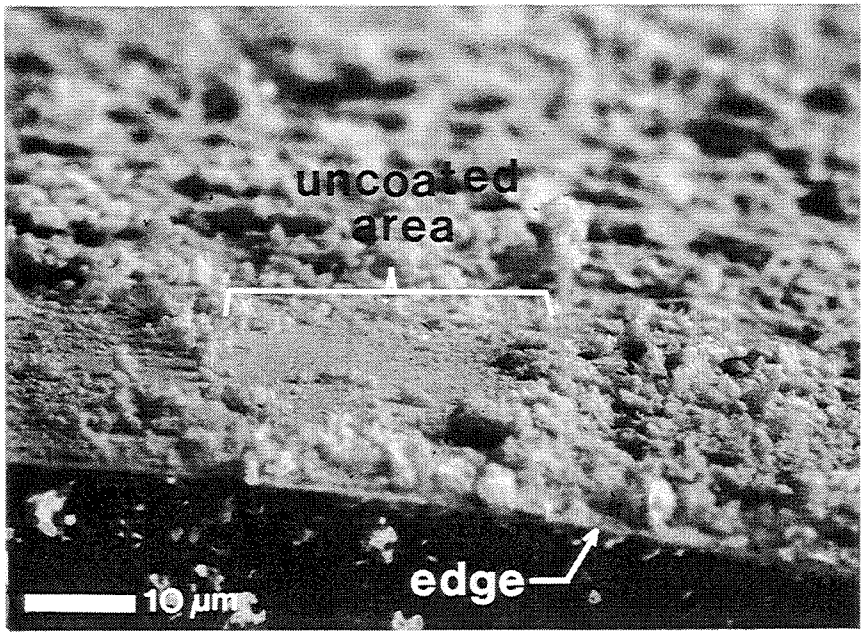

Fig. 2. SEM micrographs of Fe(III)-doped Q-sized TiO_2 on 1-mm diameter quartz optical fiber substrate: (a) 5 wt% coating, (b) oblique view.

(c)

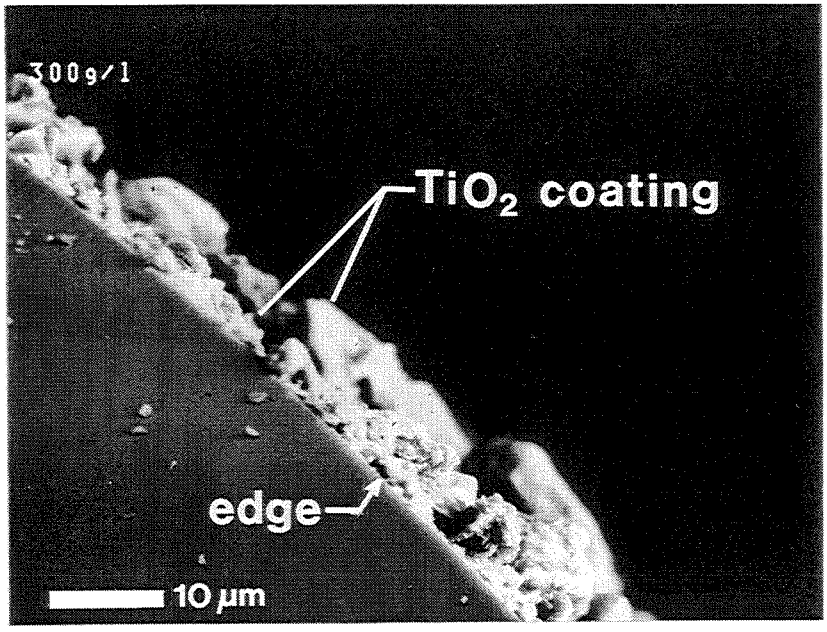

(d)

Fig. 3. SEM micrographs of Fe(III)-doped Q-sized TiO_2 on 1-mm diameter quartz optical fiber substrate: (c) 23 wt% coating, (d) oblique view.

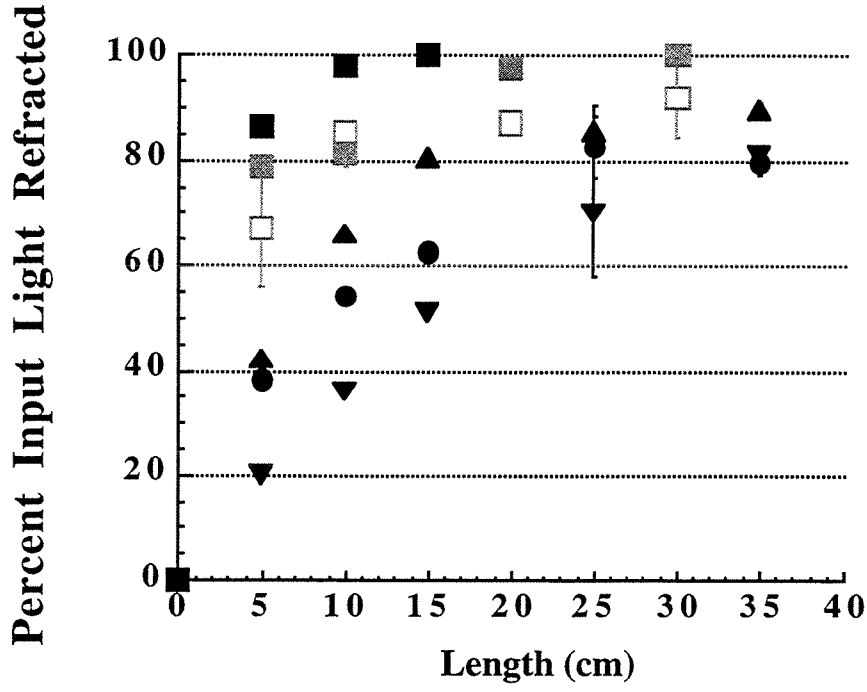

Figure 4. Percentage of input light refracted out of a single fiber as a function of coated length of fiber for (▼) 5 wt%, (●) 13 wt%, and (▲) 20 wt% Fe/Q-TiO_2 TiO_2 and (□) Fe/Q-TiO_2/P25 5/13 wt% hybrid, (shaded □) P25 13 wt%, (■) P25 17 wt% coatings.

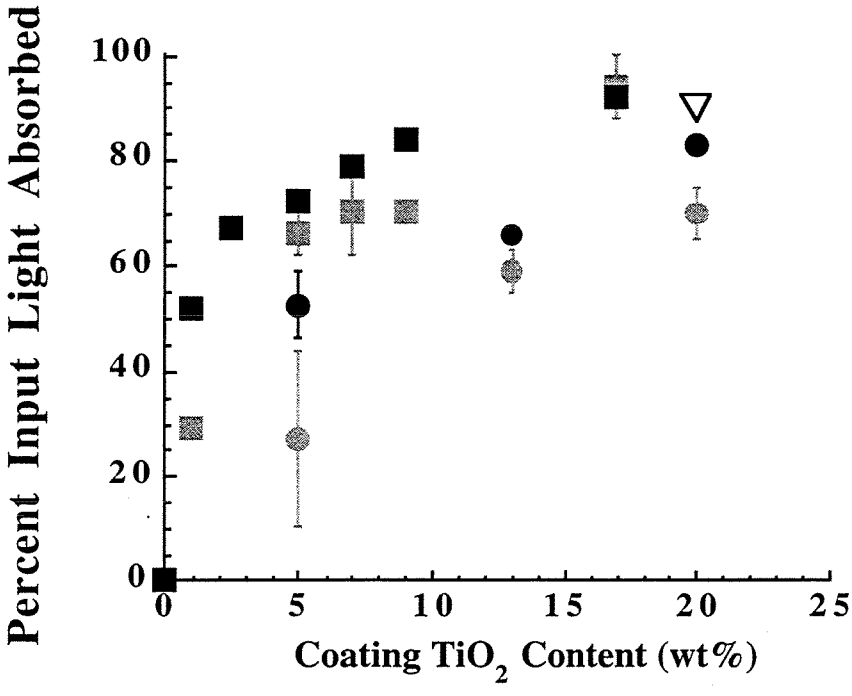

Figure 5. Percentage of input light absorbed by coating as a function of coat TiO_2 content for (shaded O) Fe/Q-TiO_2 single fiber, (●) Fe/Q-TiO_2 fiber bundle, (shaded □) P25 single fiber (■) P25 fiber bundle and (▽) Fe/Q-TiO_2/P25 (5/13 wt%) fiber. Data for single fiber length of 35 cm (Fe/Q-TiO_2) and 15 cm (P25) and fiber bundle lengths of 20 cm.

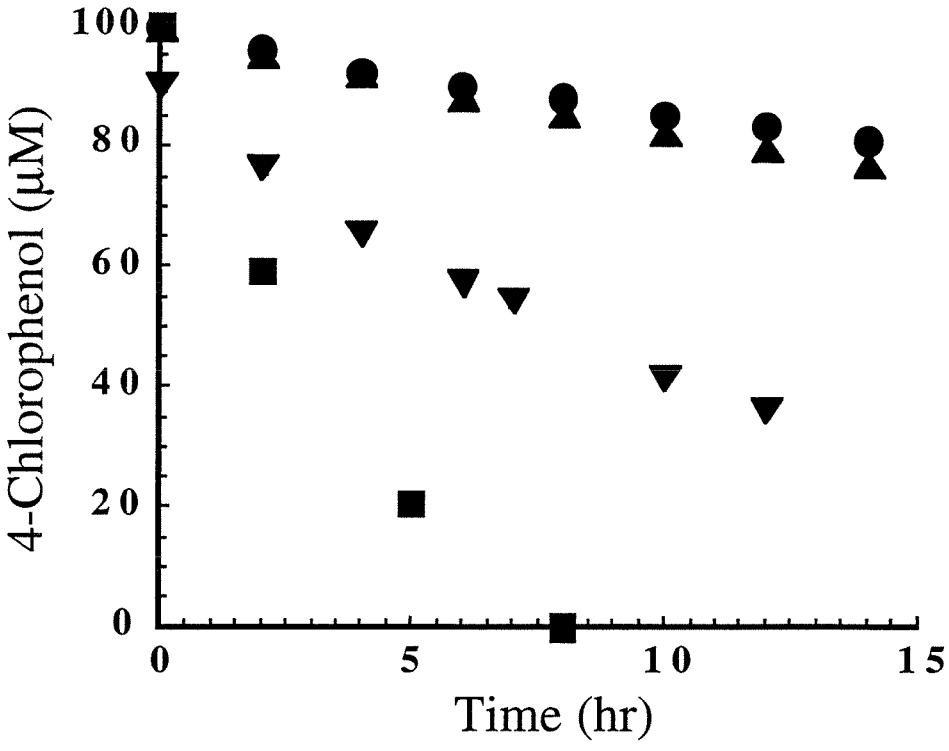

Figure 6. (●) 5 wt% Fe/Q-TiO_2 2.3/4.0 μE min^{-1}; (▲) 13 wt% Fe/Q-TiO_2, 2.7/4.0 μE min^{-1}; (▼) 20 wt% Fe/Q-TiO_2, 5.5/6.7 μE min^{-1}; and (■) 13 wt% P25, 5.3/5.9 μE min^{-1} absorbed/input light intensity. $\theta_i = 84°$, $[4\text{-CP}]_o = 0.10$ mM, $pH_o = 5.5$, $\lambda = 310 - 370$ nm.

Coating	Hydrosol Content (wt%)	Absorbed/Input Intensity ($\mu E\ min^{-1}$)	Initial Rate ($\mu M\ hr^{-1}$)	Apparent Quantum Efficiency
Fe/Q-TiO_2	0.05 (slurry reactor)	1.8 (in 50 mL)	14.4	0.002
Fe/Q-TiO_2	5	2.3/4.0	2.0	0.003
Fe/Q-TiO_2	13	2.7/4.0	2.2	0.003
Fe/Q-TiO_2	20	5.5/6.7	7.0	0.004
Fe/Q-TiO_2	5	2.9/5.9	4.5	0.005
Fe/Q-TiO_2:P25	5:13	5.1/5.9	18.0	0.011
P25	13	5.3/5.9	20.4	0.012

Table 1. Initial rate and apparent quantum efficiency comparison for photooxidation of 4-chlorophenol.

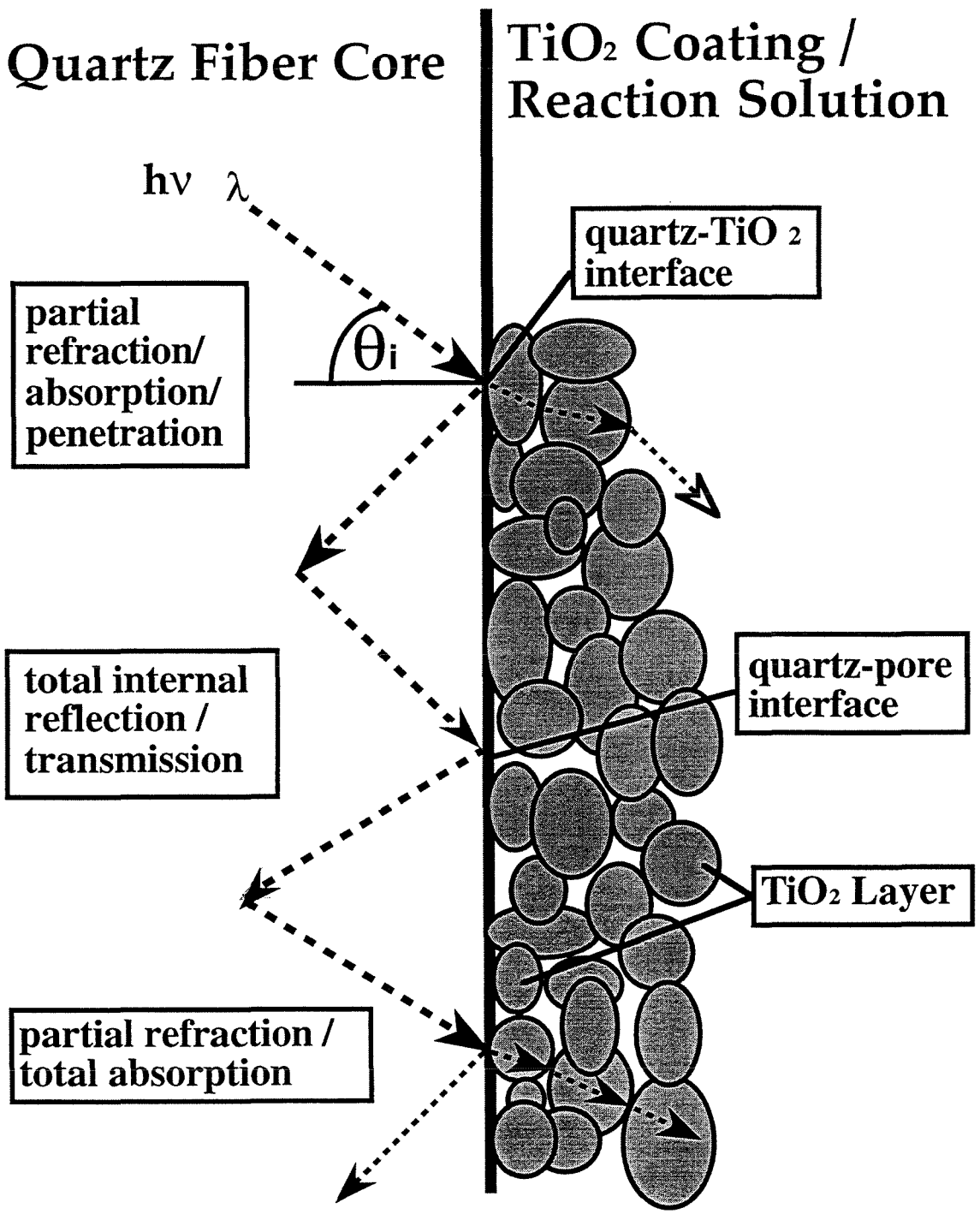

Figure 8. Photon transmission in single, coated optical fiber.

Chapter V

Solar-Powered Photocatalytic Fiber Optic Cable Reactor for Waste Stream Remediation

Abstract

The design and testing of a solar-powered fiber-optic cable reactor prototype for the photocatalytic destruction of organic pollutants is presented. A concentrating collector directs sunlight into a fiber-optic cable which transmits light to a TiO_2 photocatalyst immobilized on the fibers and immersed in a reaction solution. The performance of the reactor using solar and artificial UV radiation are compared. The system is also compared to another fiber-optic cable reactor having a 50% higher photocatalytic surface area-to-reactor volume ratio to investigate mass transport limitations. Reaction rates for the oxidation of 4-chlorophenol of 25 and 12 $\mu M\text{-}min^{-1}$ were measured for solar and artificial UV sources, respectively. The faster reaction rate using solar radiation is due to a higher UV light flux compared to the artificial source. Both fiber optic reactor systems were determined not to be mass transport limited. Relative quantum efficiencies of $\phi = 0.014$ and $\phi = 0.020$ were determined for the solar and artificial irradiations, respectively. In agreement with previous findings, enhanced quantum efficiencies are attributed to a lower absorbed light intensity-to-photocatalytic surface area ratio. The solar reactor prototype was found to degrade effectively 4-chlorophenol and may prove useful for the *in situ* passive decontamination of subsurface and other remote environments.

Introduction

The capability of metal oxide semiconductor photocatalysts to degrade effectively a wide range of hydrocarbon contaminants has been well documented (1-5). The solid photocatalyst is activated by ultraviolet light generating holes and excited electrons which combine with surface sorbed species such as water and oxygen to form highly reactive radical species (e.g., OH• and $O_2^{\bullet -}$). These radical intermediates nonselectively oxidize organic pollutants such as chlorinated hydrocarbons, pesticides, solvents, and aromatic compounds in most cases yielding only carbon dioxide, water, and dilute mineral acids (e.g., HCl) as the final products.

Many studies have addressed the immobilization of a photocatalyst in a practical fixed-bed reaqctor configuration that allows for the continuous use of a photocatalyst without the need for post-process filtration (6-12). Furthermore, several commercial photocatalytic reactor systems have been developed for aqueous- and gas-phase waste treatment (13-16). However, the photocatalytic process has been criticized as being uneconomical compared to other oxidative treatment systems due to its low photochemical conversion efficiencies that may result in higher overall energy costs (17, 18).

However, there is a growing body of laboratory and field studies which suggests that the use of solar radiation to power photocatalytic reactor systems may lead to more economical treatment alternatives for certain applications (16, 19-31). The solar spectrum consists of about 6% UV radiation which is useful for photocatalyst activation ($\lambda < 380$ nm). Sensitization of a photocatalyst can extend the useful spectrum into the visible region (32, 33). Solar-powered systems can be either nonconcentrating or concentrating. Nonconcentrating systems utilize direct and diffuse sunlight enabling operation in overcast and hazy conditions but are limited to the UV energy flux of one sun, ~40 Wm^{-2}. Concentrating systems generally require the use of a tracking device but can employ much greater UV energy fluxes resulting in higher processing capacities and/or smaller systems.

Solar-driven reactor systems involving shallow ponds, parabolic troughs, flat plates, glass fibers, and fiberglass mesh have been investigated previously (23-31, 34). In contrast to this previous work, we employ a bundled array of optical fibers to transmit light to a photocatalyst immobilized on the fibers and immersed in a reaction solution. This configuration has several advantages over conventional fixed-bed reactor designs (35, 36). Immobilization of the photocatalyst on the fibers enhances the spacial uniformity and distribution of the activated photocatalyst in the reaction solution volume. Direct delivery of light to the photocatalyst minimizes radiation losses due to scattering and absorption by the reactor and reaction solution. Transmission of light to the photocatalyst via the fiber-optic cable allows for treatment of remote environments.

A potential advantage of the optical-fiber reactor (OFR) is that it can operate in a high quantum efficiency domain characteristic of low *incident* light intensities while maintaining high reaction rates by employing high *input* light intensities (37). This combination is achieved by employing a large number of fibers and distributing the photon flux over a large photocatalytic surface area. In this paper, we discuss the design of a solar OFR2 prototype and compare its performance using solar and artificial radiation for the photocatalytic oxidation of 4-chlorophenol. We also compare the OFR2 with the performance of a previous prototype, OFR1, having a 50% higher photocatalytic surface area.

Experimental Section

Optical-fiber Reactor (OFR2). An optical-fiber bundled array reactor was constructed based on a previous design (OFR1) which is described in detail elsewhere (35). A schematic diagram of the optical-fiber photocatalytic reactor system is shown in Fig. 1. The reactor system consists of a light source, a coated fiber-optic bundle and a reaction vessel. A 1000 W Xe arc lamp (Oriel 6295) provided UV radiation for the indoor

experiments. Outdoor experiments were conducted on the roof of Keck Laboratory building at Caltech in Pasadena, California. Light is focused into the bundle and transmitted through the fibers using a quartz focusing lens (Rolyn Optics) for the artificial light source or a concentrating compound reflector device (vide infra) for sunlight collection. The fiber bundle consists of 573 1-mm diameter, 1.3 m long quartz optical fibers (3M Power-Core FT-1.0-UMT). A 30-cm length of the fibers was stripped to expose the quartz core. The stripped fibers were then threaded through two perforated Teflon plates that serve as a fiber spacer and lid for the reactor at a spacing of 3.0 mm center-to-center. The prepared fibers were bundled and polished by Fiberoptic Systems Inc., Simi Valley, CA. After bundling, the stripped portion of the fibers were coated with a 15 wt% aqueous suspension of TiO_2 (Degussa P25) and allowed to air dry for 24 h. The 4.2 L (32 x 13 cm diameter) cylindrical reactor vessel was constructed from Pyrex with a bottom glass frit (fine) and gas inlet for the introduction of air or oxygen for oxygenation and mixing of the reaction solution (~2 ml min^{-1}). Sample ports and a temperature port are located at the top and bottom of the vessel and are fitted with Teflon-coated septum screw caps. The dual lid and fiber spacer is constructed from Teflon with a 2 mm-deep groove to fit over the reactor vessel. The hole spacings are concentrically arranged at a spacing of 3.0 mm center-to-center. The fiber bundled array fits coaxially into the reactor vessel.

Solar Collector Device. The solar collector device shown in the photo in Fig. 2, along with the equatorial tracker and reaction vessel, consists of an equatorial tracking mount and gearing, and a compound reflector. The compound reflector arrangement concentrates and directs sunlight into the fiber-optic cable reactor. The bottom primary reflector is a 24" diameter silvered (concave side) parabolic glass dish (Baush and Lomb) with an 8" focal point. A thin acrylic lacquer coating (DCA 468 clear, PPG Industries, 8:1 mix with lacquer thinner) prevents oxidation of the silver coating (Peacock Laboratories). An aluminized 3.5" diameter convex lens (PCX Rolyn Optics) serves as the secondary reflector. The

aluminum coating is protected with a magnesium fluoride UV-transparent coating. The secondary reflector is positioned in front of the focal point of the primary reflector to achieve a beam spot size approximately 75% of the coupling face diameter, e.g., 0.75".

The compound reflector is supported by an aluminum equatorial tracking mount and tilted at a 34° angle (average solar zenith angle for Los Angeles, CA). After aligning the compound reflector with the sun, it is rotated by a geared (1444:1) synchronous motor at $15° \, hr^{-1}$.

Light Flux Determination. Input light intensities into the fiber bundle, I_{input}, for the solar and artificial sources were measured by chemical actinometry using ferrioxalate (FeOx) according to the method by Calvert and Pitts (38). In general, a 1 L 0.006 M solution of reagent grade potassium ferrioxalate (Pfaltz & Bauer) acidified in 0.1 M H_2SO_4 (Baker, AR) is irradiated at 10 second intervals. At each interval a 10 mL aliquot is taken and diluted to 25 mL with 2 mL of a 0.1 wt% solution of 1,10-phenanthroline (Baker, AR), 5 mL of a 1.0 N sodium acetate (EM Science, GR) buffer, and 8 mL of deionized water (Milli-Q). After standing for 1 h the absorbence of each sample solution is taken at λ = 510 nm. The tip of the uncoated bundle was immersed in the actinometry solution and irradiated using either sunlight or artificial light. A series of measurements was made and averaged. An outdoor input flux measurement was also made subsequent to coating the fiber bundle. Outdoor measurements were made at 12:00 hours.

The ambient solar flux as a function of wavelength and time of day was also measured using a spectral radiometer (LI-COR Li-1800). The absorbed light intensity, I_{abs}, of the coated bundled was assumed to be 95% of the input light intensity based on previous findings (35, 36).

Photooxidation of 4-chlorophenol. A 4.0 L, 0.10 mM solution of 4-chlorophenol (4CP) was prepared from a 1.0 mM stock solution (Aldrich, 99+%). Before irradiation,

the coated-fiber bundle was immersed in the reaction solution and allowed to equilibrate for 30 min. The irradiations were carried out until the complete disappearance of 4CP was observed. This required two days of irradiation for the outdoor experiment from 10:00 to 17:00 hours each day. Nylon (Nalgene 0.45 μm) syringe filters were used to filter all samples. 4CP was analyzed by HPLC (HP SeriesII 1090) using a Hewlett Packard ODS Hypersil (5 μm) column with an eluent (1 mL-min^{-1}) of 20/80% acetonitrile/water (pH 3). UV absorbence was measured at 224 and 250 nm. Chloride-ion production was quantified using a chloride ion selective electrode (Orion 9617BN) or by ion chromatography (Dionex BIOLC 4500i series) using an Ionpac AG11 Guard column with an eluent (1 mL-min^{-1}) of 75/25% 5 mM/100 mM NaOH. The pH was determined with a Radiometer PHM85 pH meter.

Results

Ambient solar flux data from the roof of the Keck Laboratory building were used to size the solar concentrator shown in Fig. 2. Figures 3 a and b show representative flux data taken with the spectral radiometer as a function of wavelength at 1330 h and time of day, respectively. The UV flux ($300 \leq \lambda \leq 380$) reaches a maximum at 380 nm of 2 W/m^2-nm which is less than one third of the total spectral maximum. The integrated UV flux ranges from 45 to 90 W-m^{-2} (0.88 - 1.84 μEmin^{-1}cm^{-2}) reaching a maximum at 14:00 hours. This UV flux represents about 3.7% of the total ambient solar flux.

Due to irregularities in the surface of the primary reflector, only the inner 17" radius of the reflector was useful for solar collection, representing about 1400 cm^2 of reflective surface area. Since the fiber bundle coupling face consists of 4.5 cm^2 of fiber area, this gives a concentration factor of approximately 300. A total theoretical (without losses) concentrated UV flux was estimated to be 6.3 - 12.6 W (1230 - 2520 μEmin^{-1}). UV

reflectivity losses of about 45% for the silver/lacquer coating and an overall beam-to-bundle coupling efficiency of 80% were estimated.

Actinometric flux measurements were carried out to determine the input light intensity into the OFR2. Total fluxes of 68 ± 11 and 360 ± 15 $\mu Emin^{-1}$ were measured for the artificial and solar light sources, respectively. UV fluxes were calculated to be 40% and 50%, respectively, of the total measured flux based on the Xe arc lamp output and solar spectrums and the wavelength dependency of the ferrioxalate measurement. The measured flux of the coated fiber bundle was negligible, < 5% of the uncoated bundle flux, indicating that most of the input UV light was being absorbed by the coating. The non-UV wavelengths would have passed through the coating.

4-chlorophenol was chosen as a model pollutant for its low volatility and moderate solubility. 4CP has been reported to undergo hydroxyl radical insertion as an initial step in the overall oxidation (39-41) according to the following generally accepted mechanism (1, 42):

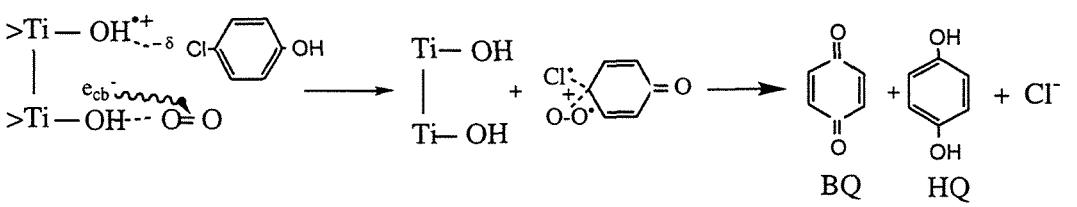

(2)

A controlled indoor irradiation experiment was carried out to compare the performance of the OFR2 using solar radiation for the oxidation of 4CP. In addition, these results are compared to 4CP oxidation experiments carried out using OFR1 (35, 36). The initial reaction rates, time to "complete degradation" ($[4\text{-CP}]_{final} \approx 0.01[4\text{-CP}]_o$), and the relative quantum efficiencies are summarized in Table 1. The higher initial reaction rate and faster time to complete degradation for the OFR2 outdoor experiment is due to the higher absorbed light intensity, 25 - 41 compared to 10 $\mu E\ L^{-1}\ min^{-1}$. The OFR2 performed comparably to the OFR1 but achieved higher relative quantum efficiencies for both the

indoor and outdoor irradiations. A relative quantum efficiency of $\phi = 0.020$ was achieved for the indoor OFR2 experiment which is comparable to previously reported values for the photocatalytic oxidation of 4CP (8, 39, 41, 43) .

The results of the 4CP oxidations using artificial and solar light are summarized in Table 1. Initial reaction rates of 12.0 and 25.0 μM/hr, $t_{1/2}$ of 5.0 and 3.5 h were measured, respectively. A two order-of-magnitude reduction in 4CP was achieved after 16 and 13 h of irradiation, respectively. Stoichiometric production of chloride was observed in both cases. A relative quantum efficiency for the indoor irradiation of $\phi = 0.020$ was determined where ϕ is defined as

$$\phi \equiv \frac{\frac{d[4CP]}{dt}}{\frac{d[hv]_{abs}}{dt}} \cong \frac{\text{initial rate}}{\text{absorbed flux}} \qquad (1)$$

A relative quantum efficiency range for the outdoor irradiation of $\phi = 0.017 - 0.010$ was estimated based on an average UV flux of 30 ± 5 μEmin^{-1} for the one hour irradiation period.

Discussion

The need for low cost novel technologies for the decontamination of subsurface water and other waste streams has spurred the development of solar-powered photocatalytic reactors which combine cheap and environmentally benign photocatalysts such as TiO_2 and sunlight. A unique feature of the OFR is the remote delivery of light to a photocatalyst allowing for *in situ* treatment of a contaminated site. This would eliminate the need to pump contaminated water to the surface for treatment required for most other treatment technologies. The OFR, as a fixed-bed reactor, is also ammenable to gas-phase operation. Photocatalytic reaction in the gas-phase has been shown to be substantially faster than in the aqueous phase (10, 44, 45). Additionally, the use of sunlight as the UV source would further reduce treatment costs. In advanced oxidation systems, the UV radiation supply

typically represents a large fraction of the capital and operating costs (46, 47). The primary objective of the present work is to demonstrate the feasibility of utilizing solar radiation in an OFR for the destruction of hydrocarbon pollutants.

Reactor Design. Critical design features of the OFR2 include: the reaction solution volume, the total UV flux, and the fiber bundle size. A batch volume of 4 L was chosen for this project which is 20 times larger than the OFR1 design. OFR1 studies suggested that a minimum input UV flux of 50 $\mu E(Lmin)^{-1}$, assuming ~100% absorption by the coating, was necessary to achieve the complete oxidation of 4CP in one day (6 h) of irradiation (36). Thus, the minimum total input UV flux desired was 200 $\mu Emin^{-1}$. An estimated photocatalytic coating surface area-to-reaction volume ratio of 23.3 m^2L^{-1} employed in the OFR1, which consisted of seventy-two 20 cm long coated fibers in a single bundle, was used as a base parameter to size the fiber bundle (36). Single-fiber light distribution experiments with 13 wt% Degussa P25 revealed that collimated light is propagated 35 cm before being completely absorbed by the photocatalytic coating. Therefore, coated fiber lengths of 30 cm were used to maximize the activated photocatalytic surface area. The fibers at the reaction end of the bundle were spaced 2 mm apart in a concentric, parallel arrangement to ensure a uniform distribution of the photocatalyst within the reaction volume. Assuming a coating thickness and porosity of 6 μm and 0.9 (36, 48) and a photocatalyst density and specific surface area of 3.9 gcm^{-3} and 50 m^2g^{-1} (49), respectively, a fiber bundle consisting of 573 1-mm diameter fibers gave a photocatalytic surface area-to-reaction volume ratio that was 68% of the OFR1. This ratio was deemed sufficiently different to be able to investigate also possible mass transport effects.

Three alternative solar collector designs were considered. They involved the use of 1) a compound Fresnel lens arrangement, 2) a combination Fresnel film and lens arrangement, as illustrated in Fig. 4, and 3) a compound parabolic reflector arrangement. The first option consists of a UV-transmitting quartz lens of sufficient collection diameter

(e.g. 30 cm) coupled with a secondary quartz lens to collimate the concentrated light. The primary lens was not commercially available and was determined to be cost prohibitive. The Fresnel film is manufactured by 3M for photovoltaic systems and consists of a continuous web of non-UV transmitting acrylic (0.6 mm thick) with prisms on one side and a smooth surface on the other. The thin film is bonded to a rigid sheet such as UV-transmitting acrylic for support. The concentrated light is collimated and coupled with the bundle using a secondary quartz lens. However, this alternative configuration was rejected because the quantity of film required (~350 cm^2) was not sufficient to cover the commercial development costs and the development time (i.e., > 6 months) was extensive. In addition, unless UV transmitting substitutes could be developed, the acrylic lens film and bonding material would absorb some portion of the UV flux. This arrangement, however, might prove to be a superior alternative for future consideration as it is simple, light weight and can probably be constructed of UV transmitting film. The third option consists of a bottom primary parabolic reflector coupled with a secondary upper reflector that is positioned in front of (convex) or behind (concave) the focal point of the primary reflector. The secondary reflector is adjusted until a collimated beam is achieved coupling the light with the fiber bundle face. This arrangement was chosen for its simplicity and availability of parts.

The primary collector diameter was set based on the desired input flux, I_{input}, the ambient solar flux data, $I_{ambient}$, (Fig. 3) and the estimated efficiencies for the primary, $\eta_{primary}$, and secondary, $\eta_{secondary}$, reflectors and the beam-to-bundle coupling efficiency, η_{couple}:

$$d_{primary} = \left\{ \frac{4 * I_{input}}{\pi * I_{ambient} * \eta_{primary} * \eta_{secondary} * \eta_{couple}} \right\}^{1/2} \qquad (2)$$

Fig. 5 is a plot of silver reflectivity data as a function of wavelength, the ambient solar flux, and the corresponding reduction of the reflected solar flux (50). The reflectivity at each

wavelength was weighted by the contribution of the wavelength to the ambient UV flux and integrated. This resulted in an estimated reflection efficiency for the silver coating of 75%. Spectral analysis of the lacquer coating used to protect the silver coating indicated a UV transmittance of about 60%. Thus, the overall reflection efficiency for the primary reflector was estimated to be $\eta_{primary} = 45\%$. The aluminum coating on the secondary reflector was estimated to have a reflection efficiency of $\eta_{secondary} \approx 100\%$ (50). Three main factors affected the beam to fiber coupling efficiency. They were 1) the input beam angle, 2) the beam spot size relative to the fiber core diameter, and 3) Fresnel losses due to refraction. The input beam angle should be within 80% of the acceptance angle, θ, given by:

$$\theta = \text{ArcSin}\left\{\gamma * (n_1^2 - n_2^2)^{1/2}\right\} \quad (3)$$

where γ is the numerical aperture of the fiber core and n_1 and n_2 are the refractive indices of the fiber core and ambient medium (e.g., air, $n_2 = 1.0$), respectively. A fiber bundle consisting of 3M Ft-1.0UMT fibers has a γ of 0.3 and a fiber core refractive index of 1.413. These values give an acceptance angle of 17°. Therefore, the beam should be incident on the fiber coupling face at an angle less than 14° with respect to the axis of the fiber for efficient coupling. The beam spot size should be 80% of the core diameter (e.g., 8 mm). Some losses may occur if this criterion is not achieved since the reflected beam diameter spans the entire fiber bundle coupling face. Fresnel losses of about 4% due to refraction of the beam off the bundle face may also be incurred. Due to a fiber packing factor that is close to 0.9 there is a 10% coupling loss due to void space in the bundle coupling face. Overall, a coupling efficiency, $\eta_{coupling}$, was conservatively estimated to be 80% and, thus the overall solar collection/coupling efficiency is reduced to 36% .

Ambient UV fluxes ranged from 0.88 to 1.84 $\mu E\ min^{-1}\ cm^{-2}$ during the summer months. Using these values in Eq. 2 yields an estimated primary reflector diameter of 28 cm (11"). The 24" primary reflector that was employed appeared to be sufficient to provide the minimum required UV flux. As a result of a mismatch between the shape of the

primary and secondary reflectors, a fully recollimated beam was not obtainable. The beam input angle ranged from 0° to 10°. However, due to irregularities in the parabolic surface of the primary reflector, only the inner 17" diameter was effective for sunlight collection.

UV Flux Determination. The input UV flux was measured to determine relative quantum efficiencies for the oxidation of 4CP and as a basis for comparing the performance of the reactor using artificial and solar light. The absorbance spectrum for ferrioxalate is shown in Fig. 6 and compared to the solar and Xe arc lamp output spectra. As can be seen, the FeOx solution may be absorbed at wavelengths above 380 nm. When the flux at each wavelength was weighted by the respective absorbance of the FeOx solution and the conversion quantum efficiency, it was estimated that only 43% and 58% of the measured flux can be attributed to the useful wavelengths for the solar and Xe arc lamp sources, respectively (38). Thus, the *absorbed* UV fluxes for the indoor and outdoor experiments were estimated to be 10 ± 1 and 37 ± 1 $\mu E\ L^{-1}\ min^{-1}$, respectively. It should also be noted that the solar flux measurements were made at 12:00 hours when the solar flux was about 90% of its peak. The quantum efficiency was calculated using an initial rate evaluated with the first hour sample irradiated between 10:00 and 11:00 hours when the solar flux was at 65-85% of its peak. An estimated value of 30 ± 5 $\mu E\ L^{-1}\ min^{-1}$ was used to calculate the relative quantum efficiency for the solar irradiation.

The estimated (from data) maximum input UV solar flux of 170 $\mu E\ min^{-1}$ is 7-14% of the theoretical flux available and about 20-40% of the predicted UV input flux after losses. This collection/coupling efficiency is 2-1/2 to 5 times lower than the empirically estimated efficiency of 35% of theoretical. The discrepancy may be due to lower reflection efficiencies for the primary and secondary reflectors and/or a lower coupling efficiency than predicted. The lower input UV flux also resulted in slower reaction rates than were predicted (vide supra).

4-Chlorophenol Oxidations. The photocatalytic surface area plays two important roles in this reactor configuration. The photocatalytic surface area-to-reactor volume ratio determines whether the reaction system is in a mass transport limited or a reaction rate limited regime, assuming the system is not limited by the input light flux. If the system is mass transport limited, an increase in the photocatalytic surface area-to-reactor volume ratio will enhance the reaction rate. In addition, the absorbed light intensity-to-photocatalytic surface area ratio can affect the quantum efficiency. Previous studies have shown an inverse relationship between the absorbed light flux and the quantum efficiency (36, 37, 39, 51-55). In illuminated semiconductor photocatalysts, the photogenerated electron-hole pair density increases with an increase in the absorbed light intensity. As a result, at a high absorbed light intensity, the rate of electron-hole recombination is increased relative to interfacial charge transfer. This leads to a lower relative quantum efficiency.

The reaction rate data for the OFR1 and OFR2 reactors suggest that the observed photochemical reaction rates are not mass transport limited. The photocatalytic surface area-to-reactor volume ratio of the OFR2 is about 65% that of the OFR1. However, a higher initial reaction rate for the OFR2 outdoor oxidation is observed despite a similar absorbed light intensity compared to the OFR1 oxidation. Other studies have reported similar findings for slurry-phase reactors (56-59). In contrast, mass transport effects in fixed-bed photocatalytic reactor systems appear to be a function of the reactor design and reaction parameters such as distribution of the photocatalyst within the reaction volume, the radiation field with respect to the exposed photocatalyst membrane, pollutant concentration, rand eaction solution flowrate, (58, 60-62).

Increasing the coated-fiber number density decreases the relative incident light intensity to which to the photocatalyst is exposed for a given input light intensity. The fiber length should equal but not exceed the propagation length of light in the coated fiber to maximize the input photon utilitzation. The fiber number, fiber number-densities, and fiber

lengths for the OFR1 and OFR2 were 72 and 573, 92 and 113 fibers-cm^{-2} and 0.20 and 0.30 m, respectively. These dimensions resulted in estimated photocatalytic surface areas of 4.4 and 63.6 m^2, respectively. In Table 1 the absorbed light intensity normalized by the photocatalytic surface area is compared to the observed relative quantum efficiencies. An inverse correlation is evident between the normalized I_{abs} and relative quantum efficiency. This confirms our previous findings that higher reaction rates can be achieved using the same power input (i.e., higher quantum efficiencies by maximizing the fiber number density (36)).

In this system, oxygen sparging (2 ml min^{-1}) serves two purposes: to mix the reaction solution and to act as the electron acceptor. Mixing of the reaction solution may be necessary to minimize mass transport effects and to enhance the sphere of influence of the activated photocatalytic bundle to treat a volume larger than the bundle volume. In an activated photocatalyst particle, surface-bound •OH radicals are produced by the oxidation of water by valence band holes. In order to maintain charge neutrality concurrent reduction of surface-bound species via conduction band electrons must occur. In an aerated system, oxygen is reduced and forms superoxide and/or hydroperoxyl radicals. These species can be further reduced to form hydroxyl radicals. In the absence of oxygen or an alternative oxidant, charge neutrality cannot be maintained and photocatalytic activity is inhibited as the generated holes, h^+_{vb}, and electrons, e^-_{cb}, recombine. In any practical photocatalytic reaction system, oxygen/air should be present at sufficient levels so as not to be rate-limiting. In the case of the treatment of subsurface environments, the addition of oxygen/air may be required.

In conclusion, a solar powered prototype OFR for the remediation of contaminated wastestreams was successfully designed and tested. Photoefficiencies with sunlight are comparable to that achieved with a Xe-arc source. In addition, a lower absorbed light intensity-to-photocatalytic surface area ratio is shown to result in a corresponding increase

in the relative quantum efficiencies. These results indicate that the OFR configuration may be useful in the passive decontamination of groundwater, underground storage tanks, or other remote sites.

Acknowledgments

We are grateful to ARPA and ONR (NAV 5 HFMN N000149J1901) for financial support and to Tim Wu, Janet Kesselman, Scot T. Martin, and Wonyong Choi for scientific support. We would also like to thank 3M and Degussa for their donations of the optical fiber samples and the P25 photocatalyst, respectively.

Literature Cited

(1) Hoffmann, M. R.; Martin, S. T.; Choi, W.; Bahnemann, D. W. *Chem. Rev.* **1995**, *95*, 69-96.

(2) Ollis, D. F.; Al-Ekabi, H. *Photocatalytic Purification and Treatment of Water and Air*; Elsevier: Amsterdam, 1993.

(3) Fox, M. A.; Dulay, M. T. *Chem. Rev.* **1993**, *93*, 341-357.

(4) Mills, A.; Davies, R. H.; Worsley, D. *Chem. Soc. Rev.* **1993**, *22*, 417.

(5) Matthews, R. W. *Wat. Res.* **1990**, *24*, 653-660.

(6) Bellobono, I. R.; Bonardi, M.; Castellano, L.; Selli, E.; Righetto, L. *J. Photochem. Photobiol. A: Chem.* **1992**, *67*, 109-115.

(7) Al-Ekabi, H.; Serpone, N. *J. Phys. Chem.* **1988**, *92*, 5726-5731.

(8) Hofstadler, K.; Bauer, R.; Novalic, S.; Heisler, G. *Environ. Sci. Technol.* **1994**, *28*, 670-674.

(9) Zeltner, W. A.; Hill, C. G.; Anderson, M. A. *Chemtech* **1993**, *23*, 21-28.

(10) Yamazaki-Nishida, S.; Nagano, K. J.; Phillips, L. A.; Cerveramarch, S.; Anderson, M. A. *J. Photochem. Photobiol. A.: Chem.* **1993**, *70*, 95-99.

(11) Bellobono, I. R.; Carrara, A.; Barni, B.; Gazzotti, A. *Photochem. Photobiol. A.: Chem.* **1994**, *84*, 83-90.

(12) Sauer, M. L.; Ollis, D. F. *J. Catal.* **1994**, *149*, 81-91.

(13) Suzuki, K. In *Photocatalytic Purification and Treatment of Water and Air*; D. F. Ollis and H. Al-Ekabi, Eds.; Elsevier Science Publishers, B. V.: Amsterdam 1993; p 421-434.

(14) Al-Ekabi, H.; Safarzadey-Amiri, A.; Sifton, W.; Story, J. *Intl. J. Environ. Pollut.* **1991**, *1*, 125-136.

(15) Xu, Y. M.; Menassa, P. E.; Langford, C. H. *Chemosphere* **1988**, *17*, 1971-1976.

(16) *Chem. Eng. News* **1985**, *41*.

(17) Wilson, E. *Chem. Eng. News* **1996**, 29.

(18) Renner, R. *Environ. Sci. Technol.* **1996**, *30*, 284.

(19) Mehos, M. S.; Turchi, C. S. *Environ. Prog.* **1993**, *12*, 194-199.

(20) Bockelman, D.; Goslich, R.; Weichgrebe, D.; Bahnemann, D. In *Photocatalytic Purification and Treatment of Water and Air*; D. F. Ollis and H. Al-Ekabi, Eds.; Elsevier Science Publishers B. V.: Amsterdam 1993; p 771-776.

(21) Matthews, R. W. *Solar Energy* **1987**, *38*, 405-413.

(22) Pacheco, J. E.; Prairie, M. R.; Yellowhorse, L. *J. Solar Energy Eng.* **1993**, *115*, 123-129.

(23) Crittenden, J. C.; Zhang, Y.; Hand, D. W.; Perram, D. L.; Marchand, E. G. *Wat. Environ. Res.* **1996**, *68*, 270-278.

(24) Zhang, Y.; Crittenden, J. C.; Hand, D. W.; Perram, D. L. *J. Solar Energy Engnrg.* **1996**, *118*, 123-129.

(25) Pugh, K. C.; Kiserow, D. J.; Sullivan, J. M.; Grinstead, J. H. In *ACS Industrial and Engineering Chemistry Special Symposium*, Atlanta, GA, 1995; pp 174-194.

(26) Minero, C.; Pelizzetti, E.; Malato, S.; Blanco, J. *Chemosphere* **1993**, *26*, 2103-2119.

(27) Muradov, N. Z. *Solar Energy* **1994**, *52*, 283-288.

(28) Wyness, P.; Klausner, J. F.; Goswami, D. Y.; Schanze, K. S. *J. Solar Energy Eng. Trans. ASME* **1994**, *116*, 2-7.

(29)Wyness, P.; Klausner, J. F.; Goswami, D. Y.; Schanze, K. S. *J. Solar Energy Eng. Trans. ASME* **1994**, *116*, 8-13.

(30) Zhang, Y.; Crittenden, J. C.; Hand, D. W.; Perram, D. L. In *American Water Works Association Annual Conference*, San Antonio, TX, 1993.

(31) Zhang, Y.; Crittenden, J. C.; Hand, D. W.; Perram, D. L. *Environ. Sci. Technol.* **1994**, *28*, 435-442.

(32) Dieckmann, M. S.; Gray, K. A.; Kamat, P. V. *Wat. Sci. Tech.* **1993**, *25*, 277.

(33) Dieckmann, M. S.; Gray, K. *Wat. Res.* **1996**, *30*, 1169-1183.

(34) Bauer, R. *Chemosphere* **1994**, *29*, 1225-1233.

(35) Peill, N. J.; Hoffmann, M. R. *Environ. Sci. Technol.* **1995**, *29*, 2974.

(36) Peill, N. J.; Hoffmann, M. R. *Environ. Sci. Technol.* **1996**, *30*, 2806-2812.

(37) Ollis, D. F.; Pelizzetti, E.; Serpone, N. *Environ. Sci. Technol.* **1991**, *25*, 1522-1529.

(38) Calvert, J. G.; Pitts, J. N. *Photochemistry*; John Wiley & Sons, Inc.: New York, 1966; p 899.

(39) Mills, G.; Hoffmann, M. R. *Environ. Sci. Tech.* **1993**, *27*, 1681-1689.

(40) Tseng, J. M.; Huang, C. P. *Wat. Sci. Technol.* **1991**, *23*, 377-387.

(41) Al-Sayyed, G.; D'Oliveira, J. C.; Pichat, P. *J. Photochem. Photobiol. A: Chem.* **1991**, *58*, 99-114.

(42) Choi, W.; Hoffmann, M. R. *Environ. Sci. Technol.* **1995**, *29*, 1646-1654.

(43) Barbeni, M.; Pramauro, E.; Pelizzetti, E. *Chemosphere* **1985**, *14*, 195.

(44) Nimlos, M. R.; Jacoby, W. A.; Blake, D. M.; Milne, T. A. *Environ. Sci. Technol.* **1993**, *27*, 732-740.

(45) Dibble, L. A.; Raupp, G. B. *Catal. Ltrs.* **1990**, *4*, 345-354.

(46) Bolton, J. R.; Safarzadeh-Amiri, A.; Cater, S. R. In *Alternative Fuels and the Environment*; F. S. Sterret, Eds.; Lewis Publishers: Boca Raton, FL 1995; p 187-192.

(47) Miller, R.; Fox, R. In *Photocatalytic Purification and Treatment of Water and Air: Trace Metals in the Environment*; D. F. O. a. H. Al-Ekabi, Eds.; Elsevier Science Publishers B.V.: Amsterdam, N.V. 1993; p 573-578.

(48) Peill, N. P.; Hoffmann, M. R. *Environ. Sci. Technol.* **1996**, *submitted 1996.*

(49) *Degussa Technical Bulletin* **1990**, Bulletin No. 56.

(50) Holland, L. *Vacuum Deposition of Thin Films*; Wiley: New York, 1958.

(51) Ollis, D. F. In *Photochemical Conversion and Storage of Solar Energy*; E. Pellizzetti and M. Schiavello, Eds.; Kluwer Academic Publishers: Dordrecht, Netherlands 1991; p 593-622.

(52) Kormann, C.; Bahnemann, D. W.; Hoffmann, M. R. *Environ. Sci. Technol.* **1991**, *25*, 494-500.

(53) D'Oliveira, J. C.; Al-Sayyed, G.; Pichat, P. *Environ. Sci. Technol.* **1990**, *24*, 990.

(54) Al-Sayyed, G.; Doliveira, J. C.; Pichat, P. *J. Photochem. Photobiol. A: Chem.* **1991**, *58*, 99-114.

(55) Albery, W. J.; Brown, G. T.; Darwent, J. R.; Saievariranizad, E. *J. Chem. Soc. Farad. Trans. 1* **1985**, *81*, 1999-2007.

(56) Ollis, D. F.; Pelizzetti, E.; Serpone, N. In *Photocatalysis: Fundamentals and Applications*; N. S. a. E. Pelizzette, Eds.; Wiley & Sons: New York 1989; p 603-637.

(57) Pruden, A. L.; Ollis, D. F. *J. Catal.* **1983**, *82*, 404-417.

(58) Turchi, C. S.; Ollis, D. F. *J. Phys. Chem.* **1988**, *92*, 6852-6853.

(59) Matthews, R. W. *J. Phys. Chem.* **1988**, *92*, 6853-6854.

(60) Matthews, R. W. *J. Phys. Chem.* **1987**, *91*, 3328.

(61) Sabate, J.; Anderson, M. A.; Kikkawa, H.; Edwards, M.; Hill, C. G. *J. Catal.* **1991**, *127*, 167-177.

(62) Sabate, J.; Anderson, M. A.; Aguado, M. A.; Gimenez, J.; Cerveramarch, S.; Hill, C. G. *J. Mol. Catal.* **1992**, *71*, 57-68.

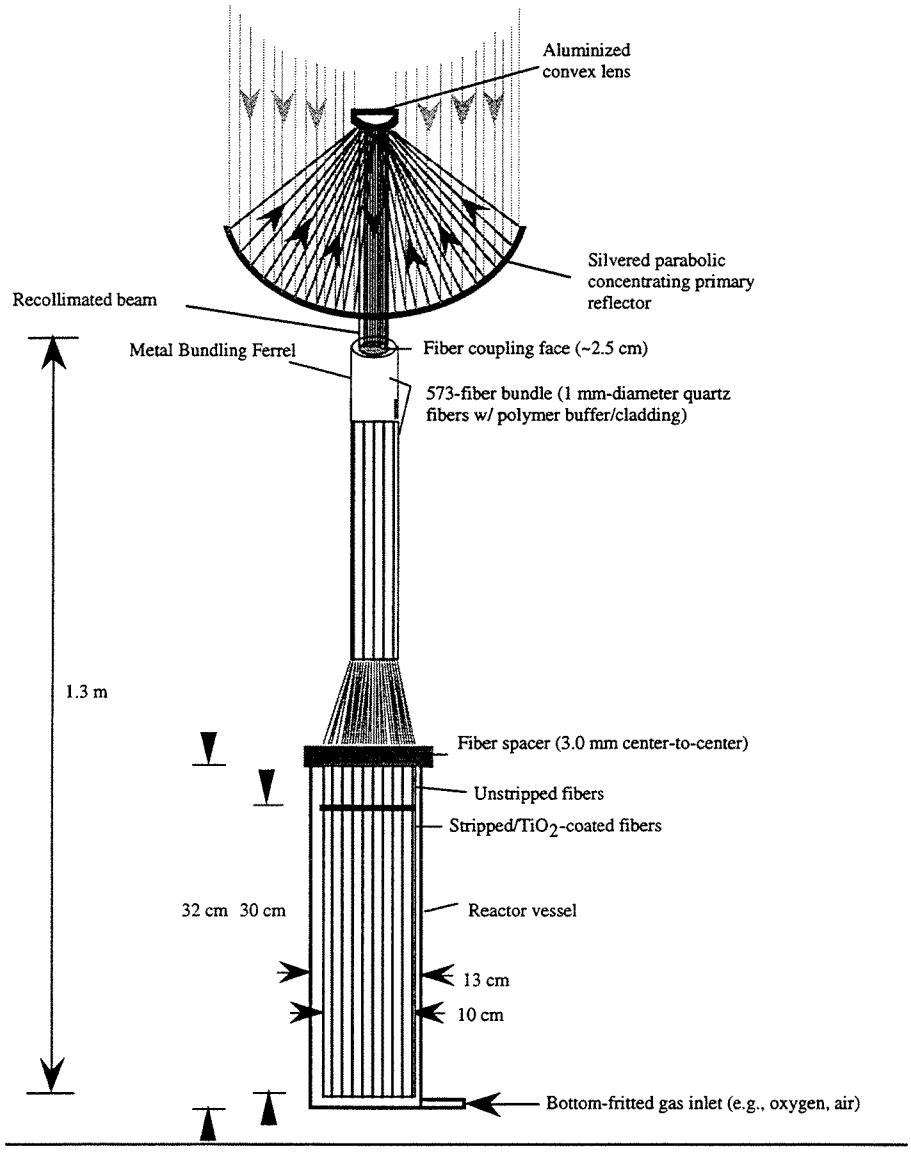

Figure 1. Schematic of OFR2 with solar collector/concentrator. Equatorial tracker not shown.

Figure 2. Photograph of OFR2 on Keck Laboratory roof complete with reactor vessel, solar collector, and equatorial tracker.

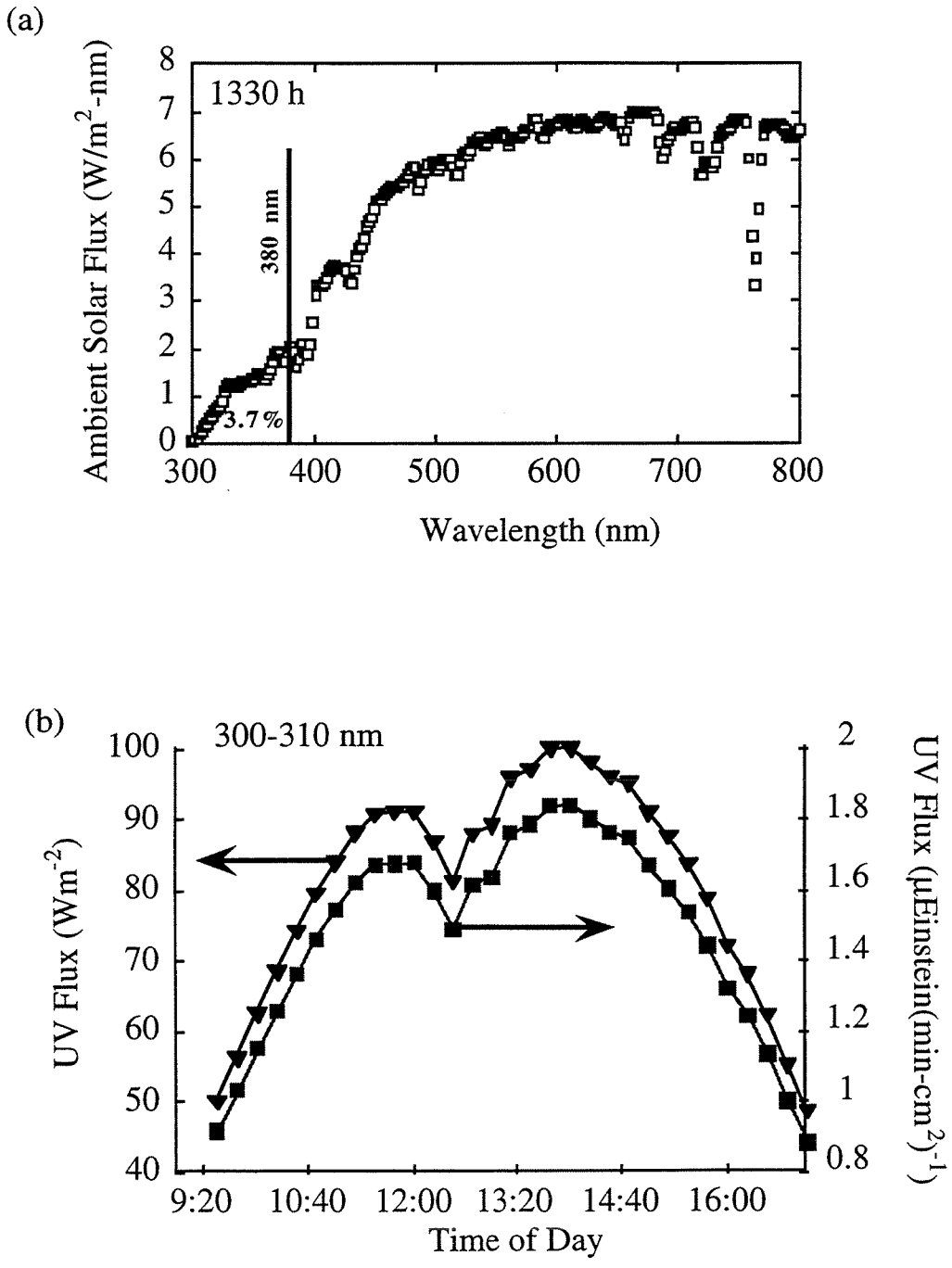

Figure 3. Representative solar flux with intermittent clouds as a function of (a) wavelength taken at 1330 h and (b) time of day measured by spectral radiometer on July 20, 1996.

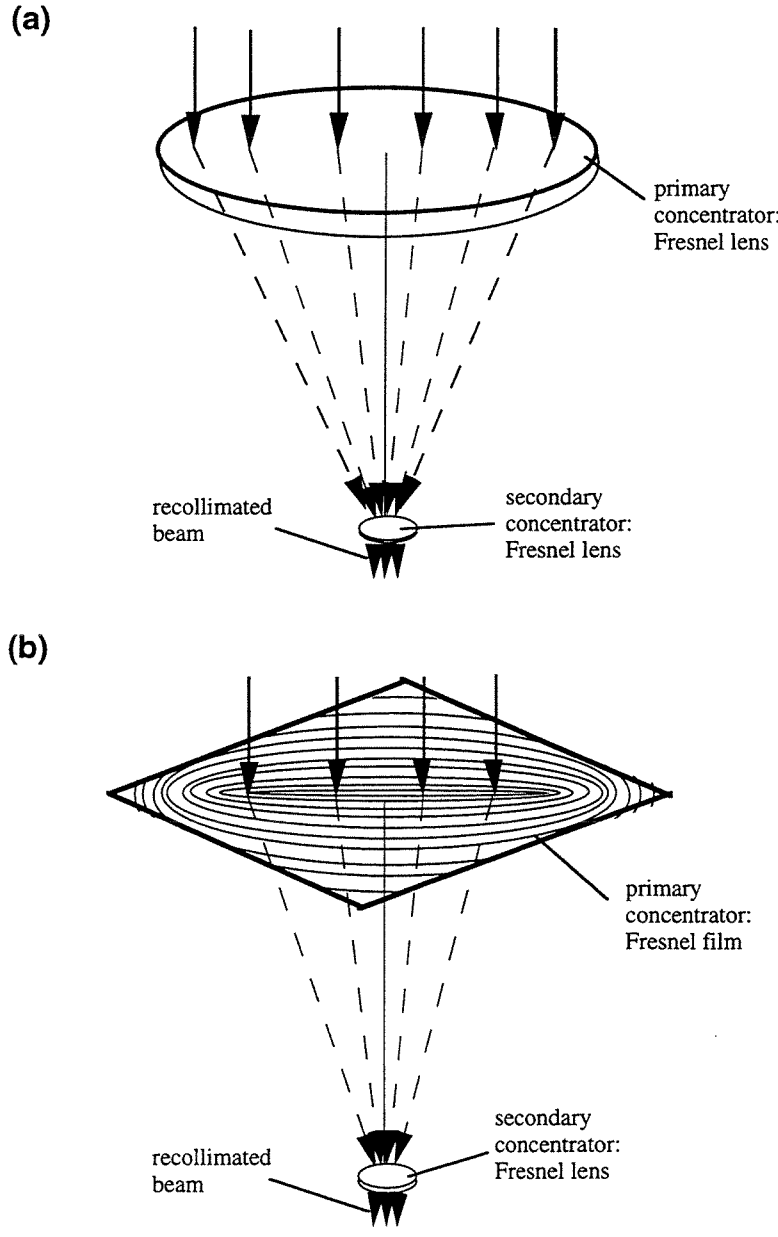

Figure 4. Alternative solar collector arrangements: (a) a large-diameter quartz Fresnel lens coupled with a smaller quartz Fresnel lens and (b) Fresnel film coupled with a quartz Fresnel lens to recollimate the light .

4CP Oxidation Experiment	I_{abs} ($\mu E\ L^{-1}\ min^{-1}$)	Initial Reaction Rate ($\mu M/hr$)	$t_{1/2}$ (hr)	Time to Complete Degradation (hr)	I_{abs}/surface area ($\mu E\ L^{-1}\ min^{-1}\ m^{-2}$)	ϕ
OFR2 Indoor	10	12	5.0	16	0.2	0.020
OFR2 Outdoor	30	25	3.5	13	0.5	0.014
OFR1	22	15.5	4.5	13	5.0	0.012
OFR1	31	17.5	3.5	13	7.0	0.009

Table 1. 4CP oxidation reaction summary carried out in the OFR1 indoor and the OFR2 indoor and outdoor with O_2 sparging. Experimental conditions for the OFR1 and OFR2 oxidations are the same except for I_{abs} (shown in table) and the reaction solution volume, 0.19 and 4 L, respectively.

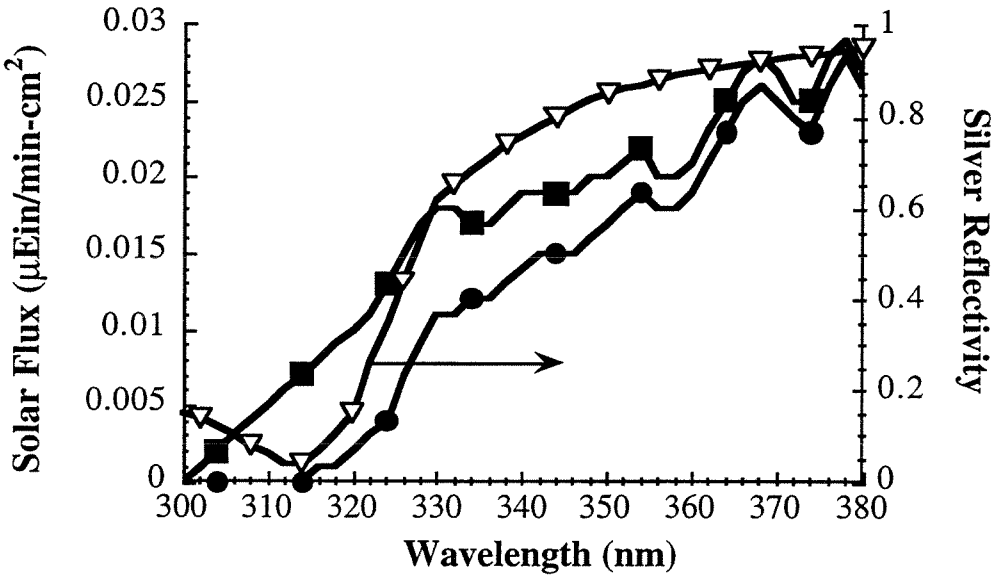

Figure 5. The (■) ambient and (●) mitigated UV flux due to the incomplete reflectivity of the silver coating (▽) are plotted as a function of wavelength.

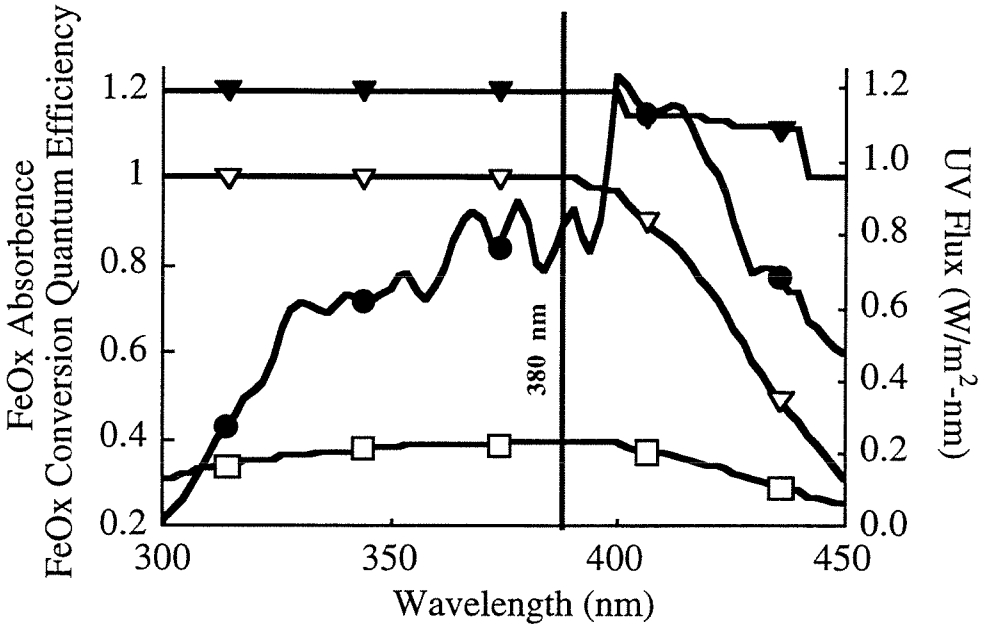

Figure 6. (●) Ferrioxalate absorbance spectrum and (□) conversion quantum efficiency is compared to (▼) solar and (▽) Xe lamp spectra for $300 \leq \lambda \leq 450$.

Chapter VI

Mathematical Model of Photocatalytic Fiber-Optic Cable Reactor for Heterogeneous Photocatalysis

Submitted to *Environmental Science & Technology*
October 1996

Abstract

A basic mathematical model to describe the degradation of a single compound in a fiber-optic bundled array photocatalytic batch reactor (OFR) using a Langmuir-Hinshelwood kinetic expression is developed. An empirical global quantum efficiency, ϕ_{global}, that incorporates reaction parameters such as the absorbed light intensity, intrinsic rate constants, concentration of adsorbed reactants, and reaction intermediates, is used as a fitting parameter. An empirical term to describe the radiation field within the coated fiber is derived experimentally and normalized by the photocatalyst particle concentration within the fiber optic coating to account for the inverse relationship observed between absorbed light intensity and reaction quantum efficiency. Results of the mathematical model are compared to experimental data generated in an OFR for the photocatalytic oxidation of 4-chlorophenol (4CP), pentachlorophenol (PCP), and dichloroacetate (DCA). The global quantum efficiency, ϕ_{global}, was found to be independent of absorbed light intensity. Calculated kinetic profiles are in excellent agreement with experimental observation.

Introduction

Fixed-bed photocatalytic optical fiber reactor systems (OFR) for the remediation of polluted waste streams (1-3) have been shown to be viable, practical alternatives to conventaional photochemical reactor systems. The fiber-optic cable is used both for remote light transmission and for the solid support of the photocatalyst. This reactor configuration has several advantages over slurry-phase and conventaionl fixed-bed reactor designs (4). Direct delivery of light to the photocatalyst minimizes losses due to absorption and scattering by the reactor and reaction solution. The dispersed coated fiber configuration provides a more uniform distribution of the photocatalyst within the reaction solution resulting in reduced mass transport limitations to photochemical conversion and allowing for higher processing capacities (3). Distribution of the input light intensity over a large number of coated fibers minimizes the incident light intensity to which the photocatalyst is exposed. This effect has been shown to enhance the relative quantum efficiency to photochemical conversion (4-11). Futhermore, the remote transmission of light to a photocatalyst via a fiber-optic cable system is not possible with other photocatalytic reactor configurations. As a result, an OFR system could be utilized for *in situ* remediation of contaminated subsurface environments and for the remote, offline treatment of either aqueous- and/or vapor-phase contaminants such as chlorinated hydrocarbons.

In order to better understand the OFR system illustrated in Fig. 1, we have developed a basic mathematical model to describe the degradation of a single compound in an OFR using a Langmuir-Hinshelwood kinetic expression. We assume that the reaction is not mass-transport limited and that the overall process can be represented by a single coated fiber immersed in a differential reaction volume, as shown in Fig. 2, and that the reaction occurs exclusively at the solution/coating interface (3). The radiation field in a coated fiber is unique from slurry-phase and other fixed-bed reactor

configurations. As light travels down a coated fiber, it is refracted out of the fiber and directly into the semiconductor coating and undergoes an exponential decay in illumination intensity downward along the length of the fiber. If the coating layer is of sufficient thickness and the coated fiber is of sufficient length, then all of the input light is absorbed by the coating over the length of the fiber. A term describing the absorbed light intensity as a function of position in the fiber, $I'_{abs}(z)$, and Langmuir-Hinshelwood constants (12) are derived experimentally. The global quantum efficiency, ϕ_{global}, which is modeled as a function of the absorbed light intensity is used as a fitting parameter. The model is tested against experimental data generated in an OFR for the photocatalytic oxidation of 4-chlorophenol (4CP), pentachlorophenol (PCP), and dichloroacetate (DCA) (2) and model values for ϕ_{global} are compared to experimental values.

Experimental Section

OFR Oxidations. The basic features of the OFR system, which is illustrated in Fig. 1, have been described in detail elsewhere (1). The key components are a xenon-arc UV-radiation source, a 310 - 375 nm band pass filter, a focusing lens, a light transmitting TiO_2-coated fiber-optic bundle consisting of 72 1-mm diameter, 1.2 m long fibers (3M Power-Core FT-1.0-UMT), and a 227 mL cylindrical Pyrex reaction vessel with a bottom-fritted gas inlet. The TiO_2-laden fibers were prepared by stripping the terminal 20 cm of the fibers to expose the quartz core, coating with a 13 wt% aqueous slurry of TiO_2 (Degussa P25), and annealing at 300°C maximum.

Input and absorbed light intensities for the single fiber light distribution and OFR oxidation experiments were measured by chemical actinometry using α-(2,5-dimethyl-3-furylethylidene) (isopropylidene) succinic anhydride (Aberchrome 540). The experimental methods have been previously described (1). Light flux measurements were made for uncoated and coated fibers. The difference between the two was taken to be the

total photon flux absorbed by the TiO_2 layer, $I_{abs(bundle)}$. The light intensities into individual fibers, I_{input}, were estimated by dividing $I_{abs(bundle)}$ by the total number of coated fibers in the bundle.

Sample solutions (190 mL) of reagent grade 4CP (Aldrich), PCP (Aldrich), and DCA (Spectrum) of varying initial concentrations and pH (Table 1) were prepared from stock solutions. Before irradiation, the coated-fiber bundle was immersed in the reaction solution and allowed to equilibrate for 30 min. Nylon (Nalgene 0.45 μm) or Teflon (Acrodisc 4CRPTFE 0.45 μm) syringe filters were used to filter all samples. Pure oxygen (Air Liquide) was used at saturation in water as the primary electron acceptor. The reactor was mixed via continuous sparging with O_2.

An equivalent slurry-phase TiO_2 loading (ESPL) of 0.5 gL^{-1} was determined by stripping 13 wt% TiO_2 coatings from the fibers by immersing the fibers in distilled water at pH 11 (KOH) and sonicating overnight. The TiO_2 sludge was recovered, dried and weighed. Several measurements were made and averaged. The ESPL is calculated as the mass of recovered catalyst divided by the reaction solution volume (0.19 L). This value is representative of the ESPL of the single fiber reaction scheme shown in Fig. 2.

Slurry-phase Oxidations. Vigorously stirred, air-saturated sample solutions (30 mL) of 4CP, PCP, and DCA of varying initial concentrations (Table 1) and containing 0.5 $g\text{-}L^{-1}$ TiO_2 (Degussa P25) were irradiated for one hour. The light intensity was adjusted using a neutral density filter to achieve an input light intensity similar to that of the OFR (50 μE $L^{-1}min^{-1}$.

Sample Analysis. 4CP and PCP were analyzed by HPLC using a Hewlett Packard ODS Hypersil (5 μm) column with an eluent (1 $mL\text{-}min^{-1}$) of 20/80% acetonitrile/water (pH 3) and 65/35% methanol/water, respectively. DCA was quantified by ion chromatography (Dionex BIOLC 4500i series) using an Ionpac AG11 Guard column with an eluent (1

mL-min^{-1}) of 75/25% 5 mM/100 mM NaOH. The pH was determined with a Radiometer PHM85 pH meter. A constant pH was maintained for the PCP and DCA oxidations by the addition of KOH (Mallinckrodt AR) (Table 1).

Model Development

A rate expression for a single-component heterogeneous photocatalytic batch reaction may be described by a Langmuir-Hinshelwood kinetic expression as follows (13):

$$-\frac{dC_R(t)}{dt} = \frac{\hat{s} * \omega}{V} * k_{obs} \frac{K_{ads}C_R(t)}{1 + K_{ads}C_R(t)} \qquad (1)$$

where $\hat{s}$ is the moles of surface sites per mass of catalyst ($\mu M g^{-1}_{catalyst}$), ω, the photocatalyst loading on the fiber (g), V, the differential reaction volume around the coated fiber (L), k_{obs}, an observed rate constant (min^{-1}), K_{ads}, the dynamic Langmuir adsorption constant (μM^{-1}), and $C_R(t)$ the time dependent concentration of reactant R (μM). Application of Eq. 1 assumes that 1) the reaction is surface mediated, and 2) the reaction system is in dynamic equilibrium and driven by reaction kinetics and not adsorption kinetics. Furthermore, it is assumed that competition for surface sites by intermediates and other solution-phase species such as O_2, are not rate limiting.

If the above assumptions are valid, then the basic elements in the reaction system include the reactants (e.g., R, O_2, etc.), the adsorption surface sites, and the photocatalytically-generated oxidants, $\bullet OH_{ads}$ and h^+_{vb}, and primary reduced dioxygen species, $O_2^{\bullet -}$. The first term in Eq. 1 quantifies the concentration of adsorption surface sites available while the Langmuir saturation term $\frac{K_{ads}C_R(t)}{1 + K_{ads}C_R(t)}$ represents the fraction of surface sites occupied by R. Together these terms quantify the surface concentration of the reactant, R. The observed rate constant, k_{obs}, then contains the remaining reaction parameters which may include the intrinsic reaction rate constant, the

rate of OH• and $O_2^{\bullet-}$ generation, a function of the absorbed photon flux, I_{abs}, $[O_2]_{ads}$, competition from intermediate species, and mass transport effects (6, 13-15).

The dependency of reaction rate and quantum efficiency on the absorbed light intensity has been well established (2, 4-11, 16), where the experimental quantum efficiency is defined as

$$\phi_{exp} \equiv \frac{\left|\frac{-d[4CP]}{dt}\right|}{\left|\frac{d[hv]_{abs}}{dt}\right|} \cong \frac{\text{initial reaction rate}}{\text{absorbed light flux}} \qquad (2)$$

where $\frac{d[hv]_{abs}}{dt} \equiv I_{abs}$. In general, the observed photochemcial reaction rates vary linearly with I_{abs} at absorbed light intensities significantly below one sun (~60 Wm^{-2}), vary as the square root of I_{abs} at moderate illumination intensities, and is independent of I_{abs} at higher light fluxes (i.e., the relative quantum efficiency varies either as I_{abs}^{0}, $I_{abs}^{-0.5}$, or I_{abs}^{-1} depending on the magnitude of I_{abs}).

A global reaction quantum efficiency, ϕ_{global}, is expressed as follows:

$$\phi_{global} = f(I_{abs}, k_{intrinsic}, [O_2]_{ads}, \sum_{i}^{n} C_{i,ads}) \qquad (3)$$

where

$$k_{obs}(\hat{I}_{abs}, \phi_{global}) = \hat{I}_{abs} * \phi_{global}(I_{abs}, k_{intrinsic}, [O_2]_{ads}, \sum_{i}^{n} C_{i,ads}) \qquad (4)$$

and $\hat{I}_{abs}$ is the light intensity absorbed by the photocatalytic coating normalized by the coating's photocatalytic particle density ($\hat{\omega}$) given by

$$\hat{\omega} = \frac{\omega}{V_{coating}} * (F.W._{TiO_2} * \gamma)^{-1} \qquad (5)$$

where γ is the number of TiO_2 molecules per TiO_2 particle with an estimated value of 4.16×10^5 for Degussa P25 (17).

In a coated fiber the absorbed light intensity varies along the length of the fiber, z, and, as a consequence, $\phi_{global}(I_{abs})$ also varies with z. We express the absorbed light

intensity as a function of fiber length and integrate the product over the length of the coated fiber:

$$k_{obs}(\phi_{global}(I_{abs}),\ \hat{I}_{abs}) = \hat{\omega}^{-1}\int_0^L \{\ I'_{abs}(z)\ *\ \phi_{global}(I'_{abs}(z))\ \}\ dz \qquad (6)$$

where $I'_{abs}(z)$ has units of $\mu E\ L^{-1} min^{-1}\ m^{-1}$ and $\hat{\omega}$ is assumed to be constant over the entire length of the fiber.

Refraction of light out of an optical fiber and into a photocatalytic coating is the primary loss mechanism as light is transmitted down the fiber (1). Experimental data suggests that the refractive loss can be represented by an exponential decay of the form (vide infra):

$$I_{fiber}(z) = I_{input}\ e^{-\alpha z} \qquad (7)$$

where $I_{fiber}(z)$ is the amount of light remaining in the fiber at position z ($\mu E\ L^{-1}\ min^{-1}$); I_{input} is the light in the fiber at position z = 0; and α is a refractive loss coefficient that is a function of the optical and physical properties of the fiber core and the photocatalytic coating (m^{-1}). The amount of light refracted out of the fiber and into the coating as a function of position along the fiber is given by

$$I'_{abs}(z) = -\frac{dI_{fiber}(z)}{dz} = \alpha\ I_{input}\ e^{-\alpha z} \qquad (8)$$

The dependence of the relative quantum efficiency on the absorbed light intensity can be fit to a power law expression

$$\phi_{global}(I'_{abs}(z)) = A\ *\ I'_{abs}(z)^{-\beta} \qquad (9)$$

Substituting the expressions for $I'_{abs}(z)$ and $\phi_{global}(I'_{abs}(z))$ into Eqs. 6 and 1 gives

$$-\frac{dC_R(t)}{dt} = \frac{\hat{s} * \omega}{V} * \frac{A}{\hat{\omega}} * \alpha^{(1-\beta)}\ *\ I_{input}^{(1-\beta)}\ * \left\{\int_0^L e^{-(1-\beta)\alpha z}\ dz\right\} * \frac{K_{ads} * C_R(t)}{1 + K_{ads} * C_R(t)} \qquad (10)$$

Integration of Equation 10 with respect to time gives an implicit solution for $C_R(t)$

$$\frac{1}{K_{ads}} \ln(C_R(t)) + C_R(t) = \frac{1}{K_{ads}} \ln(C(0)_R) + C(0)_R - * \chi * t \qquad (11)$$

where

$$\chi = \frac{\hat{s} * \omega A * \alpha^{-\beta} * I_{input}^{(1-\beta)}}{V * \hat{\omega} * (1-\beta)} \left\{1 - e^{-(1-\beta)\alpha L}\right\} \qquad (12)$$

Results

Model Parameter Estimation. Refractive light losses from single-fiber loss experiments for two coating thicknesses were fit to Eq. 7, as shown in Fig. 3. In these cases, α was found to be 20 and 40 m^{-1} for 13 and 17 wt% TiO_2 coatings, respectively. A curve fit of Eq. 9 to intensity-dependent quantum efficiency data for the photocatalytic oxidation of 4CP in the OFR gives values of 0.025 and 0.3 for A and β, respectively (Fig. 4). It should be noted that the curve fit was derived using measured values of I_{abs} rather than $I'_{abs}(z)$.

Slurry-phase photocatalytic oxidations of 4CP, PCP, and DCA were carried out at several initial concentrations and under reaction conditions similar to those of the OFR experiments for pH, $[TiO_2]$ and I_{input} to estimate values for the Langmuir adsorption constant, K_{ads}. Values for K_{ads} listed in Table 1 are derived from linear fits of $rate^{-1}$ versus $[R]^{-1}$ where the slope is $(k_{slurry} * K_{ads})^{-1}$ and the intercept equals $(k_{slurry})^{-1}$ and k_{slurry} is the observed reaction rate constant for the slurry-phase reaction. A sample plot is shown in Fig. 5.

Comparison to Experimental OFR Data. A representative plot comparing experimental data and model calculations for 4CP oxidation is shown in Fig. 6. The model is run for three $\phi_{global}(I'_{abs}(z))$ functions: Case 1: $\phi_{global} = A$; Case 2: $\phi_{global} = A*(I'_{abs}(z))^{-0.3}$; and Case 3: $\phi_{global} = A*(I'_{abs}(z))^{-0.5}$, and $I_{input} = 0.3\ \mu E\ L^{-1}\ min^{-1}$. The absorbed light intensity is normalized by $\hat{\omega}$ which has a value of 4.1 μM (i.e., TiO_2 as particles) as determined by Eq. 5. The coating thickness, length, and porosity are 5

μm, 0.20 m and 0.9, respectively, and $\omega/V_{coating}$ = 0.48 gL^{-1}. These values are consistent with previous findings (1, 2). $\hat{s}$ is estimated to be 300 μmol sites-$g^{-1}_{catalyst}$ based on a reported value of 3-4 surface sites nm^{-2} (18). "A" was varied until a reasonable fit to the data was achieved. Table 2 gives the best-fit values of A for each case and the corresponding values of ϕ_{exp} and average ϕ_{global} for the oxidation of 4CP, PCP, and DCA where

$$(\phi_{global})_{avg} = L^{-1} \int_0^L \phi_{global}(I'_{abs}(z))\, dz \qquad (13)$$

The average global quantum efficiencies are consistently higher than the experimentally-determined relative quantum efficiencies but are typically within a factor of 5. Model $(\phi_{global})_{avg}$ of 0.031, 0.077, and 0.25 are calculated for Case 1 compared to 0.012, 0.015, and 0.095 relative quantum efficiencies for the 4CP, PCP, and DCA oxidations, respectively. The intensity-independent case gave the lowest global quantum efficiency values while the inverse square root case gave values that were a factor of two higher. The model was also run for Case 1 for three different input/absorbed light intensities of 0.31, 0.43, and 0.47 μE L^{-1} min^{-1} for 4CP (Table 2). The results are plotted in Fig. 7. ϕ_{global} (= $(\phi_{global})_{avg}$ was calculated to be 0.031, 0.031, and 0.024, respectively.

Discussion

The above model characterizes mathematically the OFR system and identifies several important reactor/reaction parameters. Critical assumptions in development of the model are that the reaction occurs on the surface of TiO_2 and that the reaction rate is controlled by electron-transfer kinetics and is not controlled by adsorption kinetics or is not mass transport limited. The photochemical reactions are symmetrical with respect to each coated fiber. Furthermore, we assume that the reaction is not limited by O_2 sorption or by competitive inhibition from reaction intermediates or other solution species.

It is widely accepted that heterogeneous photocatalytic reactions occur on or near the surface and can be represented by a Langmuir-Hinshelwood kinetic expression (6, 15, 17, 19, 20). Many studies involving slurry-phase reactors have reported no evidence of mass transport limitations (13, 15, 19, 21-24). In contrast, mass transport effects in fixed-bed photocatalytic reactor systems appear to be a function of the reactor design and reaction parameters such as distribution of the photocatalyst within the reaction volume, the radiation field with respect to the exposed photocatalyst membrane, pollutant concentration, and reaction solution flowrate, (14, 22, 24-27). The close, concentric arrangement of fibers within the oxygen-saturated reaction solution of the OFR coupled with vigorous mixing and slow reaction rates (e.g., 0.3 - 2 $\mu M\text{-}min^{-1}$) suggest that it is reasonable to assume the system is in equilibrium and that it is not mass transport limited. In addition, it has been previously demonstrated that transport within the porous TiO_2 coating and within the OFR reaction volume, in general, is not limiting (1, 3). Sparging with oxygen ensures that the reaction solution is O_2-saturated. The assumption of no competitive inhibition by products or intermediates is made to simplify the model even though it has been shown that reaction intermediates can significantly affect the reaction rate of the parent compound (14, 21). In addition, Cl^- and other inorganic anions have been found to compete effectively for surface sites and may play a significant role in the reaction rate of the chlorinated parent compound (28). A more elaborate model can be developed to incorporate these non-linear competitive factors but will be assumed here to be constant and represented in the ϕ_{global} term.

The relationship between the observed reaction rate constant, the relative quantum efficiency, and the normalized absorbed light intensity is analogous to direct photolysis rate expressions of the form

$$-\frac{dC_R(t)}{dt} = \phi(\lambda) \ * \ I_{input}(\lambda,t) \ * \ (1-e^{-2.303*\varepsilon*l/C_R(t)}) \qquad (14)$$

where λ is the wavelength-dependent photolysis quantum efficiency and ε, the substrate extinction coefficient, and l, the pathlength of radiation (29-32). In the case of a heterogeneous reaction, the light-absorbing reactant (i.e., the TiO_2 photocatalyst) is assumed to be a complete absorber of the radiation and the third term in Eq. 14 becomes unity (6, 17).

In our model, the absorbed photon flux is normalized by the photocatalyst particle concentration, $\hat{\omega}$, to account for the distribution of photon flux within the photocatalytic coating. In illuminated semiconductor photocatalysts, charge-carrier (e^-, h^+) recombination and interfacial charge transfer are second- and first-order processes, respectively. The charge-carrier density increases with an increase in the absorbed light intensity. As a result, at a higher relative absorbed light intensity, the rate of charge-carrier recombination is increased relative to interfacial charge transfer, and this leads to a lower quantum efficiency. This approach is consistent with previous findings regarding the relationship between measured relative quantum efficiencies and normalized absorbed light intensities (3). Based on the above assumptions, experimental and empirical determination of the various model parameters provides a basis for calibrating the model against experimental data.

The extent of the refractive losses of light out of a coated fiber was found to be a function of the interfacial contact area between the TiO_2 particles and the quartz fiber surface (i.e., the greater the contact area, the greater the refractive loss over a given length) (1). Parameters such as the coating porosity, particle size, and coating method affect the interfacial contact area. The above phenomenon is reflected in a higher α value for the higher TiO_2 wt% coating shown in Fig. 3. An α value of 20 m^{-1} is used in the model which corresponds to a 13 wt% coating employed in the oxidations.

Similarly, an empirical relationship for the quantum efficiency dependence on the absorbed light intensity is derived from experimental data for the photocatalytic oxidation

of 4CP (Fig. 4). A fit of the data from the OFR yields $\beta \approx 0.3$. This value suggests operation in a low to moderate absorbed light intensity region (i.e., a value of β between 0 and 0.5). The spatially-averaged estimate of β is reasonable since the per fiber input light intensities, I_{input}, are on the order of 10^{-6} Einstein-min^{-1} (approximately one sun). The *local* absorbed light intensities to which the photocatalyst coating is exposed, however, is a small fraction of I_{input}. Therefore, one would expect that the corresponding *local* quantum efficiency to be independent of $I'_{abs}(z) * dz$, i.e., $\beta = 0$. The value for $I_{input} = 0.3$ $\mu E\ L^{-1}\ min^{-1}$ was estimated based on a typical measured absorbed light intensity for the bundle, $I_{abs(bundle)}$, divided by the number of fibers in the bundle $\left(\frac{22\ \mu E\ L^{-1}\ min^{-1}}{72\ fibers}\right)$. This estimation assumes uniform distribution of the input beam into the bundled fibers. Based on this analysis, we conclude that an intensity-independent quantum efficiency expression is the most appropriate.

In a photocatalytic reaction system, the quantum efficiency is a measure of the efficiency of photon utilization with respect to the disappearance of the parent compound or appearance of a reaction product (Eq. 2). ϕ embodies many elements of the reaction scheme such as charge-pair generation/recombination, formation of radical intermediates such as OH• and $O_2^{\bullet -}$, electron transfer and H-atom abstraction, etc. (Eq. 3). However, only the normalized absorbed light intensity is used to weight the quantum efficiency term in the model. In this case, all other reaction parameters are assumed to be constant and are incorporated into the preexponential term, A.

For the intensity-independent case (Case 1), A is equal to $(\phi_{global})_{avg}$ and is within a factor of 2.5, 5, and 2.5 of ϕ_{exp} for the 4CP, PCP, and DCA degradation, respectively. The higher model values indicate that the effect of competing intermediates on the reaction may not be constant and cannot be incorporated into A or may be due to inaccuracies in the estimation of some of the model parameters such as the K_{ads}, coating thickness, porosity, I_{input}, γ, $\hat{s}$, etc. When the model is run for 4CP at three different light

intensities and compared to experimental data, $(\phi_{global})_{avg}$ is reasonably constant with values of 0.031, 0.031, and 0.024. A constant value is expected since all other reaction parameters have been held constant in the experimental system.

Although the system is assumed not to be mass transport limited, a mass transport limited condition could be easily incorporated into the model by introducing a combined reaction rate constant that is a function of a mass transfer and a reaction rate term (13) as follows:

$$k_{obs} = (1/\text{mass transfer term} + 1/\text{reaction rate term})^{-1} \quad (15)$$

The empirically-derived reaction rate and adsorption equilibrium constants for 4CP agree with values found in the literature, even though they were derived under vastly different reaction conditions. The corresponding values are: k_{4CP} = 1.5 μmol/min-$g_{catalyst}$, K_{ads} = 0.030 μM^{-1} (0.5 g-L^{-1}, pH 2, 48 W black light) (33); k_{4CP} = 2.6, K_{ads} = 0.017 (2 g-L^{-1}, 125 W Hg lamp) (9); k_{4CP} = 78.6, K_{ads} = 0.006 (1 g-L^{-1}, pH 3.5, 20 W black light) (34). Ollis et al. (35) report values of k = 20 μmol-(min-$g_{catalyst}$)$^{-1}$ and K_{ads} = 0.022 μM^{-1} for the slurry-phase photocatalytic oxidation of DCA using 0.1 wt% Fisher TiO_2 (95% anatase, 7 m-g^{-1} surface area, 7 x 15W black lights, pH not given). The discrepancy between these values and those of the present study may be a result of different reactions conditions employed. No explicit reaction rates or absorption equilibrium constants were found in the literature for the photocatalytic oxidation of PCP.

A mathematical model of a fiber-optic bundled array reactor system is developed using Langmuir-Hinshelwood kinetics and compared to experimental data. A global quantum efficiency, ϕ_{global}, is defined and used as a model fitting parameter. It incorporates reaction parameters such as the absorbed light intensity, the intrinsic rate constant, and the effects of other adsorbed reactants and reaction intermediates. An empirical term to describe the radiation field within the coated fiber is derived

experimentally and normalized by the coating photocatalyst particle concentration to account for the inverse relationship between the absorbed light intensity and the reaction quantum efficiency. ϕ_{global} was determined to be independent of the absorbed light intensity and calculated values are in excellent agreement with experimental values.

Acknowledgments

We are grateful to ARPA and ONR (NAV 5 HFMN N000149J1901) for financial support and to Prof. George Gavalas, Janet Kesselman and Tom Lloyd for their helpful discussions. We would also like to thank 3M and Degussa for their donations of the optical fiber samples and the P25 photocatalyst, respectively.

Literature Cited

(1) Peill, N. J.; Hoffmann, M. R. *Environ. Sci. Technol.* **1995**, *29*, 2974.

(2) Peill, N. J.; Hoffmann, M. R. *Environ. Sci. Technol.* **1996**, *30*, 2806-2812.

(3) Peill, N. P.; Hoffmann, M. R. "Solar-Powered Photocatalytic Fiber Optic Cable Reactor for Waste Stream Remediation" *Solar Energy* **1996**, *submitted 1996.*

(4) Ollis, D. F.; Pelizzetti, E.; Serpone, N. *Environ. Sci. Technol.* **1991**, *25*, 1522-1529.

(5) Okamoto, K.; Yamamato, Y.; Tanaka, H.; Tanaka, M.; Itaya, A. *Bull. Chem. Soc. Jpn.* **1985**, *58*, 2015.

(6) Kormann, C.; Bahnemann, D. W.; Hoffmann, M. R. *Environ. Sci. Technol.* **1991**, *25*, 494-500.

(7) D'Oliveira, J. C.; Al-Sayyed, G.; Pichat, P. *Environ. Sci. Technol.* **1990**, *24*, 990.

(8) Mills, G.; Hoffmann, M. R. *Environ. Sci. Tech.* **1993**, *27*, 1681-1689.

(9) Al-Sayyed, G.; D'Oliveira, J. C.; Pichat, P. *J. Photochem. Photobiol. A: Chem.* **1991**, *58*, 99-114.

(10) Albery, W. J.; Brown, G. T.; Darwent, J. R.; Saievariranizad, E. *J. Chem. Soc. Farad. Trans. 1* **1985**, *81*, 1999-2007.

(11) Ollis, D. F. In *Photochemical Conversion and Storage of Solar Energy*; E. Pellizzetti and M. Schiavello, Eds.; Kluwer Academic Publishers: Dordrecht, Netherlands 1991; p 593-622.

(12) Ollis, D. F.; Turchi, C. *Environ. Prog.* **1990**, *9*, 229-234.

(13) Ollis, D. F.; Pelizzetti, E.; Serpone, N. In *Photocatalysis: Fundamentals and Applications*; N. S. a. E. Pelizzette, Eds.; Wiley & Sons: New York 1989; p 603-637.

(14) Lu, M. C.; Roam, G. D.; Chen, J. N.; Huang, C. P. *Journal Of Photochemistry and Photobiology a-Chemistry* **1993**, *76*, 103-110.

(15) Turchi, C. S.; Ollis, D. F. *J. Catalysis* **1990**, *122*, 178.

(16) Cassano, A. E.; Martin, C. A.; Brandi, R. J.; Alfano, O. M. *Ind. Eng. Chem. Res.* **1995**, *34*, 2155-2201.

(17) Hoffmann, M. R.; Martin, S. T.; Choi, W.; Bahnemann, D. W. *Chem. Rev.* **1995**, *95*, 69-96.

(18) Vasudevan, D.; Stone, A. *Environ. Sci. Technol.* **1996**, *30*, 1604-1613.

(19) Pruden, A. L.; Ollis, D. F. *J. Catal.* **1983**, *82*, 404-417.

(20) Hsiao, C. Y.; Lee, C. L.; Ollis, D. F. *J. Catalysis* **1983**, *82*, 418.

(21) Matthews, R. W. *J. Catal.* **1988**, *111*, 264-272.

(22) Turchi, C. S.; Ollis, D. F. *J. Phys. Chem.* **1988**, *92*, 6852-6853.

(23) Matthews, R. W. *J. Phys. Chem.* **1988**, *92*, 6853-6854.

(24) Sabate, J.; Anderson, M. A.; Kikkawa, H.; Edwards, M.; Hill, C. G. *J. Catal.* **1991**, *127*, 167-177.

(25) Aguado, M. A.; Anderson, M. A.; Hill, C. G. *J. Mol. Catal.* **1994**, *89*, 165-178.

(26) Matthews, R. W. *J. Phys. Chem.* **1987**, *91*, 3328.

(27) Sabate, J.; Anderson, M. A.; Aguado, M. A.; Gimenez, J.; Cerveramarch, S.; Hill, C. G. *J. Mol. Catal.* **1992**, *71*, 57-68.

(28) Abdullah, M.; Low, G. K. C.; Matthews, R. W. *J. Phys. Chem.* **1990**, *94*, 6820.

(29) Noyes, W. A.; Leighton, P. A. *The Photochemistry of Gases*; Dover Publications: New York, 1941.

(30) Calvert, J. G.; Pitts, J. N. *Photochemistry*; John Wiley & Sons, Inc.: New York, 1966; p 899.

(31) Seinfeld, J. H. *Air Pollution: Physical and Chemical Fundamentals*; McGraw-Hill: New York, 1975; p 523.

(32) Willberg, D. M.; Lang, P. S.; Hochemer, R. H.; Kratel, A.; Hoffmann, M. R. *Environ. Sci. Technol.* **1996**, *30*, 2526-2534.

(33) Mills, A.; Morris, S. *J. Photochem. Photobiol A: Chem* **1993**, *71*, 75-83.

(34) Matthews, R. W. *Wat. Res.* **1990**, *24*, 653-660.

(35) Ollis, D. F.; Hsiao, C. Y.; Budiman, L.; Lee, C. L. *J. Catal.* **1988**, *88*, 89-96.

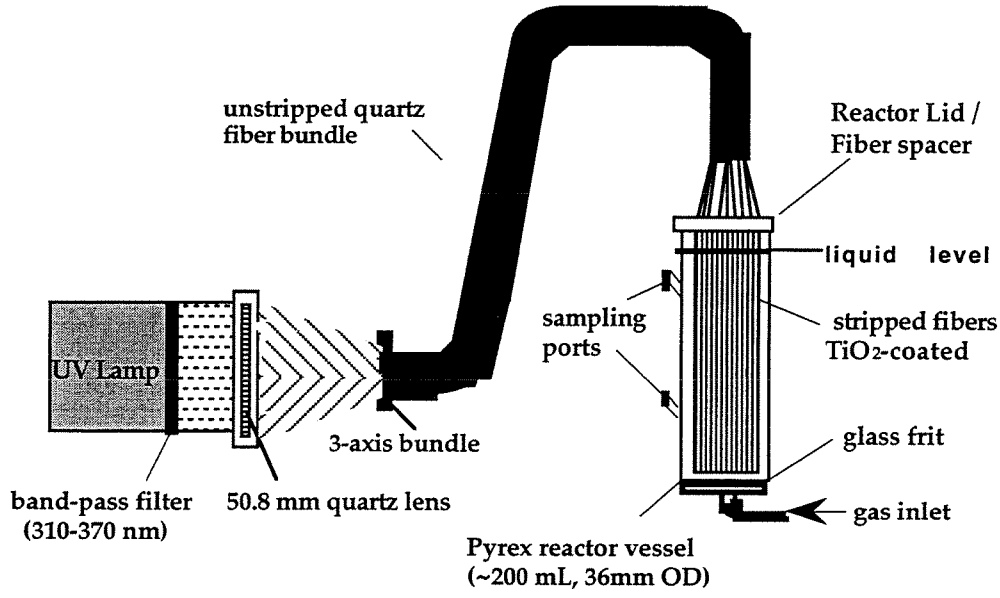

Figure 1. Schematic of optical-fiber bundled array photocatalytic reactor system.

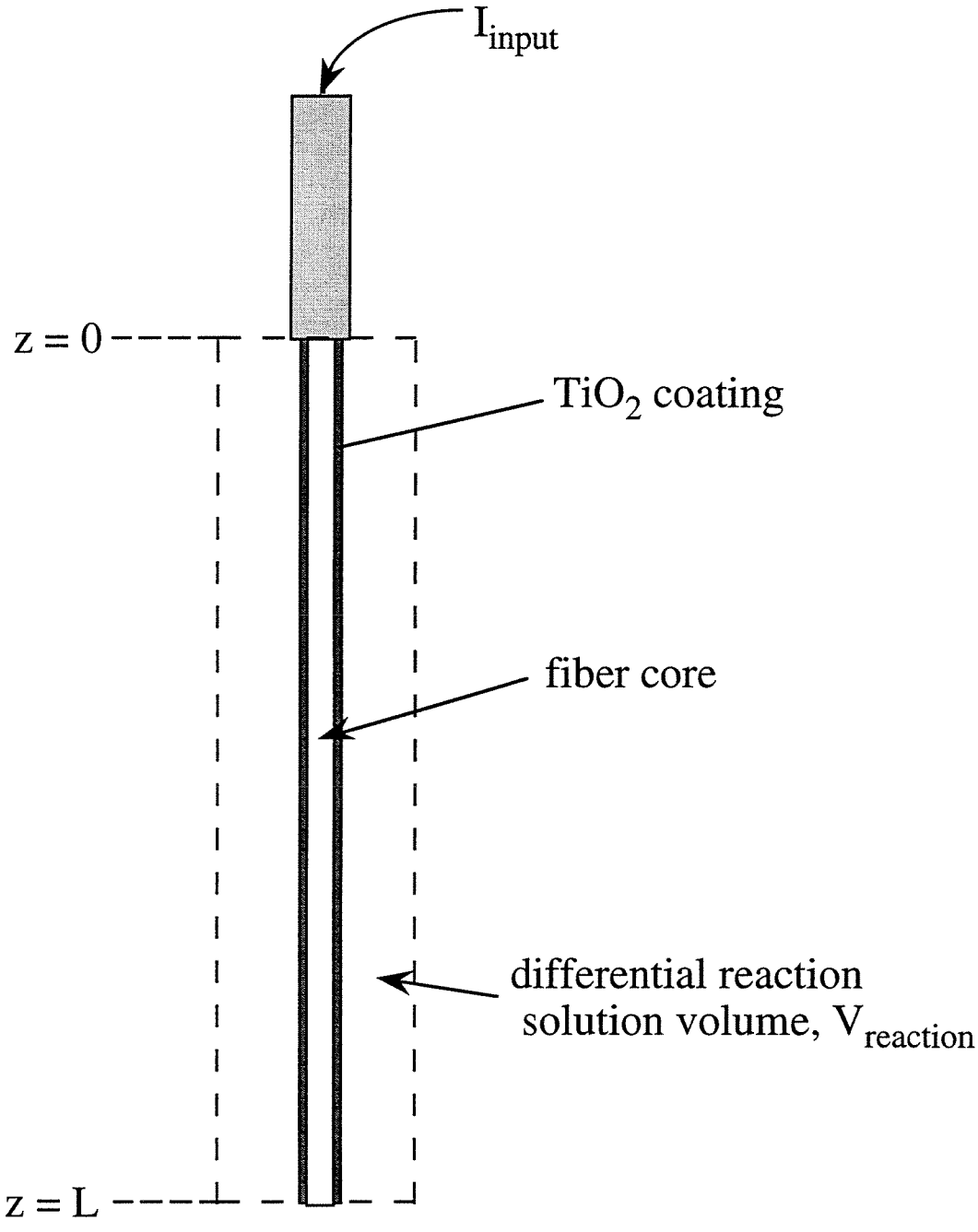

Figure 2. Model scheme: a single, coated optical fiber with length L immersed in a differential reaction solution volume, $V = V_{reactor}$/ # fibers.

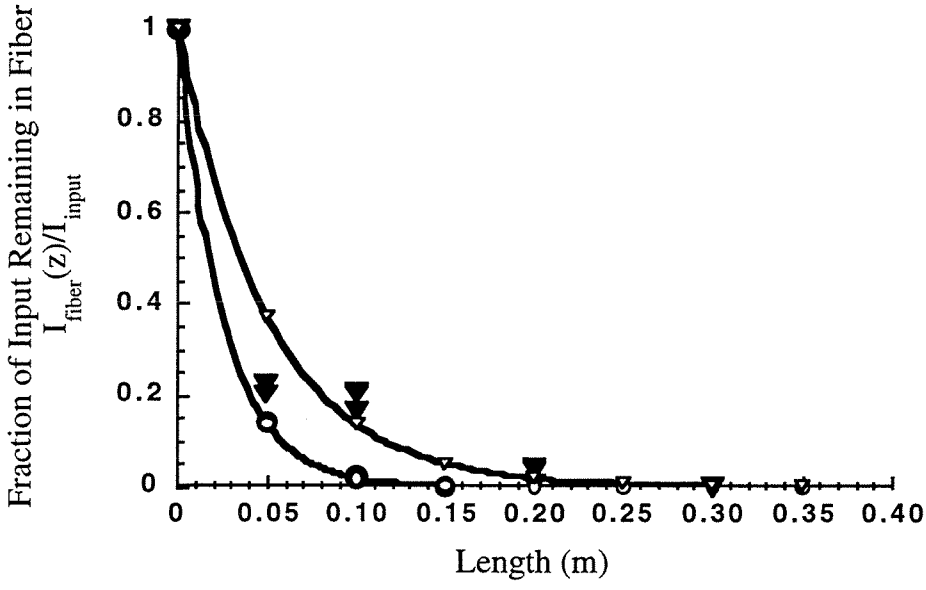

Figure 3. Light intensity distribution in a single fiber for a 13 wt % TiO_2 coating (▼) experimental data and (∇) curve fit: $I_{fiber}(z)/I_{input} = e^{-20*z}$; and 17 wt% TiO_2 coating (●) experimental data and (O) curve fit: $I_{fiber}(z)/I_{input} = e^{-40*z}$.

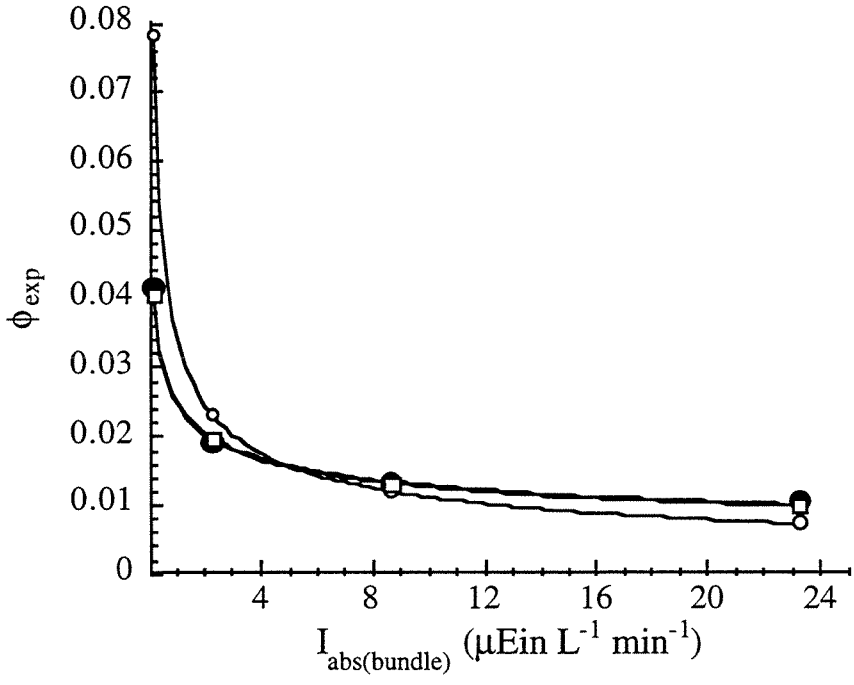

Figure 4. Relative quantum efficiency, ϕ_{exp}, as a function of absorbed light intensity for the photocatalytic oxidation of 4CP in OFR, (●) experimental data; (□) $\phi(I_{abs}) = 0.025 * I_{abs}^{-0.3}$; and (○) $\phi(I_{abs}) = 0.035 * I_{abs}^{-0.5}$ and curve fits. Reaction conditions are given in the text.

Compound	$[C]_o$ (mM) / pHinitial - pH_{final}	k_{slurry} (μmol/min-$g_{catalyst}$)	K_{ads} (μM^{-1})
4CP	0.20, 0.10, 0.060, 0.030 / 5.5	1.30	0.020
PCP	0.061, 0.040, 0.030, 0.020 / 4.5 - 5.5	2.5	0.017
DCA	2.0, 1.0, 0.3 / 3.0	10.8	0.0027

Table 1. Slurry-phase reaction conditions and measured rate constants, k_{slurry}, and absorption equilibrium constants, K_{ads}, for 4CP, PCP, and DCA. $[TiO_2]$ = 0.5 g-L^{-1} , I_{input} = 50 μE $L^{-1}min^{-1}$.

Expression for $\phi_{global}(I'_{abs})$	**I_{input}**	**4CP** A/ϕ_{avg}	**PCP** A/ϕ_{avg}	**DCA** A/ϕ_{avg}
$A*I_{abs}^{0}$	0.3	0.031/0.031[a]	0.077/0.077[d]	0.25/0.25[a]
$A*I_{abs}^{-0.3}$	0.3	0.037/0.042[a]	0.092/0.104[d]	0.31/0.35[a]
$A*I_{abs}^{-0.5}$	0.3	0.042/0.055[a]	0.105/0.137[d]	0.35/0.46[a]
ϕ_{exp}	0.3	0.012	0.015	0.095
$A*I_{abs}^{0}$	0.43	0.031/0.031[c]		
ϕ_{exp}	0.43	0.009		
$A*I_{abs}^{0}$	0.47	0.024/0.024[b]		
ϕ_{exp}	0.47	0.008		

Measured $I_{abs(bundle)}$ = [a] 22, [b] 31, [c] 34, and [d] 20 $\mu E\ L^{-1}\ min^{-1}$.

Table 2. Best model fit values for A and calculated $(\phi_{global})_{avg}$ for various expressions for ϕ_{global} having a 0, -0.3, and -0.5 power dependency on $I'_{abs}(z)$. Here, per fiber I_{input} equals the measured $I_{abs(bundle)}/72$ fibers, $\hat{s}$ = 300 μmol/g, ω = 0.48 gL^{-1} and $\hat{\omega}$ = 4.1 μM TiO_2 particles.

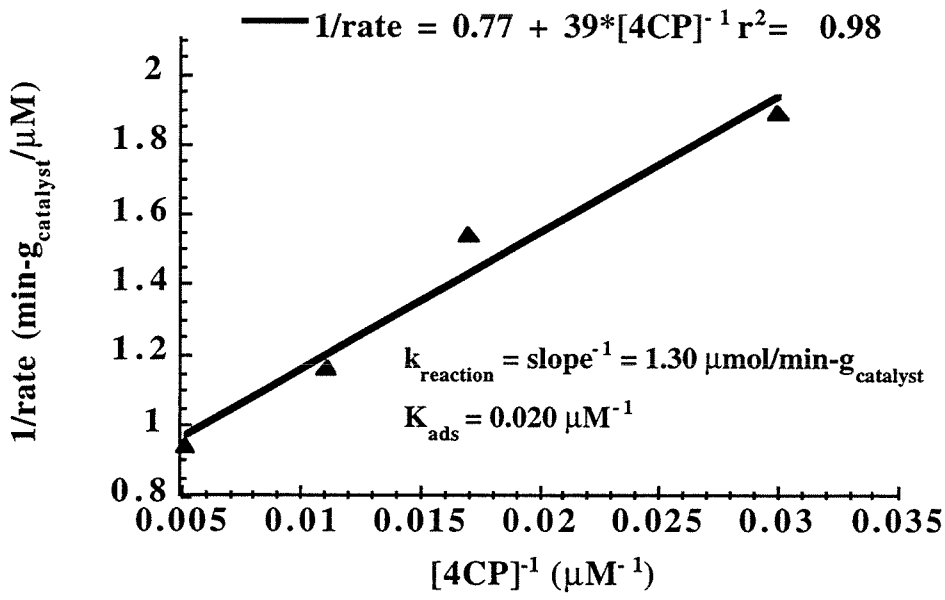

Figure 5. Langmuir-Hinshelwood reaction rate, $k_{reaction}$, and adsorption equilibrium, K_{ads}, constant determination for the slurry-phase photocatalytic oxidation of 4CP. Reciprocal reaction rate is plotted versus reciprocal concentration. Reaction conditions are given in the text.

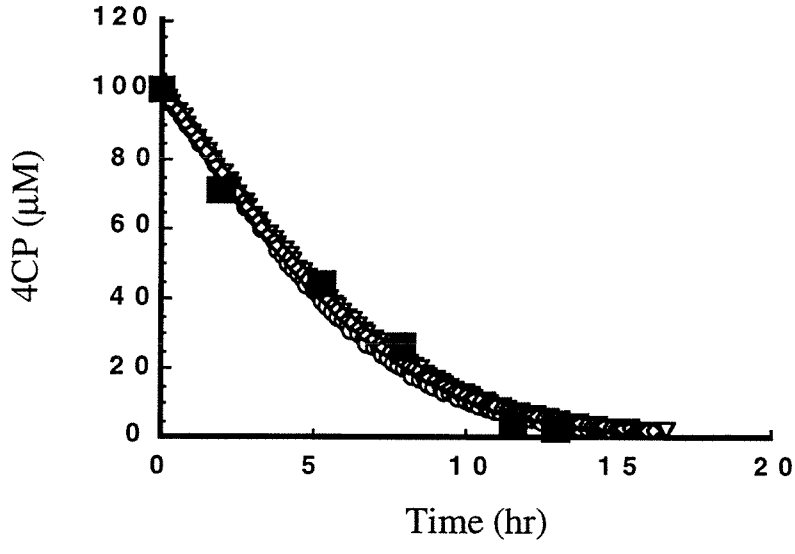

Figure 6. 4CP oxidation profile: (■) OFR experimental data; and model data for (O) $\phi_{global} = 0.031$, (▽) $\phi_{global} = 0.037 \cdot \mathcal{I}'_{abs}(z)^{-0.3}$, (▽) $\phi_{global} = 0.042 \cdot \mathcal{I}'_{abs}(z)^{-0.5}$. I_{input} = 0.31 μE L^{-1} min^{-1} and $K_{ads} = 0.020$ μM^{-1}. Reaction conditions are given in the text. $\hat{s}$ = 300 μmol/g, $\omega = 0.48$ gL^{-1} and $\hat{\omega} = 4.1$ μM TiO_2 particles.

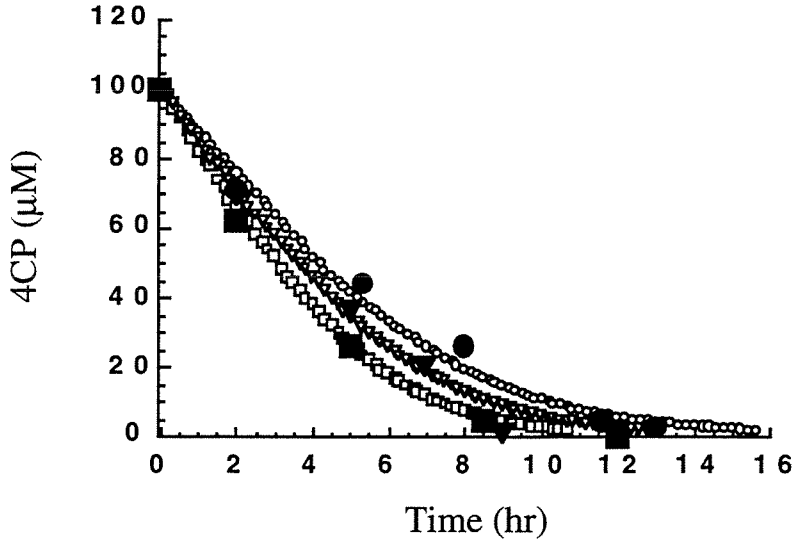

Figure 7. 4CP oxidation profiles: OFR experimental data for I_{input} equal to (●) 0.31 (■) 0.43, and (▼) 0.47 μE L^{-1} min^{-1}; and model data for Case 1: ϕ_{global} = (O) 0.031, (▽) 0.031, (▽) 0.024. I_{input} = 0.31 μE L^{-1} $min)^{-1}$ and K_{ads} = 0.020 μM^{-1}. Reaction conditions are given in the text. $\hat{s}$ = 300 μmol/g, ω = 0.48 gL^{-1} and $\hat{\omega}$ = 4.1 μM TiO_2 particles.

Chapter VII

Conclusions

The work embodied in this thesis demonstrates the viability and promise of the OFR reactor configuration for the practical application of TiO_2 photocatalysis for water purification. It extends the theoretical work of Ollis and Marinangeli (1, 2) and the experimental work of Gapen (3) and represents the first successful application of an OFR for the complete aqueous-phase oxidation of hydrocarbon contaminants. A versatile and resilient OFR system is designed and constructed that facilitates investigation of many aspects of the reactor and reaction system such as mechanism of energy transfer, angle of incident light, coatings and coating characteristics, light intensity, fiber geometry, chemical efficiency, pH, ionic strength, chemical compounds, etc. A solar-powered OFR is built and tested to demonstrate proof-of-concept for a passive system for application in areas where electricity is not easily accessible. Finally, a basic mathematical model is developed to describe the OFR system and to identify important system parameters.

The OFR system has the inherent advantages of a fixed-bed reactor, coupled with the photochemical quantum efficiencies of a slurry-phase reactor. It can used to catalyze the degradation of a broad range of chemical compounds; and it can be used in either batch- or continuous-flow operation for both liquid- and/or gas-phase reactions. Compared with other fixed-bed photocatalytic reactors, the OFR configuration enhances the spatial uniformity, distribution, and the illuminated surface area of the photocatalyst throughout a given reaction volume. The OFR is shown to result in reduced mass transport limitations to photochemical conversion and allow for higher processing capacities. Direct transmission of light to the photocatalyst coating via refraction out of the fiber core minimizes light losses due to scattering and absorption by the reactor and reaction solution. A potential advantage of the OFR is that it can operate in a high quantum efficiency domain characteristic of low incident light intensities while maintaining high reaction rates by employing high input light intensities (4).

Transmission of light to the photocatalyst via the fiber-optic cable allows for the *in situ* decontamination of groundwater, underground storage tanks, or other remote sites.

The key to maximizing the chemical efficiency of the OFR for a given bundle diameter and reaction solution volume is to maximize the utilization of incident photons. This is achieved by 1) illuminating the entire extent of the fiber's photocatalytic coating, 2) maximizing the absorption by the coating of light refracted out of the fibers, and 3) providing a coating porosity that allows for optimal access by the chemical substrate to the activated photocatalytic layers. A coating layer that minimizes the interfacial surface area of the quartz core and photocatalytic particles (where the refractive index of the fiber core is less than the photocatalytic particles (5)) and operation with collimated incident irradiation enhances light propagation down the fibers. With TiO_2 (Degussa P25), a coating thickness of 7 μm results in complete absorption of the refracted light and a porosity of 0.9 ensures no mass transport limitations within the coating.

Suggested future research directions include 1) optimization of the photocatalytic coating, 2) optimization of the fiber length, diameter, spacing and number to maximize the reaction rate and relative quantum efficiency, 3) enhancement of the beam-to-bundle coupling efficiencies, 4) demonstration of gas-phase treatment capabilities, and 5) demonstration of subsurface groundwater treatment. The use of photocatalytic coatings incorporating photonically inactive fillers, such as activated carbon and SiO_2, to reduce the interfacial surface coverage of the photocatalytic particles, should enhance the linear light transmission down the fiber. Fiber bundle parameters such as fiber number, spacing, length, and diameter will affect the distribution of activated photocatalyst throughout a given reaction solution and will directly influence the intensity and extent of coating activation. The important parameters affecting the reaction rate and relative quantum efficiency are the absorbed light intensity-to-photocatalytic surface area (ALIPSA) ratio and the activated photocatalytic surface area-to-reaction solution volume

(APSARV) ratio. Both the absorbed light intensity and the APSARV ratio will affect the reaction rate. The higher the illumination intensity and/or APSARV ratio, the higher the rate of reaction. Increasing the illumination intensity relative to the photocatalytic surface area will also result in faster degradation rates but at the expense of lower quantum efficiencies. Improvements in the beam-to-bundle coupling efficiency have the potential to greatly increase the overall OFR system efficiency. In the current work, these efficiencies are near 7 - 20% (Chapter V). Promising research is currently being conducted in the field of optics that addresses this issue (6). Reported higher reactivities in the gas-phase indicate that photocatalysis may show greater promise as a gas-phase remediation process (7-10). Testing of a continuous-flow gas-phase OFR will demonstrate its versatility. Furthermore, the application of photocatalysis to disinfection of indoor air shows potential for commercial application (11-13). Finally, there are many developmental issues that must be addressed before practical *in situ* application of an OFR system is possible. These include scale-up and distribution of the fibers throughout the treatment volume, protection of the fibers from breakage, coating lifetime and durability, control of flow through the activated bundle, filtration of particulates and other interfering species such as humic substances present in groundwater that scavenge •OH, sufficient residence times, mixing and oxygenation (aqueous-phase) or humidification (gas-phase).

The near term success of the OFR as a treatment technology will depend on identifying niche applications that capitalize on the need for remote and/or *in situ* decontamination utilizing solar photons in locations where pumping or excavating costs are high and fast treatment times are not critical. The unique characteristics of the OFR are depicted in Figure 1. The wide-scale commercial application of an OFR will require improvements in coating photoefficiencies. Current levels of 1-10% make it difficult for photocatalytic treatment technologies to compete effectively on a large scale with

alternative AOT's such as UV/peroxide or UV/O_3 for above-ground water treatment applications.

Literature

(1) Ollis, D. F.; Marinangeli, R. E. *AIChE J.* **1977**, *23*, 415-425.

(2) Ollis, D. F.; Marinangeli, R. E. *AIChE J.* **1980**, *26*, 1000-1007.

(3) Gapen, D. C., Photocatalytic Degradation of Chlorinated Hydrocarbons, M. S., Institution, 1991.

(4) Ollis, D. F.; Pelizzetti, E.; Serpone, N. *Environ. Sci. Technol.* **1991**, *25*, 1522-1529.

(5) Harrick, N. J. In *Internal Reflection Spectroscopy*; Eds.; Interscience Publishers: Briarcliff Manor, NY, 1967; p 13-65.

(6) Hunter, T., March 28, 1995, personal communication.

(7) Jacoby, W. A.; Nimlos, M. R.; Blake, D. M. *Abst. Papr. Am. Chem. Soc.* **1993**, *205*, 344.

(8) Jacoby, W. A.; Nimlos, M. R.; Blake, D. M.; Noble, R. D.; Koval, C. A. *Environmental Science & Technology* **1994**, *28*, 1661-1668.

(9) Nimlos, M. R.; Milne, T. A. *Environ. Sci. Technol.* **1992**, *26*, 545-552.

(10) Nimlos, M. R.; Jacoby, W. A.; Blake, D. M.; Milne, T. A. *Environ. Sci. Technol.* **1993**, *27*, 732-740.

(11) Sjogren, J. C.; Sierka, R. A. *Appl. Environ. Microbiol.* **1994**, *60*, 344-347.

(12) Ireland, J. C.; Klostermann, P.; Rice, E. W.; Clark, R. M. *Appl. Environ. Microbiol.* **1993**, *59*, 1668-1670.

(13) Suzuki, E.; Ollis, D. F. *Biotechnology and Bioengineering* **1989**, *34*, 1398-1402.

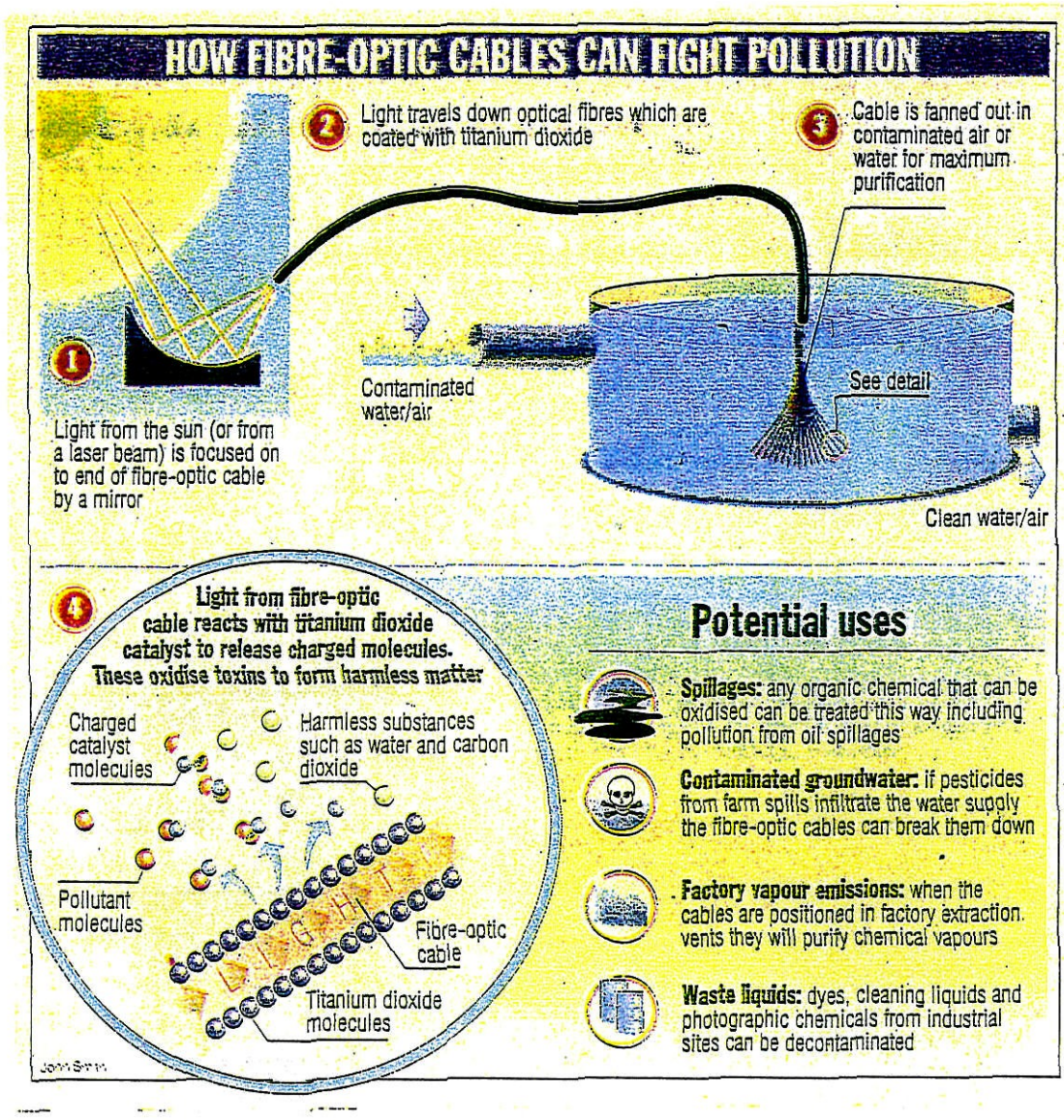

Figure 1. Artist's rendering of a solar OFR system (reprinted from the *Sunday London Times*, November 13, 1994).

Appendix

Review, Comparison and Economic Analysis of UV Advanced Oxidation Technologies for Waste Stream Remediation

Introduction

Over the last half of the twentieth century, there has been a growing need for innovative and economically viable technologies to address a wide range of environmental problems and challenges such as site remediation, end-of-pipe cleanup, and pollution prevention. Due to rapid industrialization and expansion in the 1940's and 50's and defense activities at military facilities that ignored long term environmental impacts, the nation is now faced with a plethora of environmental problems relating to hazardous waste disposal, surface and groundwater contamination, and the control of toxic air emissions. The projected costs of remediation of contaminated sites alone is staggering. Cleanup of more than 1800 U.S. military installations has been estimated to be $30 billion over the next 10 years. The U.S. produces annually more than 540 million metric tons of hazardous waste (1). The elimination of hazardous substances from waste effluents and contaminated sites has become a national priority. Current production of waste emissions from power utilities, petrochemical facilities, and small, privately-owned operations, etc., is becoming highly regulated and increasingly more costly.

In order to address these cleanup and pollution control challenges, the EPA has regulated the use of Best Available Technology (BAT). BAT technologies have been found by the EPA to meet the standards and specifications that provide safe and sufficient pollution control of industrial processes and remediation of contaminated sites. They include air stripping, carbon absorption, high-temperature incineration, biological remediation and catalytic oxidation. Only air stripping, carbon adsorption and biological remediation are typically applied to aqueous-phase waste streams, which represent the bulk of remediation and pollution control problems. Except for bioremediation, these technologies are nondestructive; that is, the contaminants are not destroyed but transferred from one phase to another which may require further processing and/or disposal.

More recently, the EPA has approved the inclusion of advanced oxidation technologies (AOT's) in the BAT category which may prove to be more economically efficient for certain remediation and pollution control applications. These AOT systems have the advantages of on-site oxidation of contaminants to very low concentrations with little to no air emissions and no generation of residuals requiring further handling, such as ash or spent carbon. These benefits alleviate the liability associated with off-site destruction and media transfer that is characteristic of the conventional pollution control technologies. AOT's include UV/oxidation, ultraviolet radiation in conjunction with oxidants and photocatalysts; chemical oxidation employing ozone, hydrogen peroxide, etc.; super critical water oxidation (SCWO); and wet air oxidation.

This paper will focus on UV/oxidation AOT systems which have been extensively researched and successfully employed to treat drinking water, ground water, industrial process water, and marine tank ballast process water in offshore drilling rigs[1]. As early as 1978, the UV/oxidation process was thought to be highly promising as an economical destructive method for PCB cleanup (2). Over the last five years, the number of full scale UV/oxidation facilities has grown from a few to several hundred as the technology and efficiencies are improved and the equipment costs are lowered. For example, the city of South Gate (CA) operates a UV/O_3 system at 950 gpm waste water treatment plant for the removal of trichloroethylene (TCE) and perchloroethylene (PCE), which are common and persistent ground water pollutants (3). Trade names such as Rayox^R, Ultrox^R, and Purox-pure^R are rapidly becoming industry standards (4).

Nonetheless, despite extensive study, there is a general lack of consistent data reporting, field experience, and long term operation necessary for the complete performance and economic evaluation of UV/oxidation systems and comparision to other AOT's and to conventional technologies. Many bench-scale, controlled experiments have

---

[1] Although gas-phase application may prove to be more competitive, thus far practical experience with gas-phase treatment is very limited.

been done to determine the mechanisms and reaction parameters for certain target pollutants. However, these findings cannot be directly extrapolated to real waste streams containing mixed pollutants and varying reaction solution conditions (pH, dissolved CO_2, humic acids, etc.). Commercial systems lack detailed and controlled studies regarding optimal performance and operating conditions.

The goal of this paper is to review the science and engineering underlying UV AOT's for the purpose of understanding the factors affecting the energy efficiencies, which have a direct impact on both the capital and operating costs of the system. Bases for technical performance and economic comparison between the various UV AOT's and conventional technologies are also explored. Most of the current practical application of UV AOT's has been for water treatment. Therefore, this review and analysis will focus on the treatment of aqueous-phase waste streams.

Conventional Pollution Control Technologies

There are three commonly used pollution control technologies employed for cleaning aqueous waste streams. These are air stripping, carbon adsorption, and biochemical treatment. The former treatment methods are nondestructive and sometimes require additional stream treatment such as incineration or thermal catalytic oxidation to destroy recovered contaminants. Cleaning of gas-phase waste streams is generally accomplished using carbon adsorption, incineration, or thermal catalytic oxidation. Because most of the current UV AOT systems have been designed for aqueous waste stream remediation, review of the more conventional technologies will be restricted to air stripping, carbon adsorption, and biochemcial treatment.

Air Stripping. Air stripping is used for the nondestructive removal of volatile organic compounds (VOC's) from an aqueous waste stream. It involves the transfer of volatile organics from an aqueous waste stream into an air stream by greatly increasing the air/water

contact area and taking advantage of the very high vapor pressures of VOC's. Typical aeration methods include packed towers, diffusers, trays, and sprays.

This technology is well established and widely understood. The critical thermodynamic data for many common VOC's are known. Air stripping systems can be accurately designed from theory and experience without the need for design tests. If air emissions are not regulated, air stripping is by far the simplest and most inexpensive solution for the removal of VOC's from aqueous waste streams. Because the VOC's are not destroyed in the transfer process, they may be recovered and reused with a corresponding materials cost savings.

However, air stripping also has several drawbacks. In a packed tower system, the packing material is susceptible to inorganic iron (e.g., $Fe(OH)_3$) and biological fouling, which can significantly increase operating and maintenance costs. For compounds that are only semi-volatile, the treatment efficiency is greatly reduced requiring much larger systems. Because this process is nondestructive, off-gas treatment of the recovered VOC's may be necessary if air emissions are regulated. These requirements will add to the system's complexity and capital and operating costs. The use of an air stripping system is limited to waste streams that contain only VOC's. Other contaminants in the waste stream would have to be removed by other methods.

Activated Carbon. Activated carbon involves the transfer of contaminants from the aqueous (or air) phase to a solid phase. The contaminated stream is passed through a bed of highly porous carbon referred to as granulated activated carbon (GAC). Contaminants collect and adhere to the carbon surface as a result of weak Van der Waals forces. Activated carbon adsorbs essentially all organics vapors with molecular weights above about 45. The amount of carbon needed for a specific application varies depending on contaminant concentration, sorption characteristics, and processing capacity, which affects capital and operating costs. Once the carbon bed is spent, determined by the breakthrough

of a contaminant, it must be disposed of or regenerated. Non-hazardous spent carbon can be inexpensively land-filled. If the spent carbon contains regulated contaminants, disposal is generally accomplished by incineration. Regeneration of the spent carbon enables recovery and reuse of the adsorbed contaminants, such as solvents, and/or the GAC. Regeneration is achieved by thermal heating of the GAC to drive off the adsorbed contaminants into an air stream. The air stream can then be incinerated or treated for contaminant recovery.

Again, this technology is well established and understood. Operation is usually simple and unmanned. Carbon adsorption can economically treat a wide variety of contaminants at low concentration. The capital cost of a GAC system is almost always less than UV/oxidation systems for the same flowrate (5).

GAC regeneration/replacement and eventual organic recovery or disposal are the primary operating cost factors. The regeneration/replacement costs for carbon are relatively high making long term operating costs of a carbon adsorption system unattractive. Aqueous-phase application of GAC is susceptible to water matrix problems such as high iron, high chemical oxygen demand (COD), and biological fouling. Carbon adsorption becomes unattractive as the contaminant concentration in a waste stream becomes high and the carbon usage and regeneration/replacement rate increases. Compounds adsorb to the carbon in varying degrees. Some compounds such as vinyl chloride, chloroform, and 1,4-dioxane do not adsorb efficiently at any concentration and would require removal by other means. Carbon adsorption, thus, becomes impractical for streams containing poor adsorbers.

Biological Oxidation. Fixed-film bioreactors such as rotating biological contactors and trickling filters use a microbial population attached to an inert support to aerobically or anaerobically digest organic matter as an energy source and to produce new cells.

Biological treatment has been used for decades at waste water treatment facilities. However, this technology is not as well established or has not been widely used for the destruction of chemical pollutants. Nonetheless, it is considered the most effective process for efficiently treating biological oxygen demand (BOD) concentrations in the hundreds of ppm.

There are many drawbacks to using biochemical oxidation as a treatment technology. In most microbial systems, the target compound cannot be treated to the low concentrations often required by emission standards. Complete removal of a contaminant and its intermediates is not guaranteed. Many chemical compounds are toxic to the microbes or are resistant to microbial degradation because the microbes do not have the enzymatic capability to breakdown these compounds. Metal contaminants may also be toxic to the microbes. The complete remediation or removal of a contaminant(s) may take place over long periods of time, extending to months and years. In addition, skilled operators are usually required to startup, run, and maintain the system. The systems are complex and easily upset by variations in flow or water quality. Extensive bench- and pilot-scale testing is required for the design of a system for a specific treatment application. Stripping of volatile organics from the waste stream is likely due to aeration requirements which would necessitate implementation of a VOC recovery/destruction system. Solid residuals from the resulting sludge may require treatment and/or hazardous disposal. These drawbacks will add to the development, capital, and operating costs of this treatment system.

Advanced Oxidation Processes

Advanced oxidation processes have been defined broadly as those aqueous-phase chemical processes whose mechanism involves primarily active radical species, typically the hydroxyl radical (•OH), leading to the complete destruction of the target pollutant. Some AOP's can also be applied to gas-phase waste streams such as UV photolysis,

UV/ozone, and UV/photocatalysis. Unlike conventional treatment technologies, oxidation of a pollutant, generally an organic molecule, such as acetone, or a halogenated hydrocarbon, such as PCB (polychlorinated biphenyl), will lead to the complete mineralization of that compound, eliminating the need for further treatment or disposal. Mineralization refers to the conversion of a compound to CO_2 and H_2O and, possibly a residual inorganic salt or acid, such as HCl. The following equation represents a generalized oxidation process:

chlorinated organic molecule $\rightarrow \xrightarrow{O_2/\bullet OH} \rightarrow$ oxygenated intermediates $\rightarrow \xrightarrow{O_2/\bullet OH} \rightarrow CO_2 + H_2O + Cl^-$ (1)

The hydroxyl radical is one of the most powerful oxidizing agents after molecular fluorine. Table 1 lists common oxidants and their oxidation potentials (6). Hydroxyl radical reacts with substrates either via H-atom abstraction or direct electron transfer as follows:

$$\bullet OH + RH \rightarrow R\bullet + H_2O \quad (2)$$

$$\bullet OH + RX \rightarrow RX^{\bullet +} + OH^- \quad (3)$$

where RH is a generic hydrocarbon compound and X is a halogen substituent such as Cl. In the presence of oxygen, these reactions (Eqs. 2 and 3) will initiate a sequence of thermal reactions involving R• and peroxyl radicals, $RO_2^{\bullet}$, that eventually lead to complete mineralization of the organic species as follows:

$$C_xH_yCl_x + (x + \frac{y-z}{4})O_2 \rightarrow xCO_2 + zH^+ + zCl^- + \frac{(y-z)}{2}H_2O \quad (4)$$

UV / Ozone - Hydorgen Peroxide - Photocatalyst. In advanced oxidation processes hydroxyl radicals are produced by the photolysis of hydrogen peroxide, H_2O_2 (Eq. 5), by the conversion of ozone (O_3) to hydrogen peroxide and finally to •OH (Eq. 6), and by the oxidation of an adsorbed OH^- species (or H_2O) on a solid photocatalytic surface, such as titanium dioxide (TiO_2) ($>Ti^{IV}OH$)

$$H_2O_2 \xrightarrow{h\nu\ (\lambda<300nm)} \bullet OH + OH^- \quad (5)$$

$$O_3 \xrightarrow{h\nu\ (\lambda<310nm)} O_2 + O(^1D) \quad (6a)$$

$$O(^1D) + H_2O \rightarrow H_2O_2 \quad (6b)$$

$$H_2O_2 + H_2O \rightarrow HO_2^- + H_3O^+ \quad (6c)$$

$$HO_2^- + O_3 \rightarrow O_3^- + HO_2^\bullet \quad (6d)$$

$$O_3^- + \rightarrow H_3O^\bullet + OH^- \quad (6e)$$

$$H_3O^\bullet \rightarrow \bullet OH + O_2 \quad (6f)$$

$$> TiO_2 \xrightarrow{h\nu\ (\lambda<375nm)} h_{vb}^+ + e_{cb}^- \quad (7a)$$

$$> Ti^{IV}OH \rightarrow \{> Ti^{IV}OH\bullet\}^+ \quad (7b)$$

The above reactions represent the basis for UV/H_2O_2 (Eq. 5), UV/O_3 (Eq. 6), and UV/TiO_2 (Eq. 7), advanced oxidation processes, respectively. In addition, any combination of H_2O_2, O_3, and TiO_2 can also be used.

Fenton Reagent-Catalyst. An alternative advanced oxidation process uses a Fenton reagent that can be regenerated with light. Traditionally, a Fenton reagent is a mixture of a transition-metal ion, typically ferric ion (Fe^{2+}), and hydrogen peroxide. The metal ion can be oxidized by H_2O_2 to produce •OH:

$$Fe^{2+} + H_2O_2 \rightarrow Fe^{3+} + \bullet OH + OH^- \quad (8)$$

Although no light is required, once oxidized, the metal ion is spent. If the decontamination reaction has not proceeded to mineralization of the target compound, then more reagent needs to be added. Ferrioxalate complexes can also be used where Fe(II) is regenerated using light as follows:

$$Fe(II)(C_2O_4^-) + H_2O_2 \rightarrow Fe(III)(C_2O_4^-) + \bullet OH + OH^- \quad (9)$$

ferrioxalate

$$Fe(III)(C_2O_4^-) \xrightarrow{h\nu<500nm} Fe(II)(C_2O_4^-) \quad (10)$$

This process has two advantages over the typical Fenton reagent process: 1) no additional reagent needs to be added to complete elimination of the target compound; and 2) the Fenton catalyst can absorb photons into the visible spectrum, thus utilizing a greater fraction of emitted photons from a lamp source for the production of •OH. This process can also utilize 18% of the solar spectrum as opposed to only 4% for the UV/TiO_2 process and 0% for other AOP's.

VUV Photolysis. Another advanced oxidation process uses high energy photons, vacuum ultraviolet, VUV, ($\lambda < 250$ nm) to photolyze directly a target pollutant. That is, a compound can absorb a photon of sufficient energy, become excited and susceptible to degradation. The rate of photolysis of a compound is generally higher at shorter, higher-energy wavelengths. Most UV/VUV lamps emit photons with specific wavelengths, or emission lines, as will be discussed later. Thus, the complete mineralization of a target compound(s) is not necessarily guaranteed since intermediates produced from the photolysis of a target pollutant may have different absorption spectra not overlapping that emitted by the radiation source. Wavelengths below 200 nm will be absorbed by the water, also creating reactive radical species. Ozone or hydrogen peroxide may be added to the system to complement the direct photolysis reactions. Lamps are currently being developed that emit over a broader spectrum in the VUV region which is critical for the practical use of this type of AOP.

Quantum Efficiency. The overall energy efficiency of an AOT is dependent on the efficiency of the UV source in producing useful photons and the efficiency of the photons in producing reactive species which will ultimately destroy a target contaminant. The efficiency, or quantum efficiency, $\phi(\lambda)$, of a chemical reaction is dependent on the photon wavelengths delivered. The quantum efficiency is defined as the ratio of the amount of product produced to the amount of photons absorbed by the reactive species (H_2O_2, O_3,

TiO_2). The product can be the •OH radical produced or the contaminant molecule destroyed. In many cases, the amount of photons absorbed by the reactive species cannot be measured. In this case, the photon flux into the system is used as an upper bound. For every photon absorbed by the oxidant or photocatalyst, only a fraction result in the production of a hydroxyl radical, or, ultimately, the destruction of a contaminant molecule. As the wavelength of incident radiation decreases, the absorbed energy and ϕ increase. Table 2 shows the aqueous-phase extinction coefficients, ε, for hydrogen peroxide, ozone, and the Fenton catalyst for a photon wavelength of 254 nm (4.9 eV) and the corresponding ϕ for the conversion to •OH. The extinction coefficient is a measure of the degree to which the species will absorb a photon of a given energy. The 254 nm wavelength represents the emission line from a typical low pressure mercury lamp often used in UV oxidation systems. While hydrogen peroxide and ozone both absorb at wavelengths below 330 nm, H_2O_2's molar absorptivity is much less at 254 nm. Figure 1 gives the gas-phase absorption spectra for H_2O_2, O_3, H_2O, and O_2 (7). Below about 200 nm, most of the photons will be absorbed by H_2O and O_2 within a few micrometers of water. The extinction coefficients for these components are slightly higher in the aqueous-phase than in the gas-phase. Below 210 nm, the absorptivity of H_2O_2 matches that of O_3.

For the photocatalytic process, Matthews et al. (8) found that the shorter wavelength, 254 nm compared to 350 nm, is considerably more effective in promoting degradation of salicylic acid and phenol. In addition, the optimum rate occurred with a lower catalyst loading than that required at 350 nm.

Table 3 gives the useful spectrum for the various advanced oxidation processes. For a given energy output, the number of photons varies as a function of the photon energy. For example, for a lamp intensity of 100 eV, twenty-250 nm, twenty-five-310 nm, thirty-one-385 nm, or forty-500 nm photons could be generated. The most efficient scenario would appear to be to produce forty-500 nm photons for use in the UV/Fenton

reagent-catalyst process assuming a quantum efficiency of unity. However, the reaction systems are complex and the quantum efficiency is a function of wavelength, generally increasing for lower wavelengths, and the oxidant used, as seen in Table 2.

The chemical makeup of a contaminated stream also plays a role in the overall reaction rates and efficiencies for all the above processes, while general aqueous system parameters such as the pH, ionic strength, the concentration of UV absorbing or •OH-scavenging species can greatly increase or decrease the reaction rates and efficiencies. These parameters can be adjusted in a pretreatment process to optimize the efficiencies.

UV Radiation Sources

The capital and annual operating costs of any AOT system is a strong function of the electrical power requirement for achieving the desired destruction and removal efficiency. The choice of the UV light source plays a major role in costing the system's equipment and operation. There are several factors in determining what constitutes the most energy and cost-efficient UV light source. They include the capital cost of the lamp and power source, the lamp lifetime, conversion efficiency from electrical to useful-photon energy, and spectral output. Generally, lamp efficiency is measured in terms of a "wall efficiency" which is the conversion efficiency from rated input power (e.g., 1000 W) to total photon flux output.

In photochemical systems, the rate of the reaction is proportional to the photon flux absorbed by the primary chromophore (e.g., the photocatalyst) multiplied by the overall reaction quantum efficiency, $\phi(\lambda)$ (9). Both the absorbed power (photons flux) and the reaction(s) quantum efficiency are wavelength dependent. Therefore, in order to maximize the reaction rate, and hence, the system's efficiency, the spectral output of the lamp should match the absorbance spectrum of the reacting species as closely as possible. Most organic compounds, as well as H_2O_2, absorb more strongly at lower wavelengths. Figure 2 shows the aqueous-phase absorption spectrum for selected organic pollutants (7). Note

that the absorbance spectra of these compounds lies between 200 and 300 nm. Thus, it is desirable to have a UV lamp whose spectral output is predominantly 200-300 nm. Wavelengths below 200 nm will be absorbed by the water, also creating reactive radical species.

There are five types of UV sources that are currently available for use in AOT systems. The are low-pressure (LPML) and medium-pressure mercury lamps (MPML), xenon arc lamps, pulsed xenon flashlamps, and medium-pressure, doped lamps. The emission spectrums for these lamps are plotted in Figs. 3a, 3b and 3c (4, 10, 11).

Mercury Vapor Lamps. Mercury vapor lamps are widely used and accepted by industry and consumers. LPML's have many advantages over other UV sources. They typically operate at ~10^{-2} torr and 40°C. Approximately 80% percent of the output is centered about 254 nm (Fig. 3a) with wall efficiencies of 40^{+}% depending on lamp type and age. That is, 40% of the power drawn from the wall is converted into useful photon flux. These lamps have long lifetimes of up to 10,000 hours and are relatively low cost, about $30 per lamp plus $45 for a ballast. The major disadvantage of these lamps is their low power output requiring large numbers of lamps to treat reasonable capacities. Their nominal power rating is limited to less than 150 W. This increases the size of a treatment system, adding to the capital cost, and also the operating costs due to lamp replacement costs.

Medium-pressure mercury lamps operate with more mercury than the low pressure lamps. As a result, their pressures and temperatures are higher, 400-600°C. However, the operating power ranges are also higher, from 0.1-60 kW, with correspondingly high power output ranges. These lamps emit over a broader spectrum, from 230-400 nm, Figs. 3abc, but the average wavelength emitted is 350 nm rather than 254 nm (12). Wall efficiencies of 5-20%, for the 200-300 nm range, lamp lifetimes of 3,000-4,000 hours, and costs of $100-150 per lamp are typical. The lower wall efficiencies and higher average

wavelength mean higher operating costs. Also, the higher operating temperatures require the addition of a cooling system. Nonetheless, systems employing MPML's can be more compact due to the higher output power which may reduce the capital and lamp replacement costs.

Medium-pressure mercury lamps contain dopants, such as iodides and magnesium, to increase the number of UV lines in the deep UV region, and operate at higher power densities than conventional medium-pressure lamps. Power ratings can range from 1 to 60 kW. Operating temperatures range from 700-1000°C, requiring a cooling system. These lamps also emit strongly below 250 nm (Fig. 3a) and are reported to have wall efficiencies of up to 30% and lifetimes of greater than 3000 hours. The doped lamps are only slightly more costly than their undoped, medium-pressure counterparts, at about $150-200 per lamp and 10^3 for the power supply. Thus, they have the efficiency advantages of the low-pressure lamps while also having the power and spectral advantages of the medium-pressure mercury and xenon flash lamps (vide infra). Although, currently, there are no regulations controlling the disposal of mercury lamps, the possibility of a future cost-of-disposal of the mercury-containing lamps should be considered.

Xenon Lamps. Xenon arc lamps have also been used as a UV radiation source. They are generally used in bench-scale studies and for analytical purposes. Due to their lower power output in the useful wavelength region (Fig. 3b), lower wall efficiencies, shorter lifetimes, and higher capital costs (e.g., $7,000), they are currently not competitive for use in commercial AOT systems.

Pulsed xenon flashlamps increase the amount of UV light generated by increasing the current density which greatly enhances the plasma temperature to about 15,000 K. Thus, a black body emission spectrum results (Fig. 3c), that is, a broader spectrum in the UV region. Theoretically, 28% of the output in the 200-300 nm range is achievable. Practically, only wall efficiencies of 18% have been obtained. Compared to the mercury

lamps, more of the output spectrum lies below 240 nm. Hydrogen peroxide has a much higher absorption efficiency below this wavelength, thus reducing the amount required for equivalent treatment. Nonetheless, the lifetimes for these flashlamps range from only 50-500 hours; and the lamps cost $3000 rendering them impractical for commercial AOT systems.

As the output power capabilities for all these UV sources increase, so does the cooling requirement. The cooling units require ultra pure water to avoid corrosion problems that will shorten the lamp life, and they add to the overall capital costs.

Solar Radiation. UV waste treatment systems utilitzing the sun have many potential applications including the treatment of industrial waste ponds, leachate runoffs from toxic dumps, agricultural runoffs, and wastes from off-shore drilling rigs. A representative solar spectral irradiance distribution is plotted in Fig. 3d (13). Less than 5% of the light is in the UV region, <400 nm. Both the UV/TiO_2 and UV/Fenton reagent-catalyst processes can utilize some portion of the solar spectrum, 4% and 18%, respectively. H_2O_2 does not absorb above 300 nm and O_3 only weakly.

The cost of solar UV radiation is dependent on the cost of the collector and the land area needed for solar radiation collection. It is high if solar collectors/concentrators are used, due to equipment costs and possible solar tracking requirements, and lower if existing *in situ* collectors such as on-site waste treatment ponds are employed. The capital cost of a solar collector has been estimated at about $200/$m^2$ based on an average cost for a domestic water solar heater and additional circulation equipment costs (13). Theoretically, since the UV/Fenton reagent-catalyst process can utilize a greater portion of the solar spectrum than UV/TiO_2, less collection area is needed for the same treatment capacity, hence, lowering the cost of the solar radiation source. Currently, solar-sourced UV systems based on TiO_2 have been found to be too costly relative to artificial-sourced UV systems.

Technical Comparison of AOT's

The AOT's discussed above employ a chemical process requiring UV radiation for the production of •OH. The engineering challenge posed by AOT's is to generate these radicals as efficiently and inexpensively as possible. Although it is by no means clear how best to do this, these AOT's have emerged and are in various stages of marketing. One issue is how best to generate the •OH and to identify the relative advantages and disadvantages of each method. The UV(VUV)/peroxide, ozone, and Fenton reagent-catalyst processes produce •OH from the decomposition of added or generated H_2O_2. The UV/TiO_2 process produces •OH from the conversion of an absorbed photon into an oxidizing species, h^+_{vb}, within the photocatalyst particle which oxidizes a surface OH or a surface-sorbed H_2O molecule to form a surface-bound •OH. This section will explore the relative process advantages and disadvantages.

The energy efficiency, and, hence, economic efficiency, of a particular AOT system is a function of the reaction system and the reactor design. Among AOT's, reaction parameters inherent to a particular reaction system may favor one AOT over others for a particular treatment application. These parameters include the photon absorption efficiency of the oxidant (H_2O_2 or O_3) or photocatalyst, the conversion efficiency from an absorbed photon to the production of a hydroxyl radical (quantum yield, $\phi_{\bullet OH}$), the reaction efficiency of the hydroxyl radical with the target compound, the presence of light absorbing species or hydroxyl radical scavengers in the reaction solution such as humic acids found in natural waters and dissolved CO_2, and the pH and ionic strength of the reaction solution which may affect the above parameters. The energy efficiency is also dependent on the reactor design, which may affect the mass transport limitations (i.e., mixing of the hydroxyl radicals with the target compound), contribute to the scattering or unproductive absorption of light, and affect the efficiency of UV radiation distribution. Furthermore, the

choice of a UV source and proper system maintenance will also affect the system's energy efficiency.

In discussing the main advantages and disadvantages of each AOT, the assumed delivered photon spectrum will be based on the current lamp technology being used in commercial units. These lamps are low to medium pressure, undoped and doped mercury fluorescent and arc lamps whose emission lines are around 185/254 nm and 185/220/254/>300 nm, respectively. Wall power efficiencies for these lamps are about 30-40%.

UV/O3. Due to the much higher absorption efficiency of ozone in the 200-300 nm region (Fig. 1), the UV/O_3 process is more efficient at producing •OH radicals on a per photon basis for these photon wavelengths. In addition to the photolytic production of H_2O_2 and, eventually, •OH from O_3 (Eq. 6a and b), ozone itself can react in dark reactions with the conjugate base of peroxide, HO_2^- (Eq. 6c), to form •OH (6d-f), and directly with the organic pollutant(s) ($O_3 + R \rightarrow RO_3 \rightarrow$ products), thus enhancing the degradation power of ozone. The reaction rate constants for direct reaction of O_3 and •OH with categories of selected organics are given in Table 4; note that the O_3 oxidation rate constants are much smaller than those for •OH. The UV/O_3 process can also be used for gas-phase waste-stream treatment.

Despite its high photon utilization and •OH generation efficiency there are several drawbacks to the use of ozone. It is highly corrosive requiring the use of stainless steel piping, fittings, and reactor vessels. Ozone is a regulated air pollutant which requires the post-process recovery or destruction of ozone in the reactor off-gas. These requirements in addition to an air preparation and ozone generator systems will add substantially to the capital costs. Ozone has a very low solubility in water compared to peroxide resulting in possible mass transfer limitations. For an 8%(v/v) air or oxygen/ozone mix, O_3 solubility is about 36 mgL^{-1} whereas H_2O_2 is miscible with water. These limitations may be

mitigated by efficient diffuser designs. Generally, ozone cannot be stored due to a short half-life and must be produced on-site which increases the electrical power requirements of the system. The generation of ozone often represents about half of both the capital and operating costs of the AOT (14).

UV/H_2O_2. Hydrogen peroxide is an economical, readily available, and easily handled oxidant. Hydroxyl radicals are generated with high quantum and electrical efficiencies (15). Although peroxide is typically 25-35% more expensive per pound than ozone, it is miscible in water and does not require any special equipment or extra operating costs for addition. It is not persistent in the treated stream and, therefore, does not require any post-process destruction. In fact, due to its low molar extinction coefficient at 254 nm, a large excess of peroxide, relative to stoichiometric concentrations, is needed in the reaction solution to generate sufficient hydroxyl radicals for the complete mineralization of a target pollutant which adds to the operating costs. Nonetheless, its lower optical density allows for easy distribution of light throughout the reaction volume reducing the mixing requirements relative to UV/O_3 and UV/TiO_2 systems.

For certain applications UV/O_3 treatment will be superior than UV/H_2O_2, and vice versa (16-20). For other applications, a hybrid UV/O_3 and H_2O_2 have been found to be more efficient both chemically and economically (21-23).

UV/TiO_2. The UV photocatalytic process has several unique characteristics compared to other AOP's. Photocatalysts such as TiO_2 can absorb photons at wavelengths into the near UV (e.g., $\lambda < 385$ nm). This means that the system can utilize a greater portion of the lamp output than UV/H_2O_2 and UV/O_3 processes. Furthermore, it can utilize 4% of the solar spectrum allowing for application in areas where sunlight is an efficient UV radiation source and/or where electrical power is not readily available or economically feasible. In addition, metals such as chromium (24-26), copper (27, 28), and mercury (26, 29, 30) can be removed via a reduction and plating process from aqueous-phase waste streams which is

unique among the UV/oxidation processes (5). UV photocatalysis can also be used for treatment of gas-phase waste streams for which UV/O_3, carbon absorption, incineration, and catalytic oxidation are also competing technologies. Unlike these other processes, though, the activated photocatalyst can effect both oxidation and reduction reactions. Thus, contaminants that are not amenable to oxidation by O_3 and H_2O_2 can be reduced by the photocatalyst. Unlike O_3 and H_2O_2, TiO_2, which has been found to be highly photocatalytically active, is inexpensive, easy to handle, robust, and environmentally benign.

The main disadvantage of the UV/photocatalyst process is that it is much less efficient than other AOP's at converting electrical power into hydroxyl radicals despite enhanced light absorption at the higher wavelengths compared to O_3 ($\lambda < 300$ nm) and H_2O_2 ($\lambda < 254$ nm). Photochemical quantum efficiencies, ϕ, (i.e., the moles of pollutant converted per moles of photons absorbed) are also correspondinly low, ~1-10% for semiconductor photocatalysts compared to 100% for H_2O_2 and 50% for O_3 (21). Furthermore, ϕ is inversely dependent on the absorbed light intensity (i.e., as the light intensity increases ϕ decreases). On the other hand, the rate of radical production and, hence, degradation rate, is proportional to the light intensity. Thus, in order to effect timely degradation, based on current reactor designs, the system needs to be operated at high light intensities in a regime where the photocatalyst is less efficient. Finally, although catalyst poisoning and deactivation is a concern, TiO_2 has been found to be long-lived and fairly resistant to poisoning. Ongoing work to enhance photocatalyst quantum efficiencies by metal ion doping (31-33), metal loading (34-36), improved electron acceptors (37, 38), periodic illumination (39, 40), the use of additional oxidants (41-46), and reducing charge carrier recombination and interfacial transfer times (47-49) continues to improve the competitiveness of this process.

Practical application of photocatalytic oxidation often requires the immobilization of the photocatalyst in the reactor that allows continued use of the photocatalyst by eliminating the need for post-process filtration and resuspension. Immobilization of the photocatalyst can lead to a mass transfer limited reaction, although these mass transfer limitations can be mitigated by efficient reactor designs. No large scale, long term operating experience exists for the UV/photocatalysis process and its proper evaluation is difficult.

UV/Fenton Reagent-Catalyst. This process has similar advantages as the UV/TiO_2 process. The Fenton reagent-catalyst is readily available and easily synthesized, although Solarchem has specific rights to the use of the ferrioxalate-H_2O_2 Fenton reagent-catalyst in AOT systems (4). Only a small amount of catalyst addition is required, 5-10 ppm. The enhanced absorption spectrum, <500 nm, and much greater molar absorptivities of the catalyst allow for greater utilization of the output UV radiation than the UV/H_2O_2, UV/O_3, UV/TiO_2 AOT's. It can utilize 18% of the solar spectrum which reduces the solar collection area required relative to the UV/TiO_2 process. Because of the enhanced absorption spectrum and molar absorptivities of the catalyst, the process can be applied to the treatment of waters containing light absorbing species, which may scavenge photons below 300 nm, and high contaminant concentrations. Because the catalyst can be photo-regenerated, no further catalyst addition during treatment is necessary. In general, this system has all the advantages of the UV/H_2O_2 system as well as a lower H_2O_2 requirement, and a lower power requirement due to the higher photon-utilization efficiencies.

In order to prevent the decomposition of the ferrioxalate during its oxidation, the reaction solution must be adjusted to a pH range between 2 and 4. Depending on the influent waste stream, pretreatment may be required with the additional cost of the added acid. The catalyst cannot be recovered from the treated stream and, therefore, fresh catalyst must be added to each process stream/batch. Because Solarchem has the patent rights

(ENOX 910TM), the Fenton reagent-catalyst cost represents about 30% of the operating cost of the system (50). Solarchem suggests that a greater than doubling of the reaction rate compared to other AOT systems is required to offset the cost of the Fenton reagent-catalyst (4).

Factors Affecting UV/Oxiation Treatment. Each of the UV AOT's relies on the ability of UV radiation to produce active radical species *in situ*.. This process can be inhibited by many factors inherent in a particular contaminated water matrix. The waste stream must be characterized to assess the extent of these inhibitors and to determine the degree of pretreatment required and interference expected. Both pretreatment requirements and reductions in treatment efficiency will add to the cost of UV AOT treatment. Table 5 lists conditions and species to be characterized, the nature of the interference, and possible pretreatment requirements (4).

Economic Comparison of AOT's

UV Source. The primary purpose of the UV radiation is the production of •OH. However, there are several factors to be considered in determining the overall economic efficiency of a particular UV source for an AOT system: the energy efficiency of useful photon production, the energy efficiency of •OH production and the capital and operating costs including initial lamp and power source cost, lamp maintenance and replacement costs and frequency, and cooling system requirements. A lamp that is very efficient at producing useful photons or •OH is not necessarily the most economical lamp to use. The practicality of these calculations and estimations depends on the availability of the lamp's spectral data and the process reaction efficiency data. If these data are not available, then a more empirical approach would need to be used, as will be discussed in the next section.

There are two phases in determining the economic efficiency of a UV source. The first phase is estimating the energy efficiency of •OH generation assuming the AOT and

reaction system is the same for each UV source. The second phase involves the capital and operating costs of utilizing a particular UV source.

The first step in determining the energy efficiency of •OH generation is to calculate the rate of useful photon production (moles per hour), $\Psi_{photons}$:

$$\Psi_{photons} = (hcN)^{-1} \int_{\lambda_{min}}^{\lambda_{max}} p(\lambda)\lambda d\lambda \quad (11)$$

where h is Planck's constant; c is the speed of light; N is Avagadro's number; λ is the photon wavelength (nm^{-1}); $p(\lambda)$ is the lamp's power output function at each wavelength ($W\ nm^{-1}$). The lamp efficiency, η_{lamp}, is given by:

$$\eta_{lamp} = \frac{\int_{\lambda_{min}}^{\lambda_{max}} p(\lambda)d\lambda}{P} \quad (12)$$

where P is the input power from the wall (W). The useful photon range, λ_{min} to λ_{max}, is defined by the AOP to be used. η_{lamp} gives the most elementary base for comparison, that is, the lamp's useful photon production efficiency. The lamp efficiency provided by the manufacturer does not always reflect the useful photon production efficiency but can be used if spectral data are not available:

$$\Psi_{photons} = (hcN)^{-1} \eta_{manuf} P \quad (13)$$

In calculating the capital and operating costs for an AOT system, it is necessary to determine the UV flux needed to achieve the required level of decontamination. The destruction capacity for a single lamp is first determined. The •OH generation rate (moles/hour), $\Psi_{\bullet OH}$, is calculated based on the quantum efficiency of •OH production, $\phi_{\bullet OH}$, for a particular AOT, H_2O_2 (0.5), O_3 (0.6), or TiO_2:

$$\Psi_{\bullet OH} = \Psi_{photons} \times \phi_{\bullet OH}$$

The number of lamps required for removal of a particular contaminant, i, n_i, is a function of the contaminant concentration and its reaction efficiency with •OH, $\phi_{i\bullet OH}$, and the AOP to be used which gives $\Psi_{\bullet OH}$:

$$n_i = \frac{Q_i}{\Psi_{\bullet OH} \times \phi_{i\bullet OH} + \sum_{j}^{m} r_{ji}} \qquad (14)$$

where Q_i is the molar flow rate of the contaminant and $\sum_j r_{ji}$ are the combined rates of other destructive contaminant removal processes, j, such as photolysis. At this point, the capital and operating costs of the UV source for the AOT system can be calculated and compared to other lamps.

AOT. The overall cost of an AOT system is based on the system's capital and operating costs. These costs vary proportionately as a function of the capacity of the system. Once the capacity requirements are known, it is usually straightforward to calculate the capital costs. The operating costs are strongly a function of the lamp replacement costs and energy requirements, often representing up to half of the total operating costs (5). As discussed above, reaction efficiency and lamp spectral data are often necessary in determining the size of the AOT system needed for achieving the required level of decontamination. For many applications, these data are not available, are only known for specific conditions, or are not constant. In addition, many waste streams contain multiple contaminants with changing composition. Without a large matrix of data, performance assessment of an AOT system across applications becomes difficult, and across AOT systems becomes impossible. It is, therefore, desirable to develop a "figure of merit" convention for bench and pilot-scale studies and operation of full-scale systems that is independent of such variables as reaction efficiencies and conditions, UV source and emission spectrum, reactor design, etc.

Previous attempts have been made to employ figures-of-merit to quantify a system's effectiveness including: the cost to achieve the desired level of decontamination (e.g., 99%) per volume of air or water treated, the cost to remove a given quantity of contaminant, the energy use per quantity of contaminant removed, the energy use per volume of water treated, and the ratio of the change in TOC to the energy consumed, etc.

(51). Although each of these performance variables is a function of easily measurable variables, they are system-specific. That is, the values for each reaction system can be compared within the same AOT system. However, it is meaningless to compare the values across AOT's. These performance variables are useful for optimization of a reaction system in an AOT, but not for performance and economic comparison.

A "figure-of-merit" has been introduced[2] that allows for the practical comparison of AOT's and can be incorporated into economic evaluations for comparison with other technologies. It is also useful for scale-up analysis of bench and pilot-scale systems. This figure-of-merit has been labeled "electrical energy per order," or EEO. EEO is defined as the electrical energy required to reduce the concentration of a pollutant by one order of magnitude in 1000 U.S. gal. of water:

Batch Operation:
$$EEO = \frac{\alpha \times P \times t}{V \times \log\left[C_o / C_f\right]} \tag{15a}$$

Continuous Operation:
$$EEO = \frac{\alpha \times P \times t}{Q \times \log\left[C_o / C_f\right]} \tag{15b}$$

where α is a constant for unit conversion; t is irradiation time; V is the batch volume treated; C_o and C_f are the pollutant initial and final concentrations, respectively; P is the lamp wall power; and Q is the influent volumetric flowrate. The EEO is a function of easily measurable parameters and is independent of lamp spectral output and reactor scaling, which makes it widely applicable. Reaction conditions and efficiencies are inherent in the $\log\left[C_o / C_f\right]$ term. The only limitation is that it is only valid if first-order kinetics for the reaction(s) hold, which means that every decade in reduction of a compound, for example, from 100 to 1 mM, requires the same treatment time and energy. Generally, the rate constants for reaction with •OH of most organics have similar order of magnitude values, as shown in Table 4. And the reaction rates *are* typically first order in

---

[2] This concept was introduced by Keith Bircher of Solarchem Environmental Systems of Markham, Ontario, Canada.

substrate assuming [•OH] is not rate-limiting. The EEO can be related to the first-order rate constant, k, by:

Batch Operation:
$$EEO = \frac{\beta P}{V \times k} \quad (16)$$

where β is a unit conversion constant.

Variations of EEO may be used compare different performance goals such as reduction in total organic carbon, (TOC), COD, biological oxygen demand (BOD), or toxicity. EEO's for various compounds should be measured under the optimal reaction conditions for a compound or waste stream and are unique to an AOT system. Within an AOT system, the EEO can be used for optimization of a particular waste stream. The EEO can also be used to estimate the total cost of a system for a specific application for comparison across optimized AOT systems and conventional technologies.

The EEO measured for a contaminant in a design test is specific to the waste stream sample. The destruction of trichloroethene (TCE), perchloroethene (PCE), and vinyl chloride in 1000 gallons of water as a function of power usage for a UV/H_2O_2 system is shown in Fig. 4a (52). Destruction over several decades is a linear function of the power used indicating first-order kinetics. The compounds' EEO is the slope of the respective curves. In this AOT system, TCE is more refractory, or resistant to degradation, than DCE which is more refractory than vinyl chloride. Figure 4b shows the destruction efficiency of N-nitrosodimethylamine (NDMA) for two initial concentrations, 3 and 30 ppb, for another AOT system (UV/photolysis) (52). Note that the EEO (slope of data) is independent of the initial concentration. Table 6 lists the EEO's for a range of hydrocarbon contaminants for an UV/H_2O_2 system (53).

EEO is specific to each AOT system and reaction system. Each remediation case must be evaluated separately unless prior experience has been established. EEO can be used throughout the evaluation process to optimize and to compare a system relative to itself, to other AOT systems, and to conventional technologies. A design test for a

contaminated water sample is conducted and an optimized EEO for each UV/oxidation system is determined. Optimization is achieved for a given water sample by adjusting the AOT system's operating parameters and reaction conditions (pH, ionic strength, dissolved CO_2 content, etc.) until a minimum EEO is obtained. EEO can be used initially to screen the viability of UV/oxidation treatment. EEO values above a threshold level will probably become recognized as uneconomical for AOT treatment without the need for pilot-scale evaluation. EEO values within a set range may be deemed suitable for further assessment and testing before a final decision is made. Design tests resulting in very low EE/O's can readily be approved for AOT treatment. Following a full economic analysis which would include capital investment and operating costs, one particular AOT system may emerge superior over the other designs. This final result can then be compared to estimates for a conventional system. Over time, a data base of optimized conditions, critical parameters, and operational experience will streamline and economize this process. More efficient designs will be developed to compete with existing systems, and bench-scale studies of new AOT's can immediately be assessed for potential viability.

System costing using EEO. The EEO for a particular application can be used to estimate the size of the AOT system and, hence, the capital and operating costs. The size is determined by the total UV dosage needed to achieve a desired level of decontamination:

$$\text{UV Power (kW)} = \gamma \times \text{EEO} \times \log\left(C_{\text{initial}}/C_{\text{final}}\right) \times \text{Flowrate} \qquad (17)$$

where γ is a unit conversion constant and $\text{EEO} \times \log\left(C_{\text{initial}}/C_{\text{final}}\right)$ is the UV dosage required per 1000 gal. treated. If the waste stream contains more than one contaminant, the UV dosage for each contaminant should be estimated. The highest UV dosage requirement is then used to calculate the UV power requirement. This method assumes that the •OH-generation mechanism is not a rate-limiting step.

The operating costs include system power, lamp-replacement, and oxidant addition costs. Lamp-replacement costs are generally 40-50% of the electrical costs (21). Therefore, the operating costs can be estimated as:

$$\text{Operating Costs } (\$/1000 \text{ gal.}) = 1.5 \times \text{electrical costs} + \text{oxidant costs} \quad (18)$$

where the electrical costs are:

$$\text{Electrical Costs } (\$/1000 \text{ gal.}) = \text{UV Dose} \times \text{Power Cost } (\$/\text{kWh}) \quad (19)$$

The capital costs are directly related to the size of the system which is a function of the UV power requirement. For a given system, an array of capital costs can be determined as a function of the size of the treatment system. An example of how the capital costs of a system scale with the power requirement is illustrated in Fig. 5 (14). As can be seen from Eq. 17, the total UV power is proportional to the flowrate and the decades of reduction in contaminant concentration. Once the total costs of an AOT system are characterized for an array of treatment applications, it can be compared to other AOT systems and conventional technologies.

Full Economic Analysis. Once the size and energy requirements of the AOT system have been established, a full economic analysis of the treatment system can be made. This analysis includes assessment of the initial capital investment and the annual operating cost, both direct and indirect costs. Table 7 is an example of a breakdown of these costs for a UV/TiO_2 system (12) based on the costing method of van der Vaart, et al. (54). Note that for a UV/oxidant system or a hybrid system (UV/oxidant-TiO_2), chemical delivery system, storage, maintenance, and chemical costs would be included.

Comparison with conventional technologies. AOT's have a distinct advantage for certain applications where conventional technologies do not perform well. Since AOT's are based on similar chemistry, they are, as a group, likely to be either economically favorable or unfavorable for a particular treatment application compared to the conventional

technologies. The AOTs' advantages lie in the ability to mineralize, nonspecifically, most contaminants in a single process, to treat a wide range of contaminant concentrations and water matrices, to treat both gas and aqueous-phase waste streams, and to provide on-site treatment of a waste stream. The initial capital investment for AOT's is generally high but long term operating expenses tend to out-compete air stripping, incineration, and carbon absorption. Glaze (3) projected the costs of several advanced oxidation process technologies such as UV/H_2O_2 and ozone/H_2O_2, as a function of contaminant concentration as compared to incineration and super critical water oxidation (SCWO) (see Fig. 6). In this analysis, UV/H_2O_2 and ozone/H_2O_2 were shown to be more favorable than either incineration or SCWO. Other economic analyses of AOT systems report favorable comparisons to carbon adsorption and incineration for certain applications (5, 12-14, 55-57).

Example. As an example, combined carbon absorption and air stripping will be compared to AOT's. Carbon absorption in conjunction with air stripping can be used to achieve the complete destruction of an aqueous-phase contaminant. The critical properties for a contaminant to be amenable to air stripping and carbon adsorption are its tendency for vapor-phase partitioning (large Henry's Law coefficient > 10^2 atm/mole fraction) and affinity for carbon absorption (Freundlich adsorption isotherm > 50 mg/g carbon at 1 ppm), respectively. Figure 7 shows an array of organic compounds, listed in Table 8, relative to their ability to be air-stripped and/or carbon adsorbed (4). From a purely mechanistic evaluation, compounds in region 5-9 can be effectively treated using carbon adsorption and/or air stripping. Compounds in region 1 are clearly candidates for AOT treatment. Compounds in Region 2-4 are application-specific requiring sample testing of waste streams to determine process competitiveness. Other non-mechanistic factors such as air emission regulations necessitating off-gas treatment, waste streams with high contaminant concentrations requiring large amounts GAC and regeneration treatment,

pretreatment requirements that may drive up the capital and operating costs, and handling and disposal concerns associated with concentrating contaminant onto the carbon bed will alter the ultimate applicability of AOT's to a particular waste stream problem.

Table 9 compares the economics for an UV/H_2O_2 versus aqueous-phase carbon adsorption for a range of contaminants and concentrations (53). This data is shown graphically in Fig. 8 (53). In general,

- The incremental unit operating costs for UV/oxidation treatment for increasing influent contaminant concentrations is lower than that for carbon adsorption. At concentrations greater than about 50 ppm, carbon absorption becomes uneconomical for even good absorbers.
- UV/oxidation treatment costs are almost always less for poor carbon adsorbers independent of concentration.
- An application-specific treatment analysis needs to be done for average carbon absorbers.
- The capital investment for UV/oxidation treatment is typically 2 to 3 times that for carbon adsorption. Long term treatment requirements favor UV/oxidation where the cumulative savings in operating costs offset the higher capital expense.
- For scale-up and determination of treatability, each of the processes require bench-top feasibility tests on the water to be treated.

Conclusion

AOT's are the latest development in the field of waste stream remediation. With the exception of photolysis, these processes have been developed and studied over several decades. At this stage, there exist few conventions and standards and little practical and commercial experience. However, as with most evolving technologies, practical data will accumulate, experience with these technologies will grow, and lamp technology will improve. Thus, efficiencies will be enhanced and costs reduced. AOT's will not be a panacea, but will find their niche in the pantheon of environmental waste remediation solutions.

Literature

(1) Hoffmann, M. R.; Martin, S. T.; Choi, W.; Bahnemann, D. W. *Chem. Rev.* **1995**, *95*, 69-96.

(2) Hackman III, E. E. In *Toxic Organic Chemicals: Destruction and Waste Treatment*; E. E. Hackman III, Eds.; Noyes Data Coporation: Park Ridge, NJ, 1978; p 285-317.

(3) Glaze, W. H. In *Chemical Oxidation: Technology for the Nineties*, Nashville, TN, 1993; pp 1-10.

(4) *The UV/Oxidation Handbook* , Solarchem Environmental Systems, 1994.

(5) Miller, R.; Fox, R. In *Photocatalytic Purification and Treatment of Water and Air: Trace Metals in the Environment*; D. F. O. a. H. Al-Ekabi, Eds.; Elsevier Science Publishers B.V.: Amsterdam, N.V. 1993; p 573-578.

(6) Legrini, E.; Oliveros, E.; Braun, A. M. *Chem. Rev.* **1993**, *93*, 671.

(7) Bolton, J. R.; Cater, S. R. In *Aquatic and Surface Photochemistry*; G. R. Heiz, R. G. Zepp and D. G. Crosby, Eds.; Lewis Publishers: Boca Raton, FL, 1994; p 467-490.

(8) Matthews, R. W.; McEvoy, S. R. *J. Photochem. Photobiol. A: Chem.* **1992**, *66*, 355-366.

(9) Seinfeld, J. H. *Air Pollution: Physical and Chemical Fundamentals*; McGraw-Hill: New York, 1975; p 523.

(10) Wekhof, A. *Env. Prog.* **1991**, *10*, 241-247.

(11) *Oriel Catalog* **1994**, *II*, I-43.

(12) T-Rassi, A., *Cost Analysis of 800 SCFM Full Scale Unit*, Florida Solar Energy Center, USF, **1995**.

(13) Bolton, J. R.; Safarzadeh-Amiri, A.; Cater, S. R. In *Alternative Fuels and the Environment*; F. S. Sterret, Eds.; Lewis Publishers: Boca Raton, FL. 1995; p 187-192.

(14) Aieta, E. M.; Reagan, K. M.; Lang, J. S.; McReynolds, L.; Kang, J. W.; Glaze, W. H. *J. Am. Wat. Wks. Assoc.* **1988**, 64-72.

(15) Pardieck, D. L.; Bouwer, E. J.; Stone, A. T. *J. Contam. Hydrol.* **1992**, *9*, 221-242.

(16) Guittonneau, S.; De Laat, J.; Duguet, J. P.; Bonnel, C.; Dore, M. *Ozone Sci. Eng.* **1990**, *12*, 73.

(17) Akata, A.; Gurol, M. D. *Ozone Sci. Eng.* **1992**, *14*, 367.

(18) Barich, J. T. In *EPA Forum on Innovative Hazardous Waste Treatment Technologies*, 1990.

(19) Lewis, N.; Topudurti, K.; Welshans, G.; Foster, R. *Air Waste Manag. Assoc.* **1990**, *40*, 540-547.

(20) Hager, D. G.; Loven, C. G.; Giggy, C. L. In *AWWA Annual Conference and Exposition*, Orlando, FL.

(21) Venkatadri, R.; Peters, R. W. *Hazardous Waste & Hazardous Materials* **1993**, *10*, 107-149.

(22) Ollis, D. F. *Acs Symposium Series* **1993**, *518*, 18-34.

(23) Scott, J. P.; Ollis, D. F. *Environ. Prog.* **1995**, *14*, 88-103.

(24) Sabate, J.; Anderson, M. A.; Aguado, M. A.; Gimenez, J.; Cerveramarch, S.; Hill, C. G. *J. Mol. Catal.* **1992**, *71*, 57-68.

(25) Aguado, M. A.; Gimenez, J.; Cervera-March, S. *Chem. Eng. Commun.* **1991**, *104*, 71-85.

(26) Prairie, M. R.; Evans, L. R.; Stange, B. M.; Martinez, S. L. *Environ. Sci. Technol.* **1993**, *27*, 1776-1782.

(27) Peral, J.; Domenech, X. *J. Chem. Techn. and Biotechnol.* **1992**, *53*, 93-96.

(28) Foster, N. S.; Noble, R. D.; Koval, C. A. *Environ. Sci. Technol.* **1993**, *27*, 350-356.

(29) Tennakone, K.; Thaminimulle, C. T. K.; Senadeera, S.; Kumarasinghe, A. R. *Photochem. Photobiol. A: Chem.* **1993**, *70*, 193-195.

(30) Serpone, N.; Ah-You, Y. K.; Tran, T. P.; Harris, R.; Pelizzetti, E.; Hidaka, H. *Solar Energy* **1987**, *39*, 491-498.

(31) Martin, S. T.; Morrison, C. L.; Hoffmann, M. R. *J. Phys. Chem.* **1994**, *98*, 13695.

(32) Choi, W.; Termin, A.; Hoffmann, M. R. *J. Phys. Chem.* **1994**, *98*, 13669-13679.

(33) Choi, W.; Termin, A.; Hoffmann, M. R. *Angew. Chem.* **1994**, *106*, 1148-1149.

(34) Harada, K.; Hisanaga, T.; Tanaka, K. *Water Res.* **1990**, *24*, 1415.

(35) Rose, T. L.; Nanjundiah, C. *J. Phys. Chem.* **1985**, *89*, 3766.

(36) Hisanaga, T.; Harada, K.; Tanaka, K. *J. Photochem. Photobiol. A: Chem.* **1990**, *54*, 113.

(37) Choi, W.; Hoffmann, M. R. *Environ. Sci. Technol.* **1995**, *29*, 1646-1654.

(38) Martin, S. T.; Lee, A. T.; Hoffmann, M. R. *Environ. Sci. Technol.* **1995**, *29*, 2567-2573.

(39) Sczechowski, J. G.; Koval, C. A.; Noble, R. D. *J. Photochem. Photobiol. A: Chem.* **1993**, *74*, 273-278.

(40) Sczechowski, J. G.; Koval, C. A.; Noble, R. D. *Abst. Pap. Am. Chem. Soc.* **1993**, *205*, 15.

(41) Tanaka, K.; Hisanaga, T.; Harada, K. *Nouv. J. Chim.* **1989**, *13*, 5.

(42) Pelizzetti, E.; Carlin, V.; Minero, C.; Grätzel, M. *New J. Chem.* **1991**, *15*, 351.

(43) Al-Ekabi, H.; Edwards, G.; Holden, W.; Safaazadeh-Amiri, A.; Story, J. In *Chemical Oxidation*; W. W. Eckenfelder, A. R. Bowers and J. A. Roth, Eds.; Technomic Publishing Company: Lancaster, PA 1992; p 254-261.

(44) Ollis, D. F.; Pelizzetti, E.; Serpone, N. *Environ. Sci. Technol.* **1991**, *25*, 1522-1529.

(45) Hackley, V. A.; Anderson, M. A.; Spooner, S. *J. Matls. Res.* **1992**, *7*, 2555-2571.

(46) Halmann, M. *J. Photochem. Photobiol. A: Chem.* **1992**, *66*, 215.

(47) Martin, S. T.; Herrmann, H.; Choi, W.; Hoffmann, M. R. *J. Chem. Soc. Faraday Trans.* **1994**, *90*, 3315.

(48) Martin, S. T.; Herrmann, H.; Hoffmann, M. R. *J. Chem. Soc. Faraday Trans.* **1994**, *90*, 3323.

(49) Martin, S. T.; Herrmann, H.; Hoffmann, M. R. *Abst. Pap. Am. Chem. Soc.* **1994**, *207*, 344.

(50) Martin, P., September, 1995, personal communication.

(51) Glaze, W. H. In *Advanced Oxidation Technologies for Water and Air Remediation*, London Ontario, Canada, 1994.

(52) Safarzadeh-Amiri, A.; Bolton, J. R.; Buckley, J. A.; Cater, S. R., *Advanced Oxidation and Reduction Technologies for Photodegradation of Organic Pollutants in Waste Streams*, Solarchem Environmental Systems, **1993**.

(53) Notarfonzo, R.; McPhee, W. *Poll. Eng.* **1994**, *26*, 74-76.

(54) van der Vaart, D. R.; Vatavuk, W. M.; Wehe, A. H. *J. Air & Waste Manag. Assoc.* **1991**, *41*, 497.

(55) Prairie, M. R.; Stange, B. M.; Showalter, S. K.; Magrini, K. A. *Environ. Sci. Technol.* **1995**.

(56) McGregor, F. R.; Piscaer, P. J.; Aieta, E. M. *Ozone Sci. Eng.* **1988**, *10*, 339-352.

(57) Topudurti, K. V.; Lewis, N. M.; Hirsh, S. R. *Environ. Prog.* **1993**, *12*, 54-60.

SPECIES	OXIDATION POTENTIAL (V)
Fluorine (F_2)	-3.03
Hydroxyl radical (•OH)	-2.80
Atomic oxygen (O)	-2.42
Ozone (O_3)	-2.07
Hydrogen peroxide (H_2O_2)	-1.78
Perhydroxyl radical ($HO_2^{\bullet}$)	-1.70
Permanganate (MnO_4^-)	-1.68
Hypobromous acid (HOBr)	-1.59
Chlorine dioxide (ClO_2)	-1.57
Hypochlorous acid (HOCl)	-1.49
Hypoiodous acid (HOI)	-1.45
Chlorine (Cl_2)	-1.36
Bromine (Br_2)	-1.09
Iodine (I_2)	-0.54

Table 1. Oxidation Potentials of various chemical species (from Legrini, O.; Oliveros, E.; Braun, A. M. *Chem. Rev.* **1993**, *93*, 671-698).

Oxidant	ε (254 nm) ($M^{-1}cm^{-1}$)	Stoichiometry	ϕ (•OH)
H_2O_2	18.6[a] (190 @ 200nm)[b]	$H_2O_2 \rightarrow 2 \bullet OH$	0.5
O_3	3300[c]	$O_3 \rightarrow 2 \bullet OH$	0.61[d]
$Fe(III)(C_2O_4^-)$	4000 (215 nm) 1800 (300 nm)	$Fe(II)(C_2O_4^-) + H_2O_2 \xrightarrow{hv} \bullet OH + OH + Fe(III)(C_2O_4^-)$	

[a] Glaze, W.H.; Kang, J.W.; Chapin, D.H. *Ozone Sci. Eng.*, **9**, 1987, 335-352.
[b] Bolton, R.J.; Cater, S.R. *Aquatic and Surface Photochemistry* G.R. Heiz, R.G. Zepp and D.G. Crosby, eds., Lewis Publishers, Boca Raton, FL, 1994, pp 467-490.
[c] Dore, M. *Chimie des Oxydants et Traitement des Eaux*; Lavoisier: Paris, 1989.
[d] Taube, H., *Trans. Faraday Soc.*, **53**, 1957, 656.

Table 2. Gas-phase extinction coefficients and the corresponding aqueous-phase quantum efficiencies for the reaction stoichiometry given for hydorgen peroxide, ozone, and the Fenton reagent-catalyst.

AOT Process	Useful Wavelength Spectrum (nm)
UV/H_2O_2	$\lambda < 310$ (4.0 eV)
UV/O_3	$\lambda < 330$ (3.8 eV)
UV/TiO_2	$\lambda < 385$ (3.2 eV)
UV/Fenton catalyst	$\lambda < 500$ (2.5 eV)

Table 3. The useful wavelength spectrums for various UV AOP's.

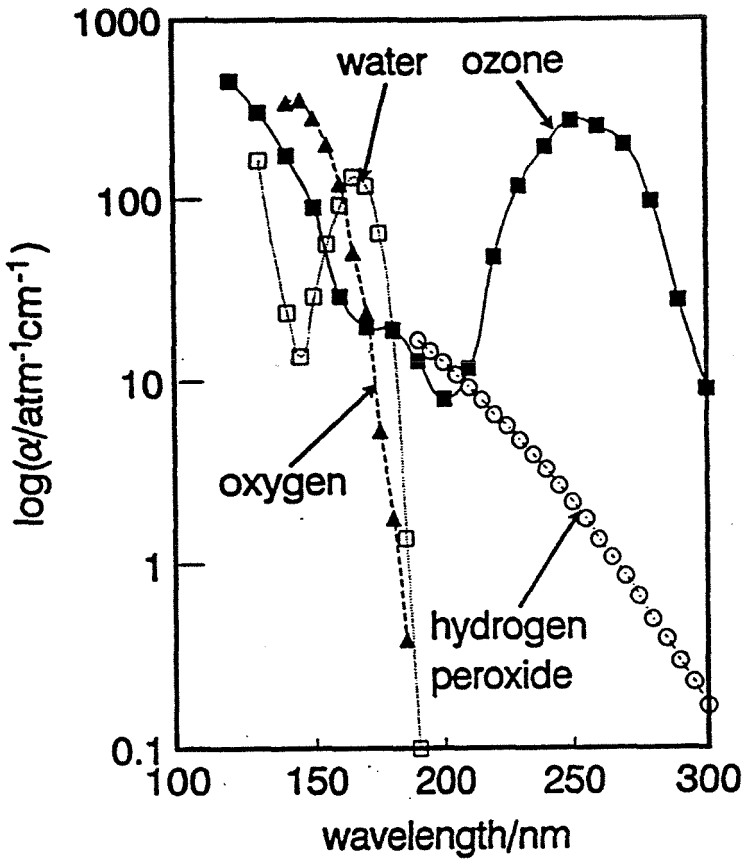

Figure 1. Gas-phase absorption spectra of O_2, H_2O, O_3, and H_2O_2 (reprinted from Bolton, J. R., Cater, S. R. In *Aquatic and Surface Photochemistry* G. R. Heiz; R. G. Zepp; D. G. Crosby, Eds. **1994**, 467-490).

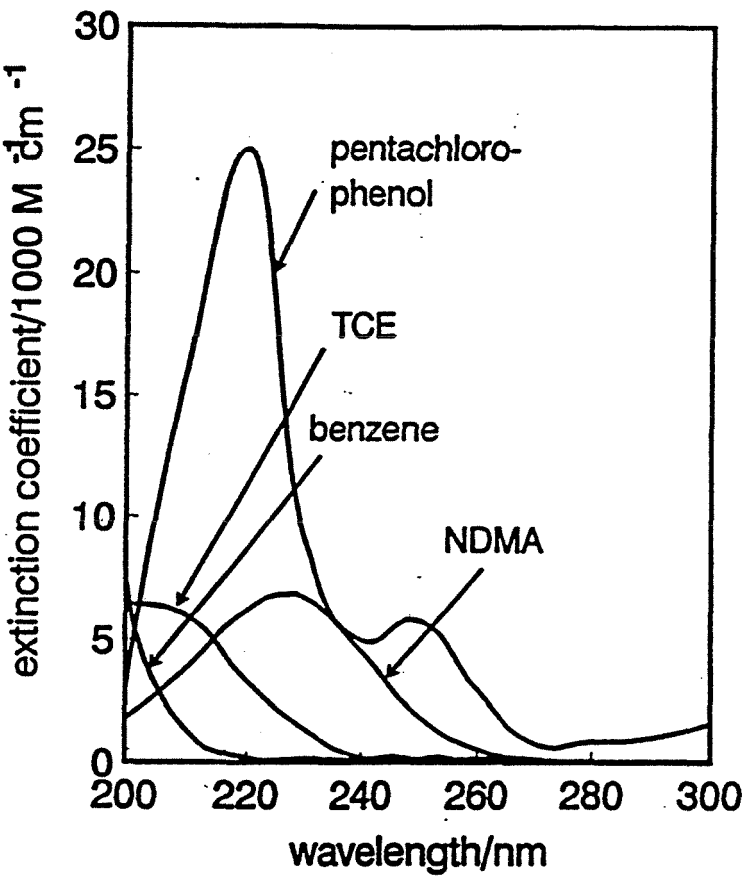

Figure 2. UV spectra of selected organic pollutants (reprinted from Bolton, J. R., Cater, S. R. In *Aquatic and Surface Photochemistry* G. R. Heiz; R. G. Zepp; D. G. Crosby, Eds. **1994**, 467-490).

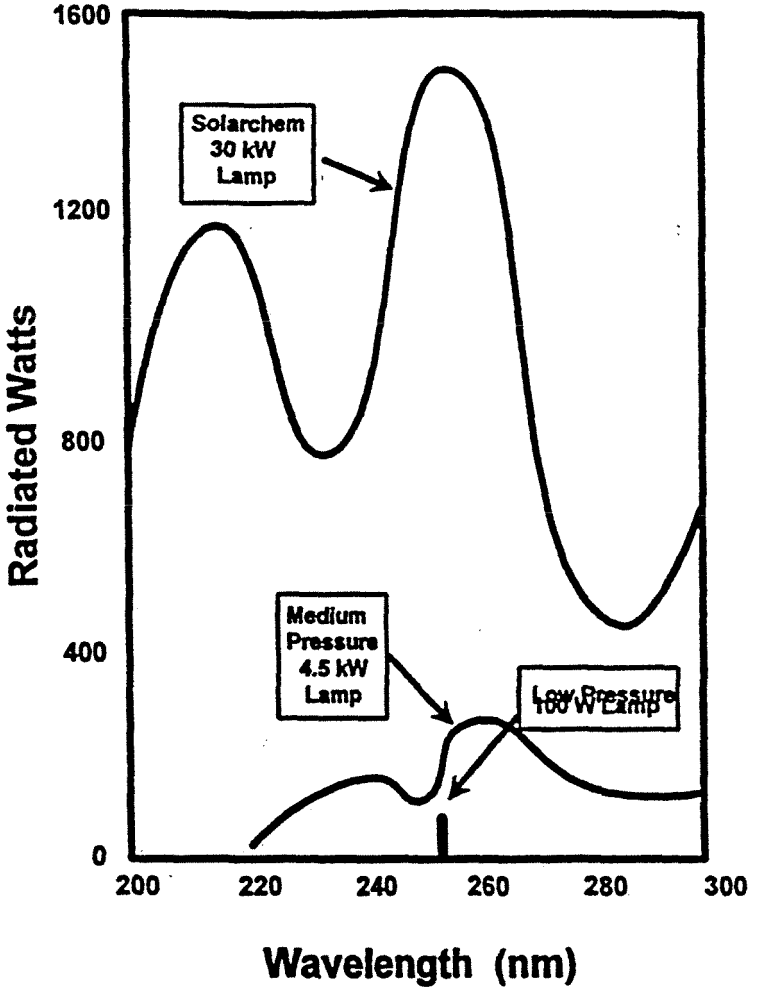

Figure 3a. Power output spectra for LPML (100W), MPML (4.5 kW), and second-generation MPML (30 kW) (reprinted from *The UV/Oxidation Handbook*, Solarchem Environmental Systems, 1994).

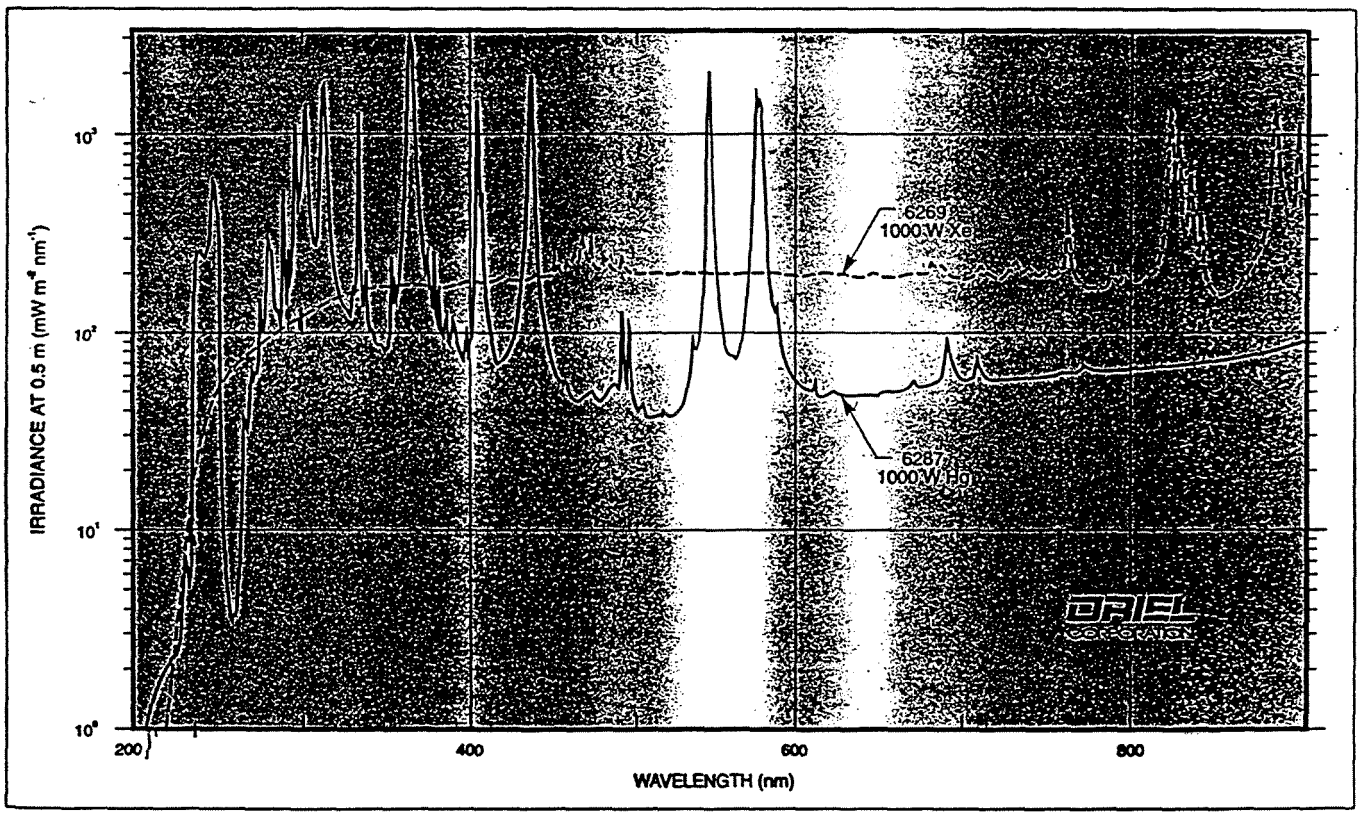

Figure 3b. Power density spectra for xenon arc lamp (kW) and MPML (kW) (reprinted from *Oriel Catalog* 1994 Vol. II, I-43).

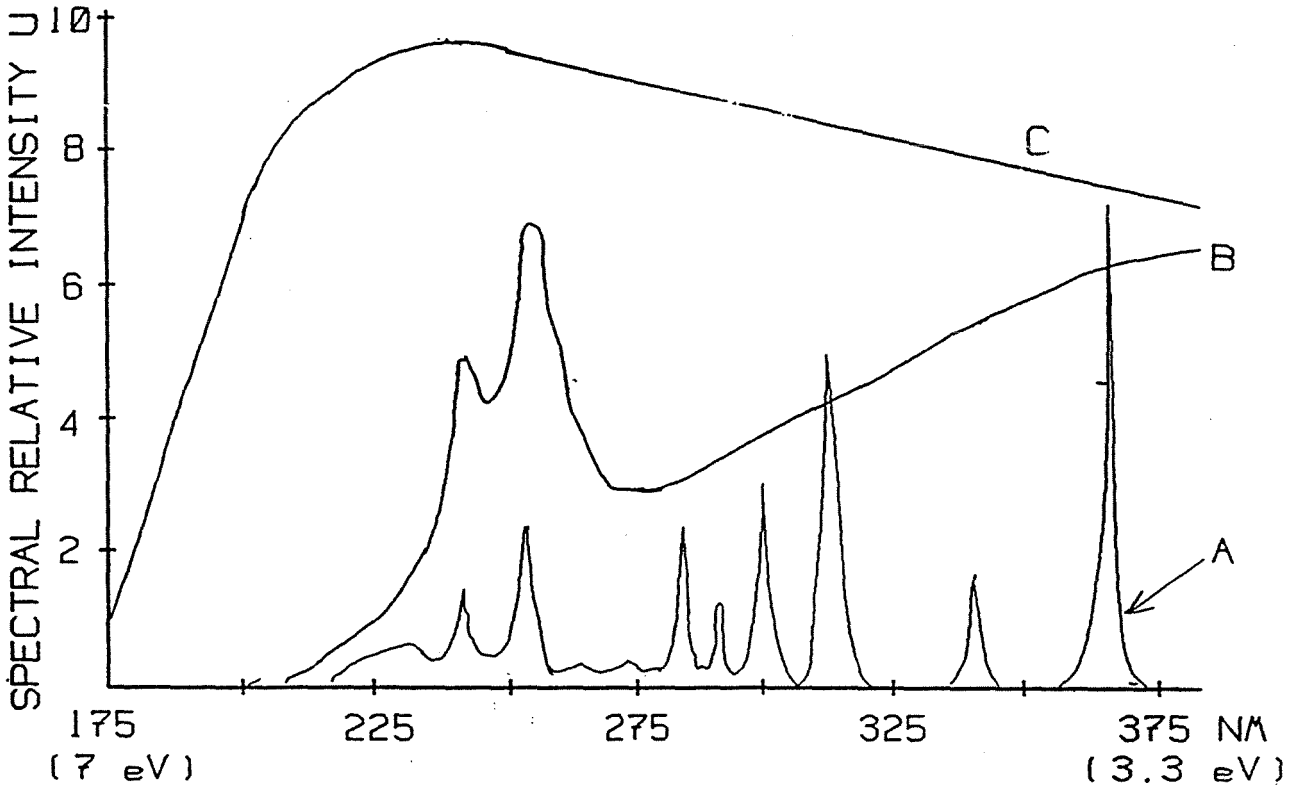

Figure 3c. UV intensity spectra for (A) MPML (60W), (B) xenon flashlamp (8700A/cm^2, 45 J/125 μsec pulse), and (C) second-generation flashlamp, WEKHOF (60W/lamp cm) (reprinted from Wekhof, A. *Env. Prog.* **1991**, *10*, 241-247).

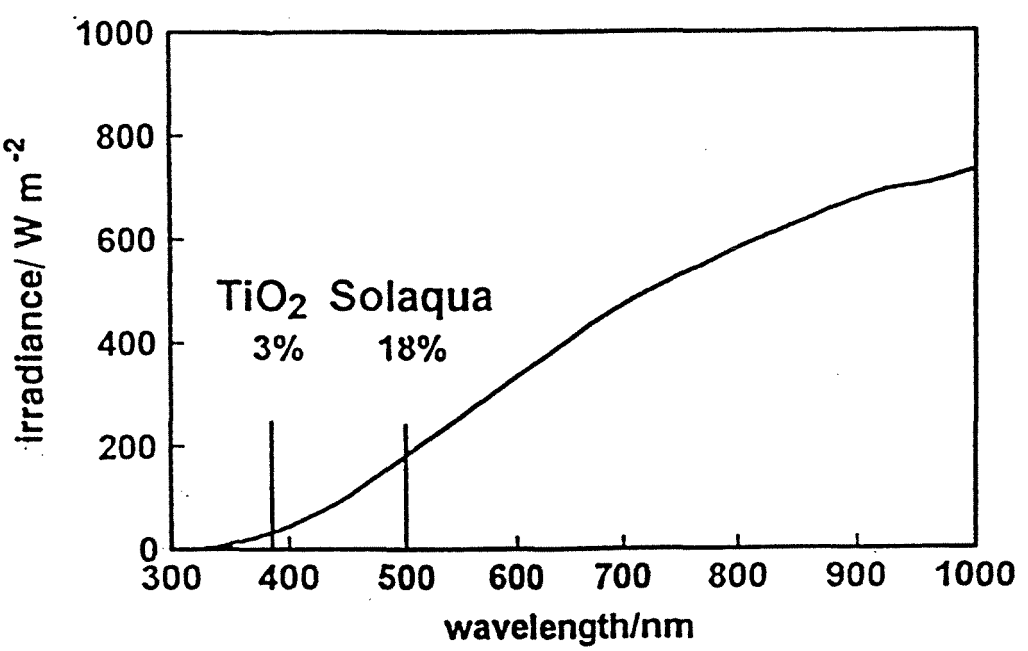

Figure 3d. Integrated solar power density spectra showing absorption capability for TiO_2 and Fenton reagent-catalyst (reprinted from Bolton, J. B.; Safarzahey-Amiri, A.; Cater, S. R. In *Alternative Fuels and the Environment*; F. S. Sterret, Ed.; Lewis Publishers: Boca Raton, FL. 1995; p 187-192).

Compound	O_3 Reaction Rate Constant, k ($M^{-1}s^{-1}$)	•OH Reaction Rate Constant, k ($M^{-1}s^{-1}$)
Chlorinated Alkenes (TCE)	10^{-1} to 10^{3} [a]	10^{9} to 10^{11} [a]
Phenols (4-chlorophenol)	10^{3} [a]	10^{9} to 10^{10} [a]
N-containing Organics	10 to 10^{2} [a]	10^{8} to 10^{10} [a]
Aromatics (benzene, toluene)	1 to 10^{2} [a]	10^{8} to 10^{10} [a]
Ketones (acetone)	1	10^{9} to 10^{10} [a]
Alcohols (isopropanol, methanol)	10^{-2} to 1[a]	10^{8} to 10^{9} [a]
Alkanes (propane, butane)	10^{-2} [a]	10^{6} to 10^{9} [a]
Acetic acid		10^{7} [b]
Methyl cyanide		10^{7} [b]
Ferrocyanide ion		10^{10} [c]
Dichloromethane		10^{7} (pH 10) [b]
Chloroform		10^{6} (pH 5.7) [b]
Chloroacetate		10^{7} (pH 1) [b]

[a] *The UV/Oxidation Handbook*, Solarchem Environmental Systems, 1994.

[b] Bolton, R.J.; Cater, S.R. *Aquatic and Surface Photochemistry* G.R. Heiz, R.G. Zepp, and D.G. Crosby, eds., Lewis Publishers, Boca Raton, FL, 1994, pp. 475.

[c] Buxton, G.V., Greenstock, C.L., Helman, W.P., Ross, A.B., *J. Phys. Chem. Ref. Data*, **17**, 513, 1988.

Table 4. Reaction rate constants for the reaction of selected organic compounds with O_3 and •OH.

Factor Affecting Treatment	Interference	Concentration of Concern	Pretreatment
UV Interferences	Species that unproductively absorb UV radiation and convert it into heat		
Nitrate (NO_3^-)		> 10 ppm	
Nitrite (NO_2^-)		> 10 ppm	
Phosphate (PO_4^{3-})		> 1%	
Chloride ion (Cl^-)		> 1%	
COD		> 100 ppm	
Ferrous ion (Fe^{3+})		> 50 ppm	Positive effect @ ~ 5 ppm and pH ~4
UV absorbance	Waters with high absorbance will have mass transport limitations	0.2-0.5 absorbance units/cm	
•OH Scavengers	Species that readily react with and unproductively consume •OH		
Chloride ion (Cl^-)	low pH: compete w/ •OH corrosion	pH < 4 > 1000 ppm	
Nitrite (NO_2^-)		> 10 ppm	
Alkalinity: Carbonates (HCO_3^- /CO_3^{2-})		pH > 7 for high alkalinity waters > 300 ppm	pH adjustment with acid
Sulfites (SO_4^{2-})		> target contaminant	
Sulfides (S^{2-})		> target contaminant	
Precipitates	Suspended particles formed *in situ* that interfere with UV distribution and adsorb organic contaminants		Filtering (10-30 μm)
Calcium		> 50 ppm	
Ferrous ion		> 50 ppm	
Magnesium		> 1000 ppm	
Other			
pH	Affects reaction efficiency and is AOP-dependent	generally 4 < pH < 9	Adjustment with acid
Suspended solids	Same as precipitates	> 50 ppm	Filtering (10-30 μm)
Oil and grease	Presence increases unproductive UV absorbance and consume •OH		Removal with oil/water separator, clarifier, and or flocculant additive

Table 5. Factors affecting UV/oxidation treatment, threshold concentrations, and possible pretreatment requirements (from *The UV/Oxidation Handbook*, Solarchem Environmental Systems, 1994).

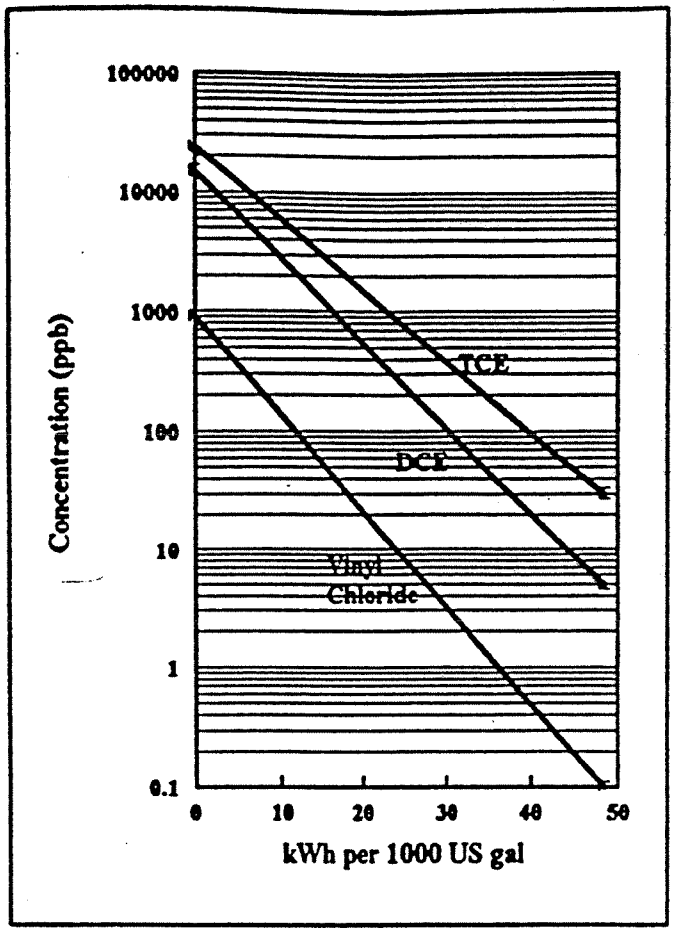

Figure 4a. UV/H_2O_2 treatment of an industrial process water containing VOC's and 100 ppm of iron. Degradation of TCE (25 ppm), DCE (15 ppm) and vinyl chloride (900 ppb) as a function of power usage for treatment of 1000 US gallons of water at varying initial concentrations. Respective EE/O values are determined from the slope of the curves (reprinted from Safarzadeh-Amiri, A.; Bolton, J. B.; Buckley, J. A.; Cater, S. R. *Solarchem Environmental Systems Report* **1993**.)

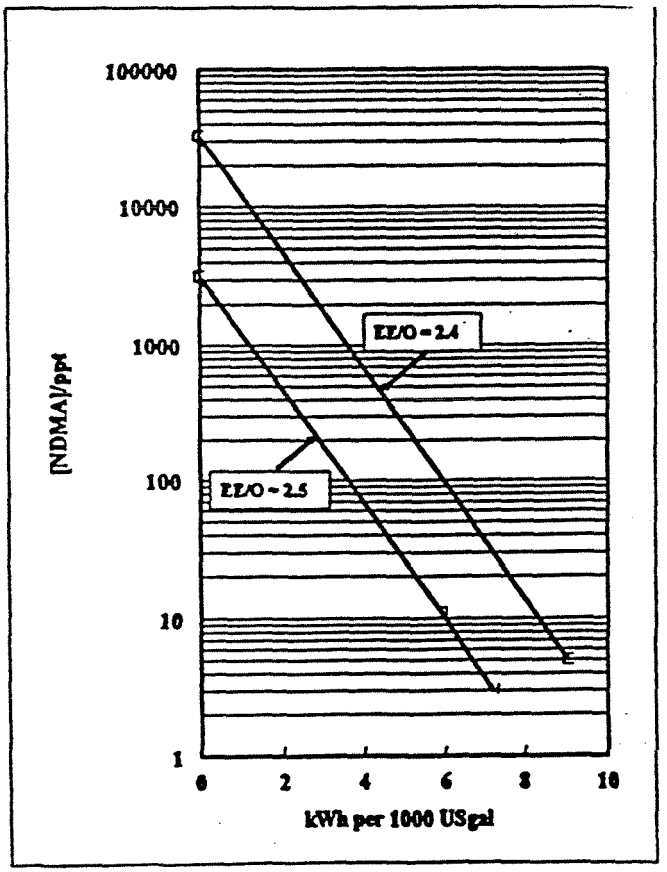

Figure 4b. UV photolysis treatment of ground water containing 3 and 30 ppt of NDMA (reprinted from Safarzadeh-Amiri, A.; Bolton, J.; Buckley, J. A.; Cater, S. R. *Solarchem Environmental Systems Report* **1993**).

Compound	EEO (kWh/1000 US gal/order)
1,4-dioxane	2-6
Atrazine	30
Benzene	2-5
Chlorobenzene	5
Chloroform	15
Dichloroethane (DCA)	15
Dichloroethene (DCE)	2-5
Freon	10
Iron cyanide (FeCN)	40
NDMA	2-5
NDMA	2-3 (UV only)
Perchloroethene (PCE)	3-8
PCP (pentachlorophenol)	10
Phenol	5
Trichloroethene (TCE)	2-4
Toluene	2-5
Xylene	2-5
Trichloroethane (TCA)	15
Trinitrotoluene (TNT)	12
Vinyl Chloride	2-3

Table 6. EE/O values for various hydrocarbon contaminants for an UV/H_2O_2 system (from Notarfonzo, R.; McPhee, W. *Poll. Eng.* **1994**, *26*, 74-76).

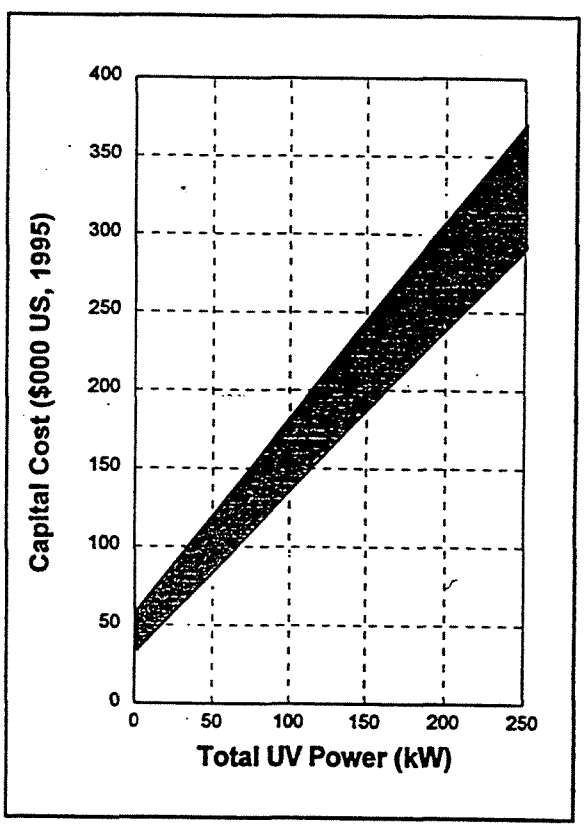

Figure 5. UV/oxidation capital costs as a function of required power capacity (reprinted from Aieta, E. M.; Reagan, K. M.; Lang, J. S.; McReynolds, L.; Kang, J. W.; Glaze, W. H. *J. Am. Wat. Wks. Assoc.*, **1988**, 64-72).

Cost Item	Cost ($)
Direct Costs (DC)	
Equipment costs (EC)	
Lamps (75 @ $30 ea.)	$2,250
Ballast (75 @ $45 ea.)	3,375
Catalyst (10 g)	100
Reaction chamber	17,200
Total	$22,925
Instrumentation, 0.1(EC)	2,293
Sales taxes, 0.03(EC)	688
Freight, 0.05(EC)	1,146
Total EC (TEC)	$27,052
Direct installation costs	
Foundation & supports, 0.08(TEC)	2,164
Handling & erection, 0.14(TEC)	3,787
Electrical, 0.04(TEC)	1,082
Piping, 0.02(TEC)	541
Insulation, 0.01(TEC)	271
Painting, 0.01(TEC)	271
Direct installation cost	$8,116
Total Direct Cost	$35,168
Indirect Costs (installation)	
Engineering, 0.10(TEC)	2,705
Construction & field expenses, 0.05(TEC)	1,353
Contractor fees, 0.10(TEC)	2,705
Start-up, 0.02(TEC)	541
Performance test, 0.01(TEC)	271
Contingencies, 0.03(TEC)	812
Total Indirect Costs	$8,387
Total Capital Investment (TCI)	**$43,555**

Table 7a. Capital Investment for a batch photocatalytic nitroglycerin detoxification system that runs six 1/2 hour batches per day, 360 days per year (from T-Raissi, A. *Cost Analysis of 800 SCFM Full Scale Unit*, Florida Solar Energy Center, USF, **1995**).

Cost Item	Suggested Factor	Unit Cost	Cost ($)
Direct Annual Cost			
Operating labor			
1) Operator	3 hr per day	$13/hr	14,040
2) Supervisor	15% of item #1	-	2,106
Maintenance			
3) Labor	1/2 hr per day	$14.26/hr	2,569
4) Material	100% of item #3	-	2,569
Catalyst replacement	100% of catalyst replaced every 3 yrs	$10/g	35
Lamp replacement	11% of lamps replaced each year	$30/lamp	243
Energy costs	-	$0.059/kWh 3 hr per day	311
Total Direct Costs	-		$21,873
Indirect Annual Costs			
Overhead	60% of sum of items 1-4	-	12,770
Administrative charges	2% of TCI	-	871
Property Taxes	1% of TCI	-	436
Insurance	1% of TCI	-	436
Capital recovery	CRF{TCI-1.08*(catalyst cost)}	-	5,284
Total Indirect Cost			$19,797
Total Annual Cost			**$41,670**

Table 7b. Annual operating costs for a batch photocatalytic detoxification system that runs six 1/2 hour batches per day, 360 days per year (from T-Raissi, A. *Cost Analysis of 800 SCFM Full Scale Unit*, Florida Solar Energy Center, USF, **1995**).

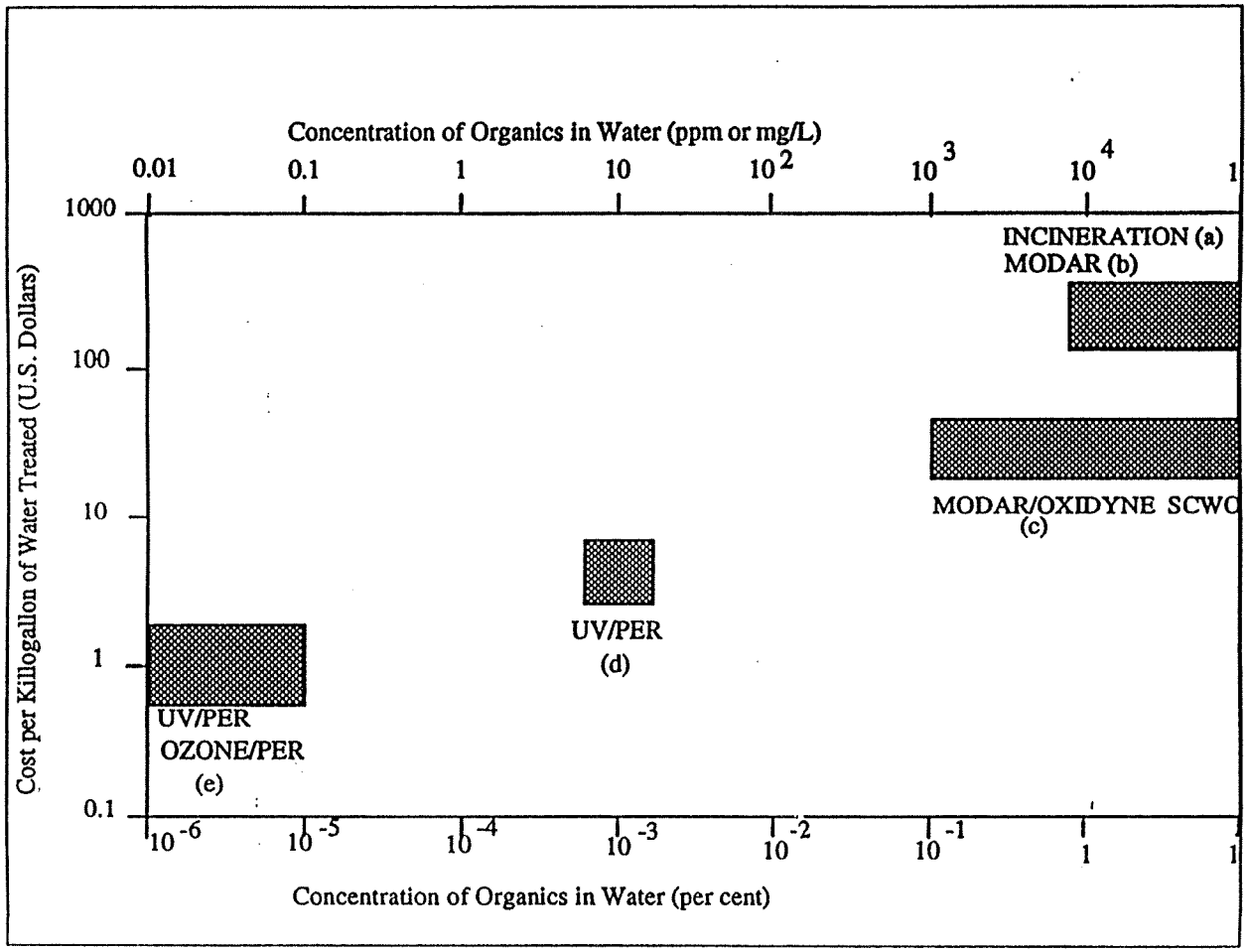

Figure 6. Projected costs of AOP's for aqueous-phase destruction of organic contaminants (reprinted from Glaze, W. H. In *Chemical Oxidation: Technology for the Nineties*, Nashville, TN, 1993; pp 1-10).

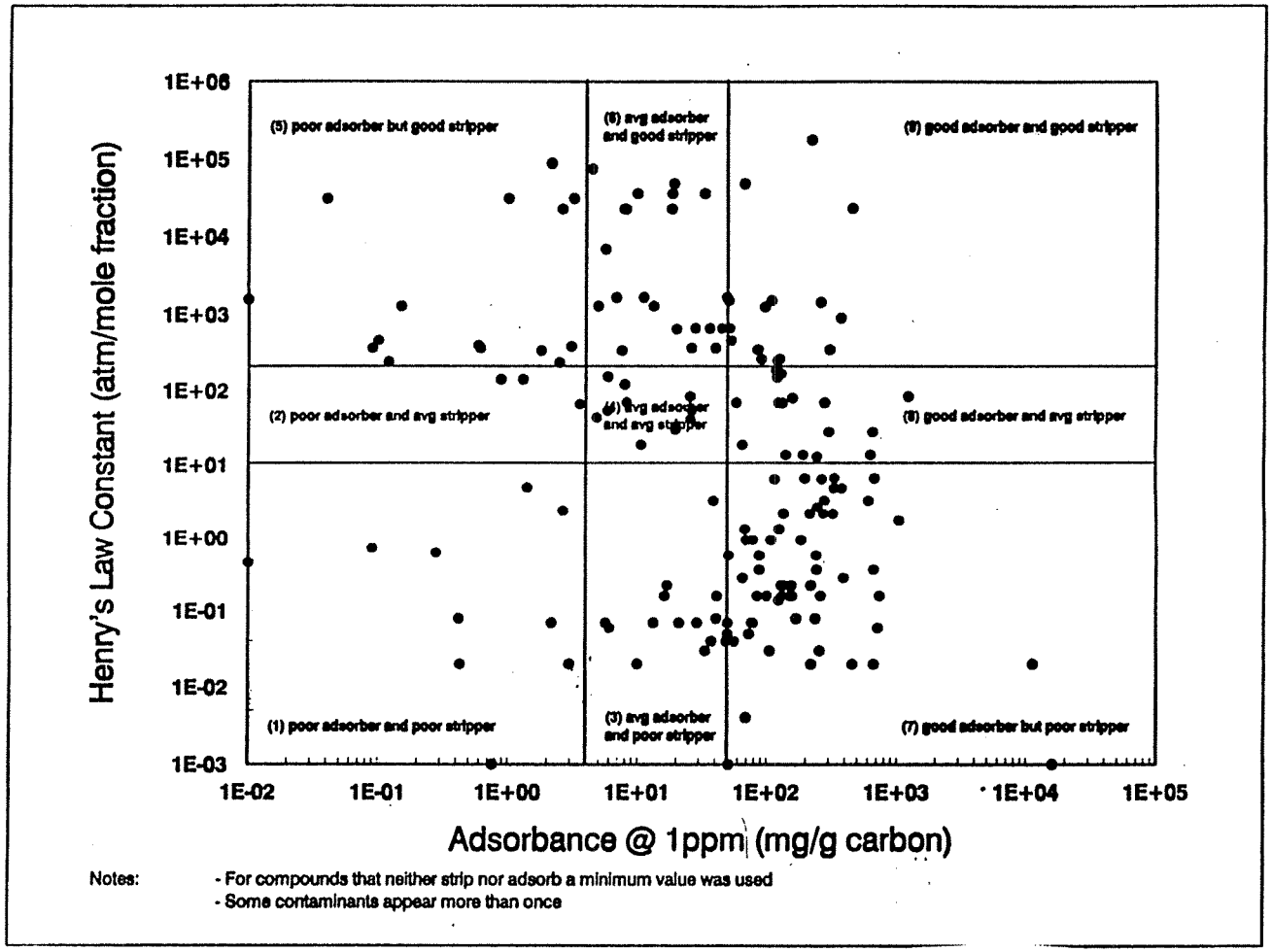

Figure 7. Henry's Law Constants vs. Freundlich Coefficients for compounds listed in Table 8 (reprinted from *The UV/Oxidation Handbook*, Solarchem Environmental Systems, **1994**).

REGION	COMPOUND	k (mg/g carbon)	H (atm/mole fraction)	REGION	COMPOUND	k (mg/g carbon)	H (atm/mole fraction)	REGION	COMPOUND	k (mg/g carbon)	H (atm/mole fraction)
8	ACENAPHTHENE	140.00	13.39	6	DICHLOROETHYLENE,1,1-	0.16	1270.00	8	NAPHTHALENE	123.00	68.27
8	ACENAPHTHENE	190.00	13.39	6	DICHLOROETHYLENE,1,1-	4.91	1270.00	8	NAPHTHALENE	132.00	68.27
8	ACENAPHTHENE	626.00	13.39	5	DICHLOROETHYLENE,1,2-TRANS-	3.05	370.70	8	NAPHTHALENE	277.00	68.27
7	ACENAPHTHYLENE	116.00	6.33	2	DICHLOROMETHANE	0.88	137.60	4	NAPTHALENE	8.18	68.27
7	ACENAPHTHYLENE	266.00	6.33	7	DICHLOROPHENOL,2,4-	85.16	0.16	7	NITROBENZENE	66.00	1.32
1	ACETONE	2.65	2.38	3	DICHLOROPHENOL,2,4-	16.20	0.16	7	NITROBENZENE	124.69	1.32
1	ACRYLONITRILE	1.40	4.89	3	DICHLOROPHENOL,2,4-	41.40	0.16	7	O-CRESOL	50.07	0.05
8	ALDRIN	299.60	27.56	7	DICHLOROPHENOL,2,4-	131.00	0.16	8	P-XYLENE	85.00	336.90
8	ALDRIN	651.00	27.56	7	DICHLOROPHENOL,2,4-	157.00	0.16	8	PCB 1221	242.00	12.61
7	ANTHRACENE	330.00	4.78	4	DICHLOROPROPANE,1,2-	5.86	148.60	7	PENTACHLOROPHENOL	100.00	0.18
7	ANTHRACENE	378.00	4.78	3	DIELDRIN	38.90	3.24	7	PENTACHLOROPHENOL	150.00	0.18
8	BENZENE	0.04	309.00	7	DIELDRIN	277.66	3.24	7	PENTACHLOROPHENOL	260.00	0.18
8	BENZENE	1.00	309.00	7	DIELDRIN	606.00	3.24	7	PENTACHLOROPHENOL	736.67	0.18
8	BENZENE	3.18	309.00	7	DIMETHYLPHENOL,2,4-	78.00	0.94	7	PHENANTHRENE	136.00	2.18
3	BENZO(a)PYRENE	33.60	0.03	7	DIMETHYLPHENOL,2,4-	108.00	0.94	7	PHENANTHRENE	216.00	2.18
1	BENZOIC ACID	0.76	0.00	7	DIMETHYLPHENOL,2,4-	70.00	0.94	7	PHENANTHRENE	273.00	2.18
7	BENZOIC ACID	61.00	0.00	7	DIMETHYLPHENOL,2,4-	184.00	0.94	1	PHENOL	2.17	0.07
7	BHC,gamma-LINDANE	258.00	0.03	3	DINITRO-O-CRESOL,4,6-	41.00	0.08	3	PHENOL	13.30	0.07
1	BIS(2-CHLOROETHYL)ETHER	0.09	0.72	7	DINITRO-O-CRESOL,4,6-	237.00	0.08	3	PHENOL	21.00	0.07
7	BIS(2-ETHYLHEXYL)PHTHALATE	11300.00	0.02	1	DINITRO-o-CRESOL,4,6-	0.42	0.08	3	PHENOL	29.00	0.07
4	BROMOFORM	19.60	29.56	7	DINITRO-o-CRESOL,4,6-	169.00	0.08	3	PHENOL	49.80	0.07
8	CARBON TETRACHLORIDE	6.80	1634.00	3	DINITROPHENOL,2,4-	9.87	0.00	3	PHENOL	80.00	0.07
8	CARBON TETRACHLORIDE	11.10	1634.00	3	DINITROPHENOL,2,4-	18.40	0.00	7	PHENOL	77.40	0.07
8	CARBON TETRACHLORIDE	49.03	1634.00	3	DINITROPHENOL,2,4-	53.00	0.00	7	PHENOL	78.10	0.07
7	CHLORDANE	246.00	2.66	1	DIOXANE,1,4-	1.73	0.00	2	PHENOL PH 11.3	5.68	0.07
7	CHLORO-m-CRESOL,p-	124.00	0.14	7	DIPHENYLHYDRAZINE,1,2-	16000.00	0.00	3	PROPYLPHENOL,4-	19.00	0.47
8	CHLOROBENZENE	81.00	252.10	7	DIPHENYLHYDRAZINE,1,2-	18000.00	0.00	7	PROPYLPHENOL,4-	67.20	0.47
8	CHLOROBENZENE	126.40	252.10	7	ENDRIN	458.50	0.02	7	PYRENE	66.60	0.28
4	CHLORODIBROMOMETHANE	4.80	43.50	7	ENDRIN	668.00	0.02	7	PYRENE	369.00	0.28
8	CHLOROETHANE	0.69	384.40	1	ETHANOL	0.01	0.45	8	STYRENE	120.00	146.30
8	CHLOROFORM	2.60	22620.00	8	ETHYLBENZENE	0.10	448.80	8	TETRACHLOROETHANE,1,1,2,2-	64.98	18.34
8	CHLOROFORM	7.80	22620.00	8	ETHYLBENZENE	83.00	448.80	4	TETRACHLOROETHANE,1,1,2,2-	10.80	18.40
8	CHLOROFORM	8.04	22620.00	7	FLUORANTHENE	88.10	0.36	8	TETRACHLOROETHYLENE	60.80	1492.00
8	CHLOROFORM	18.30	22620.00	7	FLUORANTHENE	242.00	0.36	8	TETRACHLOROETHYLENE	108.17	1492.00
7	CHLOROPHENOL,2-	61.00	0.67	7	FLUORANTHENE	684.00	0.36	8	TOLUENE	0.09	383.10
7	CHLOROPHENOL,2-	68.00	0.67	7	FLUORENE	186.00	8.60	8	TOLUENE	0.61	383.10
7	CHLOROPHENOL,2-	240.00	0.67	7	FLUORENE	330.00	8.60	8	TOLUENE	28.10	383.10
3	CHRYSENE	8.07	0.06	7	FLUORENE	674.00	8.60	8	TOLUENE	40.20	383.10
7	CHRYSENE	718.00	0.06	4	HEPTACHLOR	25.64	82.22	8	TRICHLOROBENZENE,1,2,4-	157.00	78.89
7	CRESOL,2-	73.40	0.05	8	HEPTACHLOR	1220.00	82.22	4	TRICHLOROETHANE	26.58	41.00
3	CRESOL,3-	37.60	0.04	7	HEPTACHLOR EPOXIDE	1040.00	1.78	8	TRICHLOROETHANE,1,1,1-	2.48	226.67
7	CRESOL,3-	68.00	0.04	9	HEXACHLOROBENZENE	460.00	22890.00	4	TRICHLOROETHANE,1,1,2-	8.81	85.37
1	CRESOL,4-	2.98	0.02	9	HEXACHLOROBUTADIENE	268.00	1422.22	4	TRICHLOROETHANE,1,1,2-	28.20	85.37
3	CRESOL,4-	9.97	0.02	9	HEXACHLOROCYCLOPENTADIENE	370.00	888.89	8	TRICHLOROETHYLENE	28.00	648.20
7	DDT,p,p'-	322.00	2.16	9	HEXACHLOROETHANE	96.60	1243.00	8	TRICHLOROETHYLENE	38.30	648.20
1	DI BUTYL PHTHALATE	0.43	0.02	1	HYDROXYBENZOIC ACID,4-	2.14	0.00	8	TRICHLOROETHYLENE	48.00	648.20
7	DI-n-BUTYL PHTHALATE	220.00	0.02	1	ISOPROPANOL	0.28	0.62	8	TRICHLOROETHYLENE	61.82	648.20
7	DIBENZO(a,h)ANTHRACENE	69.30	0.00	7	LINDANE	108.02	0.03	8	TRICHLOROMONOFLUOROMETHANE	5.60	6788.00
8	DICHLOROBENZENE,1,2-	129.00	183.90	3	M-CRESOL	46.87	0.04	3	TRICHLOROPHENOL,2,4,6-	18.95	0.23
8	DICHLOROBENZENE,1,3-	118.00	180.10	6	MERCURY	20.00	633.33	7	TRICHLOROPHENOL,2,4,6-	130.10	0.23
8	DICHLOROBENZENE,1,4-	121.00	240.60	3	METHOXYPHENOL,4-	4.38	0.74	7	TRICHLOROPHENOL,2,4,6-	219.00	0.23
4	DICHLOROBROMOMETHANE	7.90	117.78	2	METHYLENE CHLORIDE	1.30	137.60	7	TRICHLOROPHENOL,2,4,6-	137.00	0.72
6	DICHLOROETHANE,1,1,1-	7.61	328.20	4	METHYLTERBUTYLETHER (MTBE)	4.30	16.3	7	TRICHLOROPHENOL,2,4,6-	188.00	0.23
8	DICHLOROETHANE,1,1-	1.78	328.20	1	N-NITROSODIMETHYLAMINE (NDMA)	0.01	0.00	8	VINYL CHLORIDE	0.01	1844.44
2	DICHLOROETHANE,1,2-	3.87	66.44	7	N-NITROSODIPHENYLAMINE	220.00	0.00	8	XYLENE,o-	0.12	232.50
8	DICHLOROETHYLENE,1,1-	13.26	1270.00	8	NAPHTHALENE	58.00	68.27	8	XYLENE,p-	303.00	336.90

Sources: **EPA RREL Treatability Database and Chemical Engineering (November 1991)**

Table 8. A list of Fruendlich Coefficients and Henry's Law Constants for a range of compounds and the associated treatability region, depicted graphically in Figure 7 (reprinted from *The UV/Oxidation Handbook*, Solarchem Environmental Systems, **1994**).

Contaminant Concentration (ppm)	UV/H_2O_2 ($/1000 gal)	Poor Carbon Adsorbers ($/1000 gal)	Average Carbon Adsorbers ($/1000 gal)	Good Carbon Adsorbers ($/1000 gal)
0.1	$0.5-2.5	>$3	$0.5-3	<$0.5
1	$1.5-4	>$10	$0.7-10	<$0.7
	$2-6	>$50	$1-50	<$1
Typical Contaminants	aromatics, chloroalkenes, nitroaromatics, free/complexed cyanides	vinyl chloride, NDMA, chloroform, TCA, DCA, methylene chloride, 1,4-dioxane	benzene, DCE, phenol, carbon tetrachloride, TCE	lindane, chlordane, xylene, PCE, PCBs

Table 9. Cost comparison for an UV/HO system versus carbon absorption for a range of contaminants and concentrations (from Notarfonzo, R.; McPhee, W. *Poll. Eng.* **1994**, *26*, 74-76).

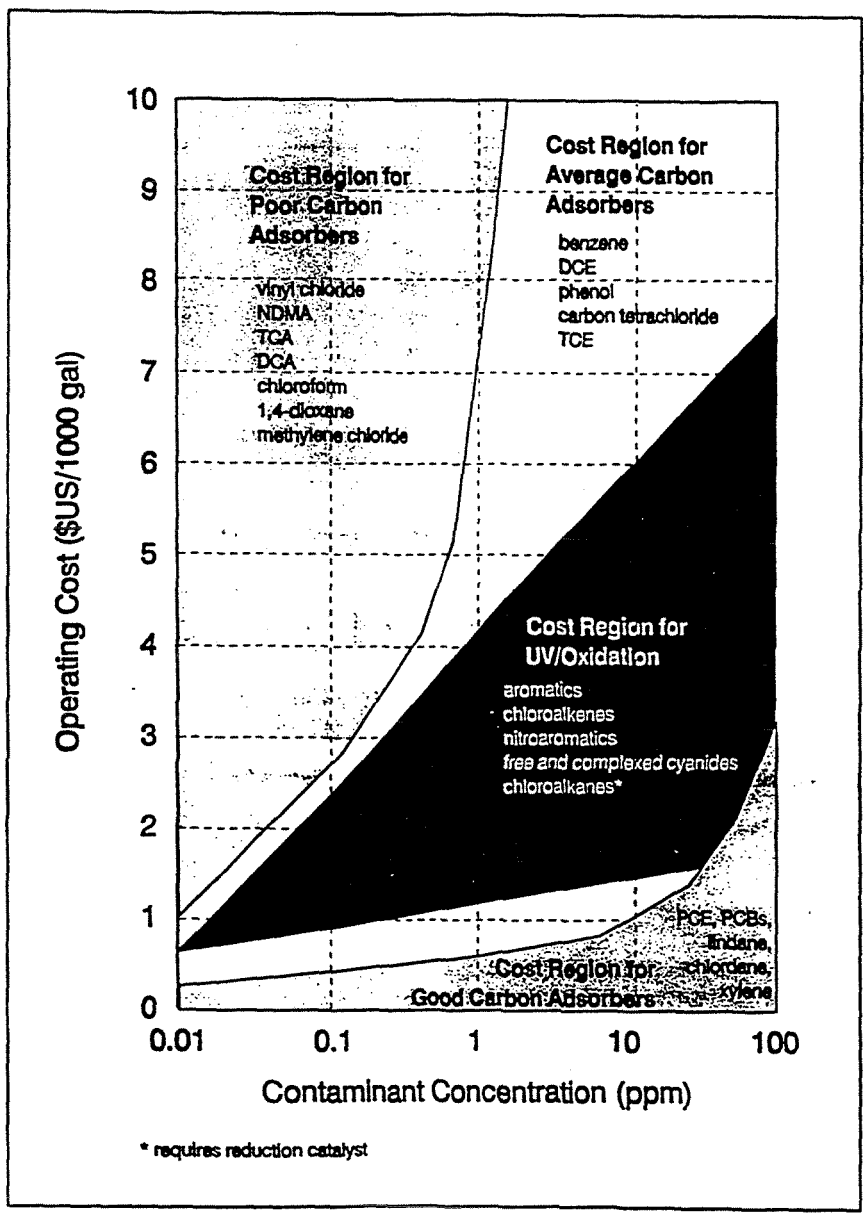

Figure 8. Operating cost regions for carbon absorption and UV/oxidation ($US, 1995) (reprinted from Notarfonzo, R.; McPhee, W. *Poll. Eng.* **1994**, *26*, 74-76).